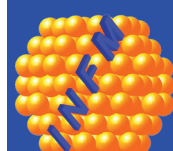
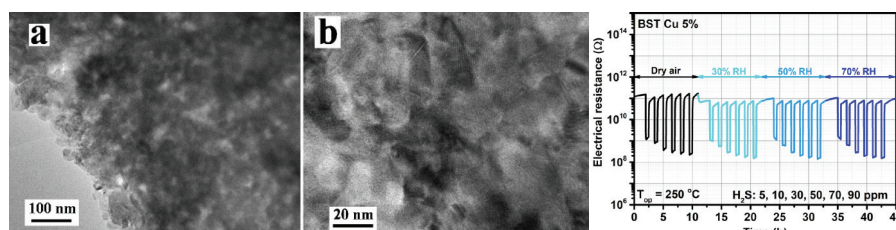
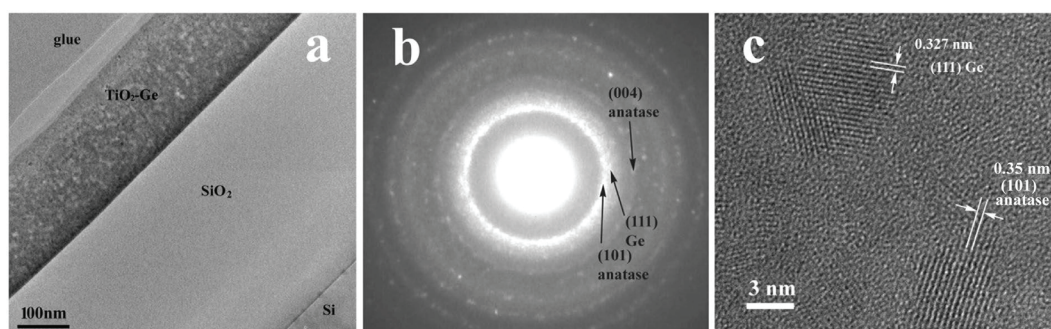
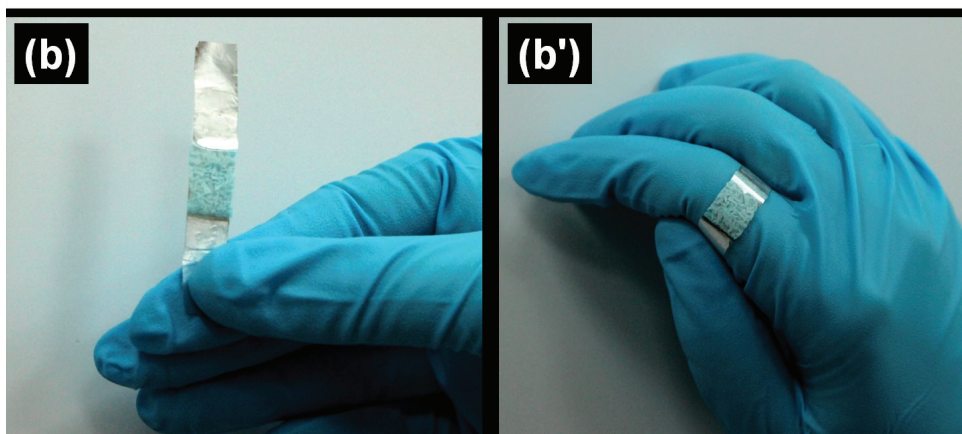
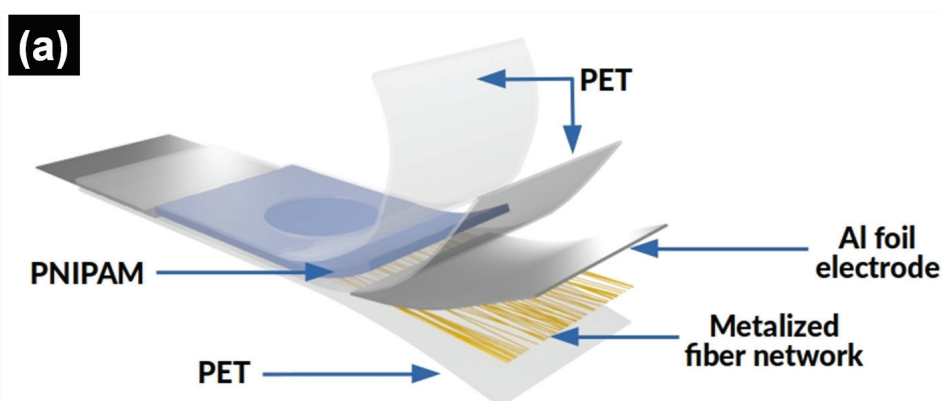


# National Institute of Materials Physics

# ANNUAL REPORT 2018





**COVER IMAGE**

Images from:

Upper image: Alexandru Evanghelidis, Mihaela Beregoi, Victor C. Diculescu, Andrei Galatanu, Paul Ganea, Ionut Enculescu Sci. Rep. 8, 17555 (2018)

Middle image: A.-M. Lepadatu, A. Slav, C. Palade, I. Dascalescu, M. Enculescu, S. Iftimie, S. Lazanu, V. S. Teodorescu, M. L. Ciurea, T. Stoica, Sci. Rep. 8, 4898 (2018).

Lower image: A. Stanoiu, R.M. Piticescu, C.E. Simion, C.F. Rusti-Ciobota, O.G. Florea, V.S. Teodorescu, P. Osiceanu, A. Sobetkii, V. Badilita, Sens. Actuators B 264, 327-336(2018).

# Directorate

---

General Director: **Dr. Ionuț Marius ENCULESCU**

Scientific Director: **Dr. Lucian PINTILIE**

Economic Director: **Ec. Gabriela IVĂNUȘ**



National Institute of Materials Physics  
405A Atomistilor Street, PO BOX MG-7, Măgurele, Ilfov, România



Phone: + 4 021 369 01 85

Fax: + 4 021 369 01 77



Email

Dr. I. ENCULESCU: [director@infim.ro](mailto:director@infim.ro)

Dr. L. PINTILIE: [pintilie@infim.ro](mailto:pintilie@infim.ro)

Website

[www.infim.ro](http://www.infim.ro)



# Contents

FOREWORD.....	6
SELECTED RESULTS .....	7
Fundamental properties of materials.....	8
Materials preparation and characterization .....	25
Advanced materials for applications .....	63
INTERNATIONAL CENTRE FOR ADVANCED TRAINING AND RESEARCH IN PHYSICS.....	84
PUBLICATIONS .....	87
CONFERENCES.....	103
INTERNATIONAL COLLABORATIONS .....	123
VISITORS .....	133
EVENTS.....	138
PERSONNEL SUMMARY .....	146
FUNDING SUMMARY .....	148

## Foreword

The turbulence continued in 2018 and the R&D sector suffered, again, of lack of predictability and insufficient funding. Only about 80 % from the allocated budget was actually consumed thus the rectification was again negative for R&D.

The Core Program was only for 10 months, generating more stress in a system already in a very critical situation. After more than 2 years from the starting of completions, finally Post-Doc (PD), Young Research Teams (TE) and Complex Research Projects at the Frontier of Science (PCCF) were contracted. The only major competition organized in 2018 was the competition for funding excellence in research (PFE) but the funds are for auxiliary and complementary measures not for funding real R&D activities.

Although the funding sources were scarce, NIMP has managed to survive for another year, continuing to publish articles in reputed journals. At the end of the year the cumulated impact factor was again nearly 600, with about 190 publications.

An important achievement in 2018 was the signing of a R&D service contract with a private company, in value of 200,000 USD, the largest private funding in the recent history of NIMP.

Two important workshops were organized in 2018, the 3rd edition of International Workshop of Materials Physics (May 2018), and the International Workshop on Advances of Nanomaterials (September 2019, in collaboration with ICTP Trieste).

Another important achievement in 2018 was the internationalization of NIMP, in the sense that an important number of foreign researchers came for work stages up to 18 months, many of them being AUF grantees (see the chapter Visitors).

Finally, towards the end of 2018 a completion for new Core Program was launched, this time for 4 years. NIMP submitted a good proposal, ranked three after evaluation. This is a good result and generates some predictability of funding for the next years. In any case, Core Program alone cannot cover all the necessary expenses for the normal functioning of NIMP. Additional funding sources should be identified, the most important being the National R&D Program 3. New competitions have to be organized, otherwise the situation will become very critical for all the national institutes.

NIMP Management Team

# FUNDAMENTAL PROPERTIES OF MATERIALS

SELECTED RESULTS

## Transport in quantum dot cavities

I. V. Dinu, V. Moldoveanu, P. Gartner

The steady-state transport properties of a quantum dot (QD) cavity system are calculated and discussed by writing down a dressed-states picture of the master equation describing the dynamics of an optically active QD embedded in a p-i-n structure which is also placed in a microcavity supporting a single radiation mode. In contrast to most studies in quantum optics we go beyond the two-level Jaynes-Cummings (JC) model and include the spin degree of freedom into the calculations, along with the corresponding optical selection rules. However, we restrict ourselves to the s-shell states from the conduction (CB) and valence bands (VB). Our approach relies on the reduced density matrix formalism and on the Kohn-Luttinger theory. We calculate and take into account the many-body effects originating from both intradot Coulomb interaction and electron-hole-photon coupling.

Now, at suitable frequencies, the electron fills the hole state in the VB, this optical recombination process being also complemented by the emission of a photon. An electronic current is therefore generated across the system only at the expense of optical recombination. The photon losses in the cavity, described by a parameter  $\kappa$  and non-radiative recombination processes ( $\gamma$ ).

Our study [1] includes: i) Analytical calculations of the system's spectral properties which suggest that around resonant regimes effective three-level  $\Lambda$  or V-systems are appropriate; ii) numerical calculations of the steady-state currents and photon number as the frequency of the cavity mode is varied and iii) a careful analysis of the dependence of the current as a function of the cavity losses parameter  $\kappa$ , especially in the strong coupling regime. We find that if the cavity is tuned to the biexciton-exciton transition the most efficient optical processes take place in a three-level  $\Lambda$ -system.

Since the cavity mode supports both  $\sigma_+$  and  $\sigma_-$  polarizations, the bright excitons  $|X_{\downarrow, n+1, n_{\pm}}\rangle$  and  $|X_{\downarrow, n+1, n_{\pm}}\rangle$  are simultaneously coupled to the ground

state  $|G_{n+, n_{\pm}}\rangle$  and biexciton state  $|XX_{n+, n_{\pm}-1}\rangle$ .

However, in real systems a non-vanishing binding energy prevents us to have equal resonant frequencies for transitions from the ground state to the exciton states and from the exciton states to the biexciton.

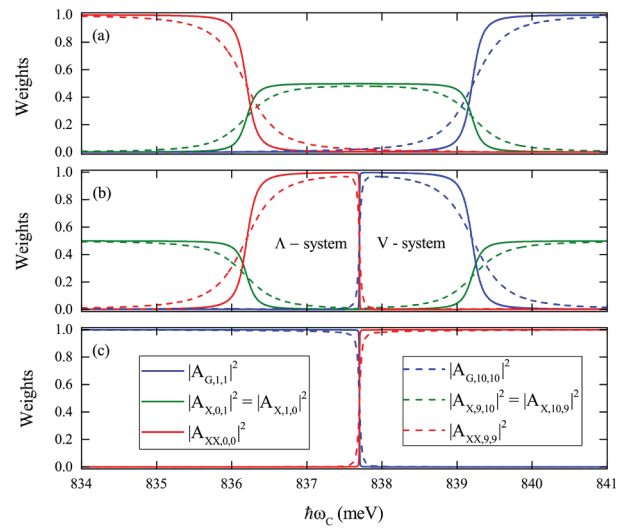


**Figure 1.** The weights of the ground state, exciton and biexciton states associated to three dressed states of the QD-cavity system as function of frequency. The quantum dot has radius  $R=15\text{nm}$  and height  $W=5\text{nm}$ .

We diagonalized numerically the QD-cavity Hamiltonian. The weights  $|A_{v,n+,n_{\pm}}|^2$  associated to three dressed states from two neutral subspaces with different photon numbers  $n_{\pm}$  are presented in Fig.1 as functions of  $\omega_c$ . It is not difficult to observe that away from  $\omega_c=837.75$  meV the three dressed states describe either a three-level  $\Lambda$ -system (if  $\omega_c < 837.5$  meV) either a V-system (if  $\omega_c > 838$  meV).

In the case of the  $\Lambda$ -system the mixing of the ground state  $|G_{n+, n_{\pm}}\rangle$  is negligible while for the V-system, the biexciton state is decoupled from the other states. Note that the weights also depend on the photon numbers except for the resonance points.

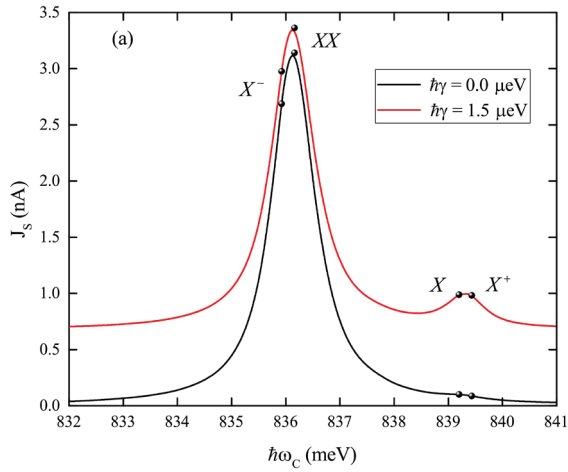


**Figure 2.** The steady-state current  $J_s$  as a function of the cavity frequency. (a)  $\mu_c = 625$  meV,  $\mu_v = -275$  meV.

We stress that under electrical injection trions and dark excitons are easily populated and contribute to the current, hence one cannot disregard them as it is safely done in the optically pumped systems.

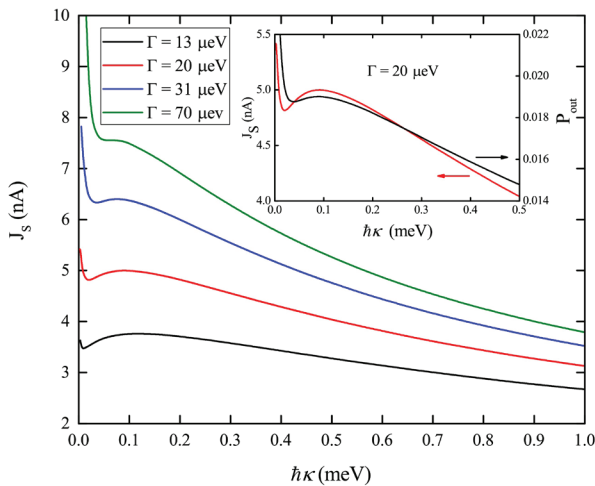


**Figure 3.** The steady-state current  $J_s$  as function of cavity losses  $\kappa$  at several values of the tunnelling strength  $\Gamma$ . The frequency of the cavity mode matches  $\omega_{XX}$ . Other parameters:  $\hbar g_c = 0.05$  meV,  $\mu_c = 625$  meV,  $\mu_v = -275$  meV,  $\hbar \gamma = 0.0015$  meV.

We present in (Fig.2) the steady-state current  $J_s$  as function of the frequency  $\omega_c$ . The largest peak around  $\omega_c = 836.25$  meV is due to the biexciton-exciton transition ( $XX \rightarrow X$ ) but also to  $X \rightarrow e$ . The separation between the two peaks is roughly given by the biexciton binding energy  $E_b$ . In contrast, around the exciton resonance the current does not differ much from the off-resonant background value, because the biexciton state is

continuously fed by the source reservoir.

The dependence of the current  $J_s$  as a function of the cavity losses  $\kappa$  is presented in (Fig.3) If  $\Gamma > 60$  eV the current decreases almost uniformly as  $\kappa$  increases, but as the coupling to the contacts decreases below  $\Gamma = 60$   $\mu$ eV a non-monotonous behavior emerges (see the inset in (Fig.3). Although  $J_s$  still drops rapidly for  $\hbar \kappa$  in the range  $[0.005, 0.025]$  meV (1st regime), then it increases until  $\hbar \kappa \sim 0.1$  meV (2nd regime) meV and eventually uniformly decreases (3rd regime).

Also, the local minimum of  $J_s(\kappa)$  shift to lower  $\kappa$  as  $\Gamma$  decreases. This complex behavior of the steady-state current is not easy to predict especially in view of the fact that  $N$  is a monotonously decreasing function of  $\kappa$  (not shown). A quite similar complex dependence is found for the output power  $P_{out} = \kappa N$  which follows closely the shape of the  $J_s$  (see inset in Fig.3). This is not surprising, since the power supplied to the system by the current injection is essentially recovered in the field coming out from the cavity. On the other hand, in the steady state  $P_{out}$  is equal to the net photon generation in the cavity and therefore the explanation of its behavior should rely on the interplay between photon emission and absorption processes.

Initially, the strong drop in the photon number with increasing  $\kappa$  leads to a decrease of  $P_{out}$ . Later, with  $N$  leveling off to small values, the photon generation decrease continues, due to the strong dephasing associated with large cavity losses.

The surprising effect is the intermediate interval of increasing behavior. It is clear from  $P_{out}$  being the product of the increasing  $\kappa$  and the decreasing  $N$ , that the whole picture is the result of competing tendencies. In the case of this middle interval, the careful examination of different contributions shows that photon emission (stimulated and spontaneous) and absorption are to a great extent compensating each other.

## References

- [1] I. V. Dinu, V. Moldoveanu, P. Gartner, Phys. Rev. B 97, 195442 (2018).

## Anomalous quantum Hall effect in a diatomic square lattice

B. Ostahie, M. Nita, A. Aldea

The paradigm of the anomalous quantum Hall effect was advanced by Haldane [1] for a hexagonal lattice model by imposing two sine qua non conditions: i) the hopping process to the next-nearest-neighbors (n.n.n), and ii) the phase attached to this process. The phase is justified in terms of a periodic internal magnetic field, chosen such that the flux through the unit cell vanishes. The phase diagram of the model contains domains with topological properties, where the Chern number is  $\nu = \pm 1$ . Such systems, which may support quantum Hall effect in the absence of an external magnetic field, have been called Chern insulators.

In principle, by virtue of the bulk-edge correspondence, alternatively to the approach based on topological invariants (which assumes Bloch functions and works for infinite systems), the topological properties can be addressed in terms of chiral edge states existing in finite systems.

This paper aims to detect chiral edge states, assumed to exist at vanishing magnetic flux under specific conditions and to support anomalous quantum Hall effect in Chern insulators. The confirmation of such states provides more physical insight into this effect, and it is by itself an interesting issue that certifies the bulk-edge correspondence also in this case. Also, in this paper we observe the presence of a semimetallic phase where edge states are intercalated with bulk states. By the use of disorder, we localize the bulk and activate the edge states, which prove to be robust and to support quantized transport. This result advances the new conceptual issue of the disorder-driven anomalous quantum Hall effect in this tip of lattice.

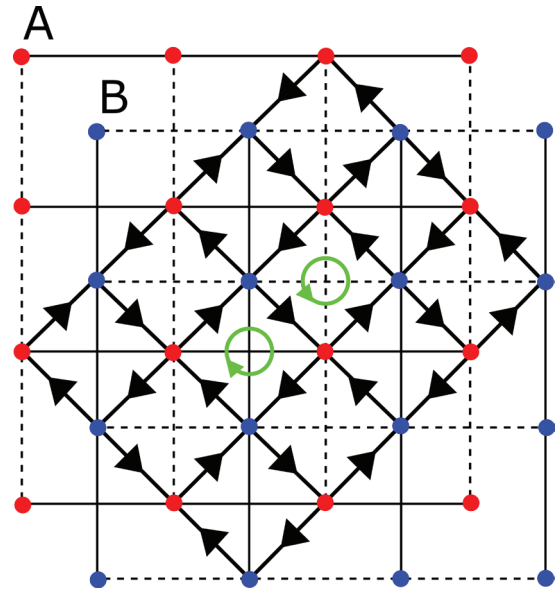


**Figure 1.** Diatomic square lattice structure: A and B atoms are interconnected by  $t_1$ , carrying the phase  $\gamma$ . The green arrows indicate the phase loops and the A-A and B-B hopping parameter  $t_2$  is real [2].

We analyze the spectral and topological transport properties of systems described by the following tight-binding model Hamiltonian:

$$\begin{aligned}
 H = & \sum_{n,m} [E_A a_{n,m}^\dagger a_{n,m} + E_B b_{n,m}^\dagger b_{n,m}] \\
 & - t_1 \sum_{n,m} [e^{-i\gamma} a_{n,m}^\dagger (b_{n,m} + b_{n-1,m-1}) \\
 & + e^{i\gamma} a_{n,m}^\dagger (b_{n,m-1} + b_{n-1,m}) + H.c.] \\
 & - t_2 \sum_{n,m} [a_{n,m}^\dagger (a_{n,m+1} - a_{n+1,m}) \\
 & - b_{n,m}^\dagger (b_{n,m+1} - b_{n+1,m}) + H.c.]
 \end{aligned}$$

where  $E_A$  and  $E_B$  are the atomic energies at the sites A and B, respectively, and  $t_1$ ,  $t_2$  are the nearest-neighbor and next-nearest-neighbor hopping parameters. Associated to  $t_1$ , the phase  $\gamma$  can be considered as resulting from a periodic magnetic field (as in Haldane's picture [1]), which does not generates any flux through the unit cell.

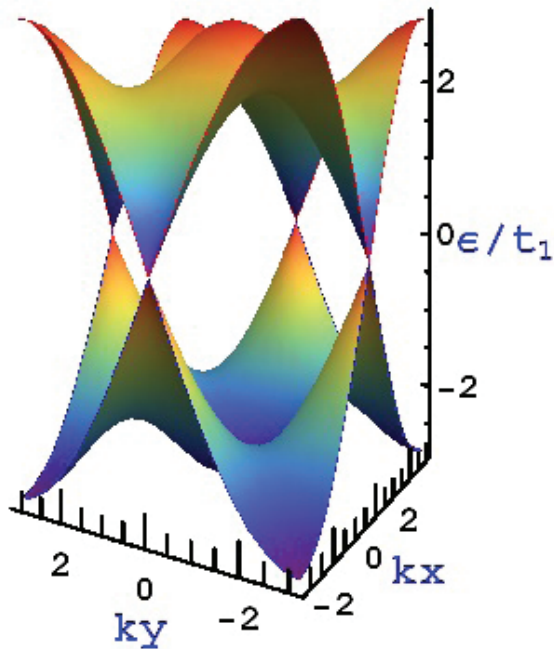


**Figure 2:** The energy spectrum of the semimetallic case showing band touching.

The energy spectrum of the Hamiltonian (1) can be obtained analytically from the characteristic equation resulting a two-band spectrum. The different phases (semimetallic, conventional insulator or Chern insulator) can be identified from the expression of the energy spectrum and the Hamiltonian symmetries. The spectral properties depend on the set of parameters  $\gamma$  (which controls the time-reversal),  $t_2$ , and atomic energies staggering. The electron-hole, time-reversal, and inversion symmetries are discussed [2]. The energy spectrum of the semimetallic phase may exhibit one or two touching points, depending on the circumstances (Fig.2).

To investigate the transport properties, we simulate the electronic Hall device by attaching four leads to a finite diatomic lattice. In our case the attention signal comes from the calculation of the Hall resistance that reveals the tendency toward quantization  $R_H = h/e^2$  as the disorder (impurities) in the system is increased gradually.

In (Fig.3) we show the Hall resistance for different strengths of the Anderson disorder characterized by the range  $[-W, W]$ , in which the diagonal energies of the tight-binding Hamiltonian are randomly distributed. It is to observe the

evolution of the curve  $R_H(\gamma)$  from the ordered case  $W = 0$  to the disordered one  $W = 6$ , which shows the quantum plateau (red curve). This outcome demonstrates that, in the disordered semimetal, the states in the bulk become localized and do not contribute to the transport process, while the edge states are robust against disorder and give rise to the anomalous quantum Hall effect.

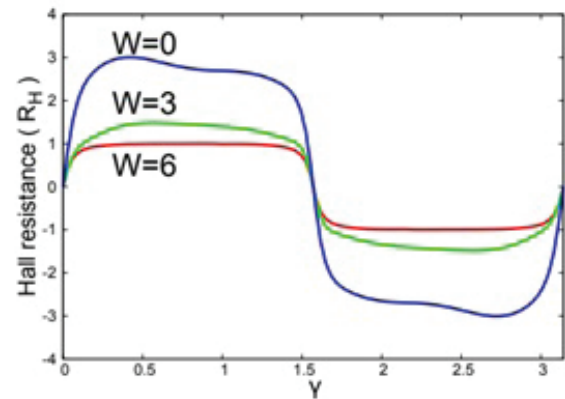


**Figure 3:** Disorder effect on the Hall resistance in the semimetallic phase as a function of  $\gamma$  for different disorder strengths.

In this paper we have studied the spectral and transport properties of diatomic lattice. By using Anderson disorder, we succeed to localize the bulk states and, at the same time, to observe a quantized Hall resistance at sufficiently strong disorder (Fig.3). This means that the edge states in the semimetallic phase are chiral and robust against disorder.

**References**

[1] F. D. M. Haldane, Phys. Rev. Lett. 61, 2015 (1988).  
 [2] B. Ostahie, M. Nita and A. Aldea Phys. Rev. B 98 125403 (2018).

## Studies on Vortex Matter, Dynamics and Pinning in Superconductors

A.Crisan, L.Miu, A.M.Ionescu, I.Ivan, V.Sandu

We investigated the AC magnetic response of a  $\text{YBa}_2\text{Cu}_3\text{O}_7$  film with embedded  $\text{BaZrO}_3$  (BZ) nanorods and  $\text{Y}_2\text{O}_3$  nanoparticles in a static magnetic field  $H_{dc}$  lower than the matching field  $H_{\Phi=4T}$ . AC-susceptibility measurements have been performed using PPMS equipment (Quantum Design) after the sample was cooled down from temperatures  $T > T_c$  to 50 K in the DC field  $H_{dc}$  perpendicularly oriented to the film surface. The AC-field amplitude  $h_{ac}$  was between 0.5 – 6 Oe at frequencies  $f$  between 11 and 5555 Hz. The measurements were performed in static DC magnetic fields of 2, 10, and 30 kOe. Complementary zero-field cooling DC magnetic relaxation curves, with the applied DC-magnetic field  $H_{DC}$  applied perpendicular to the film surface, were registered with a MPMS (Quantum Design) magnetometer.

The response of the vortex system to the AC excitation is rather complex but extremely useful for the characterization of the vortex dynamics. At small enough amplitude of the AC-field, the slow deformation of the vortex lattice at the surface propagates into the interior and vortices oscillate inside the pinning potentials. In this so-called Campbell regime, with a  $h_{ac}$ -independent screening current, it is possible to determine the average curvature of the pinning potential and to investigate the field and temperature dependence of the critical current density. At higher  $h_{ac}$ , vortices overcome the pinning well and the flux line system enters into a more dissipative regime with  $h_{ac}$ -dependent AC-susceptibility in which the effective vortex activation energy  $U_{eff}$  has a logarithmic dependence on the AC field induced current density  $J$ .

Current densities and electric fields were extracted from AC and DC magnetic measurements using the critical state model in the Clem-Sanchez approach. Pinning energy  $U_c$  (85.5 K) obtained from both  $E(J)$  characteristics and  $J(t=1/f)$  dependence at short time scale is about 900 K ( $k_B=1$ ), much higher than the ones obtained from DC magnetic

measurements, as can be seen in Figure 1. It was found that, for  $H_{DC} = 2$  kOe, the flux velocity during AC measurements is  $v=0.3$  cm s<sup>-1</sup> and only 1 nm s<sup>-1</sup> in DC relaxation measurements. Thus, the thermal smearing of the potential walls is reduced in AC experiments and the obtained  $U_c$  is always higher than  $U_c$  determined from DC magnetic measurements [1].

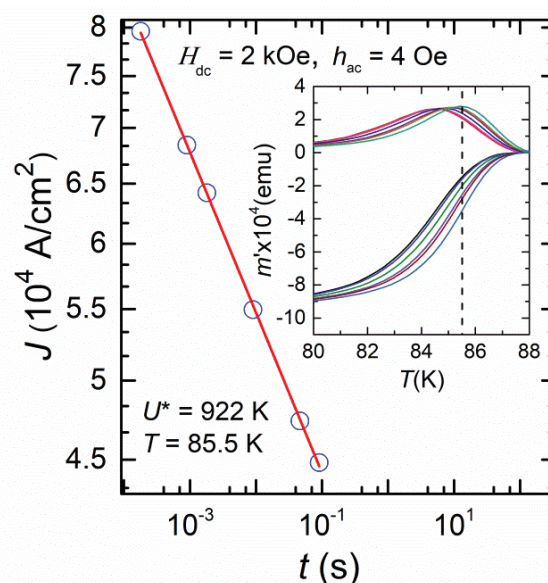


**Figure 1.** The induced current density  $J$  versus  $t = 1/f$  ( $H_{dc} = 2$  kOe,  $h_{ac} = 4$  Oe) at  $T = 85.5$  K. Inset: the temperature  $T$  dependence of the in-phase ( $m'$ ) and out-of-phase ( $m''$ ) components of the AC magnetic moment with  $h_a = 4$  Oe at various frequencies  $f$ .

The dynamic critical current  $J_d$  induced for AC driven forces at depinning frequencies was experimentally obtained by measuring the in-phase and out-of-phase magnetic responses ( $m'$ ,  $m''$ ) as a function of  $T$ , at various  $H_{DC}$ ,  $f$  and  $h_{ac}$ . The depinning frequency  $f_d$  extracted by the extrapolation of  $J$  to the order of magnitude of  $J_d \sim 10^5$  A cm<sup>-2</sup> is in agreement with the values obtained from microwave impedance measurements.

One of the most relevant features for the vortex phase diagram of superconductors is the second magnetization peak (SMP), with its on-set

$H_{on}$  and the peak field  $H_p$  located well below the irreversibility line, leading to fishtail shaped DC magnetic hysteresis curves. In the last years, several SMP models have been often considered, such as a crossover in the collective pinning regime, the square-to-rhombic structural vortex-lattice transition, an order-disorder transition, or a continuous pinning-induced disordering of the low- $H$  quasi-ordered vortex solid (the Bragg vortex glass, stable against dislocation formation) between  $H_{on}$  and  $H_p$ .

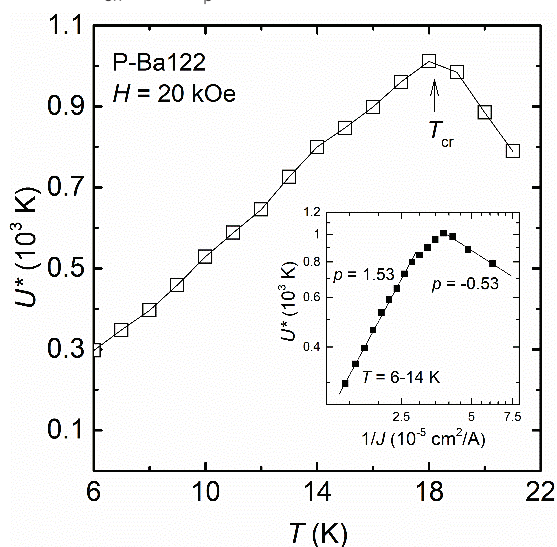


**Figure 2.** Main panel: The  $U^*(T)$  variation for P-Ba122 in  $H = 20$  kOe, with the characteristic  $U^*(T)$  maximum at  $T_{cr} \sim 18$  K, and a change of  $U^*(T)$  at a temperature  $T^* \sim 23$  K, related to the absence of an SMP on the  $m(H)$  curve at  $T = 24$  K. Inset: The  $U^*(1/J)$  dependence in log-log scales. A linear fit for  $T$  between 6 K and 14 K, where the applied field  $H = 20$  kOe  $\sim 7H_{on}(T)$ , supplies  $p \sim 3/2$ , revealing a small vortex bundle volume, whereas just above  $T_{cr}$  on has  $p \sim -0.5$ . The continuous lines represent a linear fit.

We performed detailed DC and AC magnetic measurements for an overdoped  $\text{La}_{2-x}\text{Sr}_x\text{CuO}_4$  single crystal and for two  $\text{BaFe}_2(\text{As}_{1-x}\text{P}_x)_2$  (P-Ba122) specimens: an underdoped sample (P-Ba122ud, nominal  $x = 0.28$ ,  $T_c \sim 28$  K), and an optimally doped one (P-Ba122op,  $x = 0.30$ ,  $T_c \sim 29$  K). The in-plane characteristic size of all specimens is of the order of 1 mm, while the thickness (along the  $c$  axis) is  $\sim 1$  mm for  $\text{LaSrCuO}$ , and only  $\sim 50$   $\mu\text{m}$  in the case of pnictide single crystals. The DC and AC magnetic fields were oriented along the crystallographic  $c$  axis, as usual, and strong

demagnetization effects are expected for P-Ba122, where the demagnetization factor  $D \sim 0.9$ .

The analysis of the DC magnetic hysteresis curves and of the AC magnetic response at usual frequencies and amplitudes registered for several superconducting single crystals (cuprates and pnictides) exhibiting a well developed DC SMP leads to the following conclusions [2,3]: (i) In the absence of strong demagnetization effects, the linear regime of the AC magnetic response extends above the  $H_p(T)$  line, and no distortion of the linear AC signal in the SMP domain can be detected. (ii) This behaviour appears to be related to the reduced values of the Campbell penetration depth (relative to the London penetration depth) across the SMP, located well below the DC irreversibility line. (iii) In the presence of strong demagnetization effects (plate-like specimens in perpendicular fields), where the nonlinear AC Bean regime sets in far below the DC irreversibility line, there is no nonmonotonic temperature variation of the in-phase (screening) component  $m'$  of the AC magnetic signal. This is expected for specimens with non-intersecting DC magnetic hysteresis curves (registered at various temperatures). (iv) A nonmonotonic, SMP-related variation has been obtained only for the ZFC DC field dependence of the out of phase  $m''$  component of the nonlinear AC magnetic moment.

## References

- [1] I. Ivan, A.M. Ionescu, V. Sandu, A. Crisan, L. Miu, *Superconductor Science and Technology*, 31, 105012, 2018.
- [2] L. Miu, A.M. Ionescu, D. Miu, T. Petrisor, A. Park, T. Tamegai, A. Crisan, *Physica C: Superconductivity and its Applications*, 555, 1-6, 2018.
- [3] A. M. Ionescu, D. Miu, A. Crisan, L. Miu, *Journal of Superconductivity and Novel Magnetism*, 31, 2329-2337, 2018.

## Interplay between polarization orientation in ferroelectric thin films and charge accumulation at surfaces and interfaces

I.C. Bucur, L.C. Tănase, L.E. Abramiuc, G.A. Lungu, D.G. Popescu, C. Chirilă, L. Hrib, L. Trupină, I. Pasuk, N.G. Apostol, R.M. Costescu, R.F. Negrea, L. Pintilie, C.M. Teodorescu

In our institute, one of the priorities is the study of ferroelectric (FE) materials for microelectronics applications as non-volatile memories, piezoelectric devices and catalysis.

In order to realize such devices, one must understand the mechanisms that contribute to the formation of out-of-plane polarization states.

Among the factors that are believed to influence the stabilization of the polarization, one may count the substrate properties (work function, conduction properties, dielectric constant) or atomic termination of the substrate. Other question that arises is connected to the relation between the depolarization field inside a ferroelectric, which is several order of magnitude higher than the coercive field and should destroy the single domain out-of-plane polarization state, unless inside the thin film a charge-compensation mechanism occurs. It is well known that in order to stabilize the polarization in a FE, the material uses free charge carriers to screen the depolarization field. These free charges sheets are created outside of the FE by contaminants [1] or by metal contacts [2-3]. In Ref. [4] we studied how the nature of the substrate influences the polarization orientation of a ultrathin ferroelectric film (10 nm PZT). The main technique used for characterization of the polarization state of a thin ferroelectric film is X-ray photo-electron spectroscopy (XPS) by detecting the chemical shifts of the core levels.

We start from a naive model assuming that when a ferroelectric semiconductor with a given work function is interfaced with another material with a different work function, the interface field would be oriented from the material with lower work function towards the material with higher work function, but improve it by taking into account charge transfer, self-doping, static charges created by ionized impurities and variation of work function with doping.

Two doping levels were used for the case of PZT on STO doped with Nb substrate: 0.05%

and 0.5%. From the XPS spectra, we derived that the dominant state of polarization for the clean (no contaminated) PZT film is P<sup>+</sup> (outwards polarization). The model proposed assumes that the electric field formed at the interface between ionized impurities from the depleted region in the semiconducting substrate and charge injected in the intrinsic ferroelectric is able to orient the ferroelectric polarization. Indeed, the computed interface field in both cases exceeds the coercive field  $(5-7) \times 10^7 \text{ Vm}^{-1}$  being large enough to induce outward polarization (from STON toward PZT).

However, for lower doping levels, this interface field is not enough to induce outwards polarization.

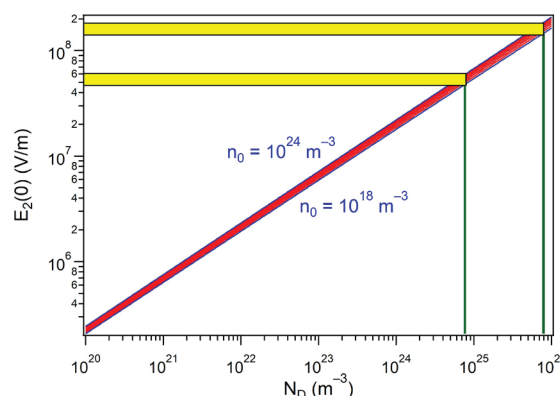


**Figure 1.** Electric field in intrinsic PZT at the interface with STON as a function on the doping level in STON. Vertical green lines represent the two Nb concentrations investigated. Solutions for different values of the carrier density in PZT ( $n_0$ ) are concentrated in the red region for  $10^{18} \text{ m}^{-3} \leq n_0 \leq 10^{24} \text{ m}^{-3}$ . Reproduced from [4] ©American Physical Society.

In the case analyzed of intrinsic PZT grown on intrinsic insulator, STO, with a lower work function, the latter is unable to inject electrons in the ferroelectric. But during the synthesis, PZT undergoes a process of p-type self-doping to allow charge transfer towards the substrate

(XPS data yielded p-type doping and also from the analysis of binding energies of core levels of PZT, inwards polarization P<sup>-</sup>). Theoretically, the interface between intrinsic STO and PZT should have been extremely abrupt and we practically noticed a smoothing of the energy bands due to the p-doping, we estimated the work function for  $\Phi_{\text{PZT}}^{(n)} \approx 4.45$  eV, and  $\Phi_{\text{PZT}}^{(p)} \approx 6.15$  eV. The calculated doping level being elevated, together with considerations on continuity of the valence band (‘common anion rule’) yields to the setup of a degenerated region in the ferroelectric material towards the surface. The field which further induces polarization is formed between the depleted region with ionized acceptors and the outer region with excess holes, its value in modulus being  $1.8 \times 10^8$  Vm<sup>-1</sup> exceeds the coercive field pointing towards the substrate.

In the case of PZT synthesized on a metal, SRO, with  $\Phi_{\text{SRO}} < \Phi_{\text{PZT}}$ , according to the simple model mentioned above, if the metal injects electrons inside the PZT, the interface field should orient the polarization towards the PZT (i. e. outwards) but after computing the value of this field, it is lower than the coercive field. From the stoichiometry of the PZT extracted from XPS data, Pb vacancies are observed, meaning p-type self doping of the sample. The mechanism proposed to explain this resembles the case of an insulating substrate with a lower work function, where the metal is „a mirror” of charges formed in the semiconductor, in which a depleted and a degenerate region simultaneously coexist. The interface field for this mechanism is estimated to be in modulus  $2.9 \times 10^9$  Vm<sup>-1</sup> large enough to orient inwards the polarization. For the opposite situation, when the ferroelectric is interfaced with a metal with a higher work function, in the vicinity of the interface a depleted region with positively ionized donors is built up, followed by a degenerate n-type self-doping region (i.e. oxygen vacancies) in the rest of the film and the orientation of the polarization is outwards. A classification of possible cases is given in (Fig.2).

In another work [2], platinum deposited on PZT/SRO, given the  $\Phi_{\text{Pt}} < \Phi_{\text{PZT}}$ , one should expect the formation of Schottky barrier for electrons but the reverse behavior is observed. From the XPS spectra, the as introduced film showed no

preferential out of plane orientation of polarization. After the deposition of Pt, a band bending near the interface towards lower energies is noticed using photoelectron spectroscopy. The possible explanation may be related to the fact that platinum provides electrons to the PZT substrate in order to compensate the depolarization field near the surface and this contributes to the induction of the ferroelectric out-of-plane outwards polarization with metal deposition.

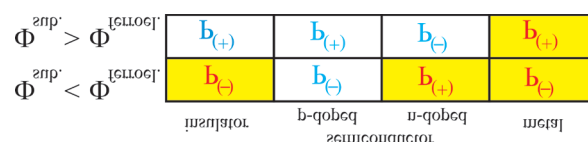


**Figure 2.** Overview of the cases investigated in terms of work function differences between the substrate and the ferroelectric film and as a function of the conduction properties of the substrate. Reproduced from [4] ©American Physical Society.

Without taking into account fine effects related to the interface termination, we sketched some mechanism explaining how charge accumulation for compensating the depolarization field, self-doping of the PZT films and the interface field drives the orientation of the polarization.

## References

- [1] L.E.Stoflea, N.G. Apostol, L. Trupină, C.M. Teodorescu, J. Mater. Chem. A 2,14386 (2014).
- [2] I.C. Bucur, L.C. Tănase, L.E. Abramiuc, G.A. Lungu, C. Chirilă, L. Trupină, N.G. Apostol, R.M. Costescu, R.F. Negrea, L. Pintilie, C.M. Teodorescu, Appl. Surf. Sci. 432, 27-33 (2018).
- [3] N.G. Apostol, L.E. Ștoflea, L.C. Tănase, I.C. Bucur, C. Chirilă, R.F. Negrea, C.M. Teodorescu, Appl. Surf. Sci. 354, 459-468 (2015).
- [4] L.C. Tănase, L.E. Abramiuc, D.G. Popescu, A.-M. Trandafir, N.G. Apostol, I.C. Bucur, L. Hrib, L. Pintilie, I. Pasuk, L. Trupină, C.M. Teodorescu, Phys. Rev. Appl. 10, 034020(1-19) (2018).

## Multiferroicity in Mn-doped ferroelectric thin films by indirect exchange mediate by charge accumulated at interfaces

I.C. Bucur, N.G. Apostol, L.E. Abramiuc, L.C. Tănase, C.A. Tache, G.A. Lungu, R.M. Costescu, C.F. Chirilă, L. Trupină, L. Pintilie, C.M. Teodorescu

Multiferroicity is the property of some materials or heterostructures to couple their magnetic and electric ordering. However, from a fundamental point of view, ferroelectric materials need strong ionic bonding, realized by ions with closed shell electronic structure, while for magnetism one needs the occurrence of ions with partially filled electronic shells, able to exhibit a nonzero total spin momentum. The only ‘natural’ multiferroic material known to date,  $\text{BiFeO}_3$ , is ferroelectric and antiferromagnetic in its pure state. For most applications, the most convenient coupling would be between the ferroelectric state and the ferromagnetic one, yielding e. g. the apparition of a magnetization when the system is subject to an external electric field or a ferroelectric polarization when the system is subject to an external magnetic field. Such systems are realized most readily by nanostructured mixing of two phases, a ferroelectric and a ferromagnetic one, and the coupling between ferroelectricity and ferromagnetism is mediated by mechanical stress, via piezoelectricity and magnetostriction.

The origin of magnetism is the exchange interaction, which can manifest between (incomplete) electron shells of separated atoms, or may occur as a characteristic of delocalized electrons, by splitting the bands corresponding to different orientation of carriers’ spin. A third way for ferromagnetism to occur is based on the interaction between localized magnetic moments and the delocalized charge carriers, which is accounted by the Zener or Ruderman-Kittel-Kasuya-Yosida (RKKY) interaction [1,2]. This is generically called indirect exchange.

A clean ferroelectric thin film exhibits quite often a single-domain out-of-plane polarization, a state which is stabilized by means of charge carriers concentrated near the surface to compensate the depolarization field, see (Fig.1) The main idea of the work from Ref. [3] was to implement insulated magnetic ions in these regions near surface

and to analyze by which extent these ions may become mutually magnetically ordered by indirect exchange mediated by the compensating charge carriers.

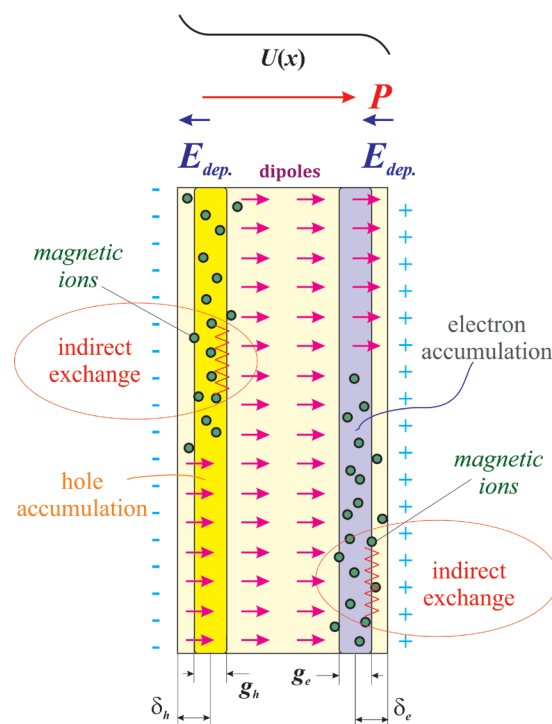


**Figure 1.** A ferroelectric thin film with out-of-plane polarization. Near the surfaces, charge carriers of opposite sign with respect to the fixed charges are accumulated to compensate the depolarization field and stabilize the ferroelectric state. Mutually insulated magnetic ions lying in these regions may be magnetically ordered by indirect exchange provided by the aforementioned charge carriers. Reproduced from [3] ©Elsevier.

The experiments were performed on 150 nm thick  $\text{Pb}(\text{Zr,Ti})\text{O}_3(001)$  thin films. Some of them were pre-sputtered with  $\text{Ar}^+$  ions (1 keV energy, 4  $\mu\text{A}$  ion current, 6 minutes) to enhance surface disorder and facilitate a deeper migration of manganese atoms inside the film. Manganese (the magnetic component) was deposited on PZT (001) held at 400 °C. At each stage, the samples were characterized by X-ray photoelectron spectroscopy (XPS). (Fig.2) presents Pb 4f spectra obtained after Mn deposition on films with and without  $\text{Ar}^+$  sputtering.

The polarization state of these films is clearly different: inwards polarization dominates in the case of sputtered films and outwards polarization dominates for unspuntered films. Piezoresponse force microscopy confirmed these attributions.

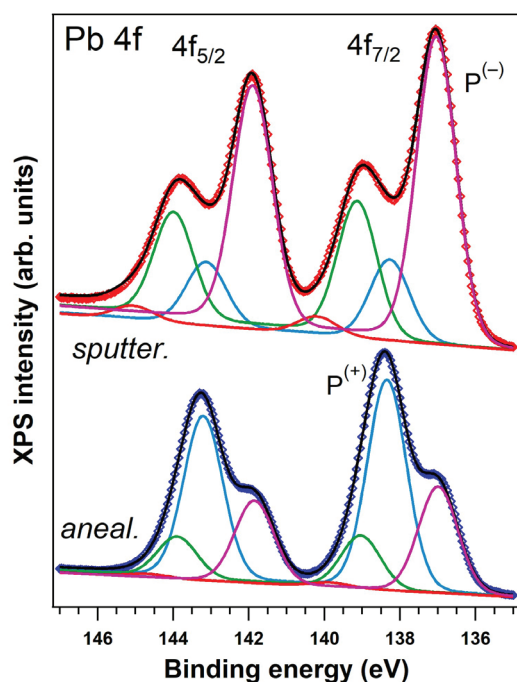


**Figure 2.** Pb 4f XPS spectra for 150 nm PZT (001) after Mn deposition at 400 °C. One PZT(001) was just annealed in ultrahigh vacuum prior Mn deposition, while the other was also sputtered with Ar<sup>+</sup> ions. Adapted from [3] ©Elsevier.

Magneto-optical Kerr effect (MOKE) measurements exhibit hysteresis loops for the sputtered sample, whereas the behavior of the unspuntered sample is ferromagnetic. From XPS, the ionization state of Mn is similar in both cases. Thus, the main difference is represented by the ferroelectric polarization in the two cases. Inwards polarization needs holes to be stabilized near the surface, and a RKKY-like mechanism mediated by holes is expected to be more robust than that mediated by electrons, owing to a larger (heavy) hole effective mass in PZT.

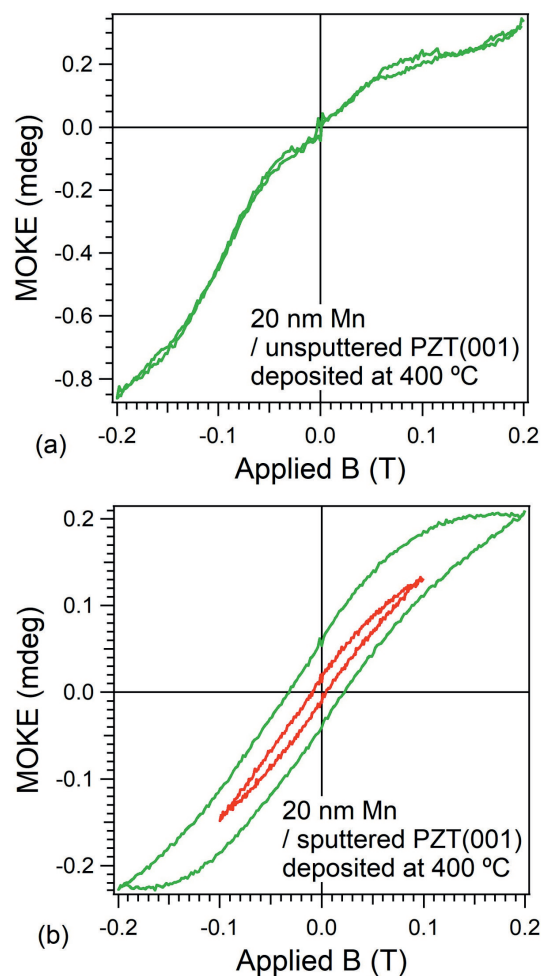


**Figure 3.** MOKE hysteresis loops recorded at room temperature on the films analyzed by XPS in Fig. 2. Reproduced from [3] ©Elsevier. Thus, the occurrence of ferromagnetism, at least at room temperature, is intrinsically connected with the orientation of the ferroelectric polarization. Technical applications may be foreseen in data storage or field controllable magneto-optic devices.

## References

- [1] G.A. Lungu, L.E. Stoflea, L.C. Tănase, I.C. Bucur, N. Răduțoiu, F. Vasiliu, I. Mercioniu, V. Kuncser, C.M. Teodorescu, *Materials* 7, 106–129 (2014).
- [2] G.A. Lungu, N.G. Apostol, C.M. Teodorescu, in *Nanomagnetism*, J.M. Gonzalez Estevez (Ed.), OneCentralPress, Manchester, pp. 74–110 (2014).
- [3] I.C. Bucur, N.G. Apostol, L.E. Abramiuc, L.C. Tănase, C.A. Tache, G.A. Lungu, R.M. Costescu, C.F. Chirilă, L. Trupină, L. Pintilie, C.M. Teodorescu, *Thin Solid Films* 669, 440–449 (2019).

## Vibrational and photoluminescence properties of composites based on carbon nanotubes and conjugated polymers

M. Baibarac, A. Matea, M. Daescu, M. Stroe, I. Mercioniu,

in cooperation with

S. Quillard, J.Y. Mevellec, S. Lefrant

Institut des Materiaux Jean Rouxel, Nantes, France

C. Serbschi

Bioelectronic SRL, Ploiesti, Romania

Composites based on polypyrrole (PPY) or polyaniline (PANI) and carbon nanotubes are extensively studied due their applications in the field sensors, photovoltaic devices and so on.[1,2] A recent topic regards the influence of SWNTs highly separated in metallic tubes (98%) and semiconducting tubes (99%) on the aniline electropolymerization in the presence of H<sub>2</sub>SO<sub>4</sub> and HCl [1]. The vibrational properties of PANI/SWNTs composites demonstrate that the aniline electropolymerization in the S and M-SWNTs presence leads to: i) SWNTs covalently functionalized with PANI-ES and PANI-LS and ii) the formation of ANI trimers and tetramers..

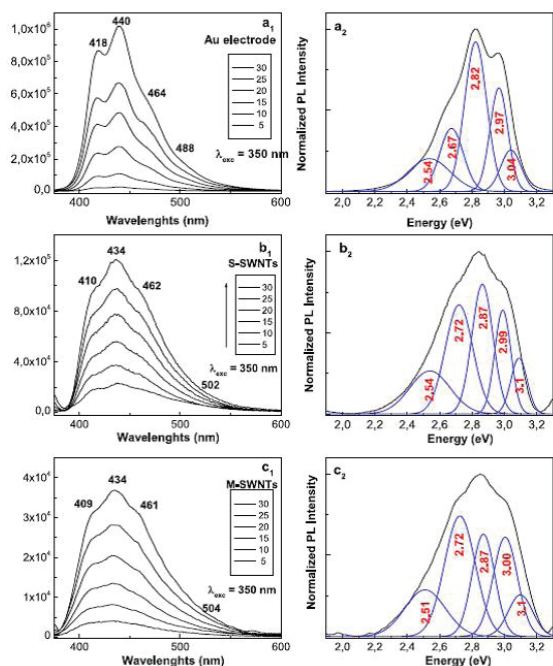


**Figure 1.** The PL spectra of PANI doped with HSO<sub>4</sub><sup>-</sup> ions electrosynthesized onto the blank Au electrode (**a**) and the Au plates covered with a film of S-SWNTs (**b**) and M-SWNTs (**c**) during 5, 10, 15, 20, 25 and 30 CVs. De-convolution of the PL spectra recorded after 30 CVs onto the blank Au electrode (**a2**) and the Au plates covered with a film of S-SWNTs (**b2**) and M-SWNTs (**c2**). [Re-print from Ref. 1]

In (**Fig. 1**), the PL spectra of PANI doped with HSO<sub>4</sub><sup>-</sup> ions, show five emission bands peaking at 408 nm (3.04 eV), 418 nm (2.97 eV), 440 nm (2.82 eV), 464 nm (2.67 eV) and 488 nm (2.54 eV). In this context, the PL band with a maximum at 3.04 eV was assigned to the ANI trimmers (TR). The last four PL bands were assigned to the electronic transitions of small MCs of tetramer (TT) type, the reduced entities of the PANI repeating units, the oxidative entities of the repeating units of PANI in an un-doped state and the oxidative entities that contain semi-quinoid structures in the repeating units of PANI doped with HSO<sub>4</sub><sup>-</sup> ions. The presence of PL bands situated at 2.67 and 2.54 eV in (**Fig. 1a2**) indicate the generation of a PANI partially doped.

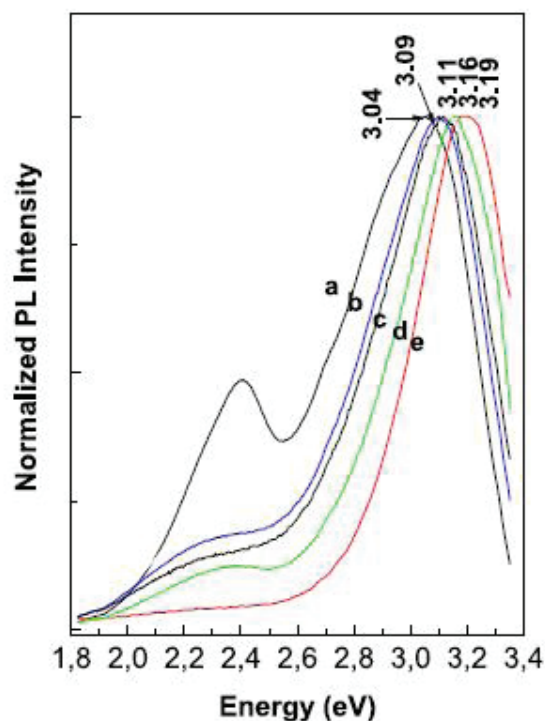


**Figure 2.** The PL spectra of the powder (**a**) and ANI TR films with thicknesses of 256 (**b**), 192 (**c**), 92 (**d**) and 32 nm (**e**). [Re-print from Ref. 1]

According to **(Fig.2)**, the PL spectra of the powder and films of ANI TR, with thicknesses of 256, 192, 92 and 32 nm, highlight an intense emission band with the maximum varying from 3.04 eV (**Fig.2**, curve a) to 3.09 eV (**Fig.2**, curve b), 3.11 eV (**Fig.2**, curve c), 3.16 eV (**Fig.2**, curve d) and 3.19 eV (**Fig.2**, curve e). [1] The addition of M-SWNTs or S-SWNTs leads to a PANI PL quenching effect that originates in a charge collector process. The quenching effect is more intense in the case of M-SWNTs in comparison with S-SWNTs (**Fig.3**). This behavior can be explained taking into account the diagrams of the electronic energy levels of S-SWNTs, M-SWNTs and PANI.

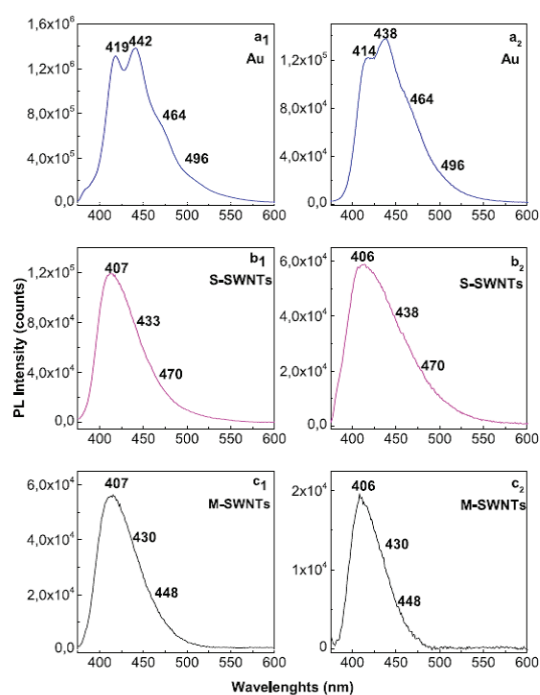


**Figure 3.** The PL spectra of the samples of PANI doped with  $\text{HSO}_4^-$  and  $\text{Cl}^-$  ions, respectively, electrochemically synthesized during the 30 CVs onto the blank Au electrode (**a<sub>1</sub>** and **a<sub>2</sub>**) and the Au plates covered with films of S-SWNTs (**b<sub>1</sub>** and **b<sub>2</sub>**) and M-SWNTs (**c<sub>1</sub>** and **c<sub>2</sub>**) after the interaction with the 1 M  $\text{NH}_4\text{OH}$  solution. [Re-print from Ref. 1]

According to **(Fig.4)**, the superposition of the HOMO levels of the two constituents, i.e. macromolecular compound and CNTs, is observed only in the case of PANI doped with  $\text{Cl}^-$  ions and M-SWNTs.

The optical band gap of PANI doped with  $\text{Cl}^-$  ions and the onset potential for the oxidation of macro-

molecular compound were equal with 1.54 eV and 0.47 eV, respectively.

The PANI PL quenching mechanism takes into account that the excitons resulted onto the MCs of PANI doped with  $\text{Cl}^-$  ions, under optical excitation, are dissociated into electrons and holes. Further, the electrons are collected of LUMO levels of S-SWNTs with the chirality (14,5) and M-SWNTs with the chirality (10,8) and successively passed on the levels with smaller energy values until to the lower LUMO level.

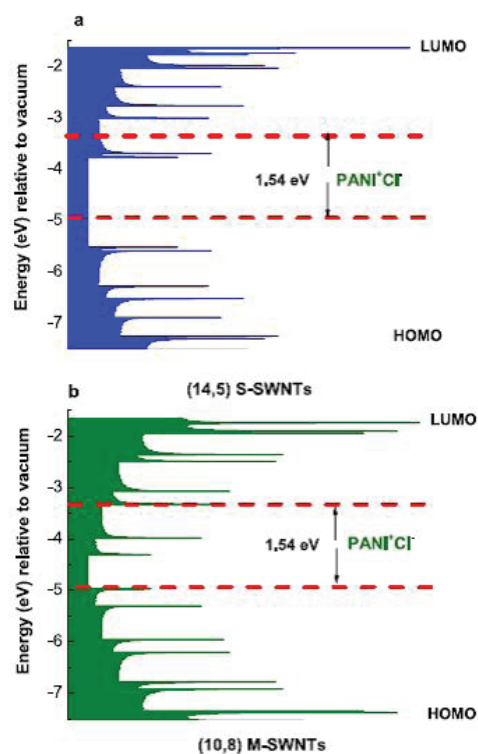


**Figure 4.** Diagram of electronic energy levels of S-SWNTs (**a**), M-SWNTs (**b**) and PANI doped with  $\text{Cl}^-$  ions (red lines). [Re-print from Ref. 1]

## References

- [1] M. Baibarac, A. Matea, M. Daescu, I. Mercioniu, S. Quillard, J.Y. Mevellec, S. Lefrant, Polyaniline photoluminescence quenching induced by single-walled carbon nanotubes enriched in metallic and semi-conducting tubes, *Scientific Reports*, 8, 9512 (2018), IF=4.122, AIS=1.356.
- [2] M. Baibarac, C. Serbschi, M. Stroe, Electrochemical Synthesis of the Composites Based on Multi-Wall Carbon Nanotubes and Polypyrrole Doped with Phosphomolybdic Acid Heteropolyanions and Their Vibrational Properties, *International Journal of Electrochemical Science*, 13(11), 10514, IF=1.369, AIS=0.231.

## Electronic structure of buried interfaces revealed in soft X-ray photoemission experiments

in collaboration with:

M. A. Husanu

V. N. Strocov, A. Chikina, M. Caputo, X. Wang, M. Radovic, B. Tobler, T. Schmitt, Paul Scherrer Institut 5232, Villigen, Switzerland;

F. Lechermann, Institut für Theoretische Physik, Universität Hamburg, Jungiusstrasse 9, Hamburg DE-20355, Germany

C. Cancellieri, Empa, Swiss Federal Laboratories for Materials Science & Technology, Ueberlandstrasse 129, Dübendorf CH-8600, Switzerland;

L. L. Lev, I. O. Maiboroda, E. S. Grichuk, N. K. Chumakov, I. S. Ezubchenko, I. A. Chernykh, M. L. Zhanaveskin, V. G. Valeyev, National Research Centre “Kurchatov Institute”, 123182, Moscow, Russia.

One of the main goals in nowadays technological developments is to pursue device miniaturisation while: i) keeping the same or even enhance the bulk efficiency, and ii) reducing their energy consumption. Such demand often requires creative strategies, involving the exploration of new materials or creating new functionality in cleverly engineered systems. One example which illustrates such approach is the work undertaken by a group of researchers from Switzerland, Germany and Romania devoted to better understanding the perspective of tuning the enhanced electron mobility appearing due to formation of a two dimensional electron gas (2DEG) at the interface between two insulating oxides

( $\text{LaAlO}_3$  - LAO and  $\text{SrTiO}_3$ -STO) [1], by engineering the concentration of oxygen vacancies ( $\text{V}_{\text{O}}$ s). In this sense, accurate understanding of the orbital character and the energetics of the VO states are crucial.

Remarkably, the results obtained in resonant angle-resolved photoemission spectroscopy, X-ray absorption spectroscopy (XAS) measurements and first-principles calculations for epitaxial LAO/STO samples prepared by pulsed laser deposition [2] indicate that VOs are featured by in-gap states (IGS) localized at  $\sim 1.3$ - $1.5$  eV below the Fermi energy and their orbital character is radically different from that of the 2DEG at the interface. This is an important aspect as it is known that creating  $\text{V}_{\text{O}}$ s comes with two additional electrons, yet it was unclear so far how and where the

excess charge builds-up and what are their triggered effects. The invoked study [2], clearly establishes the  $\text{Ti}^{3+}$  resonant character of the VO states and  $\text{Ti}^{4+}$  of the 2DEG, through their different signature in XAS and ResPE performed at the L<sub>2,3</sub> edges of Ti (456 eV-466 eV) (Fig. 1). By tuning the excitation energy at different values, probing either the IGS or the 2DEG, their band signature is revealed, and by corroborating with DMFT calculations, their orbital character is unambiguously established.

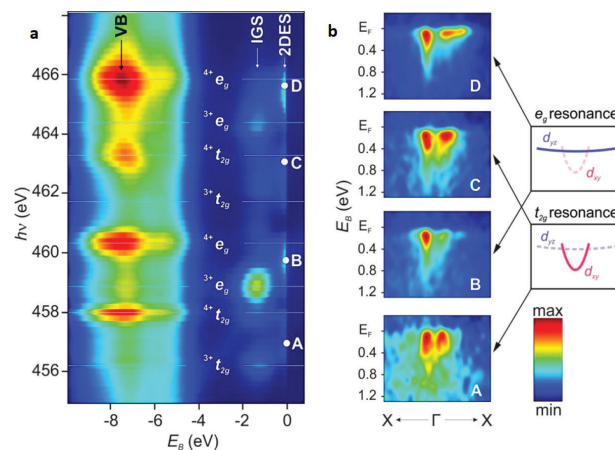


**Figure 1(a).** Resonant (angle-integrated) photoemission intensity map for LAO/STO across the Ti L<sub>2,3</sub> resonances, identifying the VB, IGS, and 2DES states. The IGSs resonate at the unoccupied  $\text{Ti}^{3+}$   $e_g$  states, and the 2DES between the  $\text{Ti}^{3+}$  and  $\text{Ti}^{4+}$   $e_g$  states. The different resonant behaviors of the IGS and 2DES reflect their different valence and orbital characters. (b) Band map of the 2DES (normalized to maximum intensity) along  $X$ - $\Gamma$ - $X$  direction of the BZ.

The schematics show the intensity enhancement of the  $d_{xy}$  ( $d_{yz}$ ) states at the  $t_{2g}$  ( $eg$ ) resonances, correspondingly. Reprinted with permission from A. Chikina et al, ACS Nano 12, 7927. Copyright 2018 American Chemical Society.

Moreover, besides their  $e_g(x^2-y^2)$  character (un-occupied in the absence of  $V_{OS}$ ) which differs from the  $t_{2g}(d_{xy,xz,yz})$  of the 2DEG, ResPE allows to shine-up and disentangle the composition of the interface mobile electrons in a) highly localized within the first interface layer ( $d_{xy}$ ) and b) more delocalized ( $d_{yz/xz}$ ), justifying the assignment of two dimensional electron system (2DES) instead of 2DEG.

Making use of the enhanced probing depth of the SX-ARPES technique, a different study of a Russian-Swiss-Romanian team [3] revealed the different effective mass of the highly mobile electron system at the AlN/GaN interface depending on crystalline orientation.

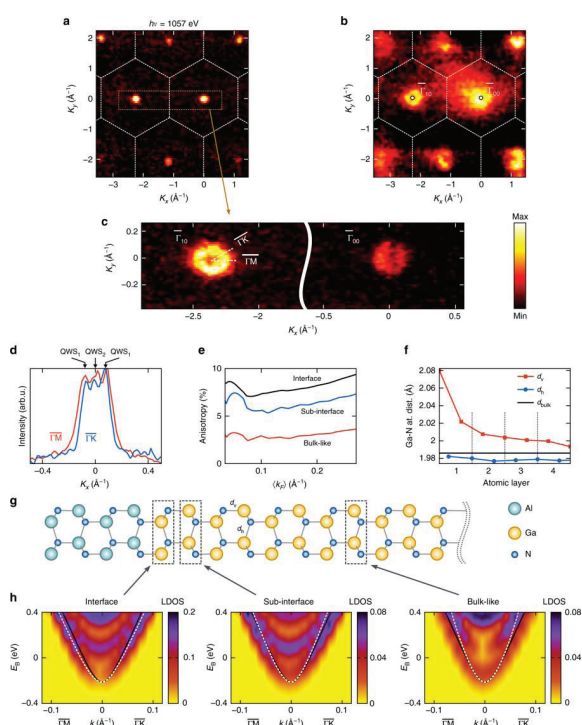


**Figure 2.** FS formed by the buried 2DEG. a) Experimental FS formed by the 2DEG in comparison with b) iso-EB surface of the VB near the VBM. The FS appears as narrow electron pockets centered at the around the  $\Gamma$ -points, consistent with the CBM-derived character of the 2DEG. Both VB and FS maps reflect the  $C_{6v}$  symmetry of the GaN crystal lattice. c) FS along the  $\Gamma_{00}$ - $\Gamma_{10}$  line acquired with high energy and angle resolution. d) MDCs of the Fermi intensity around the  $\Gamma_{10}$  point identifying the tiny QWS2 and anisotropy of the QWS1 between the  $\Gamma M$  and  $\Gamma K$  azimuths with AF ~ 12%. e) Calculated AF of QWS1 between  $\Gamma M$  and  $\Gamma K$  as a function

of band filling characterized by  $\langle kF \rangle$ , for bulk GaN and for various heterostructure layers. f) Relaxation of the Ga-N bond length as a function of depth and g) u.c. used in the slab calculations. h)  $k_{||}$ -resolved LDOS for various heterostructure layers near the CBM with EF adjusted to the experimental  $\langle kF \rangle$  and superimposed with the corresponding bulk  $E(k)$  along  $\Gamma M$  and  $\Gamma K$  (black lines). The QWS1 dispersion (white dashed in the bottom of the LDOS continuum) in the top GaN layers shows an asymmetry related to the interfacial atomic relaxation. From [2], under Creative Commons Attribution 4.0 International License ([creativecommons.org/licenses/by/4.0](https://creativecommons.org/licenses/by/4.0)).

Nitrides are currently under effervescent investigations for aerospace applications and devices working in extreme environment. Interfacing GaN and AlN induces a band alignment in such a way that the minimum of the GaN conduction band becomes electron-populated. The highly mobile electrons in the interface quantum well states were thought to have isotropic effective mass. Previously overlooked, the mass anisotropy identified in [3] could enhance the mobility in high electron mobility transistors (HEMT) with ~12% when we carefully consider the orientation of the GaN wafer with respect to the crystallographic axis.

By orienting the AlN/GaN sample, with its hexagonal symmetry along the  $\Gamma M$  or  $\Gamma K$  directions, the exact signature of the quantum well states (QWS) hosted at the interface is obtained, with the Fermi surfaces (FS) revealing their  $C_{6v}$  symmetry – derived from the conduction band minimum (CBM) of GaN, the same with that of the maximum of the valence band (VB) (Fig.2 a, b). The different values of the Fermi momenta along the two directions suggest band dispersions with different effective masses (Fig.2c,d). Indeed, first-principles calculations and Hall measurements, converged in evidencing and explaining this effect. The origin of the effective mass anisotropy lies in fact in the local relaxation of the interface layer (Fig. 2f, g), leading to modified dispersion of the interface energy bands with respect to the bulk. On technological perspective, the saturation currents of HEMTS should become higher along the direction featured by smaller effective mass ( $\Gamma K$ ) and lower for the  $\Gamma M$  orientation.

## References

- [1] A. Ohtomo, H. Y. Hwang, Nature 427, 423 (2004).
- [2] A. Chikina, F. Lechermann, M. A. Husanu, M. Caputo, C. Cancellieri, X.Q. Wang, T. Schmitt, M. Radovic, V.N. Strocov, ACS Nano 12, 7927 (2018).
- [3] L. Lev, I. Maiboroda, M. A. Husanu, E.S. Grichuk, N.K. Chumakov, I.S. Ezubchenko, I.A. Chernykh, X. Wang, B. Tobler, T. Schmitt, M.L. Zanaveskin, V.G. Valeyev, V.N. Strocov, Nature Commun. 9, 2653 (2018).

## Dynamic effects induced by measuring conditions in perovskite solar cells

Ioana Pintilie, Cristina Besleaga, Andrei Gabriel Tomulescu,  
Alexandra Palici, Lucian Pintilie, in collaboration with

G.A. Nemnes

University of Bucharest, Faculty of Physics, 077125, Magurele, Ilfov, Romania

Horia Hulubei National Institute for Physics and Nuclear Engineering, 077126 Magurele, Ilfov, Romania  
and

A. Manolescu

Reykjavik University, Menntavegur 1, IS-101 Reykjavik, Iceland

The perovskite solar cells (PSC) have attracted a considerable interest in the photovoltaics community, showing a very fast development in terms of power conversion efficiency (PCE), reaching now values of 23.3% certified PCE in not stabilized small area samples, proving that they can become real competitors to commonly used solar-cell materials. However, in spite of the rapid enhancement of the PCE during the past few years, the PSCs were shown to exhibit significant J-V hysteresis effect. The dynamic effects observed in the J-V measurements represent one important hallmark in the behavior of the perovskite solar cells.

Proper measurement protocols (MPs) should be employed for the experimental data reproducibility, in particular for a reliable evaluation of the power conversion efficiency, as well as for a meaningful characterization of the type and magnitude of the hysteresis. We show that pre-poling conditions and bias scan rate can have a dramatic influence not only on the apparent solar cell performance, but also on the hysteretic phenomena. Several MPs are discussed by comparing the experimental J-V characteristics with simulated ones using the dynamic electrical model (DEM) [1]. Under certain measurement conditions, a hysteresis-free behavior with relatively high PCEs may be observed, although the J-V characteristics may be far away from the stationary case.

Furthermore, forward-reverse (F-R) and reverse-forward (R-F) bias scans show qualitatively different behaviors regarding the type of the hysteresis, normal and inverted,

depending on the bias pre-poling. A unified picture of these two apparently independent hysteretic phenomena was provided by DEM [2], which introduces a time dependent description of the current and internal polarization, as the PSC is subjected to an arbitrary voltage scan and initial poling conditions. We show that based on DEM, the actual outcome of the chosen measurement protocol (MP) can be described [3,4]. We present in (Fig.1) a diagram showing the relations between DEM together with the employed MP and the result of the measurement, having as input experimentally accessible parameters as the pre-poling voltage bias  $V_{pol}$  applied for a time  $t_{pol}$  and the parameters related to the voltage scan  $V(t)$  (scan rate, direction and range). We investigated the dynamic effects induced by several measurement conditions, the numerical simulations in the framework of DEM being validated by experiment. We showed that both, the scan direction in consecutive R-F and F-R scans and the sign of the bias pre-poling voltage set up the type of the hysteresis: normal hysteresis (NH) or inverted hysteresis (IH).

Depending on MP and physical parameters, the hysteretic behavior can change from NH to IH, with an intermediate mixed hysteresis (MH) behavior, characterized by one or more crossing points between the forward and the reverse characteristics in  $(0, V_{oc})$  range (see Fig.2). Recurring features like the current overshoot in reverse and the crossing of the forward and reverse characteristics are analyzed in detail for experimentally relevant

conditions and are consistently explained by DEM. Our three-step MP requires that the scan range, the rate and the poling voltage are correctly set, in relation to the pre-determined  $V_{oc}$ , offering a good approximation of the stationary case (see Fig.3). We define a hysteresis

index (H) which consistently assigns the hysteresis type and magnitude [4]. We introduce here a properly scaled H index, as a global parameter for the entire working regime, with H index > 0 for NH and H index < 0 for IH.

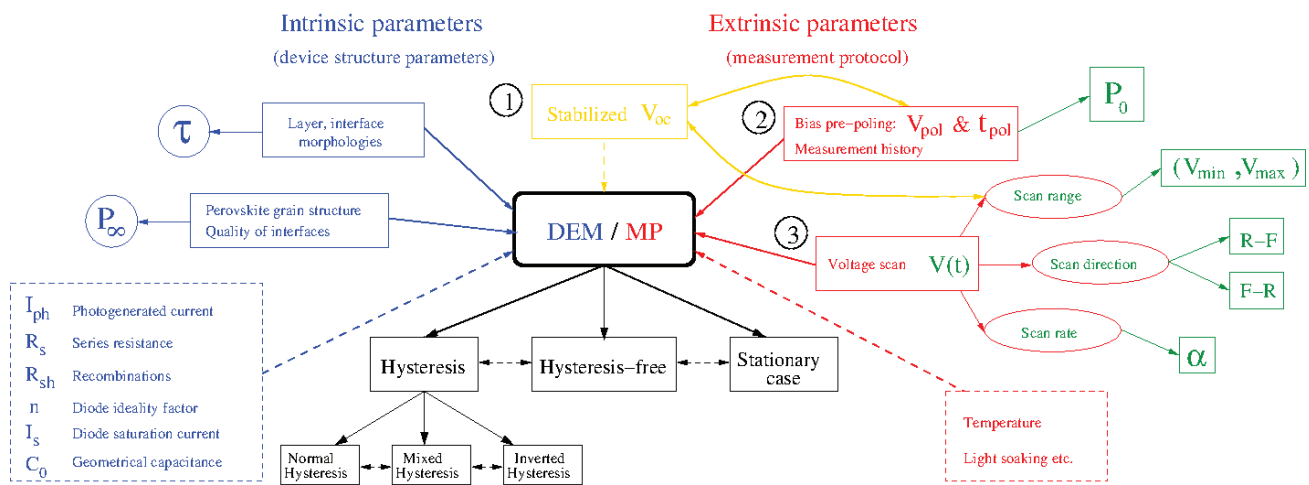


Figure 1. Intrinsic and Extrinsic parameters influencing the dynamic hysteretic phenomena as described by DEM, within a specified MP. Color codes: model (blue), experimental (red),  $V_{oc}$  stabilization step (orange), MP specific parameters considered in DEM (green) and the dynamic J-V outcome (black).

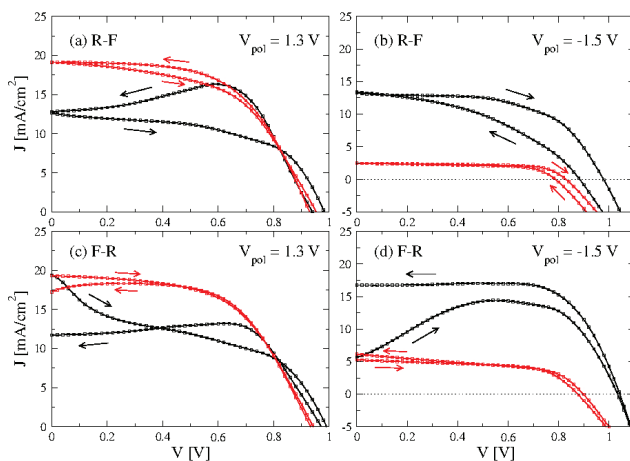


Figure 2. Experimental J-V characteristics obtained by R-F (a,b) and F-R (c,d) scans, at the scan rates  $\alpha = 20$  mV/s (black) and 500 mV/s (red).  $V_{pol}$  applied for a time  $t_{pol} = 30$  s.

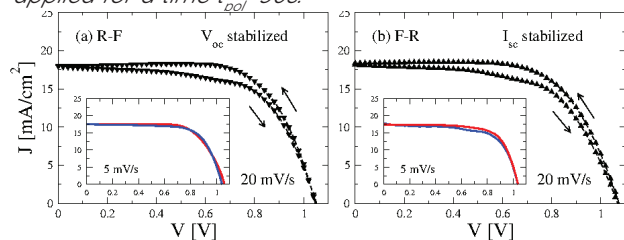


Figure 3. J-V characteristics measured under stationary poling conditions, with 20 mV/s and 5 mV/s: (a) R-F scan, preceded by stabilization at  $V_{oc}$  and (b) F-R scan, after stabilization of  $I_{sc}$ . The insets show almost hysteresis-free behavior for the lower scan rate of 5 mV/s.

Our DEM simulations, supported by experimental data, provide further guidance for an efficient and accurate determination of the stationary J-V characteristics, showing that the type and magnitude of the dynamic hysteresis may be affected by unintentional pre-conditioning in typical experiments.

References

[1] G.A. Nemnes, C. Besleaga, A.G. Tomulescu, I. Pintilie, L. Pintilie, K. Torfasan, A. Manolescu "Dynamic Electrical Behavior of Halide Perovskite Based Solar Cells", Sol. Energy Mater. Sol. C 159, 197-203 (2017).  
 [2] G. A. Nemnes, C. Besleaga, V. Stancu, D. E. Dogaru, L. N. Leonat, L. Pintilie, K. Torfasan, M. Ilkov, A. Manolescu, and I. Pintilie et al. "Normal and inverted hysteresis in perovskite solar cells", J. Phys. Chem. C 121, 11207 (2017).  
 [3]. A. Palici, et al. "The Influence of the Relaxation Time on the Dynamic Hysteresis in Perovskite Solar Cells", EPJ Web of Conferences 173, 03017 (2018).  
 [4]. G. A. Nemnes, C. Besleaga, A.G. Tomulescu, A. Palici, L. Pintilie, A. Manolescu, I. Pintilie "How measurement protocols influence the dynamic J-V characteristics of perovskite solar cells: theory and experiment", Solar Energy 173, 976 (2018).



# MATERIALS PREPARATION AND CHARACTERIZATION

SELECTED RESULTS

## Overview of the status of cation substituted hydroxyapatite: A comprehensive survey of the bio-functional range and a critical assessment of current in vitro testing protocols

T. Tite, A.C. Popa, L.M. Balescu, I.M. Bogdan, I. Pasuk, G.E. Stan

in cooperation with

J.M.F. Ferreira

Department of Materials and Ceramics Engineering, CICECO, University of Aveiro, 3810-193 Aveiro, Portugal

In the last decades it was witnessed an unprecedented demand for high-performance bioceramics capable not only to prevent failure, but to prolong the life-time of bone grafting scaffolds and osseous implants. The quality of life for millions of people has been drastically improved by using hydroxyapatite [HA,  $\text{Ca}_{10}(\text{PO}_4)_6(\text{OH})_2$ ] for bone repair and regeneration. Synthetic stoichiometric HA (having a theoretical Ca/P molar ratio of 1.67), calcium-deficient HA, or oxyapatite have been widely used as prominent bioactive materials in healthcare due to their excellent biocompatibility, osteoconductivity, bone remodelling, as well as their ability to foster stem cell proliferation and differentiation towards the osteoproliferative phenotype. Moreover, the piezoelectric effect (e.g. creation of electrical charges at the surface when subjected to stress) discovered in HA is becoming attractive for biomedical applications due to an enhancement of the biological and healing performance when the surface of HA is polarized. The piezoelectricity in low temperature monoclinic P21 and disordered non-stoichiometric high-temperature P63 phases seems to be mainly related to the polarization of OH- groups.

Recent findings in the realm of ion-substituted HA could pave the road towards significant developments in biomedicine, with an emphasis on a new generation of orthopaedic and dentistry applications, since such bioceramics are able to mimic the structural, compositional and mechanical properties of the bone mineral phase. The continuous effervescence of cationic substituted HA (SHA) is certified by a progressive increase of the number of papers published each year [1].

Various cations substituted in HA with different concentration ranges have been

explored to modify its physical, chemical and mechanical properties, as well as its in-vitro and in-vivo biological performance (Fig. 1).

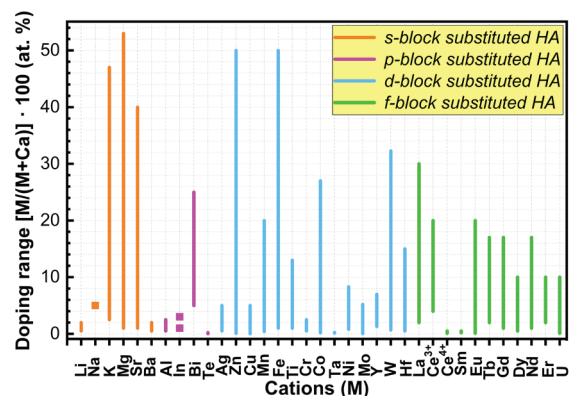
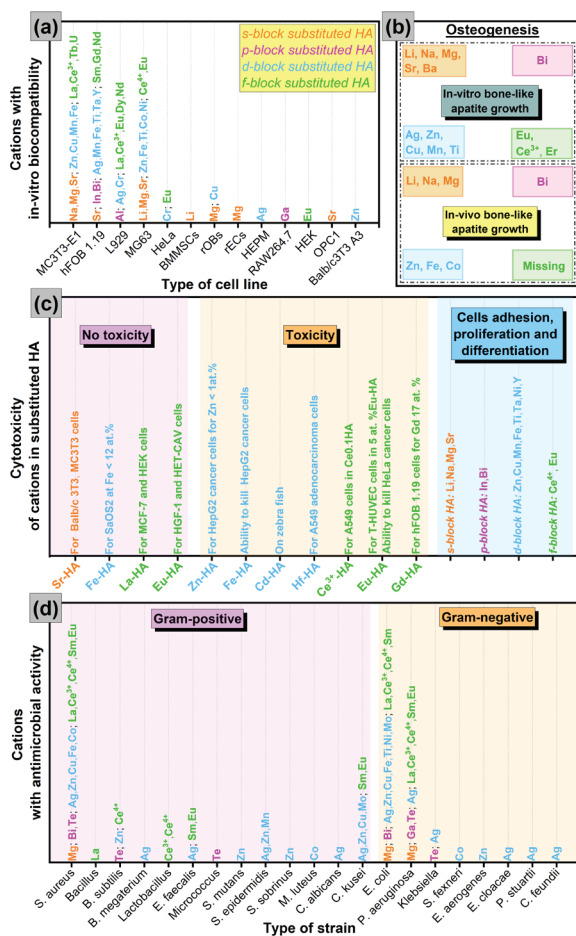


Figure 1. Doping range  $[M/(M+Ca)] \cdot 100$  (at. %) of cations (M) substituted HA. Cation dopings were categorised with respect to their electronic configuration (blocks) in the Table of Elements.

The limitation in terms of autografts and allografts has led scientists to the development of various non-synthetic (e.g. derived from natural resources) and synthetic doped/substituted HAs as alternatives [1]. A large palette of natural HA sources has been employed: animal bones (e.g. bovine, ovine, swine, camel, goat, chicken, fish), plants, and biogenic (egg-shells and sea-shells). Methods used to extract/prepare HA from natural (sustainable/renewable) resources are cheap and simple. Bovine and swine bones seem to be the preferred animal resources. Bones and shells of aquatic species are reliable sources for the production of HA since they contain a high content of minerals [1]. The synthetic routes, even though costlier, offer the possibility to fine tune the properties of HA in order to enhance its performance. Wet-chemistry methods, in particular co-precipitation, are the most widely used with this aim. The HA coating of metallic implants

by various techniques (e.g. plasma spray, magnetron sputtering, ion-beam deposition, pulsed laser ablation) is seen nowadays as the suitable solution to combine the excellent mechanical performance of metals with the superior biological properties of ceramics for reliable load-bearing applications.

In this review on the current status of SHAs, special attention was dedicated to their cytocompatibility and antimicrobial activity (Fig. 2). Also, the most used in-vitro biological tests, and their ability to mimic the in-vivo biological interactions are critically discussed.



**Figure 2** (a) In-vitro cytocompatibility; (b) in-vitro (e.g. in SBF) and in-vivo (e.g. in animal model) biomineralization capacity; (c) cytotoxicity; and (d) antimicrobial activity. The labelling of each type of cell line and bacteria/fungi strain is presented in full in [1].

Strontium (Sr) and zinc (Zn) are recognized for their good biocompatibility, low toxicity and ability to induce cell proliferation. Important to notice that the cytotoxic concentration threshold which inflicts the cells growth decreases by 50% depends on many factors, including the source and concentration of the ion, the crystalline quality, porosity, particle size, particle

morphology (e.g. spheres, polyhedra, rods) of materials, cells line type and incubation time [1]. Therefore, for trustworthy conclusions, we advocate for a more intimate understanding of SHA interaction with the physiological media and cells, by coupling bio-functional assays with the determination of the temporal ion-release profiles, assessed for instance by ICP techniques.

The most prominent cations that exhibit antibacterial properties are  $\text{Ag}^+$ ,  $\text{Zn}^{2+}$ ,  $\text{Ce}^{3+}$  and  $\text{Ce}^{4+}$  and Te (Fig. 2(c)). *C. albicans* is a common opportunistic yeast used for assessing the antifungal effect. Various discrepancies can be found in literature (e.g. for Ce) regarding the antimicrobial activity. Standardization of protocols joined with insightful chemical analyses (e.g. by ICP-MS) could be helpful in this respect.

In reference [1], a brief discussion on the positives and shortcomings of the mostly used in-vitro standardized tests is given. A poorly and outdated standard can lead to non-trustworthy data, and limit important discoveries. For instance, as reported by many authors, the current in-vitro standard for bio-activity testing (i.e. ISO 23317:2014) is obsolete, as it uses a purely inorganic solution (simulated body fluid, SBF). Tests performed in Dulbecco's modified Eagle's medium (DMEM)-like cell culture medium could be a solid alternative.

As future perspectives, co-doped and multi-ions doped HA is an attractive new research area due to its potential to couple in a single material enhanced structural, mechanical and biological features. HA has been co-substituted so far with Ag/Bi, Ag/F, Ag/Mg, Ag/Si, Ag/Sr, Ag/Zn, Ce/Fe, Ce/Eu, Sr/Ce, Sr/Cu, Sr/Zn, Zn/Cu, Zn/F, Zn/Fe, La/Ag, La/Cu, Sm/Gd, Tb/Gd, Ce/Zr/F, Ag/Ti/F, Mg/Zn/Co, Sr/Co/F, Ag/Cu/Zn/F, or Ag/Cu/Zn/Ti [1]. Co-doping of HA could yield superior bioceramics with multifunctional properties. For instance, cytotoxicity of antimicrobial Ce ions could be alleviated by adding Sr as co-dopant [1].

Our review could be of paramount importance to gather information on SHAs and provide for the fellow researchers a comprehensive inventory of progresses achieved to date.

This research was funded by the Romanian Ministry of Research and Innovation, CCCDI-UEFISCDI, in the framework of project PN-III-P1-1.2-PCCDI-2017-0062 (contract no. 58)/component project no. 2.

## References

[1] T. Tite, A.C. Popa, L.M. Balescu, I.M. Bogdan, I. Pasuk, J.M.F. Ferreira, G.E. Stan, *Materials* 11 (2018) 2081.

## Eggshell membrane (ESM) – from a bio-waste to a source for synthesis of functionalized 3D porous networks: ZnO/ESM and PPy/ESM

N. Preda, M. Beregoi, A. Costas, A. Evangelidis, I. Enculescu

Eggshell membrane (ESM), one of the ubiquitous wastes of our daily life (**Fig.1**), can be separately collected from the eggshells and transformed into a source for the synthesis of new value-added materials through eco-friendly pathways. The unique 3D porous interwoven fibrous protein network of the ESM is responsible for its interesting and useful properties: high porosity, large surface area, high absorption capacity and flexibility.

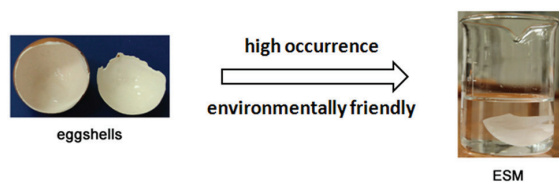


**Figure 1:** ESM – common daily bio-waste

In our studies, by coating ESM with ZnO nanostructures using electroless deposition [1] or with polypyrrole (PPy) layer by electrodeposition [2], functionalized 3D porous networks based on ZnO/ESM and PPy/ESM were fabricated (**Fig. 2**).

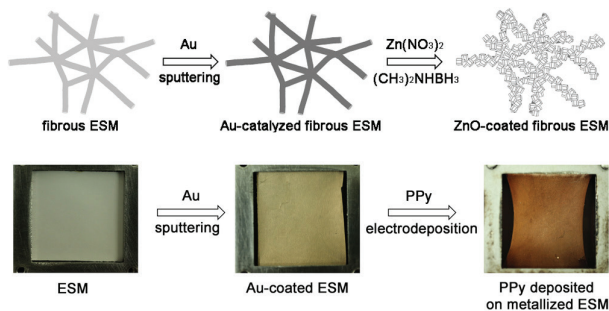


**Figure 2.** Schematic representation of the steps involved in the synthesis of ZnO/ESM (up) and PPy/ESM (down).

The ESM exhibits a porous structure formed by interpenetrating fibers with diameters having sizes in the micrometer range (**Fig.3** left and **Fig.4** up). After the ZnO electronless deposition, the original interconnected fibrous skeleton of the ESM is preserved (**Fig.3** right),

the nanostructures being grown only on the area of the ESM fibers covered with Au layer.

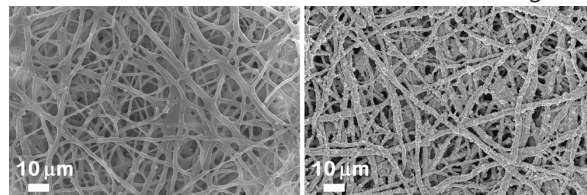


**Figure 3.** FESEM images of the ESM (left) and ZnO/ESM (right).

Additionally, at higher magnification, it can be seen that the surfaces of the ESM fibers are uniformly coated by densely packed twin hexagonal prisms (**Fig.4** middle) or with a continuous PPy film featured by a grain structure (**Fig.4** down). In this way, the large active surface of the ESM is maintained. The cross-sectional FESEM images (**Fig.4**) emphasize a core-shell structure having ESM fiber as core and ZnO or PPy as shell.

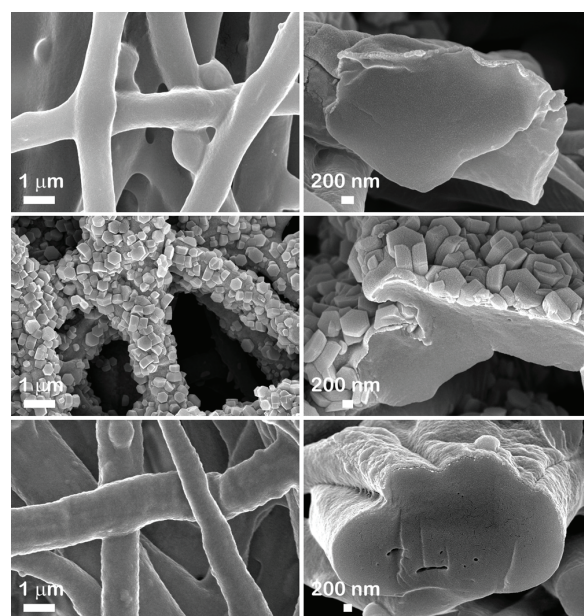


**Figure 4.** FESEM images (plan and cross-sectional views) of the ESM (up), ZnO/ESM (middle) and PPy/ESM (down).

Further, the behavior of the functionalized ESM in the presence of the water droplets (an important property for the ESM applications in water purification or photocatalysis) was evaluated (Fig. 5). Although, the ZnO/ESM exhibited a longer water droplet penetration time in comparison with that of the pristine ESM, the result indicates that the ESM characteristic regarding the water absorption is maintained after its functionalization with ZnO nanostructures.



**Figure 5:** Sequences of snapshots captured at different time intervals after the placement of a water droplet on the surface of the ESM (up) and ZnO/ESM (down).

Also, the actuation properties of the PPy/ESM were investigated in an environment with controlled relative humidity (Fig. 6). The actuating process involves the sorption/desorption of the water vapors by both components of the actuator. Thus, it can be seen that at 50% relative humidity, metalized ESM barely reaches ~0.2 cm in movement, while PPy/ESM bends (due to the contraction of PPy film) and generates a displacement of ~2.1 cm, a further decrease in the relative humidity leading to a curling movement of this actuating system.

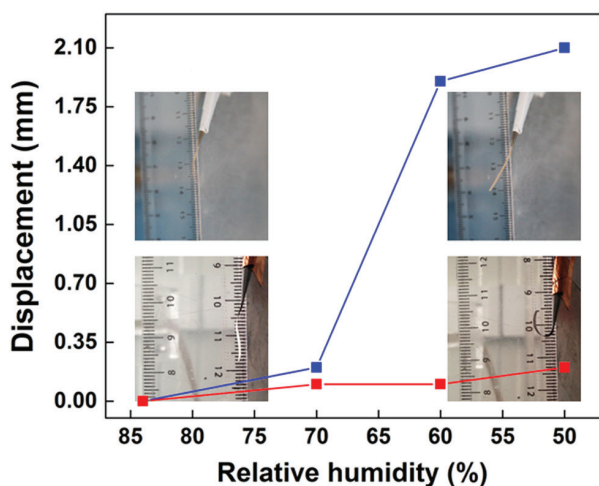


**Figure 6:** Displacement of the metalized ESM (bending motion - red curve) and PPy/ESM (curling motion - blue curve) recorded during the actuation process as function of the relative humidity and the corresponding snapshots.

The ability of the PPy/ESM actuator to manipulate lightweight objects is illustrated by two simple tests (Fig. 7): i) a fowl feather and ii) a ball from a braided yellow-gold ribbon. The motion of the actuating system takes place: i) by losing the water

vapors and resulting in the shrinking of the actuator or ii) by absorbing water vapors from the surrounding environment and leading to the swelling of the actuator. The results are an irrefutable proof that such actuators can operate as micromanipulators.

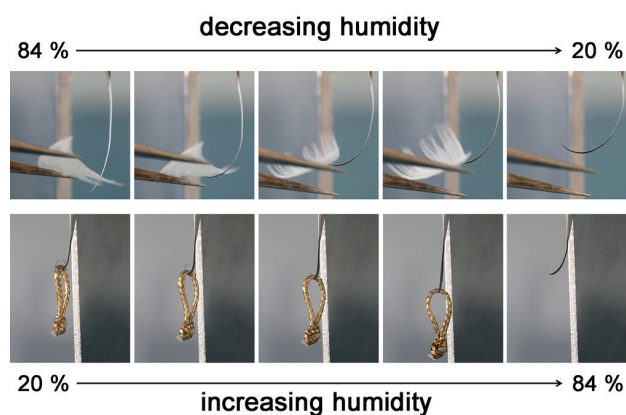


**Figure 7:** Snapshots taken during the manipulation of lightweight objects by the PPy/ESM actuating system when the relative humidity is modified: moving a fowl feather and releasing a ball from a braided yellow-gold ribbon.

Simple and inexpensive preparation methods provide affordable strategies for converting a bio-waste, ESM, into functional nanomaterials with potential applications in water purification, photocatalysis, biomimetic micromanipulators, artificial muscles field, etc.

Funding from Core Program, contract no. PN18-11; PN-IIIP2-2.1-PED-2016-1249; NANOBIO SURF-SMIS 103528.

## References

- [1] N. Preda, A. Costas, M. Beregoi, I. Enculescu, "A straightforward route to obtain organic/inorganic hybrid network from bio-waste: electroless deposition of ZnO nanostructures on eggshell membranes", *Chem. Phys. Lett.* 706, 24 (2018).
- [2] M. Beregoi, N. Preda, A. Evangelidis, A. Costas, I. Enculescu, "Versatile actuators based on polypyrrole-coated metalized eggshell membranes", *ACS Sustain. Chem. Eng.* 6, 10173 (2018).

## Functionalization with ZnO of polymer fiber mats for photocatalytic application

E. Matei, C. Busuioc, A. Evanghelidis, I. Zgura, M. Enculescu, M. Beregoi and I. Enculescu.

Functionalization by using nanostructures is an appropriate approach to add new properties and implicitly, new utilities to a particular material. Submicron polymer fibers obtained by electrospinning are of great interest for many applications and their coating with nanostructures can significantly increase this list.

Due to its electrical and optical properties (e.g. wide band gap semiconductor, direct band structure), ZnO is a suitable material for various applications in different fields.

Electrochemical deposition of ZnO is one of the methods by which nanostructured films with precisely tailored properties can be obtained by controlling the preparation parameters.

Electrodeposition of nanostructured ZnO on the fibrous web electrodes leads to transparent composite electrodes [1]. To obtain such transparent electrodes covered with ZnO, poly (methyl methacrylate) (PMMA) fiber webs were prepared by an optimized electrospinning process which were covered by sputtering with a thin layer of gold, then thermally transferred to glass substrates followed by ZnO electrodeposition (Fig.1). The metalized web covered glass was the working electrode in the electrodeposition process. The electrodeposition was performed from baths with different zinc ions concentration and electrolyte support ( $\text{KNO}_3$  and KCl). A high zinc ions concentration (tens to hundreds of millimoles) in electrodeposition bath, leading to the formation of ZnO films of hexagonal prisms and platelets and a low zinc ions concentration (tenths of millimoles), determining the growth of ZnO nanowires.

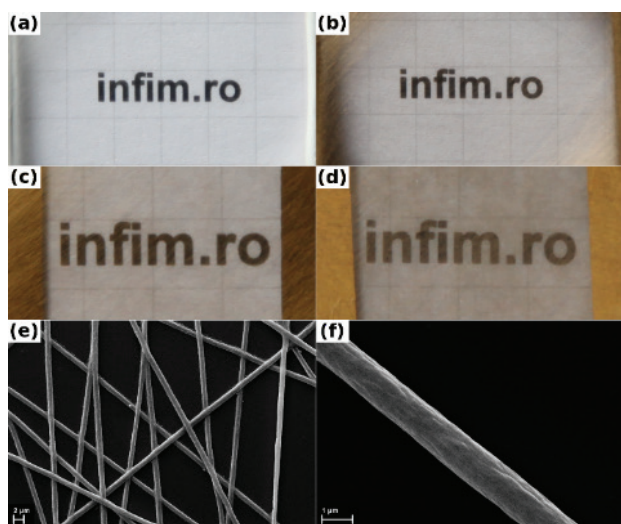


**Figure 1.** The steps in preparing the ZnO covered polymer fiber mats: (a) PMMA web, (b) Au covered web, (c) glass substrate covered with the metalized web, (d) glass substrate covered with ZnO electrodeposited on metallic web electrode, (e), (f) microscopic details of the metal covered PMMA web.

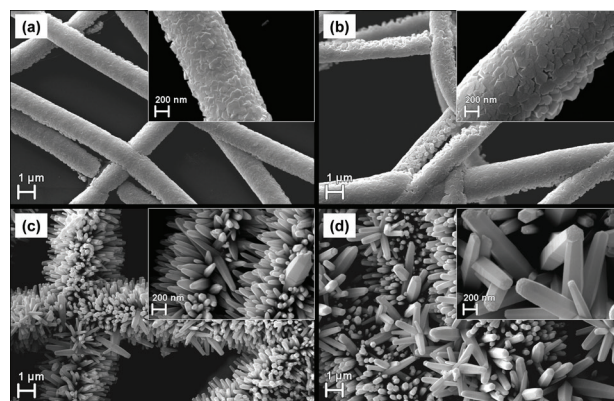


**Figure 2.** ZnO nanostructures deposited on metallic web electrodes from a bath containing 5 mM  $\text{Zn}(\text{NO}_3)_2$  and 100 mM  $\text{KNO}_3$  at: (a) -0.8 mV, (b) -0.9 mV, (c) -1 V and (d) -1.1 mV.

The morphologies of the samples prepared on metalized fiber electrodes depend on baths composition and deposition potential

(as example **Fig.2** and **Fig.3**). Thus, it has been shown that the morphology can be very well controlled by the parameters of the electrodeposition process even on such electrodes.

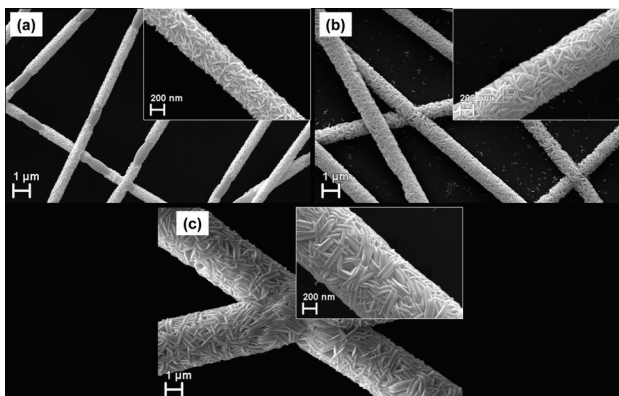


**Figure 3.** Fibers covered with ZnO from a solution with 0.2 M  $Zn(NO_3)_2$  and 100 mM KCl at: (a) -0.9 mV, (b) -1 V and (c) -1.1 mV.

The optical properties of all samples are those specific to the preparation method. The photoluminescence (PL) measurements of ZnO nanostructured film present the band-to-band associated emission and a wide band in the 500-700 nm range, associated with defects (Fig. 4(a)). It can easily be seen that the ratios between the excitonic band intensity and defects band intensity can be controlled by deposition conditions which means that the photoemission of the electrodeposited samples can be easily tuned. The measurements for structural properties have shown the formation of ZnO wurtzite hexagonal phase and a growth along the c-axis direction.

The wettability has a very important role in many applications and are determined by the morphology and surface chemistry. The ZnO covered webs are hydrophobic except for those who present a brush like morphology, demonstrating the strong dependence of the wetting properties on the micromorphological features.

ZnO coated metalized webs were investigated also for photocatalytic properties using methylene blue (MB) as a test dye (Fig.4(b)). The efficiency of a photocatalyst is strongly influenced by its optical and electronic properties. A fairly good photocatalytic activity exhibits the samples with the roughest morphology, i.e. the highest surface to volume ratio (nanorod structures grown on the metalized fibers). By correlating with optical

properties (Fig. 4(a)), the best photocatalytic activity samples are the ones with the highest excitonic peak and the lowest defects band.

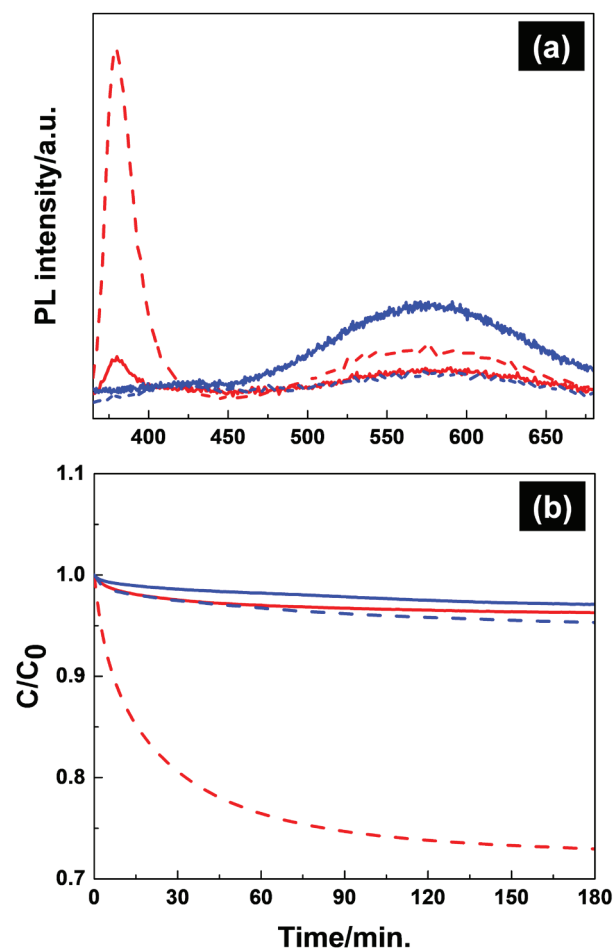


**Figure 4.** (a) PL emission spectra and (b) photocatalytic degradation curves of MB aqueous solution under UV irradiation for samples deposited from a solution containing 5 mM  $Zn(NO_3)_2$  and 100 mM  $KNO_3$  (red line) and 0.2 M  $Zn(NO_3)_2$  and 100 mM KCl (blue line) at: -0.9 V (continuous line) and -1 V (dashed line).

This approach for preparing metal covered fiber webs and ZnO layer on metalized fiber mats can offer the possibility that each type of morphology to be interesting for a particular application, such as solar cell electrodes or photocatalytic layers.

## References

- [1] E. Matei, C. Busuioc, A. Evanghelidis, I. Zgura, M. Enculescu, M. Beregoi and I. Enculescu, Applied Surface Science 458 (2018) 555–563.

## Emissive properties of polymer submicrometric fibers produced by electrospinning

M. Enculescu, A. Evanghelidis, I. Enculescu

The electrospinning method proved to be a low cost, flexible and scalable method for producing polymeric fibers that can be further functionalized by either covering the fibers with different compounds using chemical, electrochemical or physical techniques or by adding various dopands to the electrospinning solution [1].

Dye-doped polymer fibers of submicrometric sizes were produced by the electrospinning technique using polymethylmethacrylate (PMMA) in a concentration of 12.5 wt % in dimethylformamide (DMF) as the solvent.

Several dyes with emissions covering a large area in the visible spectrum were used as dopands with 10<sup>-3</sup> M concentration in the polymer solutions.

The polymer solutions were doped with dyes that exhibit emissions in the blue-green region such as coumarin 7, C<sub>20</sub>H<sub>19</sub>N<sub>3</sub>O<sub>2</sub> (C7) and coumarin 6, C<sub>20</sub>H<sub>18</sub>N<sub>2</sub>O<sub>2</sub>S (C6), with fluorescein, C<sub>20</sub>H<sub>12</sub>O<sub>5</sub> (F), that emits in the yellow region of the visible spectrum, and with dyes that present intense emissions in the orange-red region of the visible spectrum such as rhodamine 6G, C<sub>28</sub>H<sub>31</sub>N<sub>2</sub>O<sub>3</sub>Cl (Rh 6G), sulforhodamine B, C<sub>27</sub>H<sub>29</sub>N<sub>2</sub>NaO<sub>7</sub>S<sub>2</sub> (SRh B), and sulforhodamine 101, C<sub>31</sub>H<sub>29</sub>ClN<sub>2</sub>O<sub>6</sub>S<sub>2</sub> (SRh 101).

Images of the electrospun polymeric fibers collected on glass substrates are presented in (Fig.1). Images were made using the 365 nm wavelength from a UVlite lamp LF106L (6W, filter 50x150mm, 700 μW/cm<sup>2</sup>). The optical properties of the electrospun nanofibers by means of photoluminescence (PL) were evaluated using a FLS920 EDINBURGH INSTRUMENTS spectrofluorimeter (equipped with a 450 W Xe lamp and double monochromators in both excitation and emission).

The emissions of single dye doped electrospun fibers peaking at different

wavelengths in the visible region of the visible spectrum are presented in (Fig.1).

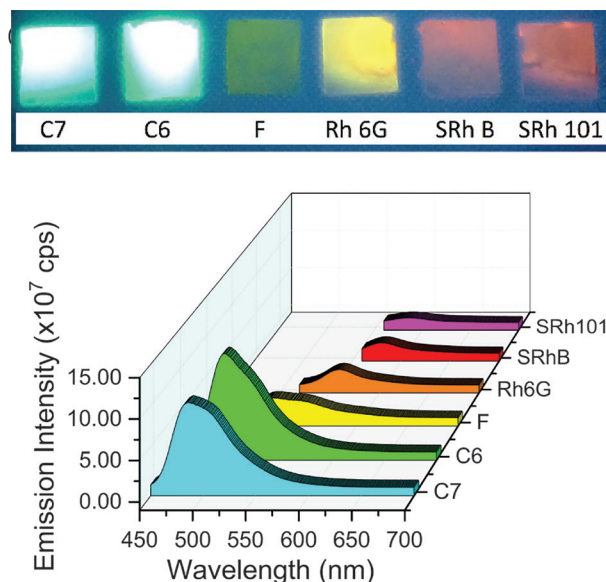


**Figure 1.** Images of the polymeric fibers' mats obtained by electrospinning collected on glass substrates and the corresponding emissions' spectra of the single dye-doped fibers excited with different wavelengths.

It can be observed in (Fig.1) that for the same concentration of the dye, the fibers' emissions have different intensities due to the dyes' different efficiencies.

The C7 doped fibers were excited with 420 nm revealing the overlapping of two peaks at 485 nm and 500 nm while for the excitation with 440 nm of the C6 doped fibers two peaks at 495 nm and 515 nm appear. The appearance of the shoulder in PL may be due to the protonated form of the dye, which was previously reported for coumarins. For the F doped fibers, the excitation with 490 nm reveals a large emission between 515 nm and 575 nm formed by an overlapping of peaks. Under 510 nm excitation, the Rh 6G doped fibers exhibit a peak at 560 nm. For the 550 nm excitation, SRh B doped fibers present a PL peak at 580 nm and SRh 101 doped fibers present a peak at 590 nm.

White-light emitting fibers' mats were prepared by the electrospinning of mixtures of single-dye-doped polymer solutions.

The overlapping of the single dye emissions results in complex emission spectra of the fibers revealing the possibility of tuning the white light emissions by balancing the concentration of different single-dye-doped solutions in the mixtures. In this manner, nine mixtures with different concentrations of single dye-doped polymer solutions were prepared. Scanning electron microscopy (SEM) was used to investigate the morphologies of the electrospun fibers with diameters around 600-800 nm. All samples present uniform distribution of the fibers' diameters of submicronical sizes, as depicted by the example shown in (Fig.2).

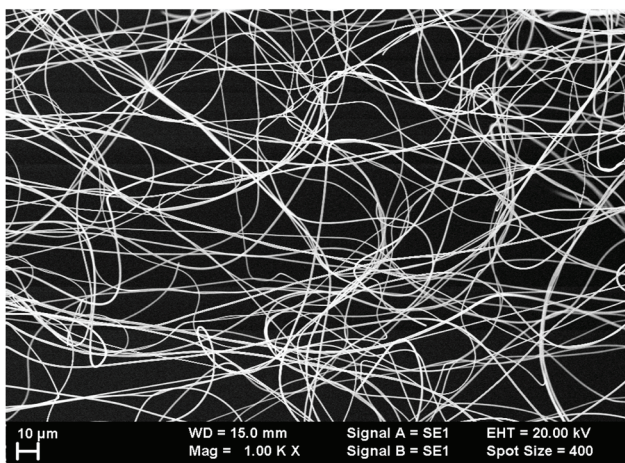


**Figure 2.** SEM image of the polymeric fibers obtained by electrospinning a mixture of single-dye-doped polymer solutions (mixture 4).

The evaluation of the fibers' morphologies was performed using a ZEISS EVO 50 XVP scanning electron microscope (SEM). In order to avoid electrical charges of the samples, a thin layer of gold was sputtered on their surfaces prior to the imaging.

Depending on the ratios of different single-dyes in the mixtures, the PL and luminance were balanced between blue and red emissions.

**Fig.3a** presents the spectra of the mixtures with an intense blue component (mixture 4), a more pronounced red component (mixture 9) and a relatively even-distributed

intensity of the emission over the visible spectra (mixture 8). CIE measurements depict this fine tuning of the colours' intensities, presenting the difference between various compositions for white light emission of the submicronic fibers' (Fig.3b).

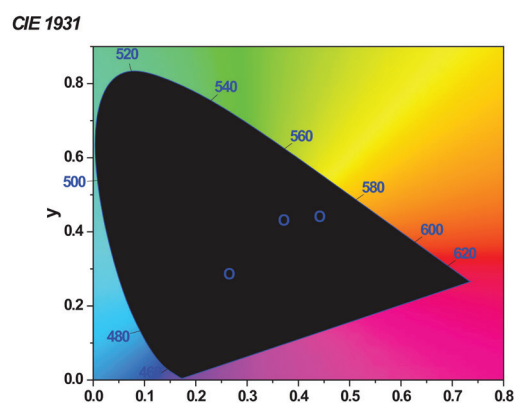
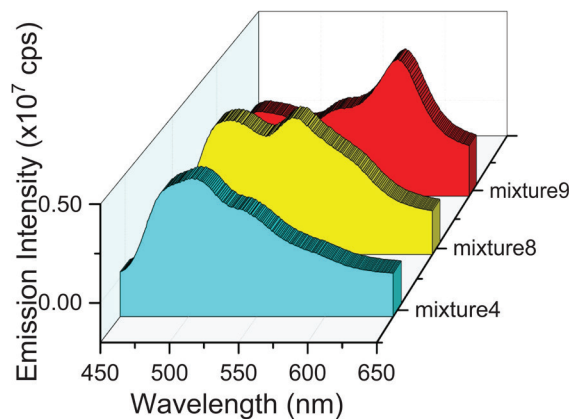


**Figure 3(a).** Emission spectra for dye-doped polymeric fibers obtained by electrospinning of different mixtures of single-dye-doped polymer solutions and (b) their corresponding coordinates on CIE 1931 color space chromaticity diagram.

Thus, tunable white-light-emitting fibers can be produced from dye-doped PMMA mixtures through the electrospinning technique.

The authors thank Silviu Polosan for the chromaticity measurements and acknowledge the financial support from the Romania-France IFA-CEA collaboration (Project No. C5-08/2016).

## References

- [1] Monica Enculescu, Alexandru Evanghelidis, Ionut Enculescu, White-Light Emission of Dye-Doped Polymer Submicronic Fibers Produced by Electrospinning Polymers 10(7), 737 (2018) <https://doi.org/10.3390/polym10070737>.

## Magneto-functionalities of Ni based magnetic nanowires

A. Costas, C. Florica, E. Matei, I. Stavarache, A. Kunser, V. Kuncser,  
M. Sima, M. Baibarac, E. Vasile, Ma. Sima, G. A. Schinteie, I. Enculescu

Nowadays, metallic magnetic nanowires are in the spotlight of researchers owed to their potential application in the smaller spintronic devices (magnetoresistance sensors, data storage elements, etc.) with complex functionalities.

In our work, alloy nanowire arrays based on Ni [1] and Ni-Cu [2] were prepared using template electrodeposition, a cost effective preparation method. Thus, Ni nanowires and Ni-Cu alloy nanowires were electrodeposited in porous anodic alumina oxide (AAO) and polycarbonate membranes, respectively. Moreover, in the multiferroic heterostructures, the magnetoelectric (ME) coupling is interfacial and can come from charge, elastic strain and exchange bias interactions. The low dimensional composite materials can provide tighter coupling between ferroelectric and ferromagnetic phases and offer additional degrees of freedom in controlling size, interface and epitaxial strain to enhance the ME coupling.

The advantage of using nanowires as magnetic components in interaction with a polymeric shell with ferroelectric properties resides in the much better activation of magnetostrictive effect in one-dimensional magnetic systems, leading to an expected better ME effect. From the polymer materials, poly(vinylidene fluoride) (PVDF) is the most used, its  $\beta$  crystalline phase exhibiting the best piezoelectric and ferroelectric properties. Therefore, a PVDF homopolymer nanotubes array with ferroelectric  $\beta$ -phase was fabricated into the AAO template. Further, by combining electrochemical and chemical routes, Ni nanowires arrays surrounded by PVDF nanotubes (Fig.1) were grown into the AAO membranes.

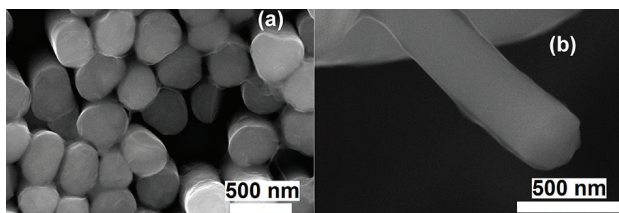


**Figure 1.** SEM images of a) Ni/PVDF wires (top view) and b) single Ni/PVDF submicron wire.

The interactions which transform PVDF film in a ferroelectric material were evidenced by XRD and FTIR investigations (Fig.2). For comparison, the FTIR spectrum of a Ni film electrodeposited in the same experimental conditions with the Ni submicron wires array were also presented (Fig.3a).

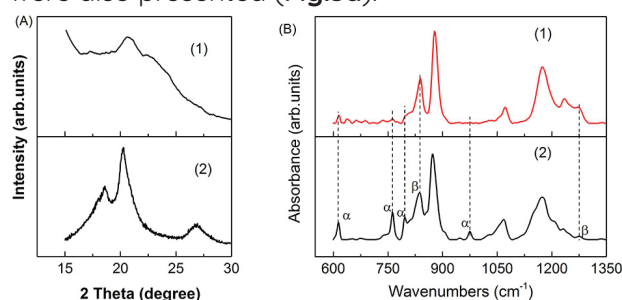


**Figure 2.** (A) XRD patterns and (B) FTIR spectra of PVDF tubes for Ni/PVDF structures (curve 1) and PVDF foil (curve 2).

The magnetic behaviour of such heterogenous multiferroic based on PVDF film and Ni nanowires were evaluated by magnetic measurements (Fig.3b).

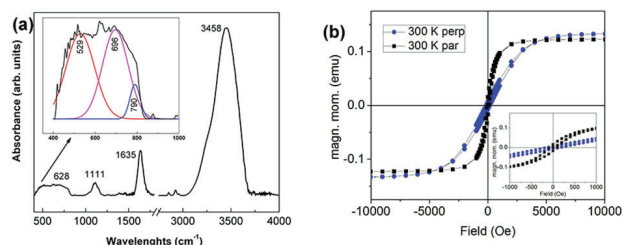


**Figure 3(a).** The FTIR spectrum of an electrodeposited Ni film. Inset: de-convolution of the complex FTIR band peaked in the spectral range 400-900  $\text{cm}^{-1}$  (b) Magnetic hysteresis loops measured in the parallel and perpendicular geometry 300 K in the case of Ni/PVDF-wires. Inset: the same loop with a better field resolution.

In this context, we suggested that the ME coupling constant in this multiferroic system has to be measured only by observing the perturbation of the electric state of the polymer shell under a magnetic excitation of the nanowire core.

The Ni-Cu alloy nanowire arrays were grown into nanoporous polycarbonate membranes by template electrodeposition at

four different electrodeposition potentials ( $-800$  mV,  $-900$  mV,  $-1000$  mV and  $-1050$  mV) in order to have different compositions of Ni (20 %, 54 %, 75 % and 92 %). The SEM images of the Ni-Cu alloy nanowires arrays (Fig.4) revealed that the nanowires have a cylindrical shape along their entire 30  $\mu\text{m}$  length and a diameter of approximately 100 nm.

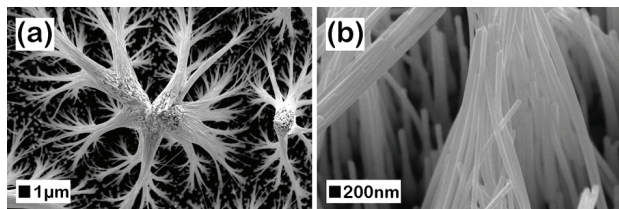


**Figure 4.** SEM images of the Ni-Cu alloy nanowire arrays grown at  $-1000$  mV in the polycarbonate membranes.

In order to evaluate the magnetoresistance properties of single Ni-Cu alloy nanowires, the nanowires were firstly transferred in the ultrapure isopropanol. Then, droplets of nanowires suspension in isopropanol were placed on top of Si/SiO<sub>2</sub> substrates patterned with Ti/Au interdigitated electrodes fabricated by combining photolithography with RF magnetron sputtering and vacuum thermal evaporation. Further, single Ni-Cu alloy nanowires placed conveniently between the Ti/Au electrodes were contacted using electron beam lithography (EBL) combined with magnetron sputtering and thermal vacuum evaporation. Fig.5 exhibits SEM images at different magnifications of a single Ni-Cu alloy nanowire contacted by EBL.

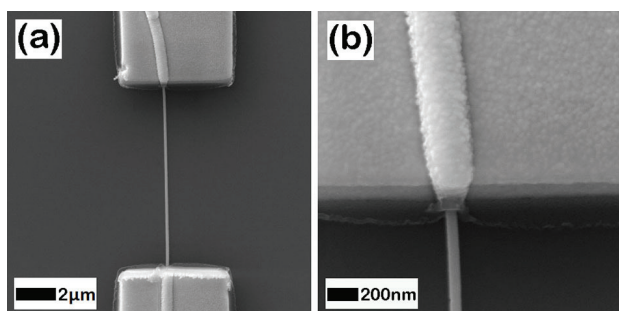


**Figure 5.** SEM images at different magnifications of a Ni-Cu alloy nanowire grown electrochemically and contacted by EBL.

Magnetoresistance measurements carried out on all four types of single Ni-Cu alloy nanowires contacted by EBL are presented in (Fig.6). The magnetoresistance measurements evidenced a magnetoresistance effect in the perpendicular geometry and the lack of any magnetoresistance effect in the parallel geometry, this type of behaviour demonstrating an anisotropic magnetoresistance effect for all investigated Ni-Cu alloy nanowires.

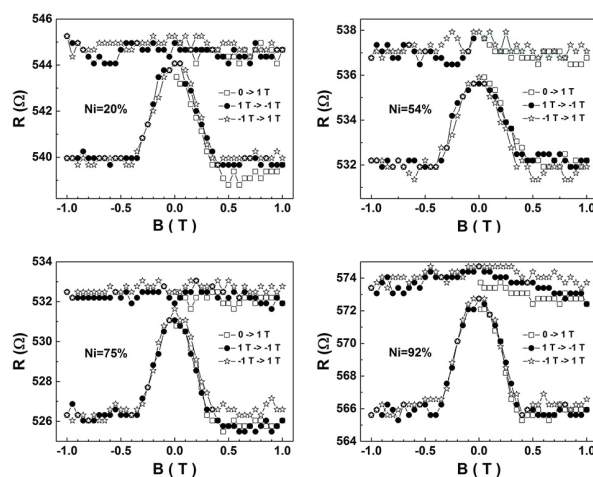


**Figure 6.** Magnetoresistance measurements carried on the single Ni-Cu alloy nanowires with different concentrations of Ni, in both parallel (upper curves) and perpendicular (peaked lower curves) geometry. With no field applied, the magnetization lies along the wire due to the strong shape anisotropy.

Magnetic metallic nanowires prepared by template electrodeposition, a simple and cost efficient method, can be easily employed as magnetic elements in spintronic devices.

Funding from Core Program, contract no. PN16-480102; PNII-ID-PCE-2011-2-0006; PNIII PED 95/2017.

## References

- [1] M. Sima, M. Baibarac, E. Vasile, Ma. Sima, G.A. Schinteie, V. Kuncser, "Investigation of the interactions of PVDF shell films with Ni core submicron wires and AAO matrix", *Physica B* 545, 503-509 (2018).
- [2] A. Costas, C. Florica, E. Matei, M. E. Tomil-Molares, I. Stavarache, A. Kuncser, V. Kuncser, I. Enculescu, "Magnetism and magneto-resistance of single Ni-Cu alloy nanowires", *Beilstein Journal of Nanotechnology* 9, 2345-2355 (2018).

## Preparation, superconductivity and mechanical properties of MgB<sub>2</sub>

P. Badica\*, G. Aldica, M. Burdusel, M. Grigoroscuta, A.M. Ionescu, S. Popa, M. Enculescu, I. Pasuk, A. Kuncser (in collaboration with University 'Politehnica' of Bucharest, Romania, Asai Germanium Research Institute Co Ltd, Japan, National Institute for Research in Chemistry, Romania, Nanyang Technical University, Singapore, and University of Glasgow, UK)

The MgB<sub>2</sub> superconductor attracts much interest from academia and industry. Low density, a relatively large coherence length, multiband superconductivity, availability and low cost, low toxicity are key advantages of MgB<sub>2</sub> in respect to other superconductors.

Studies on processing by spark plasma sintering and characterization of MgB<sub>2</sub> superconductor were continued in our lab.

Bulk samples with high density above 95 % were fabricated [1] for different dwell times of 1, 4, 7, 10 and 20 min (Fig.1). There is no significant change in the grain size (Fig.2) or phase composition.

Therefore, the superconducting properties are almost constant. For example, one observes in (Fig.3) that reduced critical current density  $J_c/J_{c0}$  ( $J_{c0}$  is the critical current density in zero magnetic field) curves vs. applied magnetic field at 20 K for samples with a different dwell time overlap each other. The main practical outcome of the work is that long dwell times are not necessary.

Short powder-in-tubes tapes of MgB<sub>2</sub> in Fe-metal sheath were subject to spark plasma sintering [2]. Tapes with open ends (OT) or with closed ends (CT) were obtained by folding and pressing. Tapes OT and CT show some differences in  $J_{c0}$  (Fig.4a) and in the maximum volume pinning force  $F_p, \max$  (Fig. 4b). In (Fig.4) as a reference are also presented data for a bulk sample obtained by SPS under similar conditions as for the tapes.

Relationships between additives and superconducting properties in MgB<sub>2</sub> are not well understood. In our study from ref. [4] different Ge-based variants with chemical formula C<sub>6</sub>H<sub>10</sub>Ge<sub>2</sub>O<sub>7</sub> (Repa-, Propa- and linear Germanium with notations R, P, and SP, respectively) were added into MgB<sub>2</sub>. RGe was from two different sources. Samples show very different  $J_c$ , especially at high magnetic fields (Fig.5).

Static (Fig.6a) and dynamic (Fig.6b) compressive mechanical properties of MgB<sub>2</sub> were investigated on pristine and SiC-Te - doped MgB<sub>2</sub> [4]. Dynamic strength as a function of strain rate

as measured from Split Hopkinson Pressure Bar (SHPB) experiments is about half of that for Al<sub>2</sub>O<sub>3</sub> (Fig.6c).

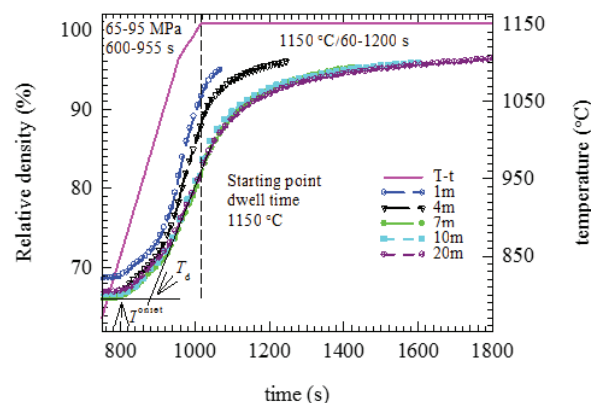


**Figure 1.** Densification curves during spark plasma sintering of MgB<sub>2</sub> samples obtained for a different dwell time (1, 4, 7, 10, and 20 min) [1].

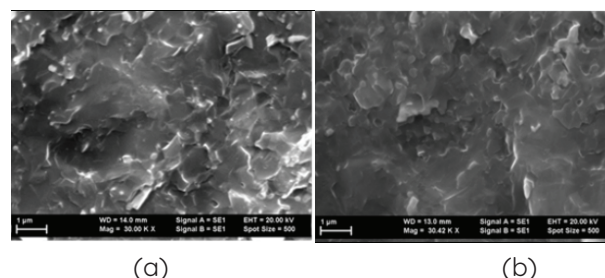


**Figure 2.** SEM images on fractured surfaces of bulk MgB<sub>2</sub> samples obtained by spark plasma sintering for a dwell time of 1 and 20 min [1].

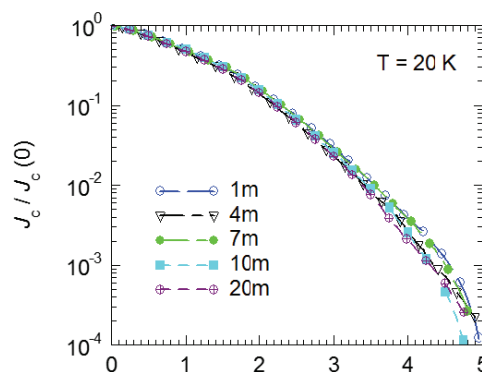


**Figure 3.** Reduced critical current density  $J_c/J_{c0}$  for bulk samples processed by SPS for different dwell times (1, 4, 7, 10, and 20 min) [1].

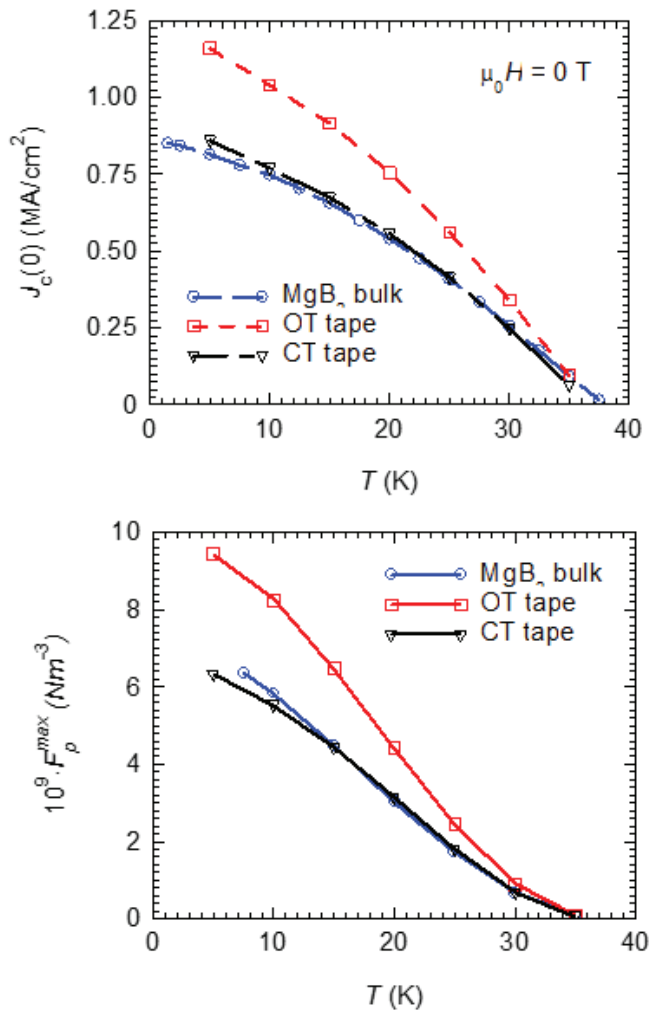


Figure 4(a). Zero-field critical current density vs. temperature; (b) – Pinning force vs. temperature. Samples are OT=open tape, CT=closed tape, and MgB<sub>2</sub> bulk sample as reference [2].

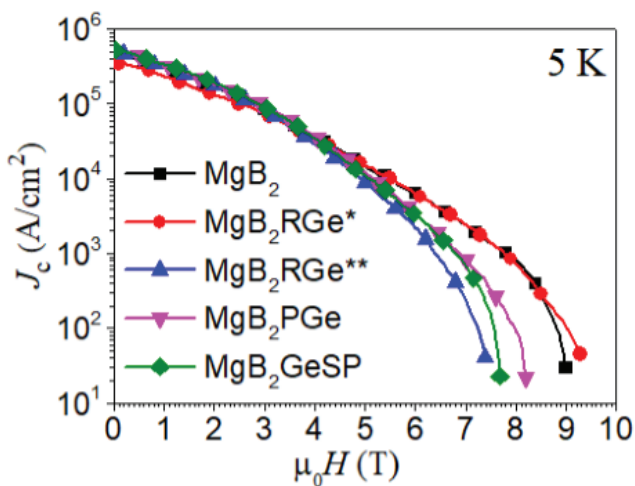


Figure 5. Critical current density vs. applied magnetic field for bulk MgB<sub>2</sub> samples added with RGe, PGe and GeSP [3]. RGe\* and RGe\*\* are from two suppliers.

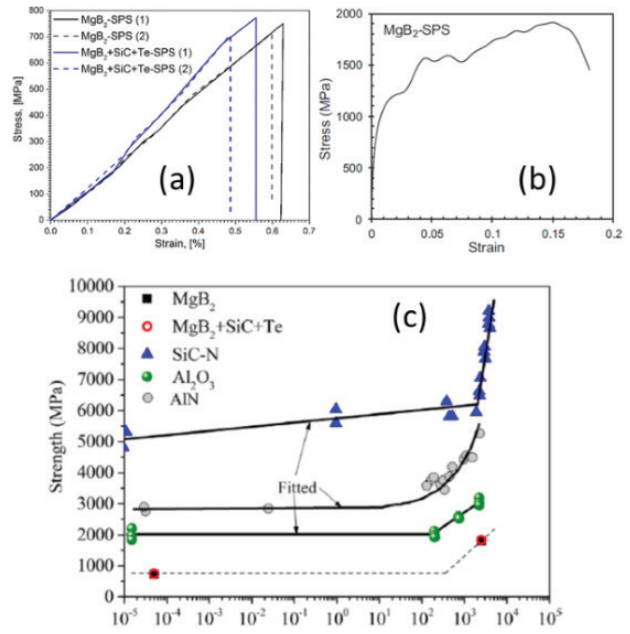


Figure 6. Compressive stress-strain curves in static (a) and dynamic-impact (b) experiments [4]. (c) Dynamic strength vs. strain rate for MgB<sub>2</sub> bulk samples. Similar curves for Al<sub>2</sub>O<sub>3</sub>, SiC-N and AlN are also presented [5-7].

References

[1] G. Aldica, S. Popa, M. Enculescu, I. Pasuk, A.M. Ionescu, P. Badica, Dwell Time Influence on Spark Plasma-Sintered MgB<sub>2</sub>, J. Supercond. Nov. Magn. 31 317-325 (2018) DOI 10.1007/s10948-017-4236-9;

[2] G. Aldica, M. Burdusel, S. Popa, I. Pasuk, A.M. Ionescu, A. Kuncser, P. Badica, Ex Situ Spark Plasma Sintering of Short Powder-in-Tube MgB<sub>2</sub> Tapes with Open and Closed Ends, J. Supercond: Nov. Magn. 31(11) 3423-3432 (2018) DOI 10.1007/s10948-018-4616-9.

[3] D. Batalu, T. Nakamura, M. Enculescu, S. Popa, I. Pasuk, G. Aldica, A.M. Ionescu, P. Badica, A comparative study of Ge-based organometallic additions to MgB<sub>2</sub>, IEEE Trans. Appl. Supercond. 28(4), 7000205 (2018), DOI.org/ 10.1109/TASC.2018.2808366.

[4] P. Badica, D. Batalu, M. Burdusel, M.A. Grigoroscuta, G.V. Aldica, M. Enculescu, R. Gabor Z. Wang, R. Huang, P. Li, Compressive properties of pristine and SiC-Te-added MgB<sub>2</sub> powders, green compacts and spark-plasma-sintered bulks, Ceram. Intern. 44 (9) 10181-10191 (2018) DOI: 10.1016/j.ceramint.2018.03.008.

[5] Z. Wang, P. Li, Dynamic failure and fracture mechanism in alumina ceramics: Experimental observations and finite element modelling, Ceram Int. 41, 12763 (2015).

[6] H. Wang, K.T. Ramesh, Dynamic strength and fragmentation of hot-pressed silicon carbide under uniaxial compression, Acta Mater. 52 355-367 (2004).

[7] G. Ravichandran, G. Subhash, A micromechanical model for high strain rate behavior of ceramics, Int. J. Solids Struct. 42, 2627-2646 (1995).

## Up-conversion films of Yb/Er-codoped CeO<sub>2</sub> on Si solar cells

M. Grigoroscuta, M. Secu, L. Trupina, M. Enculescu, C. Besleaga, I. Pintilie, P. Badica

Silicon based solar cells are widely used to harvest sun light as they absorb ~50% of the solar spectrum, but they convert ~31% due to different losses ([1] and therein refs.). Among losses we mention recombination losses, optical losses and resistivity losses. To reduce these undesirable effects, different approaches were tested: improved cell geometries [2, 3], use of transparent surface contacts and of anti-reflective coatings [4], methods leading to changes of the incident spectrum [5]. Changes to incident spectrum can be achieved by using optical phosphors where active materials are the rare earth luminescent materials. In this work [6, 7] we selected CeO<sub>2</sub>. It has good transparency in the visible-IR region, and it is substituted by other luminescent rare earth elements.

Co-doped CeO<sub>2</sub> with Yb and Er (Yb/Er = 4) was used as an up-converting thin film, applied on p+-n-n+ (100) single crystal silicon diodes (**Fig. 1**). Films were grown by pulsed laser deposition (PLD) for different laser fluencies.

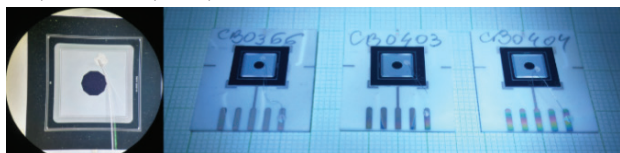


**Figure 1.** Silicon solar cells used in our experiments.

Sample	Yb/Er	EQE	Relative EQE	RMS (nm)
Reference cell	-	6.67 %	-	-
S1 (1.7 J/cm <sup>2</sup> )	3.17	6.69 %	0.34%	2.9
S2 (2.3 J/cm <sup>2</sup> )	3.86	7.21 %	8.21%	2.5
S3 (2.8 J/cm <sup>2</sup> )	3.27	6.87 %	3.13%	3.2

**Table 1.** Yb/Er ratio, EQE (external quantum efficiency), relative EQE for samples illuminated with 980 nm laser, and RMS roughness of Yb and Er co-doped CeO<sub>2</sub> thin films deposited at different laser fluencies on diodes.

The laser fluence was between 1.7 and 3.7 J/cm<sub>2</sub>. The composition (**Table 1**), thickness, and morphology of the films (**Fig.2**) depend on the laser fluence.

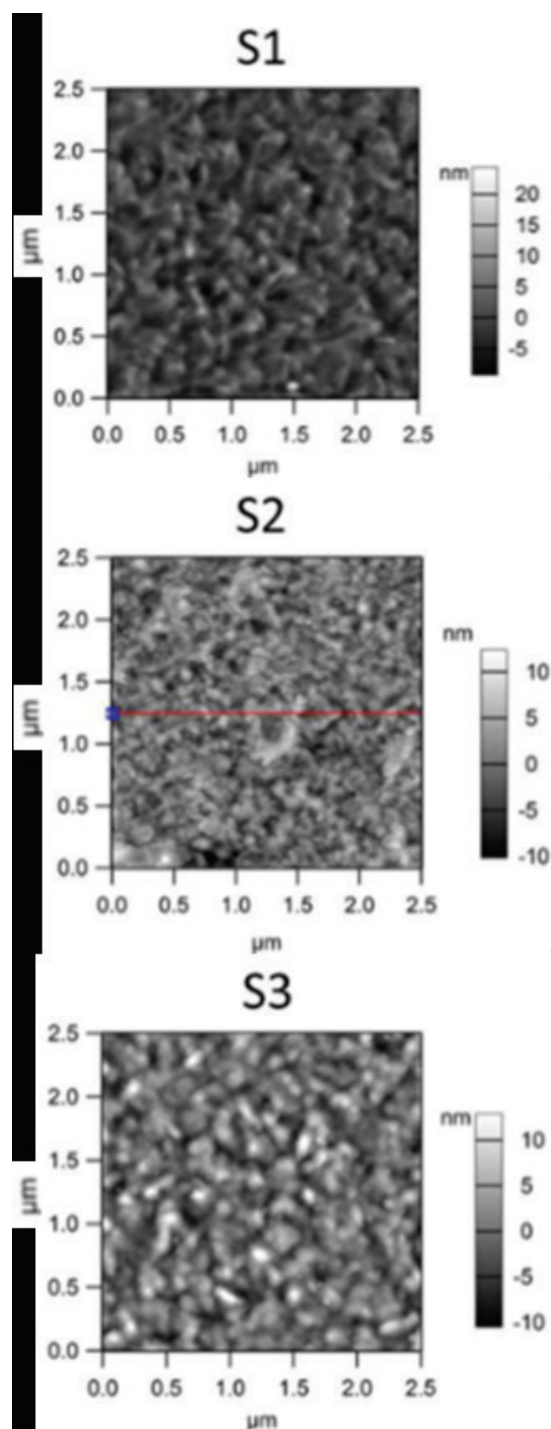


**Figure 2.** AFM images taken on the surface of the Yb/Er-doped films grown on (100) Si single crystal diodes (S1- 1.7 J/cm<sup>2</sup>, S2-2.3 J/cm<sup>2</sup>, S3-2.8 J/cm<sup>2</sup>).

The power conversion efficiency (PCE) has been determined from the current-voltage (I-V) characteristics (**Fig.3**) measured on p+-n-n+ Si diodes exposed to the solar simulator (AM 1.5 G spectrum). The relative external quantum efficiency EQE (**Table 1**) is the ratio between the EQE-enhancement of the p+-n-n+ Si diode before and after Yb/Er - co-doped CeO<sub>2</sub> thin film deposition and the EQE of the reference cell. The relative PCE was defined similar to relative EQE. Measurements of PCE and EQE of the cell before and after film deposition point on enhancement of these parameters when films are integrated.

The best results are obtained for the cell with the film grown at 2.3 J/cm<sub>2</sub>. This film has the closest ratio of Yb/Er to 4 (**Table 1**) as in the PLD target and shows the lowest roughness. The maximum values of relative PCE were 12.08 % for illumination with 1 sun and 39.19 % for 2.1 sun (**Fig.4**), while the relative EQE was 8.21 % when illuminated with 980 nm light.

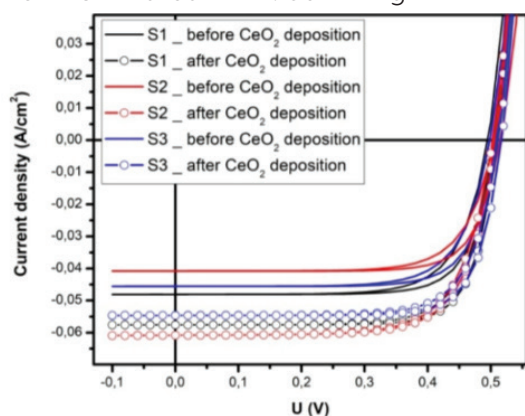


**Figure 3.** Current-Voltage characteristics of the silicon diode, before and after deposition of Yb<sup>3+</sup>/Er<sup>3+</sup> doped CeO<sub>2</sub> thin film (S1, S2 and S3), under 2.1 sun illumination.

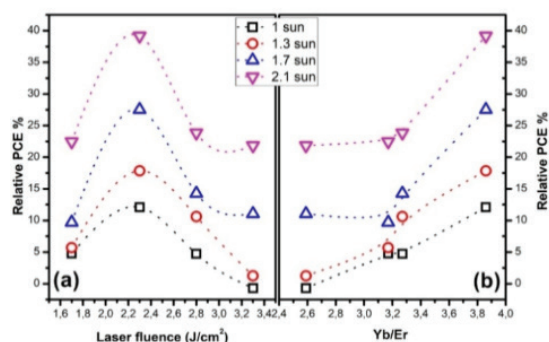


**Figure 4.** The relative PCE dependence on the laser fluence (a) and on Yb/Er elemental ratio measured at different solar simulator incident powers.

## References

- [1] W.G.J.H.M. van Sark, J. de Wild, J.K. Rath, A. Meijerink, and R. El Schropp, Upconversion in solar cells, *Nanoscale Res. Letters* 8:81 (2013) 1-10.
- [2] G. F. Martins, A. J. R. Thompson, B. Goller, D. Kovalev, and J. D. Murphy, Fabrication of 'finger-geometry' silicon solar cells by electrochemical anodisation, *J. Mater. Sci.* 48 (2012) 2977-2985.
- [3] X. Guo, H. Li, B. Y. Ahn, E. B. Duoss, K. J. Hsia, J. A. Lewis, and R. G. Nuzzo, Two- and three-dimensional folding of thin film single-crystalline silicon for photovoltaic power applications, *P. Natl. Acad. Sci. USA* 106 (2009) 20149-20154.
- [4] D.L. Young, W. Nemeth, S. Grover, A. Norman, H-C. Yuan, B.G. Lee, V. LaSalvia, and P. Stradins, Carrier selective, passivated contacts for high efficiency silicon solar cells based on transparent conducting oxides, *Energy Proced.* 55 (2014) 733-740.
- [5] S. Fischer, J.C. Goldschmidt, P. Löper, G.H. Bauer, R. Brüggemann, K. Krämer, D. Biner, M. Hermle, and S.W. Glunz, Enhancement of silicon solar cell efficiency by upconversion: optical and electrical characterization, *J. of Appl. Phys.* 108 (2010) 044912-(1-11).
- [6] M. Grigoroscuta, M. Secu, L. Trupina, M. Enculescu, C. Besleaga, I. Pintilie, P. Badica, Enhanced near-infrared response of a silicon solar cell by using an up-conversion phosphor film of Yb/Er - co-doped CeO<sub>2</sub>, *SOLAR ENERGY*, Volume: 171, 40-46 (2018); DOI: 10.1016/j.solener.2018.06.057; IF=4.374; AI= 0.9
- [7] P. Badica, Convert the light from the sun by integrating Er/Yb -CeO<sub>2</sub> thin film on the Si solar cells and generate more electric energy, *Science Trends*, Oct. 8, 2018 (<https://scicentrends.com/convert-the-light-from-the-sun-by-integrating-er-yb-ceo2-thin-film-on-the-si-solar-cells-and-generate-more-electric-energy/>)

## New insights for RE-free permanent magnet materials

Alina Daniela Crisan, Florin Vasiliu, Ionel Mercioniu, Cristina Bartha, Monica Enculescu and Ovidiu Crisan  
in collaboration with  
R. Nicula

Swiss Federal Laboratories for Materials Science and Technology EMPA, CH-3602 Thun,  
Switzerland

There has been a recent surge of interest for the L1<sub>0</sub>-based RE-free permanent magnets (PMs), mainly due to the strong hard magnetic features of the tetragonal L1<sub>0</sub> phase: high magnetocrystalline anisotropy (10 MJ/m<sup>3</sup>), high coercivity, high Curie temperature (450°C) and high chemical stability. These alloys were recently suggested as alternatives to the rare-earth permanent magnets and as potential candidates for patterned media in heat assisted or microwave assisted magnetic recording. There are however, many challenges for achieving these good magnetic properties. Additional elements sometimes have to be introduced in order to diminish the temperature of the L1<sub>0</sub> phase formation and also enhance both the magnetic and structural features. The present work deals with the study of the influence of Co and Ag addition on hard magnetic properties of CoPtAgB alloys prepared by rapid solidification from the melt or melt-spinning [1]. Another system that forms (in certain conditions) the L1<sub>0</sub> phase, more economically viable as PMs, is MnAl.

The alloys have been prepared by melt spinning under Ar protective atmosphere. The analyses of the crystal structure and the phase composition were carried out using XRD with Cu K $\alpha$  radiation. The magnetic properties were measured using a Superconducting Quantum Interference Device (SQUID) and the hysteresis loops have been performed at room temperature up to 5T applied field, parallel to the sample plane. The average grain size, lattice parameters and RMS strain, calculated from the fitting of the patterns with the full-profile MAUD algorithm, followed by the use of integral breadth method, are presented in Table I. It is seen that the average grain size increases with the annealing

temperature, ranging from around 20 nm for the as-cast state to 190 nm for the sample annealed at 670°C, due to the structural refinement imposed by the further crystallization and the disorder – order transition with formation of L1<sub>0</sub> tetragonal CoPt from the precursor fcc CoPt phase, occurring in the as-cast state.

Co <sub>48</sub> Pt <sub>8</sub> Ag <sub>6</sub> B <sub>18</sub>	Structure	Lattice parameters (Å)	Average grain size (nm)	RMS strain (%)
As cast	Fcc	3.729	20	0.78
400°C	Fcc	3.714	25	0.33
473°C	L1 <sub>0</sub>	2.650 3.679	47	0.25
670°C	L1 <sub>0</sub>	2.674 3.644	189	0.16

*Table I: Lattice parameters for CoPtAgB alloys as obtained from XRD patterns*

The magnetic behavior of the annealed sample reveal hard magnetic features. The hysteresis loop shows up to 10 times increase of the coercivity (about 4340 Oe) comparing to the as-cast sample. Such large values are typical for hard magnetic materials such as binary L1<sub>0</sub> phase alloys (either CoPt or FePt). Indeed, such large values of coercivity at 300K observed in the annealed sample, confirm the results obtained in HREM and XRD where highly ordered L1<sub>0</sub> CoPt phase is documented, inclusively by the presence of the rarely observed (003) superlattice ring in SAED patterns.

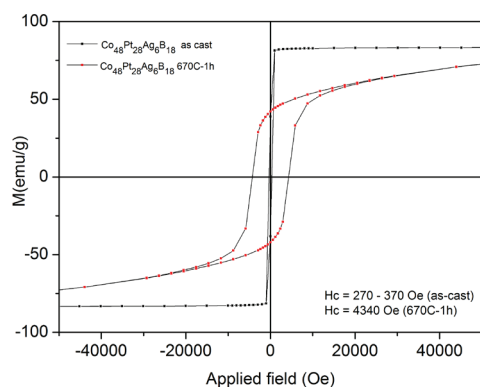


**Figure 1.** The hysteresis loops of CoPtAgB as-cast and annealed samples.

Mn-Al alloys are also promising candidates as PMs, having reasonably good magnetic properties due to the tetragonal  $\tau$ -phase, belonging to the larger class of  $L1_0$  structures. Structural and magnetic studies were also performed on MnAl as-cast and annealed alloys, using temperature-dependent synchrotron X-ray diffraction and VSM magnetometry [2]. We have observed that in the as-cast  $Mn_{55}Al_{45}$  sample, at room temperature, two crystalline phases are predominant, i.e.  $\mu_2$  phase (space group  $R\bar{3}m$  (160) ICDD file 00-032-0021) and  $\epsilon$  phase (space group  $P6/mmm$  ICDD file 00-048-1830), while  $\tau$ -phase has low relative abundance.

**Fig.2** shows the diffracted X-ray intensity recorded from X-ray patterns at various temperatures, in the range of the  $\epsilon$  to  $\beta$ -Mn phase transformation (466°C to 552°C). It can be observed that the phase transformation occurs abruptly, within a 20°C temperature range, however there is a small temperature range of about 5°C, centered at around 510-515°C where the two phases co-exist. The lines of the majority  $\mu_2$  phase have almost the same intensity throughout the whole investigated temperature range.

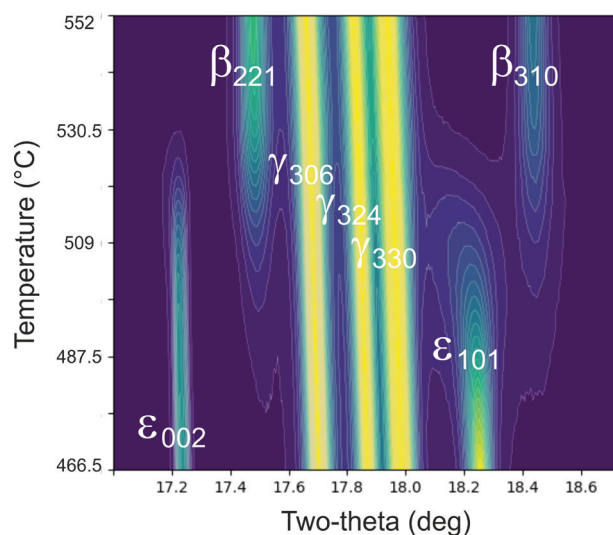


**Figure 2.** Contour plot of the diffracted X-ray intensity for the  $\epsilon$  to  $\beta$ -Mn phase transformation during heating.

In the MnAl system, we have shown that stoichiometry changes as small as 5 % produce quite different phase structure in the melt spun binary alloys. While in  $Mn_{60}Al_{40}$  only hcp  $\epsilon$  phase can be found, in  $Mn_{55}Al_{45}$  as-cast alloy, there is a quite complex phase structure with a mixture of  $\mu_2$  ( $Al_8Mn_5$ ) and  $\epsilon$  as well as hard magnetic MnAl  $\tau$ -phase. Magnetic measurements showed increased coercivity, similar with previously reported magnetization measurements and in agreement with the structural characteristics of the samples. These results are quite promising for obtaining even higher amount of MnAl  $\tau$ -phase with stronger coercive fields and pave the way for future RE-free permanent magnets.

## References

- [1] A.D. Crisan, F. Vasiliu, I. Mercioniu, C. Bartha, M. Enculescu, O. Crisan "Annealing-Induced High Ordering and Coercivity in Novel  $L1_0$  CoPt-Based Nanocomposite Magnets" *Metals* 8 (2018) 466.
- [2] A.D. Crisan, F. Vasiliu, R. Nicula, C. Bartha, I. Mercioniu, O. Crisan "Thermodynamic, structural and magnetic studies of phase transformations in MnAl nanocomposite alloys" *Materials Characterization* 140 (2018) 1-8.

## Progress in lowering temperatures of formation of 211 and 312 classes of MAX phases

Ovidiu Crisan and Alina Daniela Crisan

The ternary ceramic compounds known as MAX-phases have recently attracted considerable attention due to their nano-laminate atomic structure. There are two classes of compounds  $M_{n+1}AX_n$  where  $n = 1, 2$  or  $3$ , namely 211 and 312 that lately generated great scientific interest.  $Ti_3SiC_2$  exhibits high electric and thermal conductivity, is stiff and highly resistant to oxidation and thermal shocks. Due to its nanolaminate structure  $Cr_2AlC$  has low hardness, high Young-modulus, good compression strength, is a good electrical and thermal conductor and has very good oxidation resistance. Among possible applications of  $Cr_2AlC$  and  $Ti_3SiC_2$  one can count protective coatings for turbine propellers in avionics, self-healing materials, or other areas stretching from nuclear industry to microelectronics. The main obstacle for using MAX-phase films is perceived to be the high temperature required for synthesis of the crystalline matrix which, for many MAX phase materials, is above  $650^\circ C$  and severely limits the choice of substrate materials to those stable at this temperature. Within this work, thin films of  $Cr_2AlC$  [1] and  $Ti_3SiC_2$  [2] have been synthesized using magnetron sputtering techniques from elemental targets.

The structure and morphology are studied using EDX, WDSX and XRD. The broad line observed for the as-cast sample arises as a convolution of the several broadened Bragg lines (closely positioned) of the hexagonal structure. Some peaks (at around  $36.3^\circ$  and are nevertheless visible as kinks or tips on the broad peak feature (Fig.1). Quantitative analysis based on whole profile fitting shows that, in the crystallized sample 2a, single phase hexagonal  $Cr_2AlC$  crystalline phase is obtained, a finding that is confirmed by WDSX results.

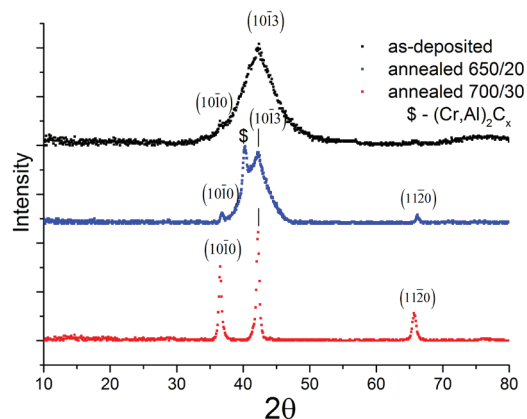


**Figure 1.** XRD spectra of as-deposited and annealed  $Cr_2AlC$  samples.

For the synthesis of  $Ti_3SiC_2$  films, we have employed dc magnetron sputtering from 3 elemental targets, Ti, Si and C. We present evidence by full-profile XRD analysis that crystalline structure composed of both hexagonal  $Ti_3SiC_2$  and cubic TiC is formed for a substrate temperature as low as  $550^\circ C$ . The hexagonal  $Ti_3SiC_2$  becomes the predominant phase for temperatures around  $700^\circ C$  for samples with little modifications of the stoichiometry (slight Si excess). The sample deposited at RT shows a typical XRD pattern consisting of very broad lines centered at around  $36, 40.5, 60$  and  $72^\circ$  which correspond to position of Bragg lines of TiC (111), (200), (220) and (311) respectively.

These broad lines witness the occurrence of small nanocrystalline grains having cubic TiC symmetry. By increasing the deposition temperature at  $300^\circ C$ , the XRD pattern exhibit rather similar pattern, with a slight narrowing of the main TiC lines (111) and (200) having as consequence the separation of the shoulder observed for deposition at RT, into a clear diffraction line TiC (111) for deposition at  $300^\circ C$ . The narrowing of the lines continues furthermore for the deposition at  $500^\circ C$  and the fifth TiC peak, the (222) reflection starts to appear.

Situation is changed for the deposition at 550°C. Here, apart from the well-defined TiC, clear peaks belonging to the 312 hexagonal phase structure appears. The 312 (101) and 312 (103) lines are visible as satellites on each side of the TiC (111) peak while the 312 (105) line is observable as a shoulder of the TiC (200) peak.

Other peaks belonging to the 312 MAX structure are also observable for the samples deposited at and above 550°C, namely the (108) and (115) lines of the hexagonal 312 structure. The almost same phase structure, i.e. mixture of cubic TiC and hexagonal  $Ti_3SiC_2$ , is preserved for the deposition at 650°C while the narrowing of the peaks, which indicates higher degree of crystallinity and larger grain sizes, continues.

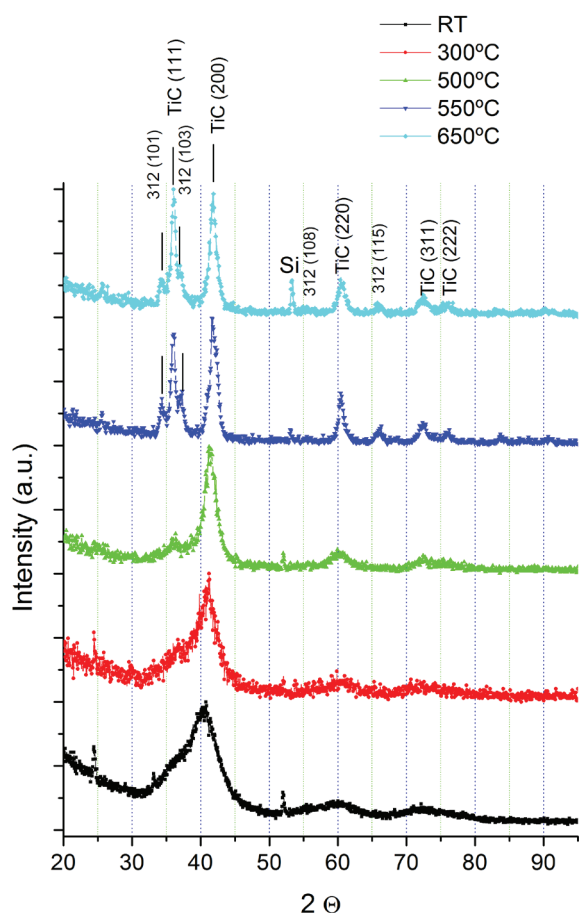


**Figure 2.** XRD spectra of TiSiC films deposited at various substrate temperatures.

Slight change in stoichiometry has been achieved by varying the Si target power from 45 W to 85 W [2]. The correspondingly obtained

samples have been also structurally investigated by XRD.

For clarity we present in (Fig.3) the comparison in the range of interest (30-50°) of the XRD patterns of samples with extreme Si powers: the one deposited with 45W and the other one deposited with 85W power of the Si magnetron. It can be seen that while the TiC peaks (111) and (200) have almost the same intensity for the two different patterns, all the 312 MAX phase main peaks show strong increase in intensity, even a 3-fold increase for the (008) peak, for the 85W Si sample than for the 45W Si sample.

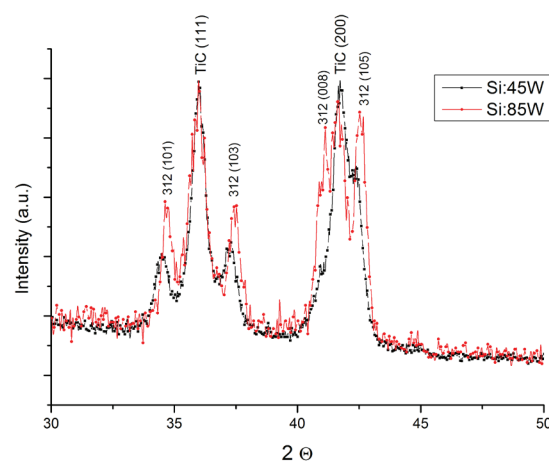


**Figure 3.** Central part of the XRD patterns of the samples deposited with Si target power of 45W and 85W respectively

We have thus proven that by finely tuning the magnetron power of the Si sputtering target, we obtain an alloy where the ternary phase of interest  $Ti_3SiC_2$  becomes predominant for deposition temperatures as low as 650°C. This finding opens good perspectives on the way of obtaining single phase  $Ti_3SiC_2$  in these systems.

## References

- [1] Crisan, O.; Crisan, A. D. "Incipient low-temperature formation of MAX phase in Cr-Al-C films" *Journal of Advanced Ceramics* 2018, 7(2): 143-151.
- [2] Crisan, A. D.; Crisan, O. "Low-Temperature Formation of 312 Phase in Ti-Si-C Ternary Compounds", *Digest Journal of Nanomaterials and Biostructures* 13 (2018) 155-162.

## Engineering magneto-optical properties by doping glasses

M.Sofronie, F.Tolea, C. Bartha, A. C. Galca, V.Kuncser, M.Valeanu,  
in cooperation with M. Elisa(INOE) and B. Sava, L. Boroica (INFLPR)

Magneto-optical glasses can be used as optical fiber isolators and as optical switchers. The both best-known magneto-optical Faraday and Kerr effects are related to the rotation of the polarization vector of light passing through or reflected from a magneto-optical material, respectively. The rotation angle,  $\theta_F$ , of the linear polarized incident light is proportional to the passing length and magnetic induction of the material via a proportionality constant, called Verdet constant ( $V_c$ ), which takes into account the intrinsic electronic properties of the material.

This wavelength dependent Verdet constant is positive for a diamagnetic material and negative for a paramagnetic material [1] and describes the magneto-optical performance of materials. A significant Faraday rotation of the polarization plane can be achieved when suitable paramagnetic or diamagnetic ions are incorporated in high enough concentration into the weakly diamagnetic matrix.  $Ce^{3+}$  and  $Tb^{3+}$ -doped [1] or CdS/ZnS quantum dots - doped [2] silico-phosphate thin films were obtained by the sol-gel method followed by the spin coating technique. Using unconventional wet methods, boro-phosphate systems were obtained by adding vitreous network modifiers and stabilizers namely  $Li_2O$ ,  $Al_2O_3$  and  $ZnO$ , together with  $PbO$  and  $Bi_2O_3$  as dopants [3] and  $Bi^{3+}$ ,  $Pb^{2+}$  and  $Bi^{3+}$ - $Pb^{2+}$ -containing alumino-phosphate glasses [4].

The morphology was investigated by Scanning Electron Microscopy and Atomic Force Microscopy. The elemental composition was determined by Energy Dispersive X-ray analysis. All samples were characterized in respect to magnetic and magneto-optical properties by magnetometry and ellipsometry.  $V_c$  was evaluated from Faraday rotation (FR) measurements over the entire visible spectrum, by transmission ellipsometry. The magnetic field assisted FR measurements were carried out with the aid of a toroidal permanent magnet, with the applied field parallel to the wave vector. Morphological analyses showed that the  $Ce^{3+}$  and  $Tb^{3+}$ -doped

silico-phosphate thin films were mostly isotropic but not totally homogeneous in appearance, Ce-doped film presenting a better quality than the Tb-doped film. The chemical elements were uniformly distributed in the deposited material for both samples. However, some undissolved particles of Tb precursor ( $TbCl_3 \cdot 6H_2O$ ) were observed on the  $Tb^{3+}$ -doped film surface, so that the physical support for antiferromagnetically coupled  $Tb^{3+}$  ions in small clusters is justified. The room temperature magnetization curves (expressed as magnetic moment per unit surface) on both rare-earth doped films denote, in addition to the ferromagnetic behavior attested by the hysteresis, a paramagnetic and a diamagnetic contribution (Fig.1-hysteresis curves with empty symbols). Responsible for the paramagnetic component are the dispersed free rare-earth ions in glass matrix while the diamagnetic reflects the contribution of the substrate and silico-phosphate matrix. By simply subtracting both the paramagnetic and diamagnetic contributions from the hysteresis loop raw data, a clear ferromagnetic contribution with a small coercive magnetic field (110 Oe for Ce-doped film and 75 Oe for Tb-doped film) is revealed (Fig.1 - hysteresis curves with full symbols). It is to note that all the magnetic parameters (as for example susceptibilities and magnetizations) for Tb-doped film are smaller compared to those for Ce-doped film (of almost similar thickness), despite both had the same mole percent of rare-earth oxide in the nominal composition and that the effective magnetic moment is higher for Tb ions. This aspect suggests that the effective number of spins of Tb per unit surface in the spin coated film is less than the nominal one. Thus, corroborating with the SEM results it may be supposed that either some undissolved  $TbCl_3$  powder remained outside the film after deposition and heat treatment or some Tb clusters are formed, with an antiferromagnetic coupling between the  $Tb^{3+}$  ions in the cluster (e.g. 5 antiferromagnetically coupled magnetic moments of  $Tb^{3+}$  is equivalent to 1 net magnetic moment of  $Tb^{3+}$ ).

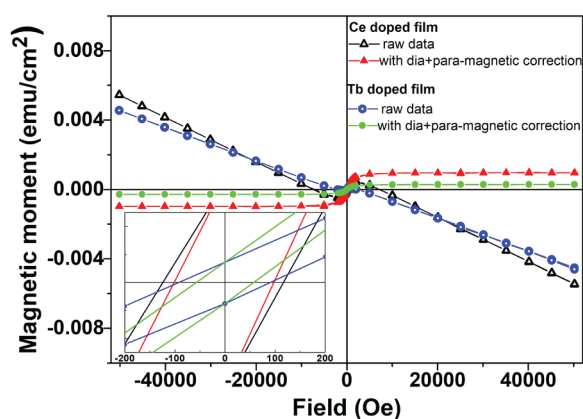


**Figure 1.** The room temperature hysteresis curves (expressed as magnetic moment per unit surface) on both rare-earth doped films. Inset: detail on the coercive field.

The results of Magneto-Optical Kerr Effect (MOKE) measurements attest the magneto-optical properties of both films. The Kerr rotation for  $\text{Ce}^{3+}$  doped film was found to be 1.03 mdeg/T, and only 0.28 mdeg/T for  $\text{Tb}^{3+}$  doped film, this value being in agreement with the magnetic data supporting the antiferromagnetic cluster formation of  $\text{Tb}^{3+}$  ions at the film surface in the  $\text{Tb}^{3+}$ -doped sample. Considering the thickness of  $\text{Ce}^{3+}$  and  $\text{Tb}^{3+}$ -doped silicophosphate films of 1.8(1)  $\mu\text{m}$  and 1.6(1)  $\mu\text{m}$ , respectively, measured by SEM analysis and the value of the films refractive index  $\sim 1.6$ , the intrinsic magneto-optical doped films characteristic (e.g. the Verdet constant) has been evaluated.

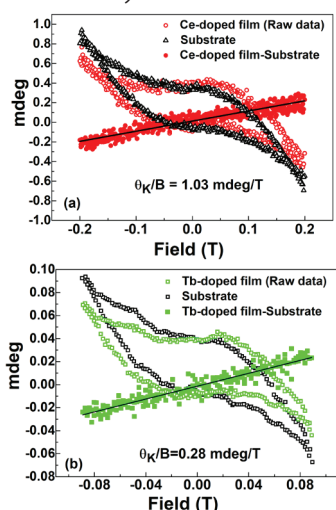


**Figure 2.** Kerr hysteresis loops obtained at room temperature for (a)  $\text{Ce}^{3+}$  (b) and  $\text{Tb}^{3+}$  -doped silico-phosphate films.

At the wavelength of 635 nm, VC is - 0.035 min/(Oe x cm) for Ce-doped film and - 0.011 min/(Oe x cm)

for Tb-doped film, calculated based on magnetic and magneto-optic experimental data. Taking into account that the magnitude of VC (or of Faraday rotation) in glasses doped with  $\text{Tb}^{3+}$  ions should be significantly higher than that for other  $\text{RE}^{3+}$  ions [1], the above reported values confirm the deficit in  $\text{Tb}^{3+}$  effective spin concentration in the  $\text{Tb}^{3+}$ -doped silico-phosphate film in concordance with the magnetic data.

The Verdet constant for  $\text{Bi}^{3+}$ ,  $\text{Pb}^{2+}$  and  $\text{Bi}^{3+}$ - $\text{Pb}^{2+}$ -containing aluminophosphate glasses appeared to have positive values proving a diamagnetic behavior of the investigated materials. The presence of high amount of  $\text{Bi}^{3+}$  and  $\text{Pb}^{2+}$  in the phosphate glass network increases more than twice the diamagnetic Verdet constant (0.1 min/Oe.cm at 400 nm) by comparison with Bi, Pb-single doped glasses at constant wavelength ( $\sim 0.05$  min/Oe.cm at 400 nm). The highly transparent Bi and Pb oxide codoped boron phosphate glass presented valuable magneto-optical properties together high transmittance over a large spectral range (e.g. from 300 to 1600 nm) whereas the Verdet constant reaches values of 0.03 min/cm/Oe for the blue light and 0.015 min/cm/Oe for the red light, comparable to the best magneto-optical commercial bulk products. All these properties recommend Bi and Pb codoped borophosphate glasses for ultra-fast opto-magnetic switching devices, magnetic storage, wave guides, optoelectronics and lasers uses.

## References

- [1] Magneto-optical properties of  $\text{Ce}^{3+}$  and  $\text{Tb}^{3+}$ -doped silico-phosphate sol-gel thin films, C. R. Stefan, M. Elisa, I. C. Vasiliu, B. A. Sava, L. Boroica, M. Sofronie, F. Tolea, M. Enculescu, V. Kuncser, A. Beldiceanu, A. Volceanov, M. Eftimie, Appl. Surface Sci. 448 (2018) p. 474-480.
- [2] CdS/ZnS-doped silico-phosphate films prepared by sol-gel synthesis, M.I. Rusu, C.R. Stefan, M. Elisa, I.D. Feraru, I.C. Vasiliu, C. Bartha, R.D. Trusca, E. Vasile, S. Peretz, J. of Non-Crystalline Solids 481 (2018) 435-440.
- [3] Bismuth and lead oxides codoped boron phosphate glasses for Faraday rotators, B.A. Sava, L. Boroica, M. Elisa, O. Shikimaka, D. Grabco, M. Popa, Z. Barbos, R. Iordanescu, A.M. Niculescu, V. Kuncser, A.C. Galca, M. Eftimie, R.C.C. Monteiro, Cer. Int. 44 (2018) Issue 6, p.6016-6025.
- [4] Magnetic and magneto-optical properties of Bi and Pb-containing aluminophosphate glass, M. Elisa, R. Iordanescu, C. Vasiliu, B.A. Sava, L. Boroica, M. Valeanu, V. Kuncser, A.C. Galca, A. Volceanov, M. Eftimie, A. Melinescu, A. Beldiceanu, J. of Non-crystalline Solids 465 (2017) p.55-58.

## Epitaxy of Ag(111) on Si(111)

A.E. Bocîrnea, R.M. Costescu, N.G. Apostol, C.M. Teodorescu

Although Ag on Si(111) is one of the most studied heterostructures in surface science due to the abrupt interface and low reactivity between Ag and Si, as well as the similar work functions of Si(111) and Ag(111) giving a low surface barrier height with applicability in the fabrication of low-barrier Schottky diodes, there was little existing work on thicker Ag(111) films grown on Si(111). Our interest in this system was sparked by the need to realize well defined Ag(111) surfaces as support for subsequent growth of 2D materials such as graphene and borophene through a more cost effective and simpler process than the sputter-annealing of single Ag crystals. [1]

We grew Ag films of up to 30 nm by molecular beam epitaxy (MBE) on Si(111)7×7 substrates at room temperature. The films, which were realized in several steps with investigations of each intermediary thicknesses, were analysed by low energy electron diffraction (LEED), X-ray photoelectron spectroscopy (XPS), and scanning tunneling microscopy (STM).

LEED images showed both Ag and Si spots starting with the deposition of 1 ML of Ag and beyond a thickness of about 1.3 ML (0.3 nm) of Ag LEED spots corresponding to Ag(111) start to appear, the LEED spots becoming more and more pronounced; beyond ~6 nm of Ag, a clear Ag(111)1×1 pattern is observed (Fig.1). The LEED results point to the formation of single crystal Ag(111) islands with in-plane axes parallel to that of the substrate, with only a slight 2.4% increase of the in-plane lattice constant of the Ag film with respect to that of bulk Ag.

The spectra of Si and Ag core levels analysed by XPS are in agreement with a model assuming the initial formation of Ag islands with linear variation of coverage vs. Ag thickness in the early stages of Ag deposition, followed by quasi layer-by-Layer growth (Fig.2). The surface is fully covered at ~21 nm of equivalent bulk Ag deposited. The interface barrier obtained from XPS analysis is in the range of 0.4 eV, lower than all values reported previously.

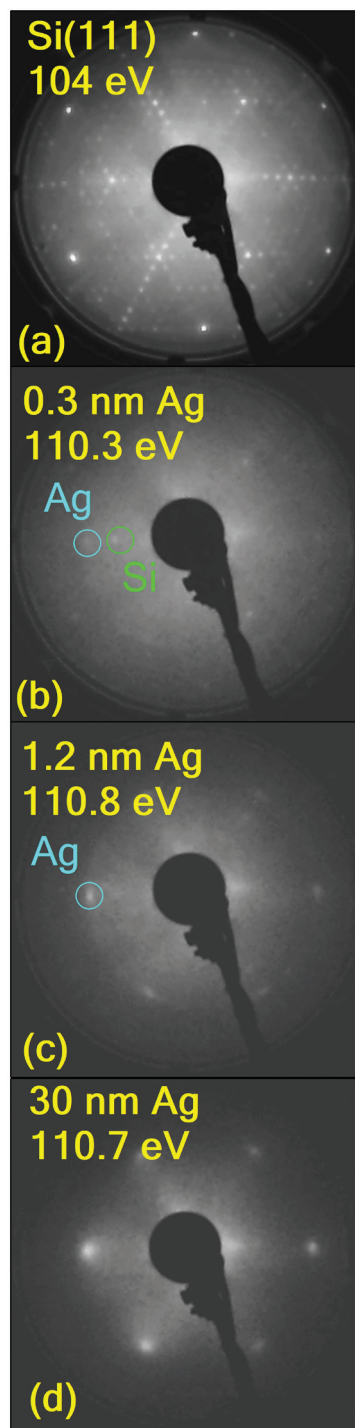


**Figure 1.** Low energy electron diffraction (LEED) images for (a) clean Si(111) 7×7 at 104 eV kinetic energy (a) and (b-d) Ag of different thickness deposited on Si(111), at similar kinetic energies. Adapted from [1] ©Elsevier.

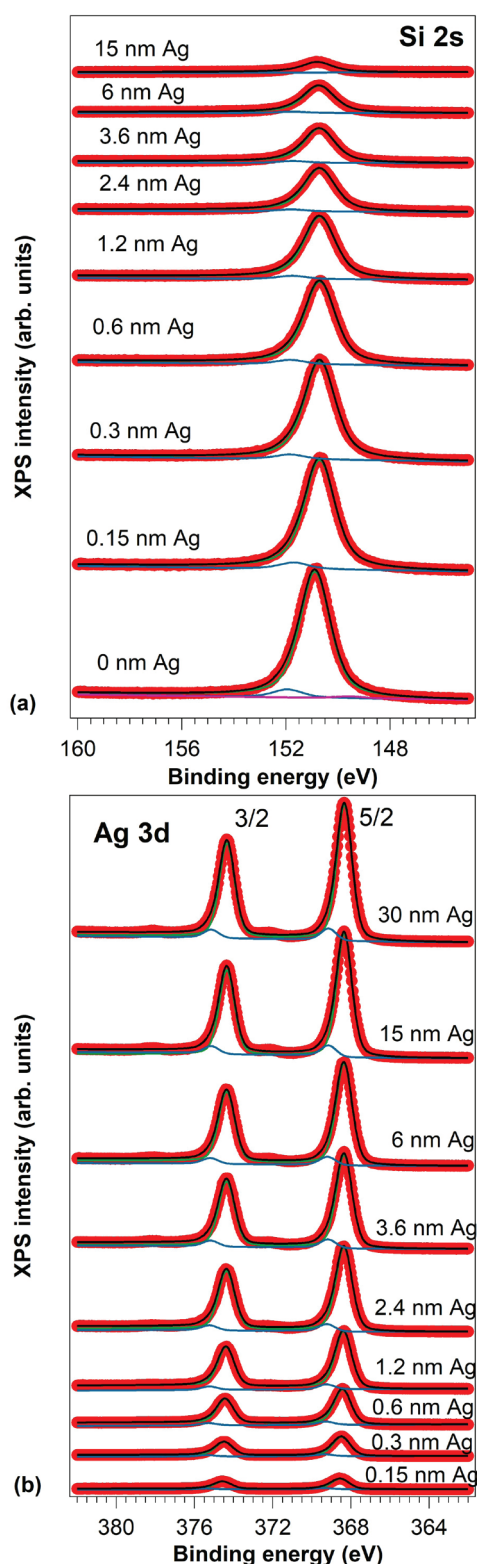


**Figure 2.** X-ray photoelectron spectroscopy (XPS) spectra of levels (a) Si 2s and (b) Ag 3d for clean Si(111) (0 nm Ag) and several thicknesses of Ag between 0.15 nm and 30 nm deposited on Si(111). The spectra are simulated with Voigt profiles, featuring a principal (bulk) component and one or two surface components. Adapted from [1] ©Elsevier.

Thus, these heterostructures are good candidates for low barrier Schottky diodes.

STM imaging (**Fig.3**) confirms the average terrace widths detected from LEED spot profile analysis of ~30 nm for clean Si(111)7×7 and about 5.5 nm for the thickest Ag(111) film. These 30 nm Ag films grown on Si(111)7×7 are remarkably flat (deviations on the order of 2%).

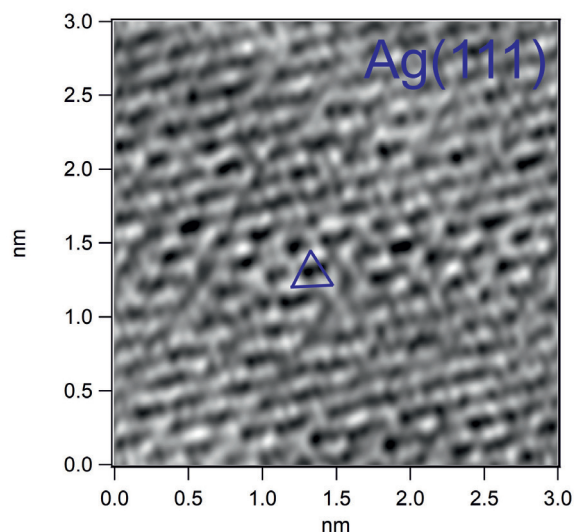


**Figure 3.** Scanning tunneling microscopy image (Fourier filtered to eliminate electronic instabilities) of the Ag(111) surface for a 30 nm Ag film on Si(111); tip voltage 1.77 V, tip current 0.16 nA. Adapted from [1] ©Elsevier.

This study showed that epitaxial Ag grown at room temperature on clean Si(111) substrates is an attractive system due both to the the low surface barrier, which makes it suitable for devices such as power sensors or high frequency mixers with cost effective semiconductor substrates, and to the fact that good quality thick Ag(111) films can be synthesized on Si (111)7×7, which gives a cheap and simple technique of obtaining single crystalline, atomically clean (111) supports for 2D structures.

## References

- [1] A.E. Bocîrneă, R.M. Costescu, N.G. Apostol, C.M. Teodorescu, Appl. Surf. Sci. 473, 433–441 (2019).

## Photoconduction of Ge nanocrystals embedded in TiO<sub>2</sub> matrix

Ana-Maria Lepadatu, Adrian Slav, Catalin Palade, Ioana Dascalescu, Monica Enculescu, Sorina Lazanu, Valentin Serban Teodorescu, Magdalena Lidia Ciurea and Toma Stoica

in collaboration with

Sorina Eftimie

Faculty of Physics, University of Bucharest

Dense Ge nanocrystals (NC<sub>s</sub>) embedded in TiO<sub>2</sub> matrix were prepared by magnetron sputtering deposition, followed by rapid thermal annealing (RTA) at different temperatures. Their optical, electrical and photoelectrical properties were investigated in correlation with crystalline structure and morphology. The morphology was characterized by high resolution transmission electron microscopy (HRTEM), selected area electron diffraction (SAED) and X-ray diffraction (XRD) measurements. Optical transmission and reflectance spectra were measured within the 300–1100 nm range. For electrical and photoelectrical measurements, coplanar samples were prepared by thermal evaporation of Al electrodes. Dark and photocurrent measurements were performed in vacuum in a cryostat with He closed-circuit cooling system, in the wavelength range from 600 to 2000 nm [1].

The nanocrystallisation occurs at 550°C. (Fig.1) evidences anatase TiO<sub>2</sub> and dense (~ 4×10<sup>18</sup> cm<sup>-3</sup>) cubic Ge NCs with size of about 4–5 nm distanced from each other by 2–3 nm, having some amorphous phase in between them.

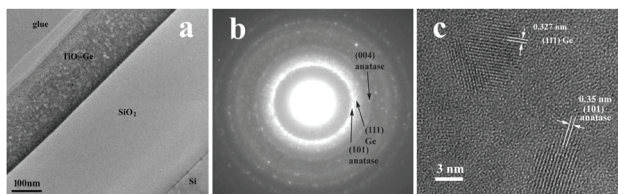


**Figure 1.** Images of sample deposited on SiO<sub>2</sub>/Si substrate after RTA at 550°C: (a) cross section TEM image, (b) SAED pattern and (c) HRTEM image showing anatase TiO<sub>2</sub> and cubic Ge NCs.

The analysis of the X ray diffractogram of the same sample reveals broad peaks corresponding to both NCs of cubic Ge (mean size of 4.7 nm) and anatase TiO<sub>2</sub>. In contrast to this sample (S550), the as-deposited one (Sasd) is amorphous, while after 700°C RTA (S700) mainly anatase TiO<sub>2</sub> peaks corresponding to TiO<sub>2</sub> NCs with 20–30 nm size and very weak diffraction from cubic Ge were evidenced, explained by the strong diffusion and oxidation of Ge that occur at high temperatures.

Optical transmittance (Tr) and reflectance (Rf) were measured on films deposited on fused quartz, and only Rf on those deposited on SiO<sub>2</sub>/c-Si substrate. By fitting the simulated curves, computed using the transfer matrix formalism, to the experimental ones, the spectral dependencies of the refractive index (n) and extinction coefficient (k) have been obtained. The results for S550 are presented in (Fig.2). For S550, the absorption threshold is about 1.14 eV. This blue-shift of the bandgap for Ge NCs in respect to bulk Ge can be explained by quantum confinement in NCs with diameter of about 5 nm in agreement with HRTEM and XRD results. S550 shows absorption in VIS-NIR, the absorption being lower than in the amorphous Sasd, but substantially enhanced in respect to TiO<sub>2</sub> (S700).

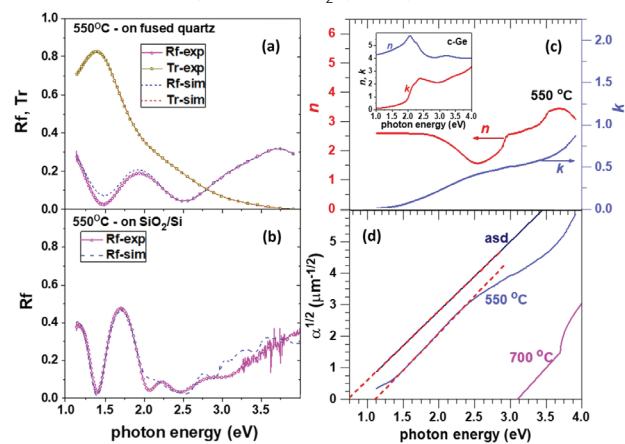


**Figure 2** (a and b) Rf and Tr for S550 on fused quartz and SiO<sub>2</sub>/Si respectively; experimental curves – continuous lines, simulated – dashed; (c) n and k for S550; (d) Tauc plot of  $\alpha^{1/2}$  for Sasd, S550 and S700.

Electrical and photoelectrical measurements were performed on Ge-TiO<sub>2</sub> films deposited on SiO<sub>2</sub>/Si substrates (Fig.3a), with the substrate left as a floating gate electrode. In the range of applied voltages between +20 and -20 V, the maximum values of the electric fields are 33 V/cm in the Ge-TiO<sub>2</sub> film, and 5×10<sup>5</sup> V/cm in SiO<sub>2</sub> respectively. Thus, there are field effect induced charges at both SiO<sub>2</sub>/Si and Ge NCs-TiO<sub>2</sub>/SiO<sub>2</sub> interfaces.

The measurements of the temperature dependence of the dark current enabled us to identify the conduction mechanisms. In S550, at high temperatures the current is given by a Boltzmann component with activation energy  $E_a$  of about 0.30 eV that can be assigned to electrons thermally excited on delocalized states. At intermediate temperatures we found a thermally activated hopping transport  $I \sim \exp(-(T_0/T)^m)$  with the exponent  $m = 1/2$  and the value of  $T_0$  of about  $2.4 \times 10^4$  K. We explain this based on a “Coulomb gap”, i.e. a quadratic decrease in the localized state distribution at Fermi level; Efros and Shklovskii (ES) demonstrated that the localized states distribution vanishes at Fermi level for an electronic system due to Coulomb interaction. Finally, at lower temperatures, the conductance has a contribution of tunnelling transport independent on temperature (Fig 3b). Ge NCs are absent in Sasd, and almost absent in S700; therefore, the conduction of these samples does not show ES hopping. There is a higher disorder in Sasd in respect to S550, and therefore the mobility on extended states is lower at high temperatures.

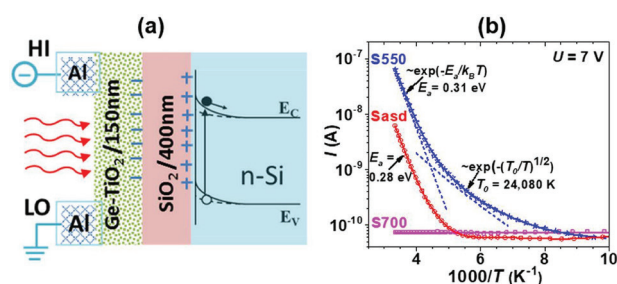


**Figure 3(a)** Schematic of coplanar samples for dark and photocurrent measurements. **(b)** Experimental temperature dependence (curves with symbols) of the dark current for 7 V bias, and fit curves

We measured the spectral photocurrent by illumination with modulated monochromatic light, with the Ge-TiO<sub>2</sub> layer isolated from the substrate by a 400 nm thick SiO<sub>2</sub> layer. In (Fig. 4) we present the photocurrent spectra of S550 measured at voltages between 7 and 20 V. We found a broad peak at high photon energies ( $\lambda \sim 870$  nm) due to photo-effects in Ge-TiO<sub>2</sub> layer and a narrow peak at lower energies ( $\lambda \sim 1100$  nm) due to surface photovoltage and gating effects in Si substrate. The voltage dependence of the intensities of the main peaks at 870 nm and 1100 nm (Fig. 4b) are obtained by deconvolution (inset of Fig. 4b). The photocurrent due to photo-effects in Ge-TiO<sub>2</sub> layer with the peak at 870 nm has the threshold at about 1100 nm ( $\sim 1.14$  eV) in good agreement with the optical bandgap value found from optical absorption

studies (Fig. 2d). The intensity of both maxima at 870 nm and 1100 nm varies exponentially for low voltages as  $I_{ph} \sim \exp(eU/E_0)$ , and differently saturates: first the peak at 1100 nm ( $U > 12$  V), then the broad one at 870 nm ( $U > 15$  V). The ac photocurrent produced by chopped light illumination (frequency of 120 Hz) may have beside the path I through the Ge-TiO<sub>2</sub> layer an important component through the Si substrate by capacitive coupling (path II) - (Fig. 4c).

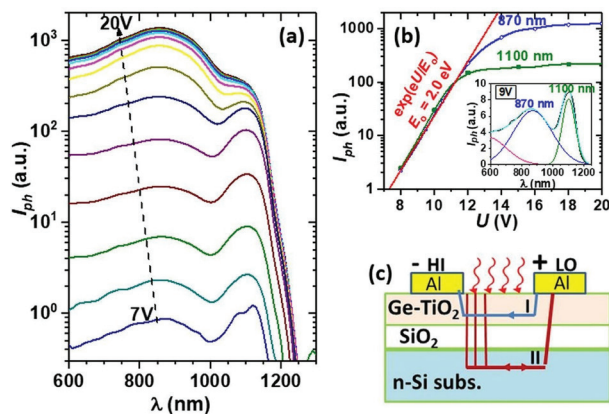


**Figure 4(a)** Photocurrent spectra at RT for voltage varied in steps of 1 V. **(b)** Voltage dependence of the intensity of peaks at 870 nm and 1100 nm. Inset - deconvolution of spectrum for 9 V. **(c)** Schematic of samples and ac photocurrent paths for chopped light.

The non-linear behaviour of the photocurrent intensity (Fig. 4b) can be explained by field assisted thermal ionization of electron-hole pairs photo-generated inside NCs and a heterojunction effect at Ge NCs/TiO<sub>2</sub> interfaces.

In conclusion, an exponential increase of the photocurrent with the applied voltage was found in coplanar films with Ge NCs embedded in TiO<sub>2</sub>, deposited on oxidized Si wafers. The behaviour was explained by field effect control of the Fermi level at the Ge nanocrystals-TiO<sub>2</sub> layer/substrate interfaces. The blue-shift of the absorption gap from bulk Ge value to 1.14 eV was evidenced in both photocurrent spectra and optical reflection-transmission experiments, in good agreement with quantum confinement induced bandgap broadening in Ge NCs with sizes of about 5 nm as found from HRTEM and XRD investigations.

## References

- [1] A.-M. Lepadatu, A. Slav, C. Palade, I. Dascalescu, M. Enculescu, S. Iftimie, S. Lazanu, V. S. Teodorescu, M. L. Ciurea, T. Stoica, Sci. Rep. 8, 4898 (2018).

## Polymeric nano-composites films with luminescent nanophosphors

C.E. Secu, E. Matei, I. Pasuk, C. Negriila and M. Secu

Hybrid inorganic nanophosphor-polymer composites, where luminescent particles are homogeneously dispersed into a polymer were considered for a broad range of applications: optoelectronic devices, white light generation displays or photovoltaic applications ([1] and references therein).

There is increasing interest on  $\text{Eu}^{2+}$ -doped  $\text{BaCl}_2$  crystal showing remarkable scintillating and storage phosphor performances. However, these properties are strongly dependent on the raw material purification and clean environment control and is chemically unstable in open atmosphere. A viable way to tackle these problems may be to use  $\text{BaCl}_2$  nanoparticles (NPs) embedded in inorganic-polymer composites.

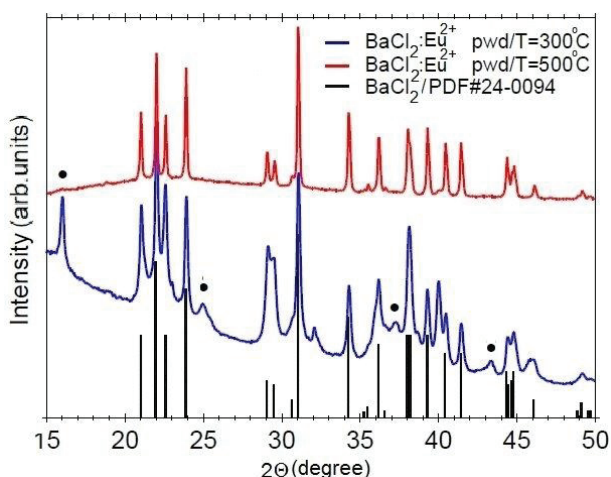


**Figure 1.** XRD patterns of the  $\text{Eu}^{2+}$ -doped  $\text{BaCl}_2$  nanocrystalline powder annealed at  $300^\circ\text{C}$  and  $500^\circ\text{C}$  by comparison to the  $\text{BaCl}_2$  (PDF file 24-0094); weaker peaks of the  $\text{BaCl}_2(\text{H}_2\text{O})$  are represented by black dots.

Luminescent  $\text{Eu}^{2+}$  (1%) doped  $\text{BaCl}_2$  nanopowders were prepared by using a hybrid sol-gel /thermal decomposition route [2,3] (Fig.1). Under UV excitation we observed strong luminescence band at  $396\text{ nm}$  assigned to the  $d \rightarrow f$  type transitions of  $\text{Eu}^{2+}$  ions (Fig.2) and much weaker  $\text{Eu}^{3+}$  related peaks (see below). The same  $\text{Eu}^{2+}$  related luminescence was observed under X-ray excitation accompanied by a weaker visible band related to synthesis defects.

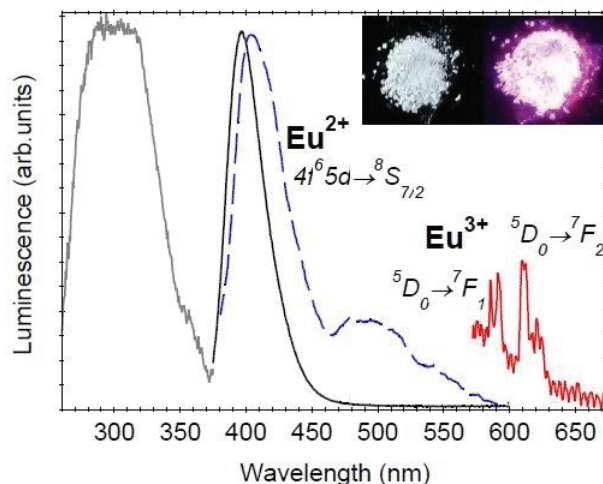


**Figure 2.** Photoluminescence spectrum recorded using  $345\text{ nm}$  excitation (right side) and the corresponding excitation spectrum (left side) of the  $395\text{ nm}$  luminescence; the dotted curve represents the X-ray excited luminescence. The inset shows the images of the  $\text{Eu}^{2+}$ -doped  $\text{BaCl}_2$  nanocrystalline powder under daylight, as compared to UV-light excitation at  $365\text{ nm}$ .

X-ray photoelectron spectroscopy indicated the formation of the  $\text{BaCl}_2$  nanocrystalline phase. Besides this,  $\text{Eu}^{3+}$  ions species resulted from the oxidation of  $\text{Eu}^{2+}$  ions at the nanocrystals surface during the calcinations (in air). Such oxidation can be responsible for the  $\text{BaO}$  presence as well as acting as a passivating layer and providing a better chemical stability with respect to the polymer.

The  $\text{Eu}^{2+}$  (1%)- $\text{BaCl}_2$  nanophosphor was used for the preparation of a  $\text{PVP}(\text{BaCl}_2:\text{Eu}^{2+})$  nanocomposite and optical response was studied by comparison to the nanopowder. The phosphor nanopowder was mixed with a  $\text{PVP}$  (poly(vinyl pyrrolidone)) solution (in isopropanol) and simply poured on teflon plate followed by drying.

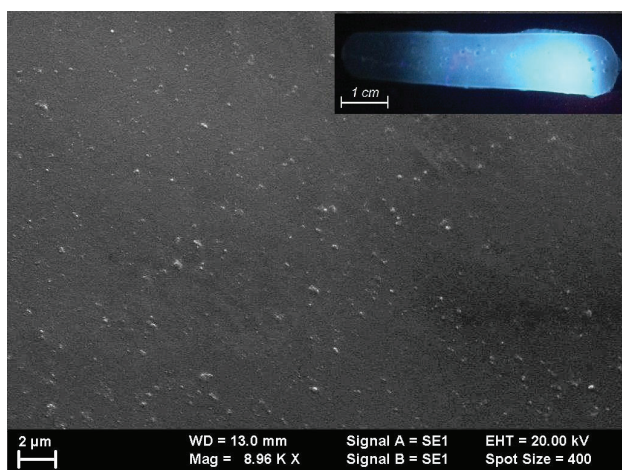


**Figure 3.** SEM image (cross section) and optical image of the polymer nanocomposite (under 360 nm spot light) (inset).

The SEM image of the polymer nanocomposite (**Fig.3**) showed a relatively uniform distribution of nanoparticles (about 100 nm). Photoluminescence properties are preserved after incorporation in the polymeric matrix (**Fig.3-inset**).

A recent application of such luminescent polymeric nanocomposites is the art work labeling by using molecular markers. They have to be resilient to external factors, personalized and relatively easy to be identified and accessible to authorized expert of art [4].

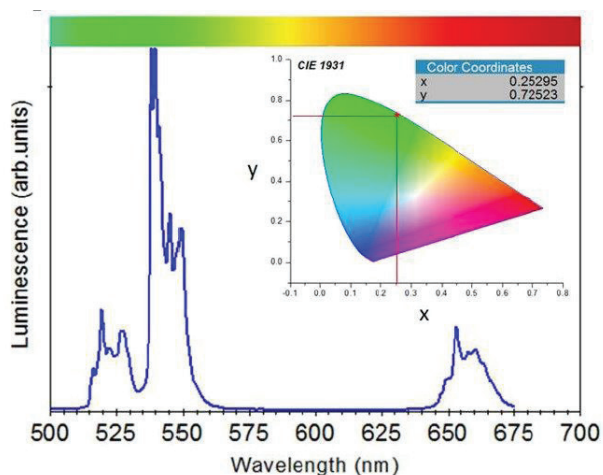


**Figure 4.** Up-conversion (UC) luminescence spectra recorded on PVP@UC-phosphor nanocomposite under IR laser light at 980nm

For the synthesis of Yb<sup>3+</sup>/Er<sup>3+</sup> co-doped NaYF<sub>4</sub> nanophosphor we used a hybrid sol-gel / thermal decomposition route [5]. The UC spectra showed (2H<sub>11/2</sub>, 4S<sub>3/2</sub>) → 4I<sub>15/2</sub>) and red

(4F<sub>9/2</sub> → 4I<sub>15/2</sub>) luminescence bands of Er<sup>3+</sup> ions (**Fig.4**). Then a PVP@UC-phosphor nanocomposite was prepared and spreaded on a textile surface. We observed that the UC properties are preserved after incorporation within polymeric matrix (**Fig.5**). Colorimetric analysis (**Fig.4-inset**) can be performed relatively easy by using commercial equipment and can provide a reliable and useful tool for the art work labelling [4].

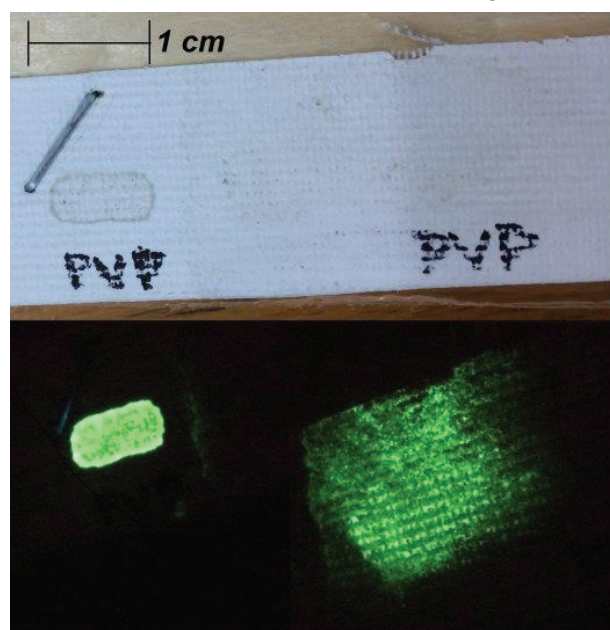


**Figure 5.** The images of the PVP@UC-phosphor nanocomposite under daylight by comparison to the 980nm IR laser light.

Further development of luminescent nanophosphor polymer nanocomposite can be seen in improving of their dispersability by using proper surface modification and a controlled/better thin film deposition.

## References

- [1] T. Hanemann and D. V Szabó Materials 3, 3468-3517 (2010).
- [2] C. E. Secu, Negrila and M Secu J. Phys. D: Appl. Phys. 51 305302 (2018).
- [3] C. Secu and M. Secu Application patent no A/00295 din 10.08.2017.
- [4] Final report of the "Marcarea moleculară a operelor de artă" project, PN-III-P2-2.1-BG-2016-0331, No. 125BG/30-09-2016.
- [5] C. Bartha, C.E. Secu, E. Matei, M. Secu CrystEngComm vol 19 (34), p.4992 (2017)

## Paramagnetic point defects in ultrapure and oxygen doped silicon irradiated with high fluence 3.5 MeV and 27 MeV electrons

A.C. Joita and S.V. Nistor

The planned upgrade of the Large Hadron Collider from CERN requires an improvement in the silicon (Si) based radiation detectors for particle tracking, in particular in their long term stable performance. One therefore needs a better knowledge of the nature, stability and transformation properties of the irradiation paramagnetic point defects (IPPDs) created over the whole operation time.

Electron Spin Resonance (ESR) is one of the best techniques for determining the presence, structure/nature and concentration of the IPPDs, offering comprehensive information about the role played by existing impurities, in particular the oxygen, in their production, stability and recombination properties [1,2,3].

Here we present the results of a comparative study concerning the nature of the IPPDs produced at room temperature (RT) in n-type (P-doped) oxygen-lean, standard float-zone (STFZ) and oxygen doped float-zone (DOFZ) silicon by irradiation with high fluence monochromatic electron beams of low (3.5MeV) and high (27MeV) energy, as well as during further thermal isochronal annealing up to 300oC. We also present the results of an ESR study concerning the long term (3.5 years) aging at 250K of the IPPDs produced by RT irradiation with 27MeV electrons in STFZ samples. The ESR methodology is similar to the one described in ref.[1]. Details about the equipment are given in refs.[4,5]. ESR relies on the presence of unpaired electrons, sometimes by additional optical “in-situ” excitation [6]. Analysing the resulting ESR spectra one could observe, evaluate and compare the temperature induced changes in the nature and concentration of the observed IPPDs [7].

The as-irradiated STFZ and DOFZ samples exhibited isotropic EPR spectra, attributed [8] to paramagnetic surface and impurity related centers and a few weak anisotropic signals, strongly enhanced by “in-situ” excitation. The analysis of

data presented in (Figs. 1a to 1d) shows that the main IPPDs produced by irradiation are thermally stable, up to 250oC in the STFZ samples (Figs.1a, 1c) and up to 200oC in both DOFZ samples (Figs.1b, 1d).

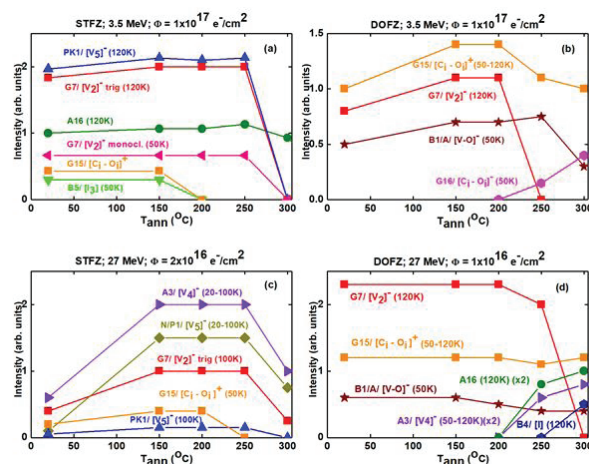


**Figure 1.** The relative concentration of the IPPDs identified in the ESR spectra of the electron irradiated Si samples subjected to isochronal annealing vs. the annealing temperature ( $T_{ann}$ ): (a) STFZ irradiated with 3.5MeV; (b) DOFZ irradiated with 3.5MeV; (c) STFZ irradiated with 27MeV; (d) DOFZ irradiated with 27MeV.

The present ESR investigations have shown that the nature and relative concentration of the IPPDs produced by irradiation at RT with high fluence electrons of 3.5MeV and 27MeV in STFZ and DOFZ, further subjected to isochronal annealing up to 300oC, depend on the oxygen concentration and on the energy of irradiating electrons. Irradiation of STFZ results in the formation of negatively charged small vacancy cluster G7/[V2]- divacancy, A3/[V4]- tetra-vacancy and PK1/[V5]- and/or N/P1/[V5]- pentavacancy defects as the main IPPDs, while irradiation of DOFZ produces dominant negatively charged G7/[V2]- divacancy, B1/A/[V-O]- vacancy-oxygen and interstitial G15/[C-Oi]+ oxygen-carbon impurity pair defects. Our investigations have also shown that the production of the dominant IPPDs by electron irradiation and thermal annealing are strongly influenced by the one order of magnitude variation in the oxygen

content from  $c(O) = 1 \times 10^{16} \text{ cm}^{-3}$  in STFZ to  $c(O) = 1.2 \times 10^{17} \text{ cm}^{-3}$  in DOFZ. One concludes that an optimum  $c(O) \sim 1.2 \times 10^{17} \text{ cm}^{-3}$  oxygen concentration level could minimize the formation of the vacancy cluster defects, which are considered to be essential in the degradation of the electrical performance of the Si based detectors [9].

The ESR study concerning the long term aging at 250K of the IPPDs produced by irradiation at RT with 27MeV electrons in STFZ, shows a complete transformation of the negatively charged multivacancy type defects in the freshly irradiated samples into neutral tetravacancies [V4]0. This process can be partly reversed by annealing at  $T_{\text{ann}} > 150^\circ\text{C}$  (Fig.2).

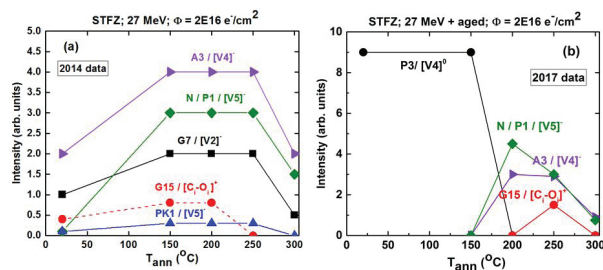


**Figure 2.** The relative concentration of the IPPDs identified in the ESR spectra of the 27 MeV electron irradiated STFZ samples subjected to isochronal annealing at increasing temperatures ( $T_{\text{ann}}$ ): (a) Sample freshly irradiated; (b) Sample irradiated and aged for 3.5 years at 250K.

We have also found that small vacancy cluster defects A3/[V4]<sup>-</sup> and N/P1/[V5]<sup>-</sup> are directly formed by high energy, high fluence electron irradiation of the STFZ samples, as previously observed only in neutron-irradiated Si. This result suggests that the direct cluster formation mechanism is active under irradiation with 27MeV electrons. It was observed that during long storage time at 250K, the main small vacancy cluster defects G7/[V2]<sup>-</sup>, A3/[V4]<sup>-</sup> and N/P1/[V5]<sup>-</sup>, as well as the minor G15/[Ci-Oi]<sup>+</sup> and PK1/[V5]<sup>-</sup> defects observed in the freshly irradiated sample, are replaced by the P3/[V4]0 centers.

This unexpected result is attributed to the diffusion of the divacancies even at 250K, resulting in their pairing in tetravacancies and by their interaction-recombination with the radiation induced tetra- and penta- vacancy centers,

resulting in larger ESR silent vacancy clusters, a process which can be accelerated by raising the temperature.

To our knowledge the presently sort of ESR studies and the results obtained on heavily irradiated Si have not been reported so-far. One concludes that such ESR investigations in condition of intense accros the gap “in-situ” illumination on both freshly irradiated and long term stored Si open a new avenue of research concerning the irradiation effects and defects in semiconductor materials, in obtaining new, interesting and unexpected results.

Financial support from projects: PN-II-PT-PCCA-2013-4-1870, PN-III-P4-ID-PCE-2016, Core Program PN18-11, PNII-ID-PCE-2011-3, PN-II-PT-PCCA-2013-4-1870 and Core Program PN16-480101.

## References

- [1] A.C. Joita, S.V. Nistor, J. App. Phys. 123, 161531 (2018).
- [2] A.C. Joita, S.V. Nistor, Mat. Sci. Semicon. Process. 83, 1-11 (2018).
- [3] S.V. Nistor, M. Stefan, D. Ghica, E. Goovaerts, Appl. Magn. Res. 39, 1-2 (2010).
- [4] M. Stefan, S.V. Nistor, J. N. Barascu, J. Magn. Reson. 210, 200, (2011).
- [5] S.V. Nistor, L. C. Nistor, M. Stefan, D. Ghica, G. Aldica, J. N. Barascu, Cryst. Growth. Des. 11, 5030, (2011).
- [6] S.V. Nistor, M. Stefan, D. Schoemaker, D. Dinca, Solid State Commun. 115, 1, 39, (2000).
- [7] S.V. Nistor, M. Stefan, D. Ghica, J. Therm. Anal. Calorim. 118, 2, 1021, (2014).
- [8] S.V. Nistor, D. Ghica, I. Pintilie, E. Manaila, Rom. Rep. Phys. 65, 3, 825, (2013).
- [9] R. Radu, I. Pintilie, L. C. Nistor, E. Fretwurst, G. Lindstroem, L. F. Macarenko, J. Appl. Phys. 117, 164503 (2015).

## Coaxial core-shell composite nanotubes for nanoelectronic devices

M. Cernea and M. Sima

in collaboration with

B. S.Vasile, V. A. Surdu and R. Trusca,

University POLITEHNICA of Bucharest, 060042, Romania

F. Craciun,

Istituto di Struttura della Materia (ISM-CNR), I-00133, Roma, Italy

C. Galassi,

CNR-ISTEC, Institute of Science and Technology for Ceramics, I-48018, Faenza, Italy

One-dimensional (1D) nanomaterials such as nanowires and nanotubes have attracted high interest due to their unique properties and specific applications [1]. We prepared and characterised composite nanotubes of the ferroelectric phase (perovskite BNT-BT<sub>0.08</sub>) and the ferro/ferrimagnetic phase (spinel CoFe<sub>2</sub>O<sub>4</sub>). This multiferroic material shows simultaneously (anti-) ferromagnetism and ferroelectricity at room temperature and can have applications in the fields of sensors, data storage, and transducers for magnetoelectric energy conversion [2]. We prepared heterostructured BNT-BT<sub>0.08</sub>/CoFe<sub>2</sub>O<sub>4</sub> core-shell composite nanotubes using a polycarbonate membrane template and sols precursors of BNT-BT<sub>0.08</sub> and CoFe<sub>2</sub>O<sub>4</sub>, following the procedure described in Ref.3. The as-prepared double-walled nanotubes have a well-defined geometry, presenting an average outer diameter of about 630 nm, wall thickness of 40-45 nm and maximum length of 23.5m (Fig.1).

The high-resolution transmission electron microscopy image (Fig.2) reveals the bilayered piezoelectric (BNT-BT<sub>0.08</sub>, outer tube)/ferromagnetic (CoFe<sub>2</sub>O<sub>4</sub>, inner tube) structure for the core-shell composite nanotubes.

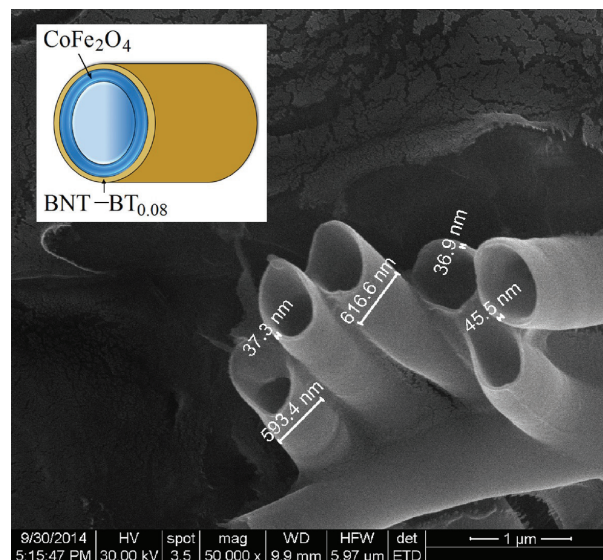


**Figure 1.** SEM photomicrograph of the heterostructured BNT-BT<sub>0.08</sub>/CoFe<sub>2</sub>O<sub>4</sub> nanotubes, dried at 100 °C. The inset is the schematic representation of the composite nanotube.

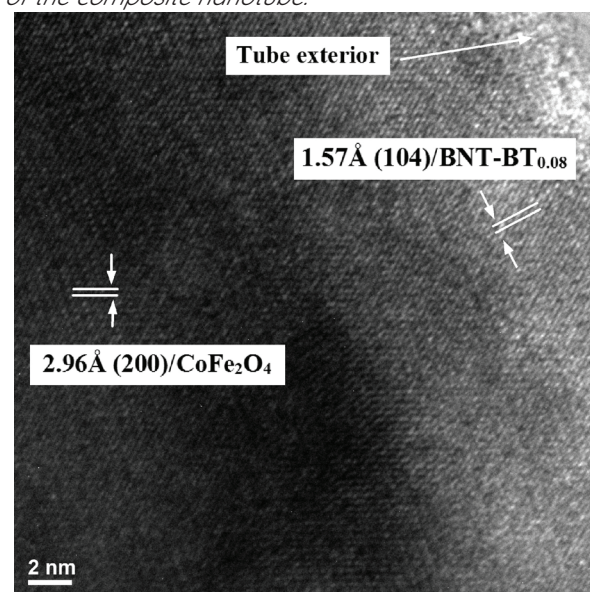


**Figure 2.** HR-TEM image of BNT-BT<sub>0.08</sub>/CoFe<sub>2</sub>O<sub>4</sub> heterostructured nanotube, calcined at 800 °C, 1h in O<sub>2</sub>.

The BNT-BT<sub>0.08</sub>/CoFe<sub>2</sub>O<sub>4</sub> composite nanotubes show:  $\epsilon_r = 74.5$  at 100 Hz which decreases down to 32 at 1000 Hz and 6.2 at 105 Hz; electrical conductivity  $\sigma = 2.88 \cdot 10^{-5} \Omega^{-1} \text{cm}^{-1}$  at 100 Hz and increases up to  $1.10 \cdot 10^{-4} \Omega^{-1} \text{cm}^{-1}$  at 1000 Hz and  $0.002 \Omega^{-1} \text{cm}^{-1}$  at 105 Hz. These results were obtained when the bias field  $E = 0 \text{ kV/cm}$  (Fig.3).

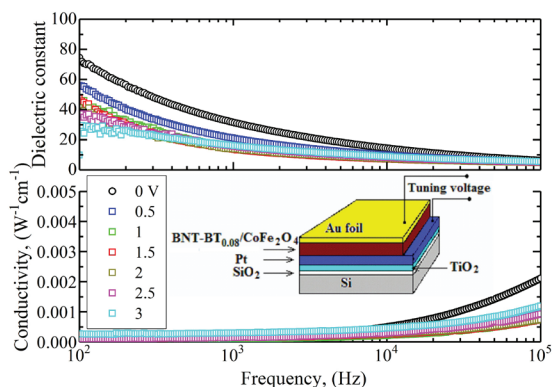


Figure 3. Dielectric constant and ac conductivity dependence on frequency, at different values of the dc electrical bias field. In the inset: schematic illustration of the capacitor used for the electrical measurements

BNT-BT<sub>0.08</sub>/CoFe<sub>2</sub>O<sub>4</sub> heterostructure nanotubes show piezo- and ferroelectric properties at the nanoscale due to the ferroelectric nature of the BNT-BT0.08 outer tube (Fig.4).

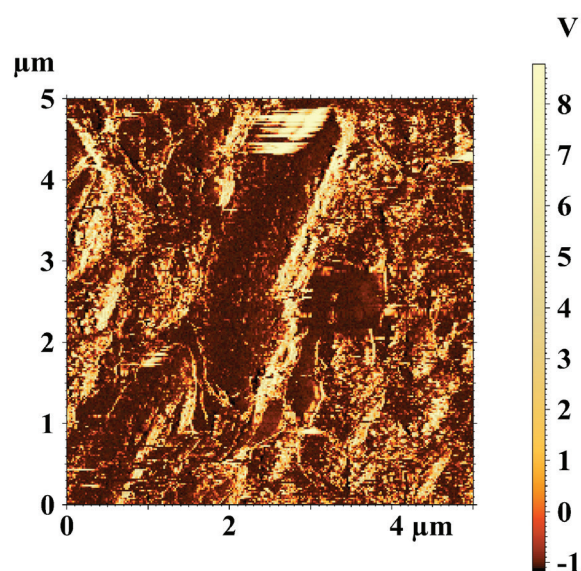


Figure 4. Amplitude of the piezoresponse signal for hybrid piezoelectric-ferromagnetic BNT-BT<sub>0.08</sub>/CoFe<sub>2</sub>O<sub>4</sub> composite core-shell nanotubes.

The low values of magnetization with a remanence of  $0.8 \cdot 10^{-4} \text{ emu/g}$  at 295 K and  $2 \cdot 10^{-3} \text{ emu/g}$  at 5 K and coercive field with a value reaching of 65 Oe at 295 K and 125 Oe at 5 K, as well as the shape of hysteresis curves, indicate the behavior of a diluted magnetic oxide (Fig.5).

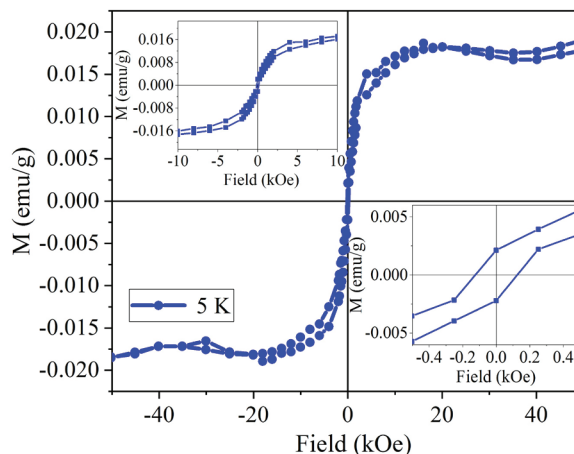


Figure 5. Magnetic hysteresis curves recorded for BNT-BT<sub>0.08</sub>/CoFe<sub>2</sub>O<sub>4</sub> composite coaxial nanotubes at 5 K. Inset left: detail up to 15 kOe; inset right: detail on coercivity and remanence hysteresis.

This work demonstrated piezoelectric and magnetic properties of the heterostructure BNT-BT<sub>0.08</sub>/CoFe<sub>2</sub>O<sub>4</sub> coaxial nanotubes. BNT-BT<sub>0.08</sub>/CoFe<sub>2</sub>O<sub>4</sub> core-shell material investigated in this work provides a novel way to exploit new applications for the multifunctional composite, such as piezoelectric sensors, magnetoelectronic sensors and data storage devices.

Funding from the Core Program PN18-110101 from Romanian Ministry of Research.

### References

- [1] K. S. Shankar et al., Mater. Sci. Eng. C, 25, (2005) 738-751.
- [2] H. Zheng et al., Science, 303, (2004) 661-663.
- [3] M. Cernea et al., J. Alloys Compd. 752, (2018) 381-388.

## Investigations aiming to grow two-dimensional layers based on semiconducting materials, followed in situ by high resolution photoelectron spectroscopy, low energy electron diffraction and scanning tunneling microscopy

N.G. Apostol

in collaboration with:

H. Bana<sup>1</sup>, E. Travaglia<sup>1,5</sup>, L. Bignardi<sup>2</sup>, P. Lacovig<sup>2</sup>, C.E. Sanders<sup>3</sup>, M. Dendzik<sup>3</sup>, M. Michiardi<sup>3</sup>, M. Bianchi<sup>3</sup>, D. Lizzit<sup>2</sup>, F. Presel<sup>1</sup>, D. De Angelis<sup>1</sup>, P.K. Das<sup>4,5</sup>, J. Fujii<sup>5</sup>, I. Vobornik<sup>6</sup>, M. Satta<sup>7</sup>, M. Dalmiglio<sup>2</sup>, F. Orlando<sup>1,8</sup>, A. Baraldi<sup>1,2,5</sup>, P. Hofmann<sup>3</sup>, R. Larciprete<sup>6</sup>, S. Lizzit<sup>2</sup>

<sup>1</sup>Univ Trieste, Dept Phys, Via Valerio 2, I-34127 Trieste, Italy

<sup>2</sup>Elettra Sincrotrone Trieste SCpA, Str Statale 14, Km 163-5, I-34149 Trieste, Italy

<sup>3</sup>Aarhus Univ, Interdisciplinary Nanosci Ctr iNANO, Dept Phys & Astron, Ny Munkegade 120, DK-8000 Aarhus C, Denmark

<sup>4</sup>Abdus Salam Int Ctr Theoret Phys, Str Costiera 11, I-34151 Trieste, Italy

<sup>5</sup>CNR, IOM, Lab TASC, Str Statale 14, Km 163-5, I-34149 Trieste, Italy

<sup>6</sup>CNR, Inst Complex Syst, Via Taurini 19, I-00185 Rome, Italy

<sup>7</sup>Sapienza Univ, CNR, ISMN, Dept Chem, Ple Aldo Moro 5, I-00185 Rome, Italy

<sup>8</sup>Omya Int AG, Baslerstr 42, CH-4665 Oftringen, Switzerland

Despite its extended 2D character and its huge carrier mobility, graphene is gapless, therefore for engineering novel devices based on two-dimensional (2D) materials, other semiconductor materials are investigated nowadays. One of them is silicene, a quasi-2D silicon layer with similar properties as graphene, with the exception of a theoretically predicted bandgap which may be adjusted by doping, reaching up to 0.5 eV. Despite early reports on the synthesis of silicene on silver single crystal surfaces [1], more careful investigations of silicon growth on selected metals and of its properties are still an intensive area of research nowadays.

For example, in Ref. [2], a comparison between real-time high resolution photoelectron spectroscopy recorded during Si growth on Ir(111), together with low energy electron diffraction (LEED) and with density functional theory simulations ruled out the silicene growth with respect to Si-Ir alloying.

Therefore, attention of a large community in the field, including the University of Trieste, the Elettra synchrotron radiation facility, the Aarhus University, the ICTP Centre from Trieste, CNR Rome and Sapienza University, was brought to other candidate 2D semiconducting materials.

Part of these investigations were realized in the CoSMoS (Combined Spectroscopy and Microscopy on a Synchrotron) facility, belonging to NIMP, installed on the SuperESCA beamline at Elettra, with the participation of one scientist from our Institute.

For instance, MoS<sub>2</sub> monolayers have semiconducting character and have a direct bandgap (1.8 eV), promoting them as valuable candidates for optoelectronics and field effect transistors with large on/off current ratios. Moreover, this material exhibits spin polarization of valence band electrons but, in order to exploit these characteristics, single domain 2D structures (i. e. without mirror domains) need to be synthesized. In particular, a complete spin polarization with opposed orientation is predicted in symmetric K and -K points in the Brillouin zone.

The results of a thoughtfully carried investigation are presented in Ref. [3]. High quality and single domain MoS<sub>2</sub> layers were synthesized by a novel method based on Mo evaporation in H<sub>2</sub>S atmosphere at a very low rate (5 × 10<sup>-3</sup> monolayers per minute) on heated Au(111) substrates (at 550°C). The growth process was followed up by fast photoelectron spectroscopy.

These layers were probed by scanning tunneling microscopy (STM, see **Fig.1**), exhibiting the single domain structure. Moreover, the 2D MoS<sub>2</sub> layer was found continuous even on single-atom terraces on the Au(111) surfaces, exhibiting a ‘carpet-like’ behavior. LEED with spot profile analysis, photoelectron diffraction and core level photoelectron spectroscopy (XPS) confirmed this growth model. In particular, from XPS, Mo atoms were found in a single state, whereas sulfur atoms are found in two different states, sulfur pointing towards vacuum and sulfur atoms between the substrate and molybdenum atoms. Concerning the electronic properties, angle- and spin-resolved photoelectron spectroscopy exhibits a robust spin polarization near the K points in the valence band spectra. The spin-resolved valence band photoelectron spectroscopy yielded about 86 % of spin polarization with opposite signs in K and -K points from the surface Brillouin zone.

These results point out that the Si/Ir(111) interface is unstable towards Si-Ir intermixing [2], but to a clear success to synthesize 2D MoS<sub>2</sub>. The synthesis method outlined in Ref. [3] could represent a breakthrough for the large scale production of high-quality MoS<sub>2</sub> monolayers with a low number of dislocation defects, and also singly oriented. These results may boost the research on the spin-valley degree of freedom in 2D materials and could be quite influential to realize mass-produced devices based on spintronics and on the ‘valleytronics’ concept, including by using other transition metal di-chalcogenides, such as WS<sub>2</sub>, MoSe<sub>2</sub>, etc.

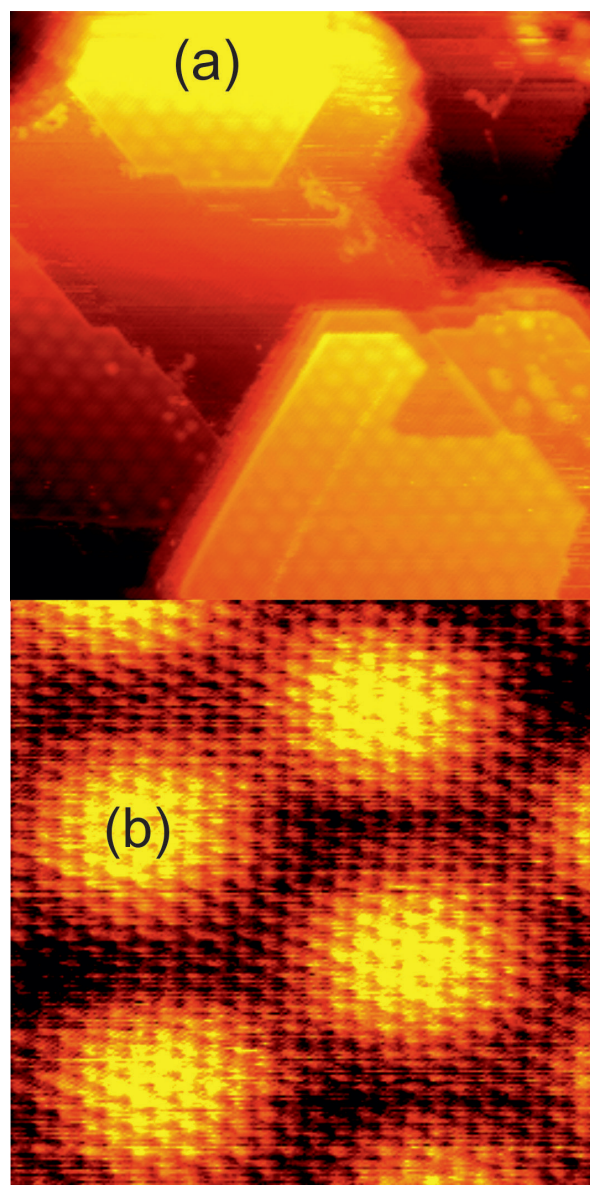


**Figure 1.** Scanning tunneling microscopy images on MoS<sub>2</sub> layers grown on Au(111). Areas investigated: (a) 50 × 50 nm<sup>2</sup>; (b) 5 × 5 nm<sup>2</sup>, exhibiting the Moiré fringes due to the lattice mismatch between the 2D MoS<sub>2</sub> structure and the underlying Au(111).

### References

- [1] A. Kara, H. Enriquez, A.P. Seitsonen, L.C. Lew Yan Voon, S. Vizzini, B. Aufray, H. Oughaddou, Surf. Sci. Rep. 67, 1–18 (2012).
- [2] M. Satta, P. Lacovig, N. Apostol, M. Dalmiglio, F. Orlando, L. Bignardi, H. Bana, E. Travaglia, A. Baraldi, S. Lizzit, R. Larciprete, Nanoscale 10, 7085–7094 (2018).
- [3] H. Bana, E. Travaglia, L. Bignardi, P. Lacovig, C.E. Sanders, M. Dendzik, M. Michiardi, M. Bianchi, D. Lizzit, F. Presel, D. De Angelis, N. Apostol, P.K. Das, J. Fujii, I. Vobornik, R. Larciprete, A. Baraldi, P. Hofmann, S. Lizzit, 2D Materials 5, 035012(1–9) (2018).

## Microstructural and microanalytical investigations on multifunctional coatings based on $0.5\text{Ba}(\text{Zr}_{0.2}\text{Ti}_{0.8})\text{O}_3\text{-}0.5(\text{Ba}_{0.7}\text{Ca}_{0.3})\text{TiO}_3$ for nonvolatile memories and solar cells

R. F. Negrea, A. C. Kuncser, C. Ghica  
in collaboration with

J. P. B. Silva, M. Pereira, M. J. M. Gomes  
University of Minho, 4710-057 Braga, Portugal  
J. Agostinho Moreira, F. Figueiras,  
University of Porto, 4169-007 Porto, Portugal

K. Kamakshi,  
Madanapalle Inst Technol & Sci, 517325 Andhra Prades, India  
J. Wang, G. Koster, G. Rijnders,  
University of Twente, NL-7500 AE Enschede, Netherlands

K. C. Sekhar,  
Central University of Tamil Nadu, 610101 Thiruvavur, India  
F. Cortés-Juan,

Valencia Nanophotonics Technology Center, 46022 Valencia, Spain  
J. P. Connolly  
GeePs, UMR CNRS 8507, 91192 Gif sur Yvette, France

Ferroelectric thin films have been intensively investigated during the recent years, for the potential of their high polarizability in enhancing the performance and efficiency of non-volatile memory devices and solar cells. This work is part of a complex study regarding the growth and characterization of functional thin films based on the perovskite-type oxide:

$0.5\text{Ba}(\text{Zr}_{0.2}\text{Ti}_{0.8})\text{O}_{3-0.5}(\text{Ba}_{0.7}\text{Ca}_{0.3})\text{TiO}_3$  (BCZT). Three different film configurations have been prepared and different specific properties have been approached for applications in solar cells or memory devices. The microstructural properties in function of the synthesis parameters have been investigated by analytical transmission electron microscopy using the JEM ARM 200F aberration corrected instrument.

BCZT/STO: The ferroelectric properties of the BCZT thin films have been measured on epitaxial single layers grown by pulsed laser deposition (PLD) on single crystalline  $\text{Nb:SrTiO}_3$  (001) substrates (STON). The low-magnification cross-section TEM images reveal BCZT layers with a compact and continuous structure. The HRTEM image and the selected area electron

diffraction (SAED) pattern exhibit the sharp film-substrate interface and the high crystalline quality of the epitaxial BCZT thin film. The crystallographic relation between the BCZT thin film and the STON substrate is:

$[100]_{\text{BCZT}} \parallel [100]_{\text{STON}}, [001]_{\text{BCZT}} \parallel [001]_{\text{STON}}$ . The chemical composition of the sample, with an accent on the structural and chemical quality of the interface, has been performed by EELS (Electron Energy Loss Spectroscopy) operated in the scanning transmission electron microscopy (STEM) working mode. The spatial distribution of the elements O, Ca, Ti, Sr, Zr and Ba clearly point to a sharp film-substrate interface without any perceptible atomic interdiffusion. The ferroelectric properties of the BCZT films, examined at the nanoscale level by PFM and at the macroscopic level by P-E hysteresis loops, exhibit a notable remnant polarization of  $21.3 \mu\text{C cm}^{-2}$  and a coercive field of  $60 \text{ kV cm}^{-1}$ . The domain growth limited switching process is appropriate to describe the reversal kinetics [1].

ZnO/BCZT/STON: MFS (metal ferroelectric semiconductor) structures  $\text{Au/BCZT/STON}$  and  $\text{Au/ZnO/BCZT/STON}$  for applications as memory

devices have been prepared and characterized, aiming for the correlation between the microstructural, ferroelectric and electrical properties. The ZnO/BCZT structures were deposited by PLD on single-crystalline STON(001) substrates. The structural quality of the ZnO/BCZT/STON coating has been investigated by analytical TEM.

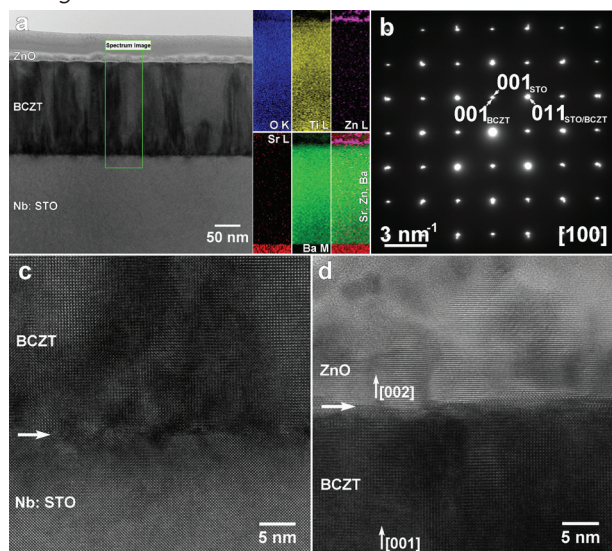


**Figure 1.** (a) Low-magnification TEM image of the ZnO/BCZT/STON structure and EELS-SI maps showing the elemental distribution inside of a green rectangle. (b) SAED pattern showing the epitaxial growth of the BCZT layer; (c), (d) HRTEM images of BCZT/STON and ZnO/BCZT interfaces.

A dense columnar structure of BCZT is observed, while the SAED pattern reveals the epitaxial growth of the BCZT layer on the STON substrate (Fig. 1a, b). The HRTEM images show the smooth ZnO/BCZT interface and the [002] growth direction of the ZnO layer on top of the BCZT thin film (Fig. 1c, d). The crystallographic relation between the substrate, BCZT, and ZnO thin films is  $[001]_{\text{STON}} \parallel [001]_{\text{BCZT}} \parallel [001]_{\text{ZnO}}$ . The interfacial chemical sharpness evidenced by EELS-STEM mapping of the atomic species in BCZT, ZnO and STON confirms the lack of atomic interdiffusion. The effect of including a semiconductor ZnO thin layer between the BCZT layer and the Au electrode upon the capacitance-electric field (C-E) and resistive switching (RS) characteristics has been evidenced, as the shape of the C-E curves changed dramatically, exhibiting a significant asymmetry due to the existence of a 12 nm depletion region

within the ZnO layer. A memory window of 47 kV/cm was observed. An unusual RS behaviour was also observed in the BCZT films, where the RS ratio can be significantly enhanced by introducing the ZnO layer [2].

ZnO/BCZT/ZnO/Pt/TiO<sub>2</sub>/SiO<sub>2</sub>: The effect of the ZnO layer position on the photovoltaic response of ZnO/BCZT/ZnO/Pt/TiO<sub>2</sub>/SiO<sub>2</sub> multilayered structures has been investigated. TEM analysis reveal the polycrystalline growth of BCZT, while STEM-EELS mapping showed that there is no diffusion at the BCZT/ZnO interfaces (Fig. 2a-c). An enhanced photovoltaic effect has been observed in the ZnO/BCZT/ZnO/Pt heterostructures, the improvement being attributed to the alignment of the internal fields and to the polarization-dependent interfacial coupling between the BCZT and the ZnO layers that can greatly influence the band structures of the heterostructure, including the depletion layer width and the potential barrier height [3].

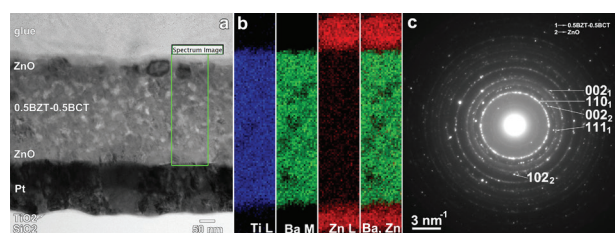


**Figure 2.** Cross-section TEM image showing the ZnO/BCZT/ZnO/Pt/TiO<sub>2</sub>/SiO<sub>2</sub> multilayered coating, (b) STEM-EELS elemental maps showing the spatial distribution of Ti, Ba and Zn. (c) SAED pattern corresponding to TEM image.

This work has been funded from the Core Project PN18-11 in the frame of an international collaboration within CERIC-ERIC.

## References

- [1] J. P. B. Silva, K. C. Sekhar, F. Cortés-Juan, R. F. Negrea, A. C. Kuncser, J. P. Connolly, C. Ghica and J. Agostinho Moreira, *Solar Energy* 167, 18-23 (2018).
- [2] J.P.B. Silva, J. Wang, G. Koster, G. Rijnders, R. Negrea, C. Ghica, K. Sekhar, J. Moreira, M. Gomes, *ACS Applied Materials & Interfaces* 10, 15240-15249 (2018).
- [3] J. P. B. Silva, K. Kamakshi, R. F. Negrea, C. Ghica, J. Wang, G. Koster, G. Rijnders, F. Figueiras, M. Pereira, M. J. M. Gomes, *Applied Physics Letters* 113, 082903 (2018).

## Different applications of ceria based materials

Mihaela Florea, Florentina Neațu  
National Institute of Materials Physics  
in collaboration with

Adriana Urdă, Bogdan Cojocaru, University of Bucharest, Faculty of Chemistry, Bucharest, Romania  
Georgeta Postole, Florina Matei-Rutkovska, Laurence Massin, Patrik Gelin, CNRS, IRCELYON, Université  
Claude Bernard Lyon 1, Villeurbanne, France

Daniel Avram, Carmen Tiseanu, National Institute for Laser, Plasma and Radiation Physics, Bucharest-  
Magurele, Romania

CeO<sub>2</sub> represents one of the most significant rare-earth oxides due to its applications in the fields of catalysis, sensor technology, and biomedical sciences. [1] The key property of ceria lies in its ease of up taking and releasing oxygen through repeatable shift between Ce<sup>3+</sup> and Ce<sup>4+</sup>, process during which oxygen vacancies are involved. Doping with isovalent and aliovalent cations distort the lattice along two pathways shaped by the formation of the oxygen vacancy and the difference between the ionic radii of the host cation, Ce<sup>4+</sup>, and the dopant cations. The purposes of the present study [2-4] were the following: i) to evaluate the influence of doping ceria with Gd and/or Pr on the redox properties and the catalytic behaviour in CH<sub>4</sub>/H<sub>2</sub>O reactions in view of their use in solid oxide fuel cells (SOFCs) operated on natural gas or biogas; the effect of H<sub>2</sub>S on the catalytic behavior was also evaluated, and ii) to investigate the potential of up-conversion as a probe tool for the dopant(s) location and distribution of doped ceria with heavy aliovalent and isovalent by wet impregnation.

Combining Ce with Pr and/or Gd oxides enabled us to tailor the properties of oxides such as the oxygen mobility and the oxygen storage capacity. Ceria-based material (Ce<sub>0.9</sub>Gd<sub>0.1</sub>O<sub>2-x</sub> (CGO), Ce<sub>0.9</sub>Pr<sub>0.1</sub>O<sub>2-x</sub> (CPO), Ce<sub>0.9</sub>Gd<sub>0.05</sub>Pr<sub>0.05</sub>O<sub>2-x</sub> (CGPO)) were prepared by a precipitation method and characterized by several physicochemical techniques.

XRD data indicate the formation of a solid solution with no diffraction lines pertaining to Gd or Pr oxides irrespective of the thermal treatment applied to the samples. All samples show the typical diffraction pattern of the CeO<sub>2</sub> pure cubic fluorite structure irrespective of the thermal treatment, with the reflections corresponding to the (111), (200), (220), (311), (222), (400), (331) and (420) planes (PDF: 00-034-039).

The influence of H<sub>2</sub>S on the catalytic behaviour of ceria samples at 750 °C was addressed by adding 220 ppm H<sub>2</sub>S for 2 h to the feed after stabilization of the catalytic activity in sulphur-free feed for 18 h. **Fig. 1** shows the variation of the concentrations of formed CO and CO<sub>2</sub> at 750 °C upon addition and suppression of 220 ppm H<sub>2</sub>S to the feed containing 50 mol% CH<sub>4</sub> and 5 mol% H<sub>2</sub>O in N<sub>2</sub> over the CGO sample. Upon H<sub>2</sub>S addition, the concentrations of CO and CO<sub>2</sub> rapidly increased.

The enhanced catalytic activity in the presence of H<sub>2</sub>S was attributed to the generation of new active sites associated with the formation of oxygen vacancies upon reduction of Ce<sup>4+</sup> by H<sub>2</sub>S. The catalytic conversion of the H<sub>2</sub>O deficient CH<sub>4</sub>/H<sub>2</sub>O mixtures into hydrogen varied in the order CPO > CGPO > CeO<sub>2</sub> > CGO. This correlates primarily and mostly with the variation of the surface area of the thermally treated samples upon doping. Pr doping inhibits thermal sintering of ceria while Gd would have the opposite effect. The proportion of surface Ce<sup>3+</sup> species ([Ce<sup>3+</sup>]/([Ce<sup>3+</sup>]+[Ce<sup>4+</sup>])) ratio) as measured by XPS can be

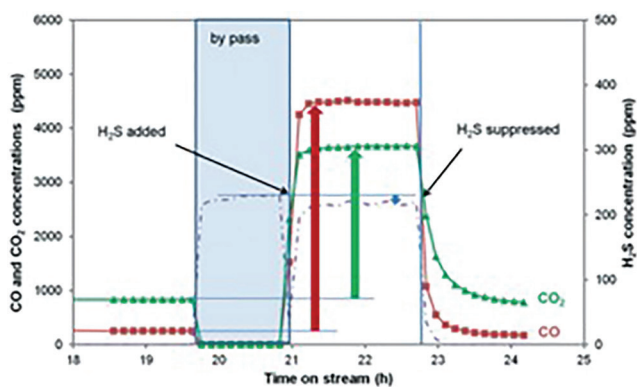


**Figure 1.** Variation of CO and CO<sub>2</sub> concentrations upon addition /suppression of 220 ppm H<sub>2</sub>S at 750 °C over CGO. Pretreatment at 900 °C in N<sub>2</sub> for 2 h; catalyst weight = 100 mg; total dry flow rate = 7 LNTP h<sup>-1</sup>; molar feed composition = 50 mol% CH<sub>4</sub>, 5 mol% H<sub>2</sub>O in N<sub>2</sub>

It is improved for undoped and Gd-doped samples, which results in better catalytic activity per m<sup>2</sup> than Pr-doped samples. The presence of 220 ppm H<sub>2</sub>S in the feed induces the sharp improvement of the catalytic activity of undoped and doped CeO<sub>2</sub> samples. The promoting effect of H<sub>2</sub>S on the catalytic properties appears to be stronger upon Pr doping than Gd doping and the phenomenon is fully reversible.

For the up-conversion study, two types of Yb(20%) Tm(1%) doped CeO<sub>2</sub> were synthesized with Yb inserted via bulk or wet impregnation. Additionally, Ca(20%) Eu(1%) doped CeO<sub>2</sub> and Zr(20, 30%) Eu(1%) doped CeO<sub>2</sub> were synthesized with Ca or Zr inserted via bulk or wet impregnation reported elsewhere [5]. The results are discussed in terms of structural properties, segregation effects, defects formation, elemental mapping distribution, dopant type and interaction with defects and local structure.

**Fig.2** compares the emission spectra and decays of Eu - CeO<sub>2</sub> (reference sample) with those of Ca and Zr - CeO<sub>2</sub>, respectively. Based on the principles of defect chemistry of trivalent doped CeO<sub>2</sub> and luminescence investigations, we have recently proposed a physical model based on a two -Ln centre distribution in CeO<sub>2</sub>. The two centres strongly differentiate by their local oxygen environment: an eight -fold EuO<sub>8</sub> cube for the so labelled isolated cubic centre (no vacancy in the nearest - neighbour) and an inversion less EuO<sup>7+</sup> defect (oxygen vacancy) VO polyhedron

labelled as Eu - vacancy associate. Spectra in **Fig. 2a,c** represent the mixed emission of isolated Eu (dominant, peak at 591 nm, blue coloured emission) and Eu-defects associates (minor, peaks at ca. 611 and 633 nm, green coloured emission) obtained with excitation into O<sup>2-</sup> - Ce<sup>4+</sup> charge-transfer (ca. 350 nm) band of CeO<sub>2</sub>.

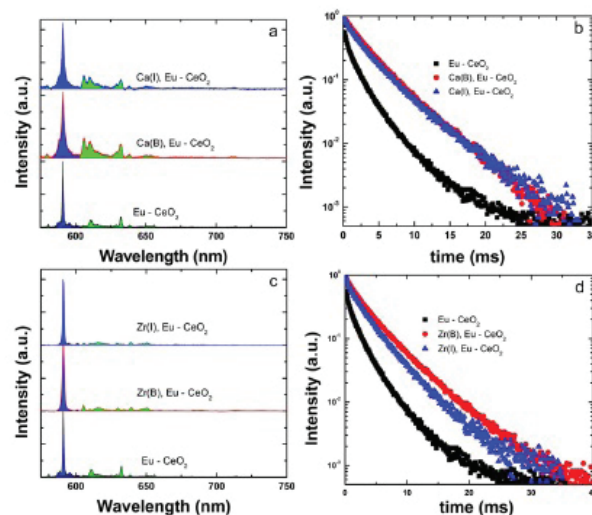


**Figure 2.** Emission spectra (a, b) and emission decays (c, d) of Ca(20%) and Zr (30%) impregnated and bulk doped CeO<sub>2</sub>

Though the presence of small metal oxide clusters dispersed on the surface or deviation from ideal homogenous distribution of dopant metals into ceria lattice cannot be excluded, our approach sustains that heavy doping ceria by wet impregnation may be used as a facile and likely more reproducible alternative to bulk doping approaches.

## References

- [1] T. Montini, M. Melchionna, M. Monai and P. Fornasiero, *Chemical Reviews*, 116 5987-6041 (2016).
- [2] M. Florea, G. Postole, F. Matei-Rutkovska, A. Urda, F. Neațu, L. Massin, P. Gelin *Catal. Sci. Technol.*, 8 1333-1348 (2018).
- [3] D. Avram, A. Maraloiu, B. Cojocaru, C. Tiseanu, *Nanoscale*, 10 18043-18054 (2018).
- [4] F. Matei-Rutkovska, G. Postole, A. Urda, F. Neatu, V.I. Pârvulescu, P. Gelin, *Catalysis Today*, 306 166-171 (2018).
- [5] D. Avram, C. Rotaru, B. Cojocaru, M. Sanchez-Dominiguez, M. Florea and C. Tiseanu, *Journal of Materials Science*, 49, 2117-2126 (2018).



# ADVANCED MATERIALS FOR APPLICATIONS

SELECTED RESULTS

## Drug delivery patch based on fibrous microheaters

Alexandru Evangelidis, Mihaela Beregoi, Victor C. Diculescu, Andrei Galatanu, Paul Ganea, Ionut Enculescu

Transdermal administration of drugs represents an interesting and important path with certain advantages such as continuous administration and lower gastric and hepatic impact. „Classical” transdermal drug delivery patches are passive ones, based on epidermal diffusion of the molecules of interest. However, new fabrication methods should be employed in order to produce such wearable devices, flexibility being one major aspect to be taken into account. Recent research showed that local heating can increase the rate of diffusion and improve the functionality of the devices. By heating a thermoresponsive structure, one can make the method for releasing active molecules even more attractive since the heat will not only promote the release of drugs, but it could also enhance skin penetration by causing the pore dilation.

The platform tested in the present report for drug delivery is based on a flexible microfiber architecture heater covered with a thermoresponsive hydrogel, namely poly(N-isopropylacrylamide), as a matrix for the incorporation of active molecules [1].

The devices' manufacturing process consists of several steps. First, poly(methyl methacrylate) submicrometer fiber networks were fabricated by electrospinning. Further these are sputter coated with a thin gold layer which made the conductive. These were later attached to flexible poly(ethylene terephthalate) substrates to obtain the heating platforms. Second, the heaters encapsulated in poly(ethylene terephthalate) foils were covered with poly(N-isopropylacrylamide) hydrogel sheets.

An important aspect regarding the performance of a material in heating applications is how uniform it distributes the energy over a given area. Thus, it was investigated whether the discrete and disordered nature of metalized fiber webs would have a significant influence on the spatial distribution of power dissipation.

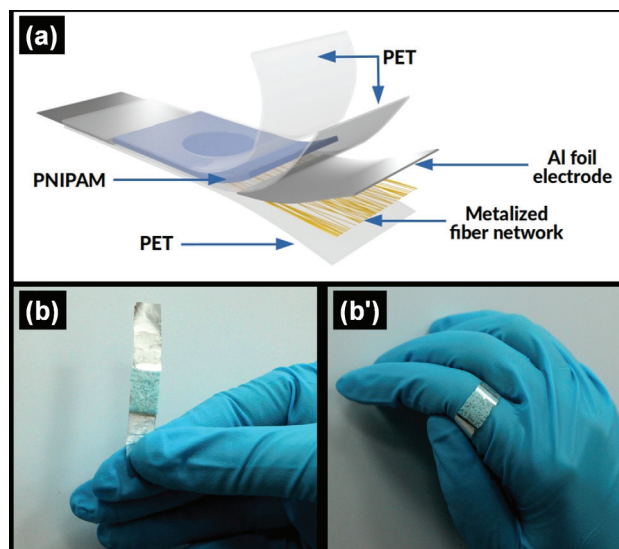


**Figure 1.** (a) Schematic representation and (b, b') digital photographs of the microheated patch.

The power distribution through such conductive fiber networks was simulated with a numerical model and it was found that the simulation results are in good agreement with thermographic images captured during the heating process. The functionality of the fabricated patch was highlighted by evaluating the capacity of the device to controlled release of an electrochemical active compound on-demand.

With this purpose, the microstructured heated patches were covered with the thermoresponsive hydrogel P1 and P2 sheets which were then swollen in methylene blue (MB) loading solutions of various concentrations. The structural and morphological characteristics of the prepared hydrogels were investigated, proving the formation of poly(N-isopropylacrylamide) and identifying its microgranular structure.

The hydrogels were swollen with 0.50 mM MB loading solution for 30 min, and SWVs were recorded always with a clean glassy carbon electrode (GCE) surface after different time intervals.

Between the voltammetric measurements, the patch was unheated or heated at about 3 V. Irrespective of the applied heating voltage, the peak increased linearly with time in agreement with the MB release from the hydrogel. Nevertheless, higher currents were registered for the heated sample.

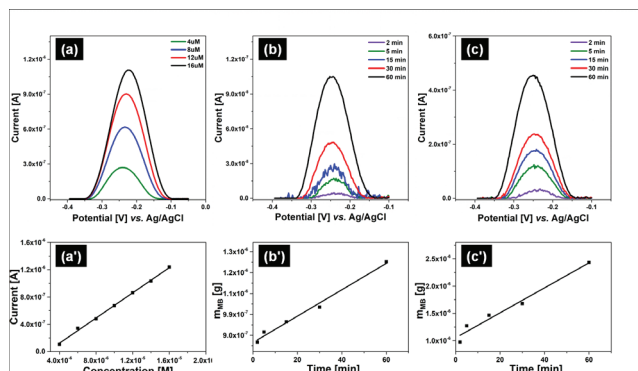


**Figure 2.** SWVs registered for samples (a, a', a'') P1 and (b, b', b'') P2, when the hydrogel sheets were swollen in MB loading solutions of (a, b) 0.25 mM, (a', b') 0.50 mM and (a'', b'') 1.00 mM with and without increasing the patch temperature at different heating voltage values.

By using a calibration curve, the recorded currents were transformed into concentration/weight values and the release rate was calculated. It was found that by heating the patch, the MB is released four times faster than without heating, thus under applied heating voltage the rate of release being  $2.29 \cdot 10^{-8}$  g/min MB, compared with  $5.68 \cdot 10^{-9}$  g/min (Fig.2).

To obtain a clear visual demonstration of delivery action, the patch and a separate, similar piece of loaded hydrogel were both covered with thin ( $\sim 0.34$  mm) pieces of unloaded, dry PNIPAM, to act as absorbent and indicator.

The patch was turned "on" at a 300 mA level for 2 minutes, until the indicator gel became fully colored and no further evolution was observed. Figure 3 shows the strong influence of heating over the diffusion of the methylene blue solution.

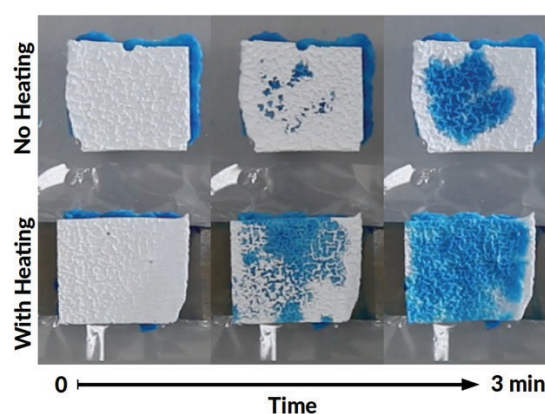


**Figure 3.** Visual demonstration of the delivery action for a hydrogel patch: unheated (top) and heated (bottom).

Due to the highly absorbent nature of dry PNIPAM hydrogel, the coloring occurs also in the unheated case, but at a much slower pace.

Summarizing, a novel flexible patch configuration which could be used as a non-invasive, controlled transdermal drug delivery system was developed. Electrospun polymer fiber networks covered with a thin gold layer and attached to flexible PET substrates were employed as microstructured heaters. A thermoresponsive hydrogel that encapsulates and releases the active compound was employed.

Therefore, the obtained results indicate that the manufactured patch is reliable for drug delivery applications and its releasing properties can be adjusted by changing the fabrication parameters.

## References

- [1] Alexandru Evanghelidis, Mihaela Beregoi, Victor C. Diclescu, Andrei Galatanu, Paul Ganea, Ionut Enculescu Scientific Reports volume 8, Article number 17555 (2018).

## Bioceramic materials for medical and environmental applications

D. Predoi, S. L. Iconaru, C. C. Negrila

in collaboration with

M.V. Predoi (Polytechnic University of Bucharest, Romania)

A.M. Prodan (Emergency Hospital Floreasca Bucharest, Bucharest, Romania and Carol Davila University of Medicine and Pharmacy)

M. Motelica-Heino (ISTO, UMR 7327 CNRS Université d'Orléans)

R. Guegan (Faculty of Science and Engineering, Global Center for Science and Engineering, Waseda)

The most pressing issues today are the increase in contaminated sites as a result of industrial rapid growing and on the other hand the apparition of antibiotic resistant microbial strains and the rising number of implant-related infections. These facts have accentuated the pressing need to work towards developing new materials that could be used in biomedical and environmental applications [1-3]. One of the most famous biocompatible materials generally used in the development of coatings for implantable devices is hydroxyapatite (HAp, a bioactive bioceramic belonging to the apatite. Due to its outstanding biological and physico-chemical properties, HAp, is widely used in biomedical applications for hard tissue replacements, scaffolds, as coating for implantable devices, and as a reinforcement material in biocomposites. It has been reported that the HAp properties could be greatly improved with the aid of different cationic and anionic substitutions, due to the fact that HAp has the ability to incorporate various substitute ions: ( $Mg^{2+}$ ,  $Ag^+$ ,  $Ce^{3+}$ ,  $Eu^{3+}$ ,  $Sm^{3+}$ ,  $Cu^{2+}$ ,  $Mn^{2+}$ ,  $Zn^{2+}$ ,  $Na^+$ ,  $Sr^{2+}$ ,  $HPO_4^{2-}$  or  $CO_3^{2-}$ ) within its lattice. Zinc is one of the most common elements involved in numerous functions in the human body and has the ability to facilitate the osteoblast proliferation and enhance the biomineralization. Nevertheless, at a certain concentration they display a great toxicity towards the human organism. The contamination of zinc in effluents often results from industry discharges.

Since zinc is not biodegradable, it travels through the food chain via bioaccumulation and possesses a high toxicity risk to humans. In this context, this study focused on using hydroxyapatite nanopowders for the removal of zinc ions from contaminated waters and also the development

of zinc and silver doped hydroxyapatite powders that could be used as antimicrobial agents [1-3].

The XRD analysis of HAp and 7ZnHAp samples using the Rietveld refinement method revealed a single phase corresponding to the hexagonal hydroxyapatite (Fig.1). The processing of XRD data collected in the  $2\theta$ , 20–90 using the Rietveld method confirmed the formation of the monophasic hydroxyapatite structure belonging to the P63/m spatial group in all analyzed HAp and 7ZnHAp [1-3].

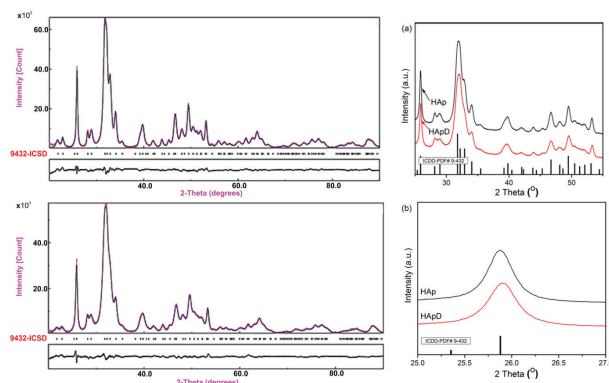


**Figure 1.** Rietveld processing of HAp and 7ZnHAp samples prepared by sol-gel method. (left) [1]; XRD patterns of hydroxyapatite (HAp) and hydroxyapatite recovered after zinc adsorption from aqueous solutions (HApD)(a)  $2\theta$  range of 25–55°; (b)  $2\theta$  range of 25 (right) [3].

Information regarding the elemental composition of HAp and 7ZnHAp samples were obtained by the XPS analysis. XPS measurements revealed the presence of  $Zn^{2+}$  ions in the hydroxyapatite structure as a result of  $Ca^{2+}$  ions substitution during the synthesis process (7ZnHAp sample). The general spectra of the HAp and 7ZnHAp samples were shown in (Fig.2). Peaks corresponding to C 1s, Ca 2p, P 2p, O 1s, and Zn 2p have been recorded for both samples investigated ( $x_{Zn} = 0$  and  $x_{Zn} = 0.07$ ). As expected in the XPS spectrum of HAp ( $x_{Zn} = 0$ ) sample, the associated Zn 2p peak was not present.

Ultrasound measurements were also conducted on the obtained solutions. The pa/P ratios along the axis, represented in red for the five frequencies (**Fig.2**), were obtained for the HAp (R=13 nm, density  $\rho_s=1.0129 \text{ kg/m}^3$  and a 5% volumetric concentration) and 7ZnHAp (R = 9.7 nm, density  $\rho_s=1.0062 \text{ kg/m}^3$  and a volumetric concentration of 5%) samples [1].

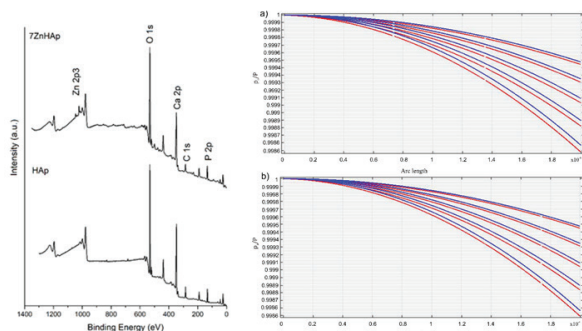


**Figure 2.** General XPS spectra of HAp and 7ZnHAp powders (left); Acoustic pressure in the biphasic environment for HAp (red) (a); Acoustic pressure in the biphasic environment for 7Zn HAp (red) (b) (right). [1].

The effects of two antifungal agents (Ag:HAp-S1 and Ag:HAp-S2) against *C. albicans* were evaluated at two different time points, the initial time (T0) and six months after the time at which the layers were made (T6). The antifungal activity of the AgHAp composite layers at T0 and T6 was assessed using *Candida albicans* ATCC 10231 microbial strain [2].

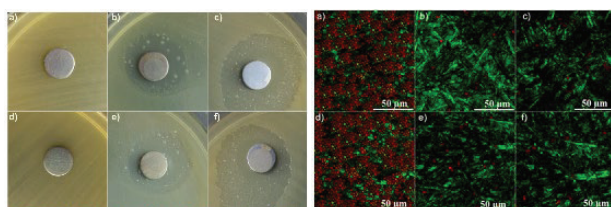


**Figure 3.** Qualitative assay of the inhibitory activity of Ag:HAp-S1 and Ag:HAp-S2 at time T0 (b) (c) and T6 (e) and (f) composite layers against *Candida albicans* ATCC 10231 microbial strain; Ti discs were used as control (a,d) (up); CLSM images of *C. albicans* ATCC 10231 cell development on Ti discs used as control (a,d) and Ag:HAp-S1 and Ag:HAp-S2 composite layers at the two time intervals T0 (b) and (c) and T6 (e) and (f) after 24 h of incubation. (down)[2].

The results of the antibacterial assays emphasized that Ti discs exhibited no antimicrobial activity against the tested fungal strain. Furthermore, the results indicated that both Ag:HAp-S1 and Ag:HAp-S2 composite layers deposited on Ti substrates presented a pronounced antifungal activity against *Candida albicans* ATCC 10231 microbial strain (**Fig.3**) [2]. The adsorption

of zinc ions from aqueous solutions using HAp nanopowders was studied in batch experiments and the removal efficiency of adsorption of zinc ions from aqueous solution by HAp is presented in (**Fig.4**).

The results suggested that the adsorption capacity increases with the increase of the initial zinc ions concentration. **Fig.4** shows that the percentage zinc ions removal increased from 30.88% to 41.57% with the increase of the initial zinc concentration from 5 mg/L to 150 mg/L. It was also noticed that, after the concentration of 110 mg/L, the removal percentage stabilized around the value of 40%. The equilibrium adsorption isotherm also shows that the adsorption capacity of zinc ions upon varying the zinc ions concentration in the aqueous solutions [3].

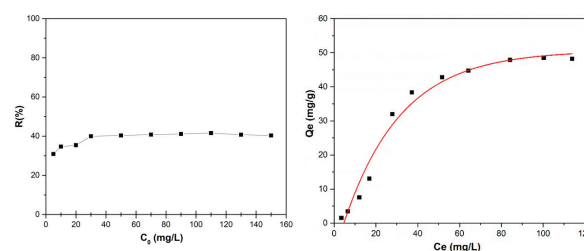


**Figure 4.** Removal efficiency of zinc ions on HAp depending on the initial zinc concentration (left); Equilibrium adsorption isotherm for zinc ions onto HAp at room temperature (right) [3].

The results of our studies bring new contributions on the biological properties such as HAp, ZnHAp and AgHAp materials. Moreover, the results obtained in this study emphasized that HAp nanopowders are good adsorbents for zinc ions and therefore can be considered for applications for removal of zinc ions from wastewater.

The authors acknowledge the Romanian Ministry of Research and Innovation through the following projects: PN-III-P1-1.2-PCCDI-2017-0629, Contract No. 43PCCDI/2018, PN-III-P1-1.2-PCCDI-2017-0134, Contract Nr. 23PCCDI/2018, PCCDI-UEFISCDI, project number PN-III-P1-1.2-PCCDI-2017-0062/contract no. 58/component project no. 2), Internal Contract No. T-IS 251801/04.05.2018, Core Program funded by Romanian Ministry of Research and Innovation (PN18-110101).

## References

- [1]. Negrița, C.C.; Predoi, M.V.; Iconaru, S.L.; Predoi, D. *Molecules* 2018, 23, 2986.
- [2]. Predoi, D.; Iconaru, S.L.; Predoi, M.V. *Coatings* 2018, 8, 276.
- [3]. Iconaru, S.L.; Motelica-Heino, M.; Guegan, R.; Predoi, M.V.; Prodan, A.M.; Predoi, D. *Materials* 2018,

## Development of interfaces in high heat flux components for fusion reactor divertor

M.Galatanu, B.Popescu, G. Ruiu, M.Enculescu, A.Galatanu  
and C.M. Ticos (INFLPR)

The nuclear fusion reactor DEMO [1] is a key point in the European fusion roadmap [2], being a reactor able to deliver energy to the grid. The materials used for it should withstand both high heat fluxes and intense neutron irradiation for long times, ranging between 2 and 5 years. In the case of its divertor, which is a reactor plasma facing part responsible for the exhaust of plasma impurities and spent fuel, an expected heat flux about 10-20 MW/m<sup>2</sup> should be extracted. A full W armour is considered as the main option, while the following heat sink part will be most likely constructed from Cu or ODS Cu alloys pipes, similar to the ITER full-W divertor design. W has an operating temperature window defined by its brittle to ductile transition temperature (BDTT, around 300-400°C) and its recrystallization temperature at about 1200°C. For the Cu-based heat sink materials, the operating temperature is between 180°C and about 350°C. Interface materials are needed from 3 main reasons: i) to keep in the ideal case W-based armour and Cu-based heat sink materials in their respective optimum operating temperature ranges, ii) to mitigate the large difference between the W and Cu thermal expansion coefficients (CTE) which generates thermos mechanical stresses during thermal cycling and iii) to facilitate the joining of these materials.

To solve the last two points, a W-Cu functional gradient material (FGM) has been proposed as possible solution. Such materials have been produced using a simple powder metallurgy route, by field assisted sintering technique (FAST). We have investigated the possibility to realize W-Cu FGMs produced from nanometric and micrometric metallic powders mixtures and also to join by FAST the consolidated interface material to W armour and CuCrZr heat sink parts [3] consolidated by spark plasma sintering (SPS) at about 900°C. Morphological and thermal properties investigations, performed for typical compositions, show that the best results are obtained using powders with micrometric dimensions.

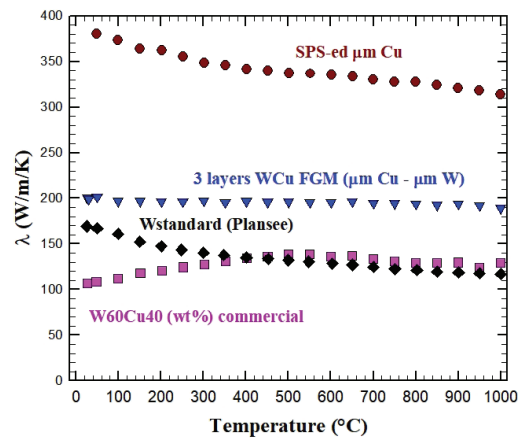


**Figure 1.** Thermal conductivity for the 1 mm thick, 3 layer W-Cu FGM produced with micrometric powders compared to thermal conductivities of a 890 °C SPS-ed micrometric grains Cu sample, a standard W plate and a commercial W60Cu40 (wt.%) sample.

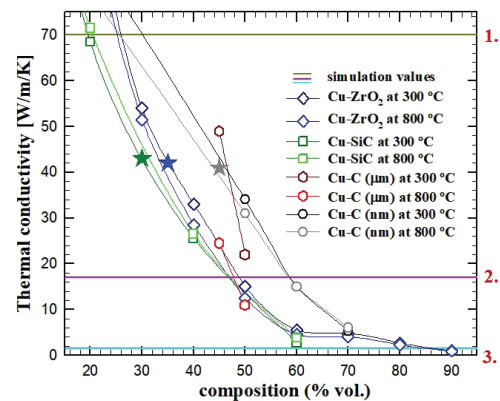


**Figure 2.** Summary of thermal conductivity data for Cu-ZrO<sub>2</sub>, Cu-SiC and Cu-C thermal barriers. The star symbols correspond to the values selected for single material thermal barrier ring fabrication and the horizontal lines marked with 1, 2, and 3, correspond to the thermal conductivity values

A resulting 1 mm thick, 3 layers W-CuFGM produced by this simple method shows a remarkable almost constant thermal conductivity value of 200 W/m/K, from room temperature up to 1000°C (see results from Fig.1), while the FGM thermal expansion coefficient gradually changes from  $\sim 16.4 \times 10^{-6} \text{ K}^{-1}$  at the Cu rich part to  $\sim 6.7 \times 10^{-6} \text{ K}^{-1}$  at the W rich part. In order to keep both W and Cu-based materials in their optimum operating temperature windows, the thermal conductivity of the interface material should be lower than both W and CuCrZr thermal conductivity values.

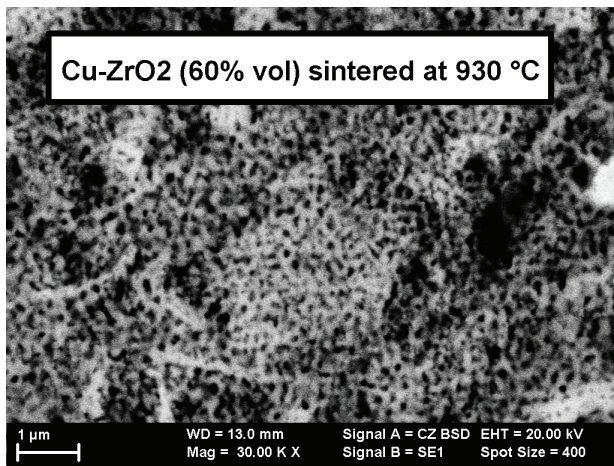


**Figure 3.** *Cu- ZrO<sub>2</sub> composites' morphology from an EBS image of the 60% ZrO<sub>2</sub> sample sintered at 930 °C.*

To achieve this, we have used again the FAST powder metallurgy route to produce Cu-based thermal barrier materials via SPS. Using micrometric Cu powders and nanometric sized ceramic powders or micrometric C powders we have produced robust and dense materials containing up to at least 40% volume concentrations of ceramic or C material [4]. The main benefits of this route are related to its versatility: on one side it allows a fine tuning of the content and the derived thermal properties, and on the other side it can be used to create a large pool of predefined shapes and dimensions.

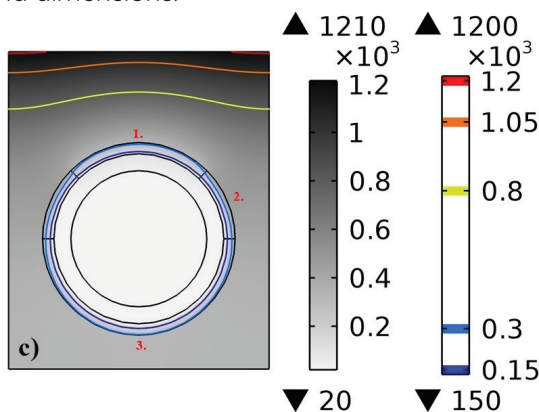


**Figure 4.** *FEM simulations of a 10 MW/m<sup>2</sup> heat flowing to the W-monoblock divertor component with optimized number and geometry of thermal barrier slices.*

Micro-structural and thermal properties of these materials have been investigated allowing to select the materials in view of their thermal conductivity and thermal expansion coefficients. Cu-based composites can be efficient thermal barrier materials, while mitigating at the same time the effects of the different thermal expansion

coefficients of W and CuCrZr. However, for the W-monoblock divertor concept, which is already selected for ITER and is also considered as the main option for DEMO, the specific design constraints (the W armour is formed here as a rectangular prism and a CuCrZr pipe is passing through the W component) impose much lower thermal conductivity values [5]. For this case we have investigated also Cu-ZrO<sub>2</sub> composites as potential candidates for the thermal barrier material [6]. These composites can be produced with a surprisingly high oxide content, up to 90% volume, having thermal conductivity values as low as 1 W/m/K (see Fig.2), lower than the pure ZrO<sub>2</sub> thermal conductivity, and in the same time retaining a metallic like electrical conductivity. This behaviour is generated by a particular honeycomb type nanostructure of Cu walls incorporating nanometric grains' clusters of ZrO<sub>2</sub> (see Fig.3).

Further we have investigated the feasibility for complete divertor components processing [7], using materials produced by FAST. This method was used firstly to produce W or W-based composites and the thermal barriers in an almost final shape and then to join the materials in realistic divertor mock-ups. The W material was produced using an optimized route with sub-micrometric powders which was proven to better withstand the effects arising from interactions with dense plasma jets [8]. A ring shaped thermal barrier interfaces can be designed and produced also with a graded composition [7]. FEM simulations have shown that is possible to design a graded interface able to keep W between 300°C and 1200°C. The thermal barrier design optimization leads to a simple solution including only 4 components from 3 different thermal barrier materials (see Fig.4).

## References

- [1] G. Federici et al., *Fusion Eng. Des.* 109-111 (2016) 1464.
- [2] T. Donne et al., "European Research Roadmap -SOFT 2018 to the Realisation of Fusion Energy", <https://www.euro-fusion.org>
- [3] M. Galatanu, M. Enculescu, A. Galatanu, *Mater. Res. Express* 5 (2018) 026502.
- [4] M. Galatanu, M. Enculescu, G. Ruiu, B. Popescu, A. Galatanu, *Fus. Eng. Des.* 124 (2017) 1131.
- [5] T.R. Barrett et al., *Fus. Eng. Des.* 98-99 (2015) 1216-1220.
- [6] M. Galatanu, M. Enculescu, A. Galatanu, *Fus. Eng. Des.* 127 (2018) 179.
- [7] M. Galatanu, M. Cioca, A. Ighigeanu, G. Ruiu, M. Enculescu, B. Popescu, A. Galatanu, *Fus. Eng. Des.* (2019),
- [8] C.M. Ticos, M. Galatanu, A. Galatanu, C. Luculescu, A. Scurtu, N. Udrea, D. Ticos, M. Dumitru, *App. Surf. Sci.* 434 (2018) 1122.

## Tuning local atomic configurations in ferritic steels of interest in nuclear fusion applications

S. Greculeasa, A. Stanciu, G. Schinteie, P. Palade, O. Crisan, A. Kuncser, A. Barsan, C. Bartha, V. Mihalache, I. Mercioniu, G. Aldica, I. Pasuk, V. Kuncser

Iron, Chromium and Molybdenum are basic elements present in the composition of stainless steels that are widely used in industrial sectors such as marine, construction and transportation, as well as for fuel cell applications and structural materials in nuclear reactors [1]. Moreover, special reduced-activation ferritic/martensitic steels such as Eurofer alloys are key candidates for ITER test blanket modules and future DEMO applications in nuclear fusion technology, playing a crucial role as underlayers for plasma facing materials. Imperative necessities for a good functioning of the alloys include ductility, workability, high strength, resistance against corrosion and stability in conditions of irradiation and exposure at heat fluxes. There is a strong interest of the scientific community to quantify the influence of high temperature or irradiation exposure on the physical properties of Fe-Cr and Fe-Mo-based alloys [2-4]. Effects on atomic intermixing, local configurations, as well as oxidation processes are of crucial importance.

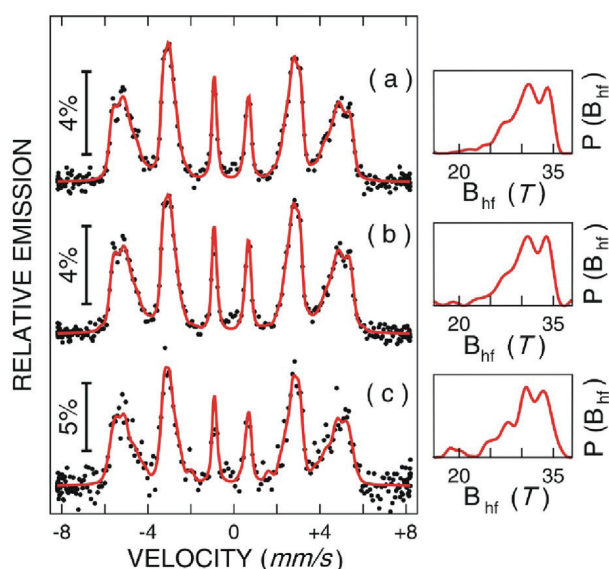


**Figure 1.** Mössbauer spectra of the samples: EU (a), EU 1 h (b), and EU 2 h (c), fitted with the probability distribution method. The probability distribution of hyperfine magnetic fields is shown on the right side of each corresponding spectrum.

**Fig.1** shows the conversion electron Mössbauer (CEM) spectra of Eurofer samples EU (as prepared), EU 1h (1h exposed to hydrogenation), and EU 2h (2 h exposed to hydrogenation) collected at room temperature.

A probability distribution of hyperfine magnetic fields was considered, revealing three main local maxima (with contribution of over 90% of the total probability distribution). The average hyperfine magnetic field values of the probability distributions increase slightly with the hydrogenation time, approaching better the  $\alpha$ -Fe value of 33.15 T at room temperature. This result suggests that in the investigated volumes, the Fe configurations are relatively reduced in Cr in the hydrogenated sample as compared to the non hydrogenated one. In fact, the escaping length of the conversion electrons (most of them of type K with an energy of 7.3 keV) is of about 100 nm, meaning a relatively reduced Cr content until a depth of 100 nm, in agreement with the expulsion of Cr atoms towards the surface layer (as evidenced by XPS - not shown here).

The involved local configurations in the as quenched as well as in annealed ribbons, depending on the evolution of the Cr and Mo content, have been further analysed in detail within the two-shell model. According to this model, the doping atoms (Cr or Mo, in this case) found in the first (1NN) and second (2NN) coordination shells influence the hyperfine parameters of Fe (isomer shift and hyperfine magnetic field) as also mentioned by [5]. The main hypotheses consist of additive contributions of the Cr/Mo atoms in the 1NN-2NN vicinity of Fe, independently of the atomic positions in the given coordination shell of the nuclear probe, with regard to both isomer shift (IS) and hyperfine magnetic field (B). However, there may be differences when comparing atoms found in unlike shells. Therefore, for each sublattice, the IS and B values can be written as linear functions of the numbers n and m of Cr/Mo atoms found in the first and second coordination sphere [5]:

$$IS(m,n) = IS(0,0) + m\Delta IS_1 + n\Delta IS_2 \quad (1)$$

$$B(m,n) = B(0,0) + m\Delta B_1 + n\Delta B_2 \quad (2)$$

The spectra of  $Fe_{1-x}Cr_x$  and  $Fe_{1-x}Mo_x$  ( $x=0.05;0.1;0.15$ ) were considered as a superposition of magnetic sublattices, taking into account the most important contributions (each accounting for at least 1%) within the binomial distribution for the specific alloy concentrations and  $(m, n)$  configurations.

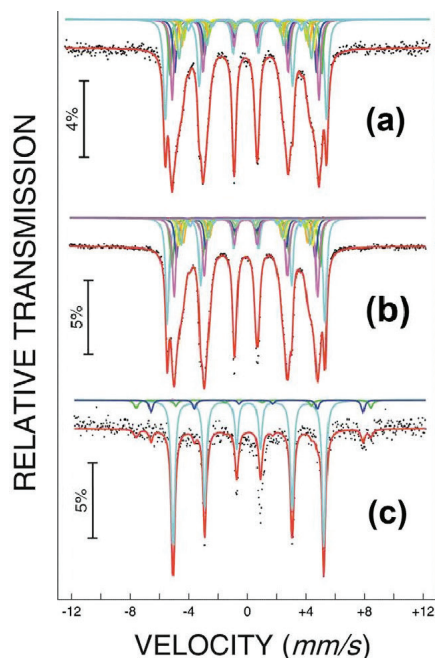


**Figure 2.** Mössbauer spectra of  $Fe_{0.90}Cr_{0.10}$  ribbons: as prepared (a), annealed at 700 °C (T1) (b), and annealed at 1250 °C (T2) (c).

Many reports revealed the deviations from the theoretical random distribution of the Cr or Mo atoms, especially due to annealing, for  $Fe_{1-x}Cr_x$  alloys between 400 and 1000°C, and  $Fe_{1-x}Mo_x$  alloys at 1000°C [6]. In [3], the samples were annealed at 700 and 1250°C (see Fig.2 for Fe-Cr). The Cr/Mo distribution in the bcc Fe lattice, the phase composition, the short range order parameters, as well as clusterization processes are strongly influenced by the annealing temperature. Concerning applications for DEMO, Fe-Cr-W-Ti oxide dispersion strengthened ferritic steels (ODSFs) with nanostructuring induced by mechanical alloying (MA) are under intense development as materials with superior high-temperature mechanical properties [7]. During mechanical milling, the contamination with nitrogen and oxygen from air is nearly inherent.

The quality of three batches of Fe-14Cr-3W-0.4Ti-0.25Y<sub>2</sub>O<sub>3</sub> powders milled for up to 170 h in three different conditions was compared: under

an argon atmosphere with interruptions of the milling process (batch A), under an argon atmosphere without interruption of the milling process (batch B) and in air (batch C) (Fig.3) [8]. The contamination of powders of batch B is insignificant (corresponding to less than 0.5 % mass/nitrogen loss in TG (Fig.3b) as compared to powders obtained in the other two milling conditions - the ultrafine particles capable to fill the container leaks are the main impediment against contamination. The traces of N improve the interstitial- and precipitation- solid solution strengthening or induce the grain refinement increasing the Hall-Petch strengthening. At higher contamination levels, the precipitation of coarse Cr-rich nitrides/oxides and the resulted Cr-depleted regions may damage the mechanical properties.

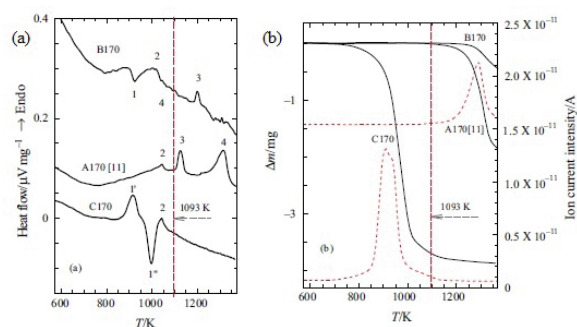


**Figure 3.** (a) DTA and (b) TG and QMS (for  $m/z$  28) curves measured on Fe-14Cr-3W-0.4Ti-0.25Y<sub>2</sub>O<sub>3</sub> powders milled for 170 h: A170, B170 and C170.

The local structure and atomic configurations of Fe-Cr and Fe-Mo alloys, of special reduced-activation ferritic/martensitic steels (Eurofer) after different annealing processes were addressed. Also, the quality of the ferrite phase in the ODSFs (after MA) and its thermal stability was investigated. New approaches to minimise the contamination from air are suggested.

## References

- [1] R.A.Pitts et al, J.Nucl.Mater. 415 (2011) S957.
- [2] S.M.Dubiel et al, J.Alloy.Compound. 624 (2015) 165.
- [3] A.Stanciu, S.Greculeasa, C.Bartha, G.Schinteie, P.Palade, A.Kuncser, A.Leca, G.Filoti, A.Birsan, O.Crisan, V.Kuncser, Phil Mag 98 (2018) 1053.
- [4] S.Greculeasa, P.Palade, G.Schinteie, A.Kuncser, A.Stanciu, G.Lungu, C.Porosnicu, C.Lungu, V.Kuncser, Appl Surf Sci 402 (2017) 114.
- [5] S.M. Dubiel and J. Cieślak, Mater. Lett. 107 (2013) 86.
- [6] R.Idczak, et al, Solid State Commun. 159 (2013) 22.
- [7] G.R.Odette, J Mineral Metal Mater Soc 66 (2014) 2427.
- [8] V.Mihalache, I.Mercioniu, G.Aldica, I.Pasuk, J Thermal Analysis Calorimetry 134 (2018) 4.

## Floating gate memories based on Ge nanocrystals embedded in dielectric matrix

Catalin Palade, Adrian Slav, Ana-Maria Lepadatu, Adrian Valentin Maraloiu, Ioana Dascalescu, Sorina Lazanu, Toma Stoica and Magdalena Lidia Ciurea

in collaboration with  
Sorina Eftimie

Faculty of Physics, University of Bucharest

The structures based on Si and Ge nanocrystals (NCs) embedded in different dielectrics are of great scientific and applicative interest in charge storage devices (floating gate memories), as well as in photonics (light emitters, detectors, photovoltaics).

The trilayer memory capacitors based on Ge NCs in  $\text{HfO}_2$  were studied pursuing two purposes: to reveal the efficiency of the photo-induced changes of the hysteresis loop under continuous illumination or by light exposure during the writing time, and to determine the intrinsic material parameters of each component layer.

The structure  $\text{HfO}_2$  tunnel oxide/intermediate layer of Ge NCs in  $\text{HfO}_2/\text{HfO}_2$  control oxide (see **Fig.1(a)**) was deposited by magnetron sputtering on Si substrates, with the intermediate layer obtained by co-depositing Ge and  $\text{HfO}_2$ .

After deposition, the samples were subjected to rapid thermal annealing (RTA) at 600 °C for 8 min for nanostructuring [1]. We investigated the internal morphology of the memory layers using high resolution TEM (HRTEM) with high-angle annular dark field-scanning TEM (HAADF-STEM) in order to reveal the formation of Ge NCs by RTA, as exemplified in **Fig.1(b)**. An Al electrode was deposited on the backside of the Si substrate after the removal of native oxide. The top electrode of semitransparent Au with  $3 \times 3 \text{ mm}^2$  area was then deposited by thermal evaporation, and its thickness was determined by X-ray reflectivity (XRR) (**Fig.1(c)**). The capacitance measurements were performed 1 MHz frequency, while for integral light illumination a tungsten lamp of  $20 \text{ mW/cm}^2$ , calibrated with a Thorlabs PM100D-S140C meter was used.

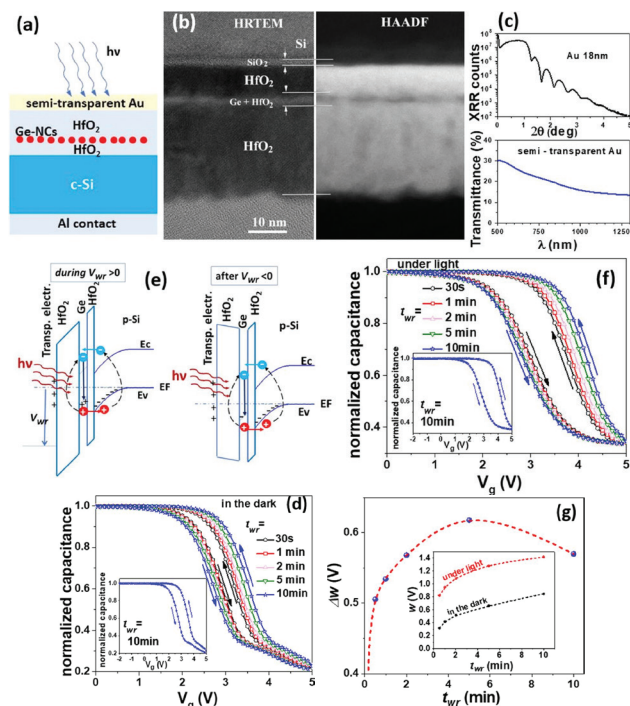


**Figure 1** (a). Schematic of the optoelectric memory capacitor; (b) HRTEM and HAADF-STEM images of the trilayer after RTA; (c) XRR measurement and spectral transmittance of Au electrode; (d) C-V hysteresis curves for different values of  $t_{wr}$  - programming, and measurements in the dark; (e) schematic of light induced negative charging; (f) C-V hysteresis curves under continuous light - programming and measurements under light illumination for different  $t_{wr}$ ; (g) dependence on  $t_{wr}$  of the photo-induced change of  $\Delta w$  (inset:  $\Delta w$  versus  $t_{wr}$  from (d) and (f)).

The charging and discharging of NCs was obtained by sweeping the voltage  $V_g$  between  $-2 \text{ V}$  and  $+5 \text{ V}$ , and by maintaining a writing voltage  $V_{wr}$  at sweep ends for a writing time  $t_{wr}$  between 30 s and 10 min, in dark - see **Fig.1(c)**. A schematic illustration of the mechanism of light assisted negative charging during positive  $V_{wr}$  and after negative  $V_{wr}$  is shown in **Fig.1(d)**. The photocarriers contribute to the charge tunnelling transfer, increasing this way the hysteresis window.

This charge tunnelling is dependent on the alignment of the conduction and valence bands in Ge NCs and Si substrate, respectively, the main photo-effect being due to the tunnelling of photo-carriers in the conduction band.

We studied first the operation mode in which both the programming and C-V measurements are performed under light illumination, OM1. The hysteresis window  $\Delta w$  increases with writing time up to about 5 min, and decreases at longer times – **Fig.1(f)** and **Fig.1(g)**, because electrical writing itself is saturated at longer writing times, leaving not much room for the light assisted NCs charging process.

Then, we performed experiments in which the memory is illuminated only during the writing process, OM2, to separate the light exposure effect on the writing process. From the analysis of the C-V curves after writing at voltage sweep ends, under integral light illumination, we found that the main photo-effect is due to illumination during writing time.

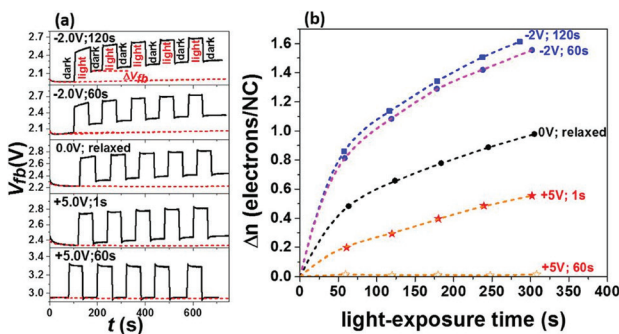


**Figure 2.** Time dependence of  $V_{fb}$  with sequential exposure to light pulses and in the dark periods, after writing in the dark for different values of  $V_{wr}$  and  $t_{wr}$ . The curves are shown in comparison with corresponding relaxation curves of  $V_{fb}$  without light illumination (dotted lines); (b) cumulative number of electrons transferred into a single NC as a function of light exposure time.

Another operation mode, OM-3, is defined as cumulative effect of exposure to light during relaxation after writing in the dark. We thus extracted the time dependence of the variation of the flat band induced by light exposure as the sum of changes induced by light pulses before and after illumination – **Fig.2(a)**. The charge stored in Ge NCs was evaluated, and then the dependence of number of electrons transferred on a single Ge NC on the light exposure time found, the density of NCs being obtained from TEM investigations – see **Fig.2(b)**.

For the investigated memory structure, a sensitive detection and storage of the light illumination event in the retention mode was obtained after negative voltage programming.

The permittivities and resistivities of the 3 layers of the structure are obtained from the modelling of the experimental curves of the frequency dependence (100 kHz–1 MHz) of the capacitance and resistance in accumulation regime [2]. For this, we considered an equivalent parallel RC circuit for each layer.

The contribution of both contacts and of the resistance of the Si substrate were modelled with a series resistance. A very good fit of the simulated curves to the measured frequency dispersions of both capacitance and resistance was found [2]. The effect of different contributions of the capacitor components on the simulated curves was evidenced, and the corresponding values of dielectric constants ( $\epsilon_r$ ) and resistivities ( $\rho$ ) were found – see **Table 1**.

**Table 1**  $\epsilon_r$  and  $\rho$  obtained from fit

Layer	$\epsilon_r$	$\rho$ ( $\Omega \times \text{cm}$ )
Gate $\text{HfO}_2$	12.9	$8.39 \times 10^8$
Ge NCs in $\text{HfO}_2$ FG	16.4	$3.10 \times 10^8$
Control $\text{HfO}_2$	15.2	$2.37 \times 10^9$
Interfacial $\text{SiO}_x$	2.0	$1.76 \times 10^6$

In conclusion, we investigated 3 working modes of the optoelectric memory, i.e. changes of the hysteresis loop under continuous illumination, effect of light on the memory writing process and cumulative effect of light pulses on photo-changes of  $V_{fb}$ . We found that the photo-effect corresponds to a negative charge tunnelling transfer from the Si substrate to Ge NCs. The intrinsic parameters of the component layers of our trilayer were determined by modelling the frequency dispersion of capacitance and resistance measured in accumulation regime, in C-V characteristics.

### References

[1] C. Palade, A. Slav, A. M. Lepadatu, A. V. Maraloiu, I. Dascalescu, S. Iftimie, S. Lazanu, M. L. Ciurea, and T. Stoica, Appl. Phys. Lett. 113, 213106 (2018).  
 [2] C. Palade, A.M. Lepadatu, A. Slav, S. Lazanu, V.S. Teodorescu, T. Stoica, M.L. Ciurea, Appl. Surf. Sci. 428, 698 (2018).

## Organic heterostructures with nanostructured and/or multilayer electrodes

A. Stanculescu, M. Socol, O. Rasoga, C. Breazu, E. Matei, N. Preda, C. Florica, A. Costas,  
C. M. Istrate

in cooperation with  
F. Stanculescu,

University of Bucharest, Faculty of Physics, Magurele, Romania

F. Gherendi

National Institute for Laser, Plasma and Radiation Physics, Magurele, Romania

M. Girtan

University of Angers, LPHIA Angers, France

R. Mallet

University of Angers, SCIAM, Angers, France

The performances of any electronic and optoelectronic devices based on organic semiconductors are determined by the charge carriers generation, injection, transport, recombination and collection by electrodes, both metallic and conductor transparent (TCE). The nano-patterning of the metallic electrode creates an intense electric field improving the mobility of the carriers and modifies the contact area favouring the charge carriers injection/collection.

The properties of single/multi layer organic heterostructure with conventional flat and nano-patterned Al electrode and/or triple layer TCE, (ZnO/Au/ZnO, ZnO/Ag/ZnO) have been investigated [1,2]. We analysed the effect of a 2D array of nanostructures (diameter=400 nm, depth=300 nm, periodicity=1.1  $\mu\text{m}$ ) realized by UV Nanoimprint Lithography and covered by Al (**Fig.1**), on the properties of the heterostructure with single/multilayer organic [1].

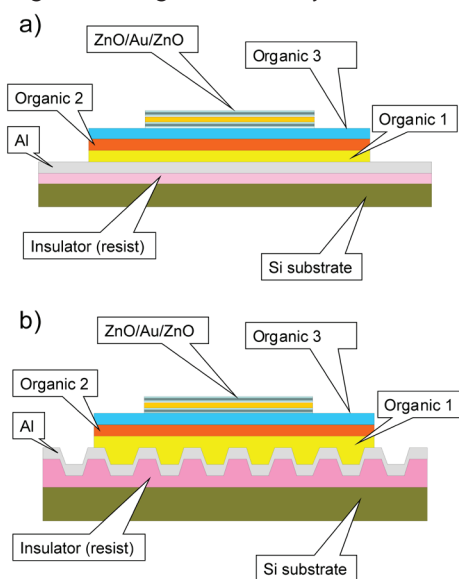


**Figure 1.** Representation of the heterostructure built on: Si covered by flat Al layer (a); Si covered by nano-patterned Al layer (b) [1].

The multi layer TCEs show good stability of the electrical and mechanical properties and offer the possibility to obtain cheaper devices with improved performances, decreasing or avoiding the consumption of limited natural resources.

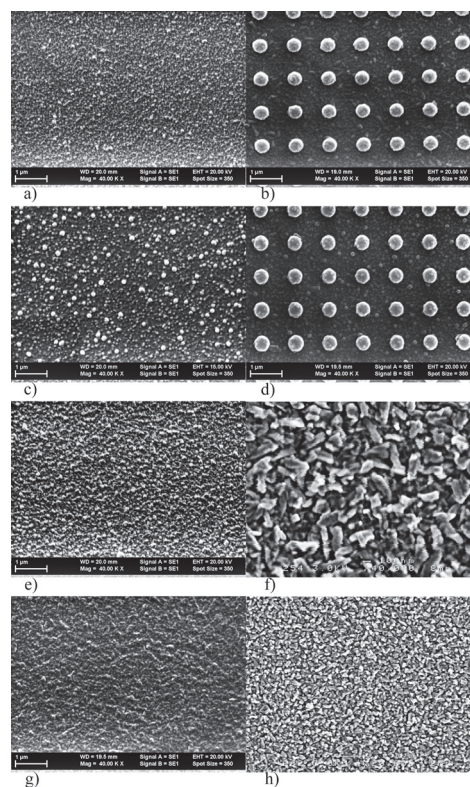


**Figure 2** SEM images on single [ZnPc (zinc phthalocyanine): a,b; C60 (fullerene): c,d] multi (C60/ZnPc: e,f; NTCDA (1,4,5,8-naphthalen-tetracarboxylic dianhydride)/C60/ZnPc: g,h) layer organic with triple TCE on flat (a,c,e,g) and nano-patterned (b,d,f,h) Al [1].

SEM (**Fig.2**) and AFM (**Fig.3**) [1] evidenced the well defined grains morphology for the organic layers, deposited both on Al flat (Al) and patterned (Alp) and the filling of the holes patterned in the Al layer in correlation with the particularities of the organic molecules accommodation on the substrate and thickness of the layers [1].

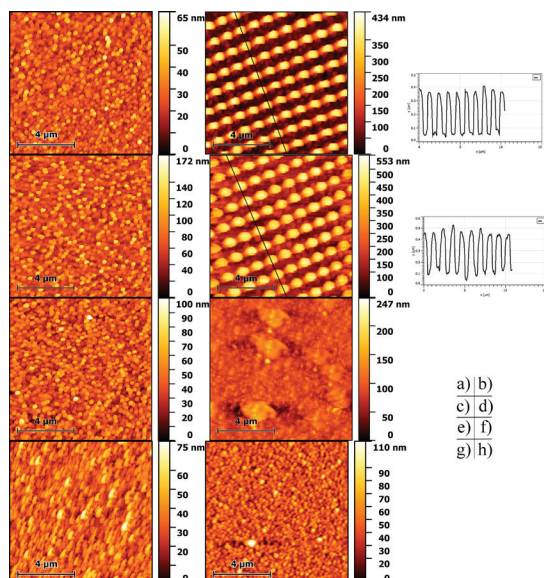


**Figure 3:** AFM images on the samples from Fig.2 [1]. High value of the dark current ( $10^{-4}$ - $10^{-5}$  A) at voltages  $< 1$  V have been obtained for single and multi layer organic heterostructures with Al flat electrode and triple ZnO/Au/ZnO layer TCE [1].

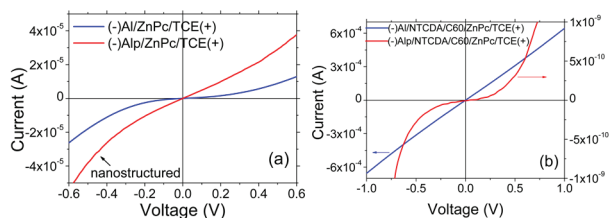


**Figure 4:** I-V characteristics for: Si/Al (Alp)/ZnPc/TCE (a); Si/Al (Alp)/NTCDA/C60/ZnPc/TCE (b) [1].

The Al patterning has determined an enhancement in the current in the single layer organic heterostructure, Al/ZnPc /ZnO/Au/ZnO (**Fig.4a**) and a change from linear to symmetric non-linear injection contact behavior for Si/Al/NTCDA/C60/ZnPc/ZnO/Au/ZnO multi layer organic heterostructure (**Fig.4b**) [1].

We also investigated the properties of other heterostructure with triple layer organic N,N'-diphenyl-N,N'-bis(1-naphthyl)-1,1'-biphenyl-4,4'-diamin ( $\alpha$ -NPD)/5,12-dihydro-5,12-dimethylquino [2,3-b]acridine-7,14 dione (DMQA)/4,7 diphenyl-1,10-phenanthroline (BPhen) deposited on ZnO/Ag/ZnO electrode [2].

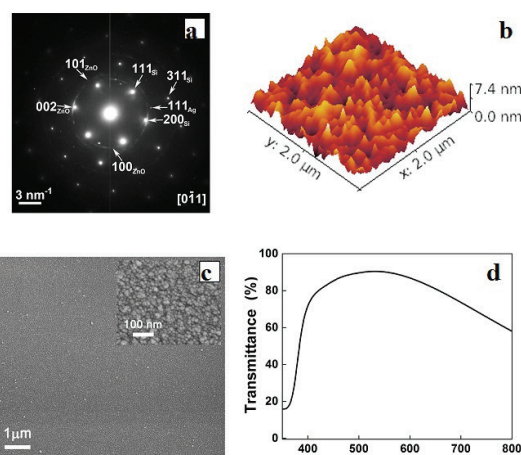


**Figure 5:** Different method (SAED, SEM, AFM, UV-VIS) for ZnO/Ag/ZnO characterization [2].

The SAED and SEM patterns (**Fig.5a,b**) confirmed the crystallinity (hexagonal structure for ZnO and cubic structure for Ag), AFM (**Fig.5c**) the smooth surface, UV-VIS (**Fig.5d**) the high transmittance of the ZnO/Ag/ZnO triple layer with reduced electrical resistivity [2].

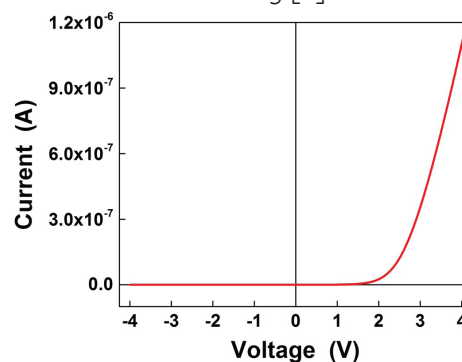


**Figure 6:** I-V characteristic of the heterostructure: ZnO/Ag/ZnO/ $\alpha$ -NPD/DMQA/Bphen/Al [2].

The heterostructure obtained on triple layer electrode, ZnO/Ag/ZnO, evidenced a typical diode behavior (**Fig.6**) with rectifying properties [2].

Funding from National Core Founding Program Contract No: PN16-480102, Bilateral cooperation Romania-France project 783/2014 and PN-II-PT-PCCA-2011 No. 153/2012.

## References

- [1] C. Breazu, M. Socol, N. Preda, E. Matei, O. Rasoga, M. Girtan, R. Mallet, F. Stanculescu, A. Stanculescu, Appl. Surf. Sci. 443, 592-602 (2018).
- [2] M. Socol, N. Preda, C. Breazu, C. Florica, A. Costas, C. M. Istrate, A. Stanculescu, M. Girtan, F. Gherendi, Vacuum 154, 366-370 (2018).

## Phase change in stacked chalcogenide films

C. Mihai, F. Sava, I. D. Simandan, A. C. Galca, V. Dumitru, A. M. Vlaicu, C. Bucur, A. Lőrinczi and A. Velea  
National Institute of Materials Physics

in collaboration with G. Socola, C. Porosnicua, C. N. Borcab, D. Grolimundb  
aNational Institute for Laser Plasma & Radiation Physics Bucharest-Magurele, Romania  
bPaul Scherrer Institute, CH-5232 Villigen-PSI, Switzerland

The stacked phase change chalcogenide films is a solution for increasing storage capacity of nonvolatile memories by storing multiple bits in a single memory cell which exhibits multiple resistance levels.

A cellular automata (CA) [1] model was developed based on the crystallization temperature ( $T_c$ ) of materials, to see if stacked chalcogenide structures exhibit multiple resistance levels. The materials investigated were GeTe/GaSb, GeTe/SnSe and SnSe/GaSb. Overall, the GeTe/SnSe stacked structure has shown the best characteristics for PCM applications among all studied materials. In Fig.1 is shown the dynamics of the number of amorphous sites (analogous of resistance vs. temperature) in the CA models.

Simulations suggest that in order to have good memory characteristics one needs thinner films of the material with the highest threshold energy among the materials in the structure. The study of external energy pulses has revealed that the crystallization dynamics can be controlled by fine tuning the amount of external energy given to the system, in such a way that an optimum balance between nucleation and growth in phase change behaviour is to be achieved.

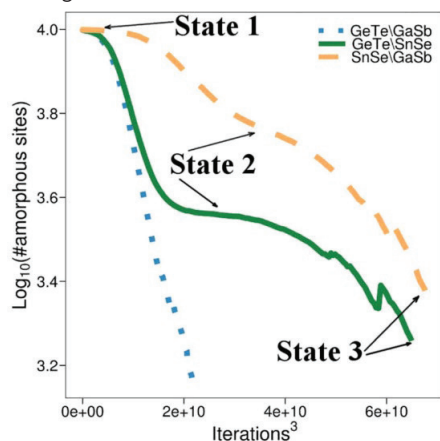


**Figure 1.** Double stacked films' cellular automata (CA) simulations:  $\text{Log}_{10}$  (mean number of amorphous sites) vs Iterations<sup>3</sup>.

Further, we experimentally investigated the stability of stacked films by applying different thermal stresses and observed the structural transformation of the layers and the irreversible inter-layer diffusion of atoms.

The stability of GeTe/SnSe (500 nm / 300 nm) stacked films was tested under thermal stress up to 350°C [2] (the crystallization temperatures of GeTe and SnSe single films are 138°C and 292°C, respectively) in an oven with inert (Ar) atmosphere. Thus, after annealing at 350°C, in the GeTe/SnSe films (Fig.2) the SnSe orthorhombic phase is decomposed, Se is almost entirely evaporated (only 16% remains in the film), Sn diffuses in the GeTe film and forms a single film with composition  $\text{Ge}_{0.75}\text{Sn}_{0.25}\text{Te}$ . The study shows that at 350°C the stacked films are irreversibly destroyed. A buffer conductive layer to avoid diffusion and a capping layer to block the evaporation should be included when designing such memory cells.

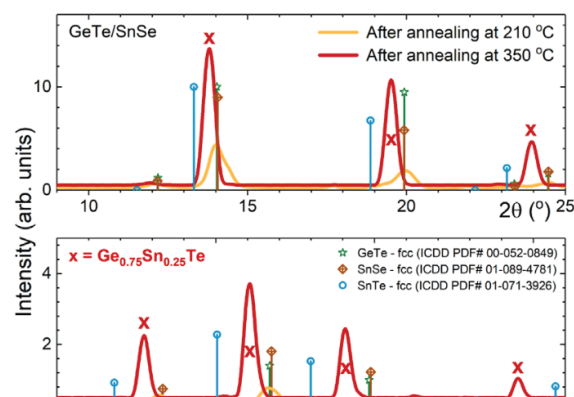


**Figure 2.** XRD data for GeTe/SnSe stacked films annealed at 210 °C and 350 °C. A new, unindexed phase,  $(\text{GeTe})_{0.75}(\text{SnTe})_{0.25}$  face-centered cubic, space group  $Fm-3m$  (225) with  $a=6.082 \text{ \AA}$ , appears after annealing the sample at 350 °C. It seems to be a solid solution of GeTe and SnTe. The patterns are divided into two plots for different angular domains, and shifted on the Y axis to better visualize the changes in the structure.

EXAFS measurements on double stacked films were also performed at Ge (11.31 keV) and Se (12.65 keV) K edges. In the as-deposited state, Ge is tetrahedrally coordinated, surrounded by two Ge atoms and two Te atoms at 2.45 Å and 2.62 Å, respectively, while Se is surrounded by six Sn neighbors in the first shell (at 2.66 Å, 2.74 Å, 3.19 Å, 3.59 Å). After annealing at 350°C, in the GeTe/SnSe films Ge is still tetrahedrally coordinated

(surrounded by 1 Ge atom and 2.3 Te atoms at 2.55 Å and 2.90 Å, respectively), while Se is surrounded by two Sn neighbours at 3.46 Å.

In order to establish at which temperature the diffusion begins in stacked films, we used X-ray reflectometry [3]. The most stable stacked structure, lasting up to 300 °C, is GaSb\GeTe (**Fig.3**), which might be used in multiple state switching devices.

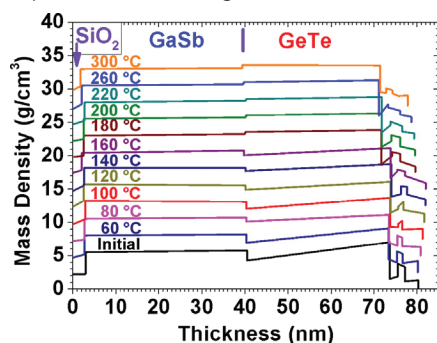


**Figure 3.** The mass density (the diagrams are displaced relative to each other with a fixed value) of GaSb\GeTe stacked films as resulted from fitting of XRR diagrams.

The other two heterostructures, namely SnSe\GeTe and GaSb\SnSe, show strong atom diffusivity between films at temperatures as low as 120°C (**Fig.4a**) and 100°C (**Fig.4b**), respectively.

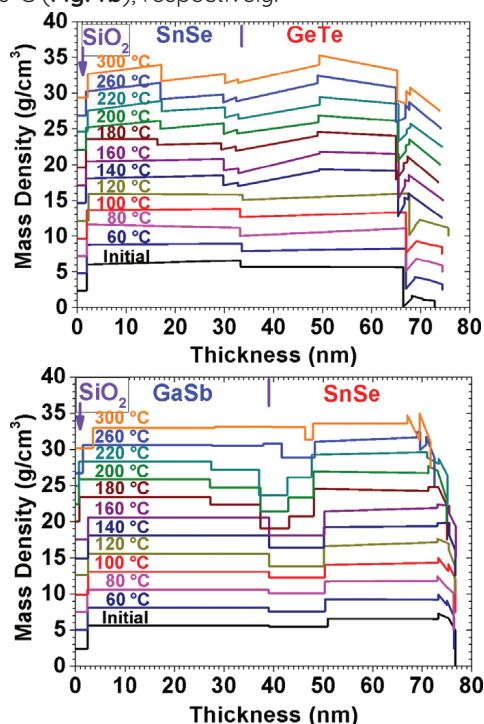


**Figure 4.** The mass density (the diagrams are displaced relative to each other with a fixed value) of SnSe\GeTe (top) and GaSb\SnSe (bottom) stacked films as resulted from fitting of XRR diagrams.

The interdiffusion leads to the formation of new solid solutions and mixed crystalline phases, respectively.

In these two cases a diffusion barrier is necessary and hafnium (Hf) was used. Hf successfully blocked atom diffusion and stabilized the SnSe crystalline phase. Moreover, it increased the crystallization temperature of GeTe up to 250°C, which could be useful for targeted applications. Additionally, a capping film is needed in the GaSb\SnSe to avoid Se evaporation.

Chalcogenide amorphous materials, such as GeTe, are known to have optical and structural properties dependent on the deposition method. Moreover, for emerging memories applications it is very important to have a fine tuned composition in order to obtain the desired properties. However, the formation of a single and homogeneous amorphous GeTe ( $\alpha$ -GeTe) phase is questionable since the deposited films can be mixtures of mono-elemental amorphous nanoclusters. Thus, during co-sputtering (MS) from two distinct Ge and Te targets, in order to obtain homogeneous  $\alpha$ -GeTe thin film, the substrate must be kept at 180 °C as revealed by X-ray photoelectron spectroscopy (**Fig.5**) [4].

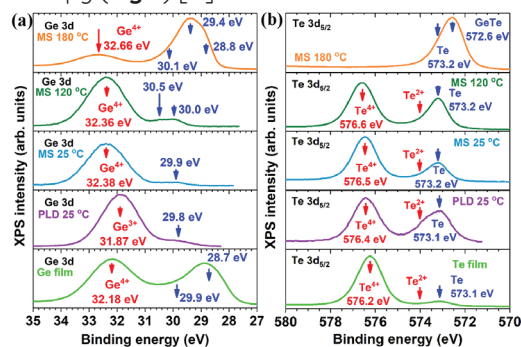


**Figure 5.** XPS results for the  $\alpha$ -GeTe samples deposited by PLD and MS at different substrate temperatures (a) Ge 3d and (b) Te 3d<sub>5/2</sub> core-level spectra. For comparison, the binding energies of single Ge and Te films were added to this graph.

To conclude, we show that it is possible to store multiple bits in a stacked chalcogenide memory cell if the composition and thickness of each layer in the stacked structure are carefully tuned.

Funding from TE 74/2015 (PN-II-TE-2014-4-0498) and Core Program PN18-11 projects.

## References

- [1] C. Mihai, A. Velea, Modelling and Simulation in Materials Science and Engineering. 26 (2018) 045006. <https://doi.org/10.1088/1361-651X/aab62f>
- [2] F. Sava, C. N. Borca, A.C. Galca, G. Socol, D. Grolimund, C. Mihai, A. Velea, Physica Status Solidi (B). 255 (2018) 1700552. <https://doi.org/10.1002/pssb.201700552>
- [3] A. Velea, F. Sava, G. Socol, A. M. Vlaicu, C. Mihai, A. Lőrinczi, I. D. Simandan, Journal of Non-Crystalline Solids. 492 (2018) 11–17. <https://doi.org/10.1016/j.jnoncrysol.2018.02.033>.
- [4] A. C. Galca, F. Sava, I. D. Simandan, C. Bucur, V. Dumitru, C. Porosnicu, C. Mihai, A. Velea, Journal of Non-Crystalline Solids 499 (2018) 1–7. <https://doi.org/10.1016/j.jnoncrysol.2018.07.007>

## Photoanodes for solar water oxidation based on titania and hematite films

Marian Sima in cooperation with

Eugeniu Vasile - Polytechnic University of Bucharest and

Adrian Sima-National Institute for Lasers, Plasma and Radiation Physics

Semiconductor photocatalysis is a green technology to produce hydrogen and oxygen by water splitting, using solar light energy under ambient conditions. Titania ( $\text{TiO}_2$ ) and hematite ( $\alpha\text{-Fe}_2\text{O}_3$ ) are among the most tested semiconductors in photoelectrochemical water splitting applications.  $\text{TiO}_2$  has suitable conduction and valence band energies to drive water reduction and oxidation. However, only 4% of the incident solar energy is absorbed by  $\text{TiO}_2$  because the absorption edge of this oxide is 3.2 eV. The band gap of hematite allows the absorption of a good part of the solar spectrum (<620 nm) and has the valence band edge position suitable for water oxidation. However, the conduction band of the hematite has an inadequate position for water reduction process. On the other hand, the recombination of the electron-hole pairs could be suppressed by strong built-in electric fields created of heterogenous interfaces in a  $\text{TiO}_2\text{-Fe}_2\text{O}_3$  cocatalyst used as photoanode.

We studied the photoactivity of  $\text{TiO}_2/\text{Fe}_2\text{O}_3$  photoanodes prepared via anodic electrodeposition of hematite in  $\text{TiO}_2$  mesoporous layers. Mesoporous  $\text{TiO}_2$  layers were deposited on FTO substrate by spin-coating  $\text{TiO}_2$  paste (Dyesol 18NR-T) diluted further in ethanol absolute at 1:3, 1:6 and 1:9 by weight at 2000 rpm for 60s. The layers were then annealed at 550°C for 1h. The hematite films were synthesized on FTO and FTO/ $\text{TiO}_2$  substrates by electrochemical and annealing processes. The electrodeposition process was performed potentiostatically at 1.2V/Ag-AgCl for 2200s at room temperature using as electrolyte an aqueous solution of 0.1M  $\text{FeSO}_4$ .

The photoelectrochemical measurements were carried out in 1M NaOH electrolyte with a three-electrode electrochemical system composed of the hematite films as the working electrode, Ag/AgCl/saturated KCl as the reference electrode, and a Pt foil as the counter electrode. The potentials measured vs. Ag/AgCl were

reported against reversible hydrogen electrode (RHE)  $E_{\text{RHE}} = E_{\text{Ag/AgCl}} + 0.059\text{pH} + E_{\text{Ag/AgCl}}^0$  with  $E_{\text{Ag/AgCl}}^0 = 0.1976\text{ V}$  at 25°C. The working surface area of the measured photoanodes was 1  $\text{cm}^2$ .

$E_{\text{Ag/AgCl}}^0 = 0.1976\text{ V}$  at 25°C. The working surface area of the measured photoanodes was 1  $\text{cm}^2$ .

Sample code	Structure description	Q (mC/cm <sup>2</sup> )	Thermal treatment	Thickness (nm)
H	FTO/ $\alpha\text{-Fe}_2\text{O}_3$	62	525 °C, 2h; 800 °C, 10 min	-
T1	FTO/ $\text{TiO}_2$ 1:3	-	550 °C, 1 h	-
T2	FTO/ $\text{TiO}_2$ 1:6	-	Idem T1	-
T3	FTO/ $\text{TiO}_2$ 1:9	-	Idem T1	-
HT1	FTO/ $\text{TiO}_2$ 1:3/ $\alpha\text{-Fe}_2\text{O}_3$	71	Idem T1+H	400
HT2	FTO/ $\text{TiO}_2$ 1:6/ $\alpha\text{-Fe}_2\text{O}_3$	48	Idem HT1	155
HT3	FTO/ $\text{TiO}_2$ 1:9/ $\alpha\text{-Fe}_2\text{O}_3$	39	Idem HT1	104

**Table 1.** Sample code and sample structure description of  $\alpha\text{-Fe}_2\text{O}_3$ ,  $\text{TiO}_2$  and  $\text{TiO}_2/\alpha\text{-Fe}_2\text{O}_3$  films. The quantity of electricity (Q) passed to electrodeposition of  $\alpha\text{-Fe}_2\text{O}_3$  precursor, thermal treatment and thickness of the  $\text{TiO}_2/\alpha\text{-Fe}_2\text{O}_3$  films.

$\text{FeOOH}$ , the hematite precursor was electrodeposited on FTO/mesoporous  $\text{TiO}_2$  substrates resulting three samples HT1, HT2 and HT3 with different thicknesses and containing different amounts of hematite ( **Table 1**). The thicknesses of the FTO/ $\text{TiO}_2$  substrates T1, T2 and T3 are close to those of the samples HT1, HT2 and HT3, respectively (**Fig.1**) since the deposited hematite amounts are small and the deposition process of hematite precursor has been carried out both in the volume of the mesoporous  $\text{TiO}_2$  layer and on its surface.

Although the thickness of the sample T3 is lower than that of the samples T1 and T2, the quantity of electricity passed to  $\text{FeOOH}$  deposition is small. This suggests that the FTO surface area connected to the open pores of the T3 sample is the smallest of the three compared samples.

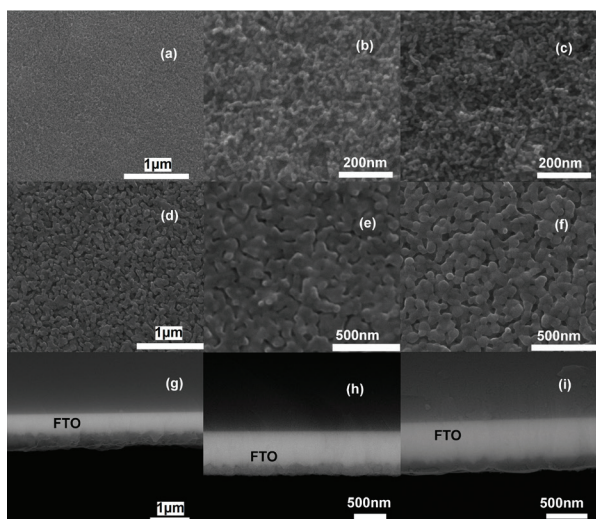


**Figure 1.** SEM images of the samples (a) T1; (b) T2; (c) T3; (d) HT1; (e) HT2; (f) HT3; (g) cross-section of HT1; (h) cross-section of HT2; (i) cross-section of HT3.

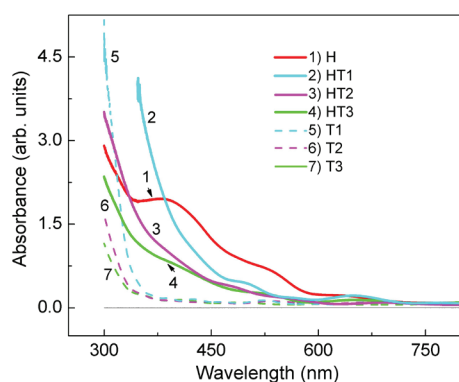


**Figure 2.** Optical absorption spectra of the samples H, HT1, HT2, HT3, T1, T2 and T3.

**Fig.2** shows the optical absorption spectra of the samples H, HT1, HT2, HT3, T1, T2 and T3. The TiO<sub>2</sub>-only photoanodes, T1, T2, T3 show absorption edge at around 370 nm. Light absorption starts at 670 nm for the samples HT1, HT2, HT3 and H which gradually increases over the ultraviolet. Hematite sample H exhibits three absorption bands in visible spectrum at around 380 nm, 525 nm and 637 nm which is connected with a direct transition, an indirect transition and subband gap transitions, respectively. It is observed that light absorption in the visible region (>420 nm) has not improved by using TiO<sub>2</sub>-hematite structures. On the other hand, only sample HT1 shows an improved absorption of UV photons compared to that of sample H. The conduction band of hematite is below that of TiO<sub>2</sub> (**Fig.3**). As a result, electrons excited by visible light to the conduction band of hematite cannot be transferred to the TiO<sub>2</sub> conduction band.

In order to reach the FTO substrate the photoexcited electrons in hematite have to tunnel through titanium dioxide layer. In our case the TiO<sub>2</sub> layer behaves like a template for FeOOH deposition, resulting composite structures.

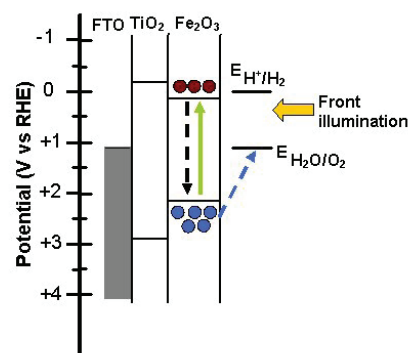


**Figure 3.** The band structure of TiO<sub>2</sub>/ $\alpha$ -Fe<sub>2</sub>O<sub>3</sub> and charge generation at illuminated semiconductor/electrolyte interface.

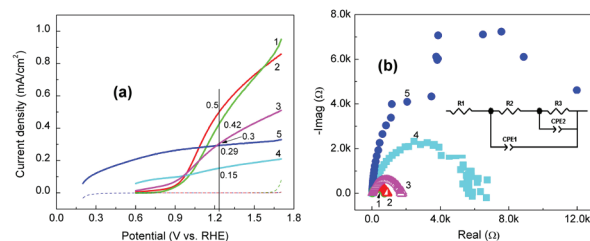


**Figure 4.** (a) J-V characteristics obtained under simulated solar illumination (AM 1.5, 100 mW/cm<sup>2</sup>) of the samples H, HT3, HT2, HT1, T3 in 1 M NaOH solution. (b) Electrochemical impedance spectra collected at 1.23 V vs. RHE, under illumination for samples H, HT3, HT2, HT1, T3.

J-V plots (**Fig.4**) showed the highest current density for the photoanode with the thinnest TiO<sub>2</sub> layer and the largest surface area of the hematite film. It has the lowest value for the resistance of the charge transfer process at photoanode-electrolyte interface. This behavior, revealed through impedance measurements was attributed to the minimizing of charge carriers losses by recombination in TiO<sub>2</sub>/Fe<sub>2</sub>O<sub>3</sub> heterostructure.

## References

- [1] M. Sima, E. Vasile, A. Sima, Photoanode for solar water oxidation based on titania and hematite films, Thin Solid Films 658 (2018) 7-11.

## Photocatalytic activity of semiconductor nanostructures based on ZnO

I. Zgura, L. Frunza, S. Frunza, C.P. Ganea,

in cooperation with

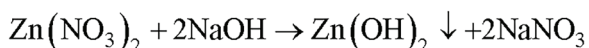
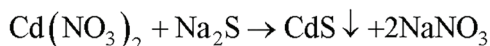
N. Preda, M. Enculescu, C. Ghica, D. Ghica, L. Nedelcu

Composite materials containing semiconductor nanostructures, such as TiO<sub>2</sub>, ZnO, CdS, Ag<sub>2</sub>S, CdSe became very attractive due to their applications as photocatalysts for decomposing environmental pollutants [1].

Recently, various studies were dedicated to the degradation of Rhodamine B, an important xanthene dye pollutant from the textile industry [2]. Using ZnO nanostructures, CdS nanostructures] or ZnO-CdS composites, the photocatalytic measurements were performed at different pH values for pristine materials and at a single pH value in the case of the composite compounds.

In this context, we present results on ZnO-CdS composites with enhanced photocatalytic activity obtained by a facile wet chemical method [3] which allows the control of the morphology and properties of the final products. Thus, ZnO and ZnO-CdS composites (with different amount of CdS) were characterized from the morphological, structural and photocatalytic point-of-view. The photocatalytic measurements regarding the degradation of Rhodamine B (RhB) were carried out at different pH values evidencing that the composites have higher degradation efficiency than the pristine compounds. The intrinsic point defects in the synthesized samples were also investigated and correlated with the photocatalytic activity.

Firstly, CdS nanoparticles were prepared and in the next step the ZnO-CdS composites were prepared in the presence of different amounts of CdS nanoparticles. The chemical reactions involved in the synthesis of CdS and ZnO are:



The crystalline phase of the powders was identified by X-ray diffraction (XRD). The XRD patterns (Fig.1) of ZnO-CdS composites exhibit mixed diffraction peaks only from ZnO (hexagonal wurtzite phase) and CdS (face-centered cubic phase).

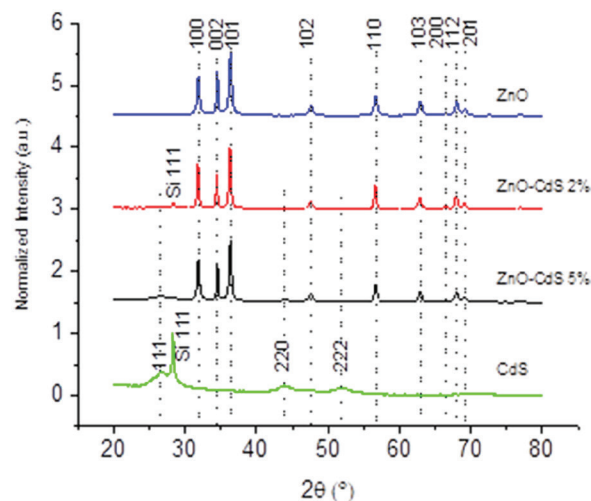


**Figure 1.** XRD patterns of the samples. The SAED patterns and TEM images shown in Fig.2 support also the morphology presented by the SEM images and the crystalline structure gave by XRD investigations.

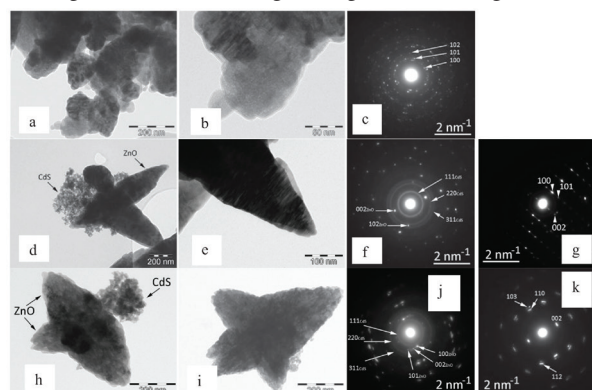


**Figure 2.** TEM images and corresponding SAED patterns for: ZnO (a, b, c); ZnO-CdS 2% (d, e, f, g) and ZnO-CdS 5% (h, i, j, k)

In agreement with the data reported in literature, the reaction rate constant (*k*) was assessed by fitting the experimental curves with a pseudo-first-order linear regression,  $\ln(C_0/C) = kt$  and the values being given in Table 1.

pH	3		7		10	
Sample	k/min-1	R <sup>2</sup>	k/min-1	R <sup>2</sup>	k/min-1	R <sup>2</sup>
ZnO	0.00069	0.983	0.021	0.987	0.036	0.971
ZnO-CdS 2%	0.00241	0.949	0.0361	0.983	0.0626	0.99
ZnO-CdS 5%	0.00093	0.995	0.0236	0.995	0.0368	0.997

**Table 1.** The reaction rate constant *k* and the coefficient of determination *R*<sup>2</sup>

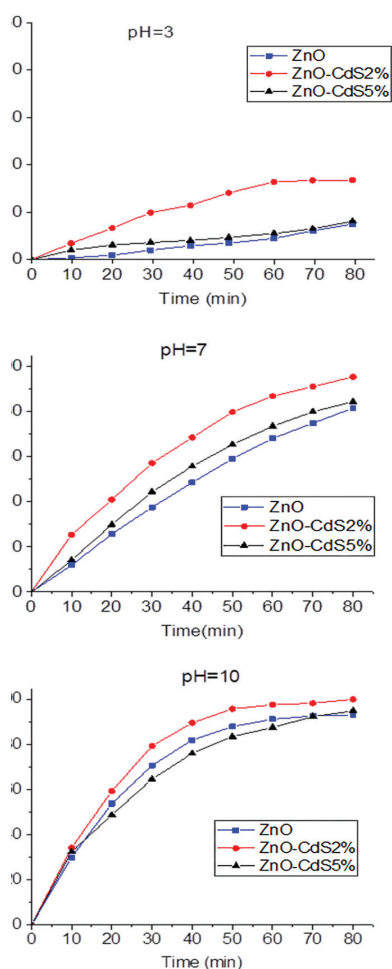


**Figure 3.** Time dependence of RhB degradation efficiency, at different pH values, in the presence of ZnO, ZnO-CdS2%, ZnO-CdS5%.

It is known from literature that a photo-catalyst with a large surface area can provide more numbers of active sites where the photogenerated charge carriers are able to interact with the adsorbed molecules and also to form hydroxyl or superoxide radicals which can later decompose the organic molecules. The large surface area, accompanied by small particle sizes is not sufficient for obtaining high conversion and reaction rate in the degradation of RhB.

The presence of the intrinsic defects (**Fig.2e**) in ZnO-CdS2% sample is an important factor, which influences the photocatalytic activity, can act as electron/hole traps, leading to the reduction of the recombination rate of electrons and holes. In this way the higher photocatalytic effect obtained in the case of ZnO-CdS2% composite can be explained in comparison with that obtained on ZnO-CdS5% sample. In order

to sustain this hypothesis, the EPR investigations were performed on the synthesized powders to evidence the presence of the intrinsic point defects.

The intensity of the EPR line linked to the SD centers varies, being proportional to the concentration of the corresponding paramagnetic defects. Thus, the concentration of the SD defects is the highest in the ZnO-CdS2%, 5.5 times higher than in the case of pristine ZnO. The SD defects are barely observed in the EPR spectrum of ZnO-CdS5%.

The degradation efficiency (**Fig. 3**) is higher for the composites comparatively with that of the pristine ZnO, the enhancement depending on the catalyst morphology (related to the CdS amount added to the composites) and on the pH value. The EPR data showed the presence of intrinsic shallow donor defects in different relative concentration in the investigated samples. These SD centers release electrons in the conduction band of ZnO being responsible for the generation of supplementary electron-trapped hydroxyl radicals which are further involved in the photocatalytic process.

## References

- [1] A. O. Ibhaddon, P. Fitzpatrick, Heterogeneous Photocatalysis: Recent Advances and Applications, *Catalysts* 3 (2013) 189-218.
- [2] C. Zaharia D. Suteu, Textile Organic Dyes - Characteristics, Polluting Effects and Separation/ Elimination Procedures from Industrial Effluents - A Critical Overview, Dr. Tomasz Puzyn (Ed.), *Organic Pollutants Ten Years After the Stockholm Convention - Environmental and Analytical Update*, InTech, 2012, pp. 55-86.
- [3] I. Zgura, N. Preda, D. Ghica, G. Socol, C. Ghica, M. Enculescu, I. Negut, L. Nedelcu, L. Frunza, C. P. Ganea, S. Frunza Wet chemical synthesis of ZnO-CdS composites and their photocatalytic activity, *Mater. Res. Bull.*, 99, 2018, 174-181.

## H<sub>2</sub>S selective sensitivity of Cu doped BaSrTiO<sub>3</sub> under operando conditions and the associated sensing mechanism

A. Stănoiu, C.E. Simion, O.G. Florea, V.S. Teodorescu,  
in cooperation with

R.M.Piticescu<sup>1</sup>, C.F. Rusti-Ciobota<sup>1</sup>, V. Badilita<sup>1</sup>, P. Osiceanu<sup>2</sup>, A. Sobetkii<sup>3</sup>

<sup>1</sup>National Institute for Non-ferrous and Rare Metals, Ilfov, Romania

<sup>2</sup>"Ilie Murgulescu" Institute of Physical Chemistry, Romanian Academy, Bucharest, Romania

<sup>3</sup>MGM Star Construct SRL, Romania

In this report, thin films of nanostructured Cu mol. 5% doped perovskite Ba<sub>0.75</sub>Sr<sub>0.25</sub>TiO<sub>3</sub> (BST) were prepared via hydrothermal treatment and further pressed into pellets of 2 inches needed for the RF sputtering system [1]. The obtained pellets of BST sensitive material have been used in the RF sputtering, leading to the deposition of thin compact film onto Al<sub>2</sub>O<sub>3</sub> substrates provided with interdigital Pt electrodes and heater. Details about the possible gas sensing mechanisms were acquired via simultaneous electrical resistance and work function changes measurements. Transmission Electron Microscopy (TEM) techniques was involved in order to reveal morphological appearances (Fig.1a and b).

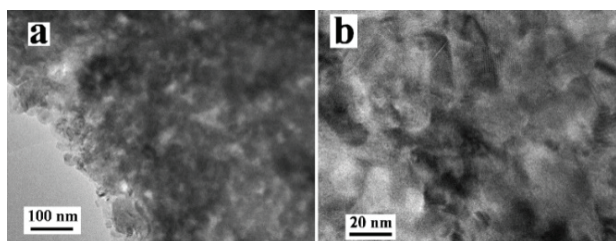


**Figure 1.** TEM images (a and b) of BST Cu 5% sensitive material.

Images reveal that the film structure is fully crystallized lacking in porosity. Thus, the compact aspect ratio of the film is highlighted. Moreover, the crystallite sizes were found in the range of 15 to 30 nm.

It is known that the gas sensing performances of semiconducting metal oxide materials depend on the operating temperature, as a consequence of the activation energies interplay between that gas species and the sensitive surface. Thus, the electrical resistance dependence of R<sub>air</sub>

(0 and 50% RH as medium value), R<sub>gas</sub> (10ppm H<sub>2</sub>S) and consequently of the sensor signal S<sub>red</sub> are shown in (Fig.2).

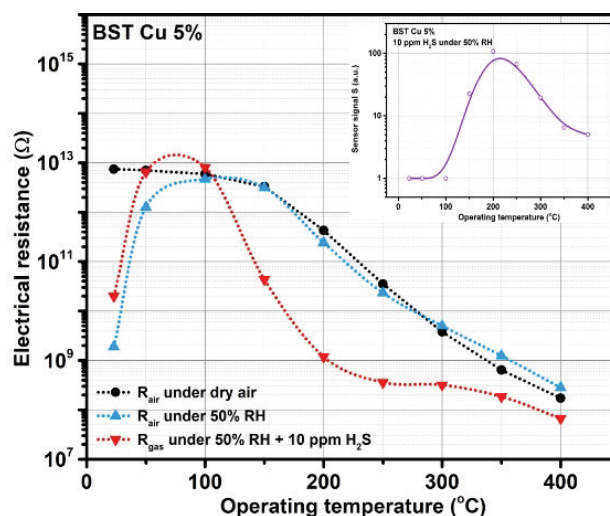


**Figure 2.** Electrical resistance evolution under 0%, 50% RH and 50% RH + 10 ppm H<sub>2</sub>S at different operating temperatures.

The associated sensor signal was calculated according to the formula:  $S = R_{air} / R_{H_2S}$ .

Above 100°C under 0% RH the electrical resistance decreases abruptly since in the case of 50% RH different behaviours are reflected with respect to the operating temperature. While for the former the increase in free charge carrier concentration might be responsible for such effect, for the later different desorption rates are likely to occur. As can be seen, the maximum sensitivity is reached around 200°C. As a trade-off between gaining optimum sensitivity with fast response/recovery transients, we select 250°C as optimum operating temperature for further gas sensing investigations.

Consequently, the electrical resistance changes towards different H<sub>2</sub>S concentrations have been analysed (see **Fig.3**). No RH influence over the base resistance could be observed.

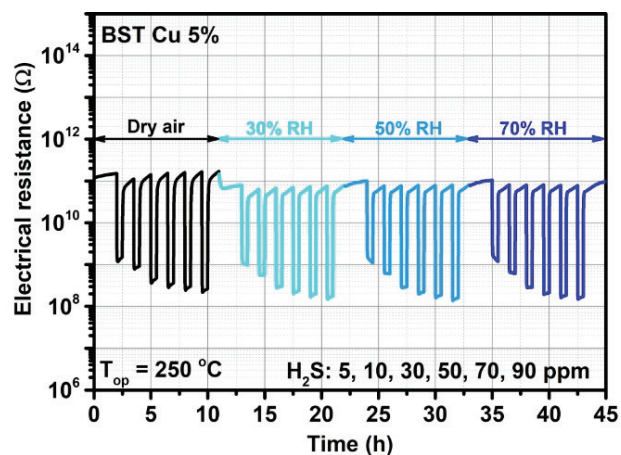


**Figure 3.** RH influence over the electrical resistance changes of BST Cu 5% exposed to different H<sub>2</sub>S concentrations.

The effect of different H<sub>2</sub>S concentrations over the sensor signal with respect to the background RH levels are presented in (**Fig.4**).

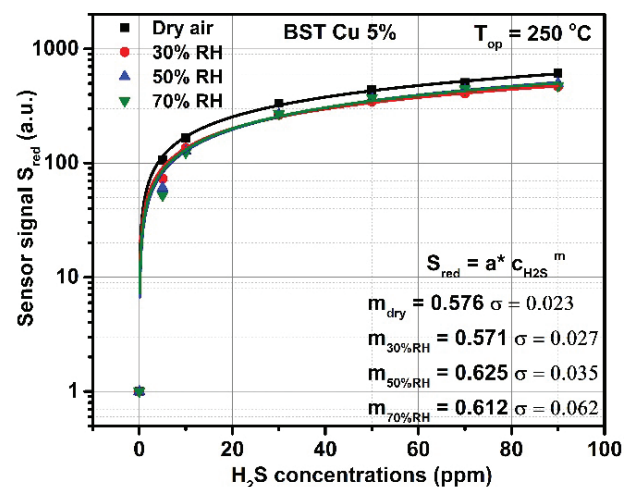


**Figure 4.** Sensor signal dependence for different H<sub>2</sub>S concentrations.

The calibration curves perfectly resemble a power law dependence revealing the possibility to have two possible gas-surface interaction mechanisms:

- the interaction between H<sub>2</sub>S and the pre-adsorbed oxygen species according to the following equation:



- the high ionization potential of H<sub>2</sub>S (4.10eV) which follows a heterolytic S-H break on interaction [2] with the Cu(OH)<sub>2</sub>: H<sub>2</sub>S + Cu(OH)<sub>2</sub> ↔ CuS + 2H<sub>2</sub>O (2)

The influence of H<sub>2</sub>S exposure in the presence of different RH levels over the energetic relative changes is shown in (**Fig5**).

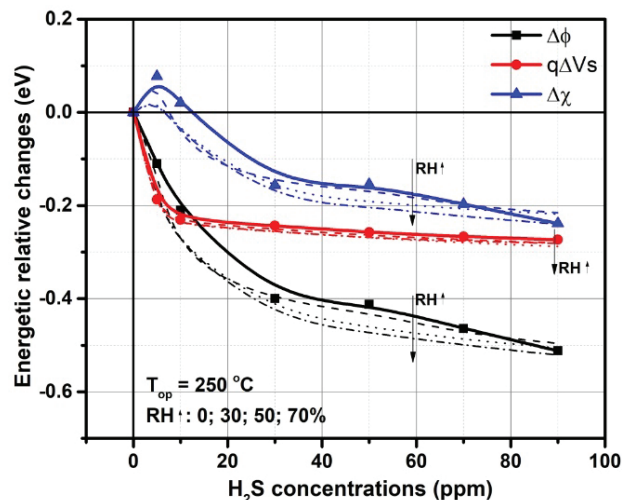


**Figure 5.** Energetic relative changes with respect to H<sub>2</sub>S exposure under different RH background.

A striking aspect is revealed by the gradual decrease in work function ( $\Delta\phi=500\text{meV}$ ) upon exposure to H<sub>2</sub>S. On the other hand, the band bending strongly decreases with about 200meV for the first two H<sub>2</sub>S levels (5, 10 ppm) remaining almost constant for higher concentrations.

By resembling the above mentioned behaviours, one can decouple between the proposed gas sensing mechanisms (eq. 1 and eq. 2) based on the electronic affinity ( $\Delta\chi$ ) behaviour: for the lowest H<sub>2</sub>S concentrations, the electronic affinity shows a small turning slope in the positive region values, followed by a constant decrease for the highest H<sub>2</sub>S concentrations.

We could demonstrate the applicative potential of BST Cu 5% towards H<sub>2</sub>S detection under real operation conditions (the presence of RH) and its associated gas sensing mechanism.

### References

[1] A. Stanoiu, R.M. Piticescu, C.E. Simion, C.F. Rusti-Ciobota, O.G. Florea, V.S. Teodorescu, P. Osiceanu, A. Sobetkii, V. Badilita, Sens. Actuators B, 264 (2018) 327-336.  
 [2] Y. Cudennec, A. Lecerf, Solid State Sci. 5 (2003) 1471-1474.

**INTERNATIONAL CENTRE FOR ADVANCED  
TRAINING AND RESEARCH IN PHYSICS**

**International Centre for Advanced Training and Research in Physics**  
**Centre International de Formation et de Recherche Avancées en Physique (CIFRA),**  
**A category 2 Centre under the auspices of UNESCO**

**Report of Activity - 2018**

CIFRA was created under the Agreement between the Government of Romania and UNESCO, as a Category 2 Center under the auspices of UNESCO (ratified by Government Decision 847/30 October 2013 published in the Official Gazette. no. 691, the 1/12 part November 2013).

CIFRA is operating as a subsidiary with legal independence of the National Institute of Materials Physics, Magurele, Romania (Government Decision no. 1.312/1996 published in the Official Gazette. no. 7/6 January 2016).

**CIFRA's mission**

Developing training and capacity building activities with a focus on:

- advanced training and development through scientific research in cooperation with national and international institutions
- scientific events and knowledge transfer through short term activities developed in cooperation with UNESCO including workshops, conferences and seminars compatible with UNESCO programmes.

**CIFRA's objectives:**

Providing facilities, training opportunities and advanced research for researchers in the Central and Eastern Europe countries, besides those in less developed countries in Africa, with an additional mandate of promoting women in science through its programs;

The conduct and coordination of Advanced studies oriented towards research in physics and related interdisciplinary topics;

Providing expertise of the decision factors, educational factors and the general public to strengthen the national research and development potential;

Carrying out promotional activities (seminars, conferences, workshops), in

cooperation with national and international institutions that would provide an international forum of discussion and encourage the formation of regional networks of collaboration between scientists from different countries.

**Projects:**

1. Neutrino properties derived from the study of rare decay processes at low and high Energies,

Project director: S. Stoica

Project code: PN-III-P4-ID-PCE-2016-0078

2. Spontaneous symmetry breaking and dissipative processes in single quantum dot lasers. Lasing as phase transition.

Project director: P. Gartner

Project code: PN-III-P4-ID-PCE-2016-0221

3. Extensive capitalization of experience in space and security activities (partnership with 10 institutions, coordinator Institute of Space Science, director V. Popa)

CIFRA's responsible: S. Stoica

4. PULSE project, "Professionalization and international opening of experimental scientific licenses in West Africa" (CIFRA is associate member of a consortium which includes 20 international institutions from Europe and Africa)

CIFRA's responsible: S. Stoica

5. Theoretical Study of the Double Beta Decay - JINR (Dubna) - CIFRA project

CIFRA's responsible S. Stoica

## **Publications**

### **Articles**

- S. Stoica, Double-beta decay and its potential to explore beyond SM physics, *Int. J. Mod. Phys. A* 33, 1845012 (2018).
- I. V. Dinu, V. Moldoveanu, P. Gartner, Many-body effects in transport through a quantum-dot cavity system, *Phys. Rev. B* 97, 195442 (2018).
- F. Lohof, R. Barzel, P. Gartner, C. Gies, Delayed Transition to Coherent Emission in Nanolasers with Extended Gain Media, *Phys Rev. Applied* 10, 054005 (2018).

### **Conferences**

- S. Stoica, Double Beta Decay and its potential to investigate BSM physics, TESNAT, Antalya, Turkey, April 20 -23, 2018(invited lecture).
- S. Stoica, Double-beta decay and its potential to explore beyond SM physics, SEENET, BW2018, Nis, Serbia, June 10-14, 2018 (invited lecture).
- S. Stoica, Neutrino properties deduced from the neutrinoless double beta decay study, 6th Symposium on Neutrinos and Dark Matter in Nuclear (NDM2018), Daejeon, June 29 – July 4, 2018 (oral presentation).
- S. Stoica, Neutrino properties deduced from the double beta decay study, 39th International Conference on High Energy Physics (ICHEP2018), Seoul, July 4 -11, 2018(oral presentation).

### **Organizing meeting**

CIFRA's Opening ceremony event, September 20<sup>th</sup> –21<sup>st</sup> 2018, Măgurele, Romania.

On September 20 and 21, the official opening of the International Center for Advanced Training and Research in Physics (CIFRA) took place in Magurele-Bucharest, Romania.

With this occasion, the CIFRA's International Governing Board meeting also took place.

Agenda and more details about this meeting can be found at:

<http://cifra.infim.ro/cifra-opening.php>

### **Invited visitors:**

- Prof. Samoil Bilenky, ( TRIUMF, Canada and JINR, Dubna)
- Prof. Fedor Simkovic, Comenius University, Bratislava and JINR, Dubna)
- Prof. Ivan Stekl, (Czech Technical University in Prague)
- Prof. Sandro Scandolo, ICTP-Trieste
- Prof. George Thompson, ICTP, Trieste
- Prof. Joe Niemela, ICTP, Trieste
- Dr. ZEBAZE KANA Martiale
- Dr. Romain Murenzi, TWAS, Trieste.

**PUBLICATIONS**

No	Title	Journal	Authors	FI	AIS	DOI	Q
1	Near infrared emission properties of Er doped cubic sesquioxides in the second/third biological windows	SCIENTIFIC REPORTS,8,18033	Avram, D; Tiseanu, I; Vasile, BS; Florea, M; Tiseanu, C	4.122	1.356	10.1038/s41598-018-36639-y	Q1
2	Probing the dielectric, piezoelectric and magnetic behavior of CoFe <sub>2</sub> O <sub>4</sub> /BNT-BT0.08 composite thin film fabricated by sol-gel and spin-coating methods	SCIENTIFIC REPORTS,8,17883	Cernea, M; Vasile, BS; Surdu, VA; Trusca, R; Bartha, C; Craciun, F; Galassi, C	4.122	1.356	10.1038/s41598-018-36232-3	Q1
3	Flexible Delivery Patch Systems based on Thermoresponsive Hydrogels and Submicronic Fiber Heaters	SCIENTIFIC REPORTS,8,17555	Evangelidis, A; Beregoi, M; Diculescu, VC; Galatanu, A; Ganea, P; Enculescu, I	4.122	1.356	10.1038/s41598-018-35914-2	Q1
4	Full Tetragonal Phase Stabilization in ZrO <sub>2</sub> Nanoparticles Using Wet Impregnation: Interplay of Host Structure, Dopant Concentration and Sensitivity of Characterization Technique	NANOMATERIALS 8,988	Colbea, C; Avram, D; Cojocaru, B; Negrea, R; Ghica, C; Kessler, VG; Seisenbaeva, GA; Parvulescu, V; Tiseanu, C	3.504	0.696	10.3390/nano8120988	Q1
5	(Fe, Nd) codoped ZnO micro- and nanostructures with multifunctional characteristics like photocatalytic activity, optical and ferromagnetic properties	CERAMICS INTERNATIONAL, 44, pp.21962-21975	Diamandescu, L; Cernea, M; Tolea, F; Secu, EC; Trusca, R; Secu, M; Enculescu, M	3.057	0.437	10.1016/j.ceramint.2018.08.310	Q1
6	Delayed Transition to Coherent Emission in Nanolasers with Extended Gain Media	PHYSICAL REVIEW APPLIED,10,54055	Lohof, F; Barzel, R; Gartner, P; Gies, C	4.782	2.124	10.1103/PhysRevApplied.10.054055	Q1
7	Optoelectric charging-discharging of Ge nanocrystals in floating gate memory	APPLIED PHYSICS LETTERS,113,213106	Palade, C; Slav, A; Lepadatu, AM; Maraloiu, AV; Dascalu, I; Iftimie, S; Lazanu, S; Ciurea, ML; Stoica, T	3.495	0.927	10.1063/1.5039554	Q1
8	Hierarchical functionalization of electrospun fibers by electrodeposition of zinc oxide nanostructures	APPLIED SURFACE SCIENCE, 458, pp.555-563	Matei, E; Busuioac, C; Evangelidis, A; Zgura, I; Enculescu, M; Beregoi, M; Enculescu, I	4.439	0.627	10.1016/j.apusc.2018.06.143	Q1
9	Zinc Oxide Spherical-Shaped Nanostructures: Investigation of Surface Reactivity and Interactions with Microbial and Mammalian Cells	LANGMUIR,34, pp.13638-13651	Visinescu, D; Hussien, MD; Moreno, JC; Negrea, R; Birjega, R; Somacescu, S; Ene, CD; Chifiriuc, MC; Popa, M; Stan, MS; Carp, O	3.789	0.964	10.1021/acs.langmuir.8b02528	Q1
10	Particularities of photocatalysis and formation of reactive oxygen species on insulators and semiconductors: cases of SiO <sub>2</sub> , TiO <sub>2</sub> and their composite SiO <sub>2</sub> -TiO <sub>2</sub>	CATALYSIS SCIENCE & TECHNOLOGY,8, pp.5657-5668	Anastasescu, C; Negrila, C; Angelescu, DG; Atkinson, I; Anastasescu, M; Spataru, N; Zaharescu, M; Balint, I	5.365	1.105	10.1039/c8cy00991k	Q1
11	Reduced graphene oxide/iron oxide nanohybrid flexible electrodes grown by laser-based technique for energy storage applications	CERAMICS INTERNATIONAL, 44, pp.20409-20416	Queraltó, A; del Pino, AP; Logofatu, C; Datcu, A; Amade, R; Bertran-Serra, E; Gyorgy, E	3.057	0.437	10.1016/j.ceramint.2018.08.034	Q1
12	Structural and optical properties of optimized amorphous GeTe films for memory applications	JOURNAL OF NON-CRYSTALLINE SOLIDS,499, pp.1-7	Galca, AC; Sava, F; Simandan, ID; Bucur, C; Dumitru, V; Porosnicu, C; Mihai, C; Velea, A	2.488	0.427	10.1016/j.jnoncrysol.2018.07.007	Q1
13	Networked mesoporous SnO <sub>2</sub> nanostructures templated by Brij (R) 35 with enhanced H <sub>2</sub> S selective performance	MICROPOROUS AND MESOPOROUS MATERIALS,270, pp.93-101	Stanoiu, A; Simion, CE; Sackmann, A; Baibarac, M; Florea, OG; Osiceanu, P; Teodorescu, VS; Somacescu, S	3.649	0.671	10.1016/j.micromeso.2018.05.008	Q1

No	Title	Journal	Authors	FI	AIS	DOI	Q
14	Rolling dopant and strain in Y-doped BiFeO <sub>3</sub> epitaxial thin films for photoelectrochemical water splitting	SCIENTIFIC REPORTS,8,15826	Haydous, F; Scarisoreanu, ND; Birjega, R; Ion, V; Lippert, T; Dumitrescu, N; Moldovan, A; Andrei, A; Teodorescu, VS; Ghica, C; Negrea, R; Dinescu, M	4.122	1.356	10.1038/s41598-018-34010-9	Q1
15	Lincomycin-embedded PANI-based coatings for biomedical applications	APPLIED SURFACE SCIENCE,455, pp.653-666	Popescu-Pelin, G; Fufa, O; Popescu, RC; Savu, D; Socol, M; Zgura, I; Holban, AM; Vasile, BS; Grumezescu, V; Socol, G	4.439	0.627	10.1016/j.ap-susc.2018.06.016	Q1
16	Heavy doping of ceria by wet impregnation: a viable alternative to bulk doping approaches	NANOSCALE,10, pp.18043-18054	Florea, M; Avram, D; Maraloiu, VA; Cojocaru, B; Tiseanu, C	7.233	1.704	10.1039/c8nr03695k	Q1
17	How measurement protocols influence the dynamic J-V characteristics of perovskite solar cells: Theory and experiment	SOLAR ENERGY,173, pp.976-983	Nemnes, GA; Besleaga, C; Tomulescu, AG; Palici, A; Pintilie, L; Manolescu, A; Pintilie, I	4.374	0.799	10.1016/j.solener.2018.08.033	Q1
18	Hydroxyapatite coatings on Mg-Ca alloy prepared by Pulsed Laser Deposition: Properties and corrosion resistance in Simulated Body Fluid	CERAMICS INTERNATIONAL,44, pp.16678-16687	Rau, JV; Antoniac, I; Filipescu, M; Cotrut, C; Fosca, M; Nistor, LC; Birjega, R; Dinescu, M	3.057	0.437	10.1016/j.ceramint.2018.06.095	Q1
19	Palladium pincer complex incorporation onto the Fe <sub>3</sub> O <sub>4</sub> -entrapped cross-linked multilayered polymer as a high loaded nanocatalyst for oxidation'	JOURNAL OF MOLECULAR LIQUIDS,266, pp.393-404	Zohreh, N; Hosseini, SH; Tavakolizadeh, M; Busuioc, C; Negrea, R	4.513	0.57	10.1016/j.molliq.2018.06.076	Q1
20	Wide-Range Columnar and Lamellar Photoluminescent Liquid-Crystalline Lanthanide Complexes with Mesogenic 4-Pyridone Derivatives	CHEMISTRY-A EUROPEAN JOURNAL,24, pp.13512-13522	Chiriac, LF; Pasuk, I; Secu, M; Micutz, M; Circu, V	5.16	1.26	10.1002/chem.201801781	Q1
21	Polarization Orientation in Lead Zirconate Titanate (001) Thin Films Driven by the Interface with the Substrate	PHYSICAL REVIEW APPLIED,10,34020	Tanase, LC; Abramiuc, LE; Popescu, DG; Trandafir, AM; Apostol, NG; Bucur, IC; Hrib, L; Pintilie, L; Pasuk, I; Trupina, L; Teodorescu, CM	4.782	2.124	10.1103/PhysRevApplied.10.034020	Q1
22	Enhanced near-infrared response of a silicon solar cell by using an up-conversion phosphor film of Yb/Er - co-doped CeO <sub>2</sub>	SOLAR ENERGY,171, pp.40-46	Grigorescu, M; Secu, M; Trupina, L; Enculescu, M; Besleaga, C; Pintilie, I; Badica, P	4.374	0.799	10.1016/j.solener.2018.06.057	Q1
23	Magnetism and magnetoresistance of single Ni-Cu alloy nanowires	BEILSTEIN JOURNAL OF NANOTECHNOLOGY,9, pp.2345-2355	Costas, A; Florica, C; Matei, E; Toimil-Molares, ME; Stavarache, I; Kuncser, A; Kuncser, V; Enculescu, I	2.968	0.745	10.3762/bjnano.9.219	Q1
24	Ferroelectric switching dynamics in 0.5Ba(Zr <sub>0.2</sub> Ti <sub>0.8</sub> )O <sub>3</sub> -0.5(Ba <sub>0.7</sub> Ca <sub>0.3</sub> )TiO <sub>3</sub> thin films	APPLIED PHYSICS LETTERS,113,82903	Silva, JPB; Kamakshi, K; Negrea, RF; Ghica, C; Wang, J; Koster, G; Rijnders, G; Figueiras, F; Pereira, M; Gomes, MJM	3.495	0.927	10.1063/15044623	Q1
25	Orbital Ordering of the Mobile and Localized Electrons at Oxygen-Deficient LaAlO <sub>3</sub> /SrTiO <sub>3</sub> Interfaces	ACS NANO,12, pp.7927-7935	Chikina, A; Lechermann, F; Husanu, MA; Caputo, M; Cancellieri, C; Wang, XQ; Schmitt, T; Radovic, M; Strocov, VN	13.709	4.045	10.1021/acsnano.8b02335	Q1
26	Highly Efficient, Easily Recoverable, and Recyclable Re-SiO <sub>2</sub> -Fe <sub>3</sub> O <sub>4</sub> Catalyst for the Fragmentation of Lignin	ACS SUSTAINABLE CHEMISTRY & ENGINEERING,6, pp.9606-9618	Tudorache, M; Opris, C; Cojocaru, B; Apostol, NG; Tirsoaga, A; Coman, SM; Parvulescu, VI; Duraki, B; Krumeich, F; van Bokhoven, JA	6.14	1.142	10.1021/acssuschemeng.7b04294	Q1

No	Title	Journal	Authors	FI	AIS	DOI	Q
27	Versatile Actuators Based on Polypyrrole-Coated Metalized Eggshell Membranes	ACS SUSTAINABLE CHEMISTRY & ENGINEERING,6, pp.10173-10181	Beregoi, M; Preda, N; Evanghelidis, A; Costas, A; Enculescu, I	6.14	1.142	10.1021/acssuschemeng.8b01489	Q1
28	Magneto-optical properties of Ce <sup>3+</sup> and Tb <sup>3+</sup> -doped silico-phosphate sol-gel thin films	APPLIED SURFACE SCIENCE,448, pp.474-480	Stefan, CR; Elisa, M; Vasiliu, IC; Sava, BA; Boroica, L; Sofronie, M; Tolea, F; Enculescu, M; Kuncser, V; Beldiceanu, A; Volceanov, A; Eftimie, M	4.439	0.627	10.1016/j.apusc.2018.04.067	Q1
29	Thermal stability of phase change GaSb\GeTe, SnSe\GeTe and GaSb\SnSe double stacked films revealed by X-ray reflectometry and X-ray diffraction	JOURNAL OF NON-CRYSTALLINE SOLIDS,492, pp.11-17	Velea, A; Sava, F; Socol, G; Vlaicu, AM; Mihai, C; Lorinczi, A; Simandan, ID	2.488	0.427	10.1016/j.jnoncrysol.2018.02.033	Q1
30	k-space imaging of anisotropic 2D electron gas in GaN/GaN high-electron-mobility transistor heterostructures	NATURE COMMUNICATIONS,9,2653	Lev, LL; Maiboroda, IO; Husanu, MA; Grichuk, ES; Chumakov, NK; Ezubchenko, IS; Chernykh, IA; Wang, X; Tobler, B; Schmitt, T; Zhaneskin, ML; Valeyev, VG; Strocov, VN	12.353	5.685	10.1038/s41467-018-04354-x	Q1
31	Piezoelectric ferromagnetic BNT-BT0.08/CoFe <sub>2</sub> O <sub>4</sub> coaxial core-shell composite nanotubes for nanoelectronic devices	JOURNAL OF ALLOYS AND COMPOUNDS,752, pp.381-388	Cernea, M; Vasile, BS; Surdu, VA; Trusca, R; Sima, M; Craciun, F; Galassi, C	3.779	0.574	10.1016/j.jallcom.2018.04.146	Q1
32	White-Light Emission of Dye-Doped Polymer Submicronic Fibers Produced by Electrospinning	POLYMERS,10,737	Enculescu, M; Evanghelidis, A; Enculescu, I	2.935	0.7	10.3390/polym10070737	Q1
33	Different-Length Hydrazone Activated Polymers for Plasmid DNA Condensation and Cellular Transfection	BIOMACROMOLECULES,19, pp.2638-2649	Priegue, JM; Lostale-Seijo, I; Crisan, D; Granja, JR; Fernandez-Trillo, F; Montenegro, J	5.738	1.279	10.1021/acs.biomac.8b00252	Q1
34	Inhibitory effect of three phenacyl derivatives on the oxidation of sphalerite (ZnS) in air-equilibrated acidic solution	CORROSION SCIENCE,138, pp.154-162	Chirita, P; Duinea, MI; Sandu, AM; Birsu, LM; Sarbu, LG; Baibarac, M; Sava, F; Popescu, M; Matei, E	4.862	0.89	10.1016/j.corsci.2018.04.017	Q1
35	Localization Properties of Zig-Zag Edge States in Disordered Phosphorene	PHYSICA STATUS SOLIDI-RAPID RESEARCH LETTERS,12,1800051	Nita, M; Ostahie, B; Tolea, M; Aldea, A	3.721	0.755	10.1002/pssr.201800051	Q1
36	Epitaxial growth of single-orientation high-quality MoS <sub>2</sub> monolayers	2D MATERIALS,5,35012	Bana, H; Travaglia, E; Bignardi, L; Lacovig, P; Sanders, CE; Dendzik, M; Michiardi, M; Bianchi, M; Lizzit, D; Presel, F; De Angelis, D; Apostol, N; Das, PK; Fujii, J; Vobornik, I; Larciprete, R; Baraldi, A; Hofmann, P; Lizzit, S	7.042	2.646	10.1088/2053-1583/aabb74	Q1
37	H <sub>2</sub> S selective sensitivity of Cu doped BaSrTiO <sub>3</sub> under operando conditions and the associated sensing mechanism	SENSORS AND ACTUATORS B-CHEMICAL,264, pp.327-336	Stanoiu, A; Piticescu, RM; Simion, CE; Rusti-Ciobota, CF; Florea, OG; Teodorescu, VS; Osiceanu, P; Sobetkii, A; Badilita, V	5.667	0.787	10.1016/j.snb.2018.03.013	Q1
38	The improvement of SiO <sub>2</sub> nanotubes electrochemical behavior by hydrogen atmosphere thermal treatment	APPLIED SURFACE SCIENCE,444, pp.216-223	Spataru, N; Anastasescu, C; Radu, MM; Balint, I; Negrila, C; Spataru, T; Fujishima, A	4.439	0.627	10.1016/j.apusc.2018.03.074	Q1

No	Title	Journal	Authors	FI	AIS	DOI	Q
39	Polyaniline photoluminescence quenching induced by single-walled carbon nanotubes enriched in metallic and semiconducting tubes	SCIENTIFIC REPORTS,8,9518	Baibarac, M; Matea, A; Daescu, M; Mercioniu, I; Quillard, S; Mevellec, JY; Lefrant, S	4.122	1.356	10.1038/s41598-018-27769-4	Q1
40	Compressive properties of pristine and SiC-Te-added MgB <sub>2</sub> powders, green compacts and spark-plasma-sintered bulks	CERAMICS INTERNATIONAL,44, pp.10181-10191	Badica, P; Batalu, D; Burdusel, M; Grigoroscuta, MA; Aldica, GV; Enculescu, M; Gabor, RA; Wang, ZY; Huang, RX; Li, PF	3.057	0.437	10.1016/j.ceramint.2018.03.008	Q1
41	Synthesis and characterization of CoFe <sub>2</sub> O <sub>4</sub> /BNT-BT0.08 core shell nanotubes by a template based sol-gel method	CERAMICS INTERNATIONAL,44, pp.10813-10819	Cernea, M; Vasile, BS; Surdu, VA; Trusca, R; Craciun, F; Galassi, C	3.057	0.437	10.1016/j.ceramint.2018.03.123	Q1
42	On the properties of organic heterostructures prepared with nano-patterned metallic electrode	APPLIED SURFACE SCIENCE,443, pp.592-602	Breazu, C; Socol, M; Preda, N; Matei, E; Rasoga, O; Girtan, M; Mallet, R; Stanculescu, F; Stanculescu, A	4.439	0.627	10.1016/j.apusc.2018.02.103	Q1
43	Combined use of Mossbauer spectroscopy, XPS, HRTEM, dielectric and anelastic spectroscopy for estimating incipient phase separation in lead titanate-based multiferroics	PHYSICAL CHEMISTRY CHEMICAL PHYSICS,20, pp.14652-14663	Craciun, F; Cordero, F; Vasile, BS; Fruth, V; Zaharescu, M; Atkinson, I; Trusca, R; Diamandescu, L; Tanase, LC; Galizia, P; Cernea, M; Galassi, C	3.906	1.078	10.1039/c8cp01456f	Q1
44	Engineering active sites on reduced graphene oxide by hydrogen plasma irradiation: mimicking bifunctional metal/supported catalysts in hydrogenation reactions	GREEN CHEMISTRY,20, pp.2611-2623	Primo, A; Franconetti, A; Magureanu, M; Mandache, NB; Bucur, C; Rizescu, C; Cojocaru, B; Parvulescu, VI; Garcia, H	8.586	1.58	10.1039/c7gc03397d	Q1
45	Thermodynamic, structural and magnetic studies of phase transformations in MnAl nanocomposite alloys	MATERIALS CHARACTERIZATION,140, pp.1-8	Crisan, AD; Vasiliu, F; Nicula, R; Bartha, C; Mercioniu, I; Crisan, O	2.892	0.692	10.1016/j.matchar.2018.03.034	Q1
46	Ferroelectric photovoltaic characteristics of pulsed laser deposited 0.5Ba (Zr <sub>0.2</sub> Ti <sub>0.8</sub> )O <sub>3</sub> -0.5(Ba <sub>0.7</sub> Ca <sub>0.3</sub> )TiO <sub>3</sub> /ZnO heterostructures	SOLAR ENERGY,167, pp.18-23	Silva, JPB; Sekhar, KC; Cortes-Juan, F; Negrea, RF; Kuncser, AC; Connolly, JP; Ghica, C; Moreira, JA	4.374	0.799	10.1016/j.solener.2018.03.072	Q1
47	Gallium incorporation into phosphate based glasses: Bulk and thin film properties	JOURNAL OF THE MECHANICAL BEHAVIOR OF BIOMEDICAL MATERIALS,82, pp.371-382	Stuart, BW; Grant, CA; Stan, GE; Popa, AC; Titman, JJ; Grant, DM	3.239	0.791	10.1016/j.jmbm.2018.03.041	Q1
48	Branch-like NiO/ZnO heterostructures for VOC sensing	SENSORS AND ACTUATORS B-CHEMICAL,262, pp.477-485	Kaur, N; Zappa, D; Ferroni, M; Poli, N; Campanini, M; Negrea, R; Comini, E	5.667	0.787	10.1016/j.snb.2018.02.042	Q1
49	New bio-active, antimicrobial and adherent coatings of nanostructured carbon double-reinforced with silver and silicon by Matrix-Assisted Pulsed Laser Evaporation for medical applications	APPLIED SURFACE SCIENCE,441, pp.871-883	Duta, L; Ristoscu, C; Stan, GE; Husanu, MA; Besleaga, C; Chifiriu, MC; Lazar, V; Bleotu, C; Miculescu, F; Mihailescu, N; Axente, E; Badiceanu, M; Bociaga, D; Mihailescu, IN	4.439	0.627	10.1016/j.apusc.2018.02.047	Q1
50	Large positive linear magnetoresistance in the two-dimensional t(2g) electron gas at the EuO/SrTiO <sub>3</sub> interface	SCIENTIFIC REPORTS,8,7721	Kormondy, KJ; Gao, LY; Li, X; Lu, SR; Posadas, AB; Shen, SD; Tsoi, M; McCartney, MR; Smith, DJ; Zhou, JS; Lev, LL; Husanu, MA; Strocov, VN; Demkov, AA	4.122	1.356	10.1038/s41598-018-26017-z	Q1

No	Title	Journal	Authors	FI	AIS	DOI	Q
51	Photocatalytic activity of wool fabrics deposited at low temperature with ZnO or TiO <sub>2</sub> nanoparticles: Methylene blue degradation as a test reaction	CATALYSIS TODAY,306, pp.251-259	Frunza, L; Diamandescu, L; Zgura, I; Frunza, S; Ganea, CP; Negrița, CC; Enculescu, M; Birzu, M	4.667	0.868	10.1016/j.cattod.2017.02.044	Q1
52	Influence of Mn content on the catalytic properties of Cu(Mn)-Zn-Mg-Al mixed oxides derived from LDH precursors in the total oxidation of methane	CATALYSIS TODAY,306, pp.276-286	Raciulete, M; Layrac, G; Papa, F; Negrița, C; Tichit, D; Marcu, IC	4.667	0.868	10.1016/j.cattod.2017.01.013	Q1
53	Voltammetric and atomic force microscopy characterization of chymotrypsin, trypsin and caspase activities of proteasome	CATALYSIS TODAY,306, pp.287-293	de Jesus, CSH; Paquim, AMC; Diculescu, VC	4.667	0.868	10.1016/j.cattod.2017.01.012	Q1
54	Structure of high-resolution K beta(1,3) x-ray emission spectra for the elements from Ca to Ge	PHYSICAL REVIEW A,97,52505	Ito, Y; Tochio, T; Yamashita, M; Fukushima, S; Vlaicu, AM; Syrocki, L; Slabkowska, K; Weder, E; Polasik, M; Sawicka, K; Indelicato, P; Marques, JP; Sampaio, JM; Guerra, M; Santos, JP; Parente, F	2.909	0.899	10.1103/PhysRevA.97.052505	Q1
55	Hysteretic Characteristics of Pulsed Laser Deposited 0.5Ba(Zr <sub>0.2</sub> Ti <sub>0.8</sub> )O-3-0.5(Ba <sub>0.7</sub> Ca <sub>0.3</sub> )TiO <sub>3</sub> /ZnO Bilayers	ACS APPLIED MATERIALS & INTERFACES,10, pp.15240-15249	Silva, JPB; Wang, J; Koster, G; Rijnders, G; Negrea, RF; Ghica, C; Sekhar, KC; Moreira, JA; Gomes, MJM	8.097	1.634	10.1021/acsaami.8b01695	Q1
56	Antimicrobial Activity of New Materials Based on Lavender and Basil Essential Oils and Hydroxyapatite	NANOMATERIALS,8,291	Predoi, D; Iconaru, SL; Buton, N; Badea, ML; Marutescu, L	3.504	0.696	10.3390/nano8050291	Q1
57	Photoelectrochemical response of carbon dots (CDs) derived from chitosan and their use in electrochemical imaging	MATERIALS HORIZONS,5, pp.423-428	Zhang, DW; Papaioannou, N; David, NM; Luo, H; Gao, H; Tanase, LC; Degousee, T; Samori, P; Sapelkin, A; Fenwick, O; Titirici, MM; Krause, S	13.183	3.148	10.1039/c7mh00784a	Q1
58	Physical-chemical characterization and biological assessment of simple and lithium-doped biological-derived hydroxyapatite thin films for a new generation of metallic implants	APPLIED SURFACE SCIENCE,439, pp.724-735	Popescu, AC; Florian, PE; Stan, GE; Popescu-Pelin, G; Zgura, I; Enculescu, M; Oktar, FN; Trusca, R; Sima, LE; Roseanu, A; Duta, L	4.439	0.627	10.1016/j.apusc.2018.01.008	Q1
59	Influence of cobalt ferrite content on the structure and magnetic properties of (CoFe <sub>2</sub> O <sub>4</sub> ) <sub>x</sub> (SiO <sub>2</sub> -PVA) <sub>(100-x)</sub> nanocomposites	CERAMICS INTERNATIONAL,44, pp.7891-7901	Dippong, T; Cadar, O; Levci, EA; Deac, IG; Diamandescu, L; Barbu-Tudoran, L	3.057	0.437	10.1016/j.ceramint.2018.01.226	Q1
60	Influence of the modulated two-step synthesis of biogenic hydroxyapatite on biomimetic products' surface	APPLIED SURFACE SCIENCE,438, pp.147-157	Miculescu, F; Mocanu, AC; Stan, GE; Miculescu, M; Maidaniuc, A; Cimpean, A; Mitran, V; Voicu, SI; Machedon-Pisu, T; Ciocan, LT	4.439	0.627	10.1016/j.apusc.2017.07.144	Q1
61	Graphene growth by molecular beam epitaxy: an interplay between desorption, diffusion and intercalation of elemental C species on islands	NANOSCALE,10, pp.7396-7406	Presel, F; Tetlow, H; Bignardi, L; Lacovig, P; Tache, CA; Lizzit, S; Kantorovich, L; Baraldi, A	7.233	1.704	10.1039/c8nr00615f	Q1
62	Ambiguous Role of Growth-Induced Defects on the Semiconductor-to-Metal Characteristics in Epitaxial VO <sub>2</sub> /TiO <sub>2</sub> Thin Films	ACS APPLIED MATERIALS & INTERFACES,10, pp.14132-14144	Mihalescu, CN; Symeou, E; Svoukis, E; Negrea, RF; Ghica, C; Teodorescu, V; Tanase, LC; Negrița, C; Giapintzakis, J	8.097	1.634	10.1021/acsaami.8b01436	Q1

No	Title	Journal	Authors	FI	AIS	DOI	Q
63	The adsorption of silicon on an iridium surface ruling out silicene growth	NANOSCALE,10, pp.7085-7094	Satta, M; Lacovig, P; Apostol, N; Dalmiglio, M; Orlando, F; Bignardi, L; Bana, H; Travaglia, E; Baraldi, A; Lizzit, S; Larciprete, R	7.233	1.704	10.1039/c8nr00648b	Q1
64	Strong composition dependence of resistive switching in Ba <sub>1-x</sub> Sr <sub>x</sub> TiO <sub>3</sub> thin films on semiconducting substrates and its thermodynamic analysis	ACTA MATERIALIA,148, pp.419-431	Mohammadmoradi, O; Sen, C; Boni, AG; Pintilie, L; Misirlioglu, IB	6.036	1.673	10.1016/j.actamat.2018.02.015	Q1
65	Bismuth and lead oxides codoped boron phosphate glasses for Faraday rotators	CERAMICS INTERNATIONAL,44, pp.6016-6025	Sava, BA; Boroica, L; Elisa, M; Shikimaka, O; Grabco, D; Popa, M; Barbos, Z; Iordanescu, R; Niculescu, AM; Kuncser, V; Galca, AC; Eftimie, M; Monteiro, RCC	3.057	0.437	10.1016/j.ceramint.2017.12.205	Q1
66	H <sub>2</sub> S sensing mechanism of SnO <sub>2</sub> -CuWO <sub>4</sub> operated under pulsed temperature modulation	SENSORS AND ACTUATORS B-CHEMICAL,259, pp.258-268	Simion, CE; Somacescu, S; Teodorescu, VS; Osiceanu, P; Stanoiu, A	5.667	0.787	10.1016/j.snb.2017.12.027	Q1
67	Synthesis of graphene-based photocatalysts for water splitting by laser-induced doping with ionic liquids	CARBON,130, pp.48-58	del Pino, AP; Gonzalez-Campo, A; Giraldo, S; Peral, J; Gyorgy, E; Logofatu, C; deMello, AJ; Puigmarti-Luis, J	7.082	1.39	10.1016/j.carbon.2017.12.116	Q1
68	Yellow laser potential of cubic Ca <sub>3</sub> (Nb,Ga)(5)O <sub>12</sub> :Dy <sup>3+</sup> and Ca <sub>3</sub> (Li,Nb,Ga)(5)O <sub>12</sub> :Dy <sup>3+</sup> single crystals	JOURNAL OF ALLOYS AND COMPOUNDS,739, pp.806-816	Gheorghe, C; Hau, S; Gheorghe, L; Voicu, F; Greculeasa, M; Enculescu, M; Belikov, KN; Bryleva, EY; Gaiduk, OV	3.779	0.574	10.1016/j.jallcom.2017.12.259	Q1
69	Dense Ge nanocrystals embedded in TiO <sub>2</sub> with exponentially increased photoconduction by field effect	SCIENTIFIC REPORTS,8,4898	Lepadatu, AM; Slav, A; Palade, C; Dascalescu, I; Enculescu, M; Iftimie, S; Lazanu, S; Teodorescu, VS; Ciurea, ML; Stoica, T	4.122	1.356	10.1038/s41598-018-23316-3	Q1
70	Cracks and nanodroplets produced on tungsten surface samples by dense plasma jets	APPLIED SURFACE SCIENCE,434, pp.1122-1128	Ticos, CM; Galatanu, M; Galatanu, A; Luculescu, C; Scurtu, A; Udrea, N; Ticos, D; Dumitru, M	4.439	0.627	10.1016/j.apusc.2017.11.057	Q1
71	Influence of Gd and Pr doping on the properties of ceria: texture, structure, redox behaviour and reactivity in CH <sub>4</sub> /H <sub>2</sub> O reactions in the presence of H <sub>2</sub> S	CATALYSIS SCIENCE & TECHNOLOGY,8, pp.1333-1348	Florea, M; Postole, G; Matei-Rutkovska, F; Urda, A; Neatu, F; Massin, L; Gelin, P	5.365	1.105	10.1039/c7cy02192e	Q1
72	Effect of green body annealing on laser performance of YAG:Nd <sup>3+</sup> ceramics	CERAMICS INTERNATIONAL,44, pp.4487-4490	Yavetskiy, RP; Parkhomenko, SV; Vorona, IO; Tolmachev, AV; Kosyanov, DY; Kuryavyi, VG; Mayorov, VY; Gheorghe, L; Croitoru, G; Enculescu, M	3.057	0.437	10.1016/j.ceramint.2017.11.192	Q1
73	Triggering surface ferroelectric order in Pb(Zr, Ti)O <sub>3</sub> (001) by deposition of platinum	APPLIED SURFACE SCIENCE,432, pp.27-33	Bucur, IC; Tanase, LC; Abramiuc, LE; Lungu, GA; Chirila, C; Trupina, L; Apostol, NG; Costescu, RM; Negrea, RF; Pintilie, L; Teodorescu, CM	4.439	0.627	10.1016/j.apusc.2017.04.238	Q1
74	Spherical cobalt/cobalt oxide - Carbon composite anodes for enhanced lithium-ion storage	ELECTROCHIMICA ACTA,264, pp.191-202	Patrinoiu, G; Etacheri, V; Somacescu, S; Teodorescu, VS; Birjega, R; Culita, DC; Hong, CN; Calderon-Moreno, JM; Pol, VG; Carp, O	5.116	0.832	10.1016/j.electacta.2018.01.098	Q1

No	Title	Journal	Authors	FI	AIS	DOI	Q
75	Thermophysical properties of Cu-ZrO <sub>2</sub> composites as potential thermal barrier materials for a DEMO W-monoblock divertor	FUSION ENGINEERING AND DESIGN,127, pp.179-184	Galatanu, M; Enculescu, M; Galatanu, A	1.437	0.281	10.1016/j.fusengdes.2018.01.011	Q1
76	CdS/ZnS-doped silico-phosphate films prepared by sol-gel synthesis	JOURNAL OF NON-CRYSTALLINE SOLIDS,481, pp.435-440	Rusu, MI; Stefan, CR; Elisasa, M; Feraru, ID; Vasiliu, IC; Bartha, C; Trusca, RD; Vasile, E; Peretz, S	2.488	0.427	10.1016/j.jnoncrysol.2017.11.025	Q1
77	Impact of thickness variation on structural, dielectric and piezoelectric properties of (Ba, Ca) (Ti, Zr)O-3 epitaxial thin films	SCIENTIFIC REPORTS,8,2056	Ion, V; Craciun, F; Scarioreanu, ND; Moldovan, A; Andrei, A; Birjega, R; Ghica, C; Di Pietrantonio, F; Cannata, D; Benetti, M; Dinescu, M	4.122	1.356	10.1038/s41598-018-20149-y	Q1
78	Enhanced UV- and visible-light driven photocatalytic performances and recycling properties of graphene oxide/ZnO hybrid layers	CERAMICS INTERNATIONAL,44, pp.1826-1835	Gyorgy, E; Logofatu, C; del Pino, AP; Dacu, A; Pascu, O; Ivan, R	3.057	0.437	10.1016/j.ceramint.2017.10.117	Q1
79	Coordination environment of Zn in foraminifera Elphidium aculeatum and Quinqueloculina seminula shells from a polluted site	CHEMICAL GEOLOGY,477, pp.100-111	de Giudici, G; Meneghini, C; Medas, D; Buosi, C; Zuddas, P; Iadecola, A; Mathon, O; Cherchi, A; Kuncser, AC	3.57	1.56	10.1016/j.chemgeo.2017.12.009	Q1
80	Dielectric properties of a bisimidazolium salt with dodecyl sulfate anion doped with carbon nanotubes	BEILSTEIN JOURNAL OF NANOTECHNOLOGY,9, pp.164-174	Maximean, DM; Circu, V; Ganea, CP	2.968	0.745	10.3762/bjnano.9.19	Q1
81	Material parameters from frequency dispersion simulation of floating gate memory with Ge nanocrystals in HfO <sub>2</sub>	APPLIED SURFACE SCIENCE,428, pp.698-702	Palade, C; Lepadatu, AM; Slav, A; Lazanu, S; Teodorescu, VS; Stoica, T; Ciurea, ML	4.439	0.627	10.1016/j.apusc.2017.09.038	Q1
82	Influence of In-Gap States on the Formation of Two-Dimensional Election Gas at ABO(3)/SrTiO <sub>3</sub> Interfaces	SCIENTIFIC REPORTS,8,195	Li, CJ; Xue, HX; Qu, GL; Shen, SC; Hong, YP; Wang, XX; Liu, MR; Jiang, WM; Badica, P; He, L; Dou, RF; Xiong, CM; Lu, WM; Nie, JC	4.122	1.356	10.1038/s41598-017-18583-5	Q1
83	Surface States- and Field-Effects at GaAs(100) Electrodes in Sodium Dodecyl Sulfate Acid Solution	JOURNAL OF THE ELECTROCHEMICAL SOCIETY,165, pp.H3008-H3017	Enache, M; Negrila, C; Anastasescu, M; Dobrescu, G; Lazarescu, MF; Lazarescu, V	3.662	0.726	10.1149/2.0031804jes	Q1
84	Effect of Li doping on the electric and pyroelectric properties of ZnO thin films	APPLIED SURFACE SCIENCE,427, pp.29-37	Trinca, LM; Galca, AC; Boni, AG; Botea, M; Pintilie, L	4.439	0.627	10.1016/j.apusc.2017.08.009	Q1
85	X-ray Crystal Structure, Geometric Isomerism, and Antimicrobial Activity of New Copper(II) Carboxylate Complexes with Imidazole Derivatives	MOLECULES,23,3253	Vlaicu, ID; Borodi, G; Scaeteanu, GV; Chifiriu, MC; Marutescu, L; Popa, M; Stefan, M; Mercioniu, IF; Maurer, M; Daniluc, CG; Olar, R; Badea, M	3.098	0.631	10.3390/molecules23123253	Q2
86	Zinc incorporation in marine bivalve shells grown in mine-polluted seabed sediments: a case study in the Malfidano mining area (SW Sardinia, Italy)	ENVIRONMENTAL SCIENCE AND POLLUTION RESEARCH,25, pp.36645-36660	Medas, D; Carlomagno, I; Meneghini, C; Aquilanti, G; Araki, T; Bedolla, DE; Buosi, C; Casu, MA; Gianoncelli, A; Kuncser, AC; Maraloiu, VA; De Giudici, G	2.8	0.557	10.1007/s11356-018-3504-y	Q2
87	Functional properties improvement of Ag-ZnO thin films using Inconel 600 interlayer produced by electron beam evaporation technique	THIN SOLID FILMS,667, pp.76-87	Lungu, MV; Sobetkii, A; Sobetkii, AA; Patroi, D; Prioteasa, P; Ion, I; Negrila, CC; Chifiriu, MC	1.939	0.356	10.1016/j.tsf.2018.09.055	Q2

No	Title	Journal	Authors	FI	AIS	DOI	Q
88	Adsorption of Pb (II) Ions onto Hydroxyapatite Nanopowders in Aqueous Solutions	MATERIALS,11,2204	Iconaru, SL; Motelica-Heino, M; Guegan, R; Beuran, M; Costescu, A; Predoi, D	2.467	0.625	10.3390/ma11112204	Q2
89	Cationic Substitutions in Hydroxyapatite: Current Status of the Derived Biofunctional Effects and Their In Vitro Interrogation Methods	MATERIALS,, pp.-	Tite, T; Popa, AC; Balescu, LM; Bogdan, IM; Pasuk, I; Ferreira, JMF; Stan, GE	2.467	0.625		Q2
90	Development of Zinc-Doped Hydroxyapatite by Sol-Gel Method for Medical Applications	MOLECULES,23,2986	Negrila, CC; Predoi, MV; Iconaru, SL; Predoi, D	3.098	0.631	10.3390/molecules23112986	Q2
91	From Glucose Direct to Succinic Acid: an Optimized Recyclable Bi-functional Ru@MNP-MWCNT Catalyst	TOPICS IN CATALYSIS,61, pp.1866-1876	Podolean, I; Cojocaru, B; Garcia, H; Teodorescu, C; Parvulescu, VI; Coman, SM	2.439	0.603	10.1007/s11244-018-1012-4	Q2
92	Organometallic compounds for photovoltaic applications	INORGANICA CHIMICA ACTA,483, pp.448-453	Ciobotaru, IC; Polosan, S; Ciobotaru, CC	2.264	0.292	10.1016/j.ica.2018.08.042	Q2
93	Crystal growth and structural characterization of Sm <sup>3+</sup> , Pr <sup>3+</sup> and Dy <sup>3+</sup> - doped CNGG and CLNGG single crystals	OPTICAL MATERIALS,84, pp.335-338	Gheorghe, L; Greculeasa, M; Voicu, F; Gheorghe, C; Hau, S; Vlaicu, AM; Belikov, KN; Bryleva, EY; Gaiduk, OV	2.32	0.403	10.1016/j.optmat.2018.07.029	Q2
94	Thermal analysis, microstructure and impurity phases evolution in Fe <sub>14</sub> Cr ferritic steel powders ball-milled in air and under an argon atmosphere	JOURNAL OF THERMAL ANALYSIS AND CALORIMETRY,134, pp.463-474	Mihalache, V; Mercioniu, I; Aldica, G; Pasuk, I	2.209	0.279	10.1007/s10973-018-7274-z	Q2
95	Thermal, spectral and biological investigation of new nickel complexes with imidazole derivatives	JOURNAL OF THERMAL ANALYSIS AND CALORIMETRY,134, pp.503-512	Vlaicu, ID; Olar, R; Scaeteanu, GV; Silvestro, L; Maurer, M; Stanica, N; Badea, M	2.209	0.279	10.1007/s10973-018-7133-y	Q2
96	Vortex dynamics driven by AC magnetic field in YBCO thin films with complex pinning structures	SUPERCONDUCTOR SCIENCE & TECHNOLOGY,31,105012	Ivan, I; Ionescu, AM; Sandu, V; Crisan, A; Miu, L	2.861	0.821	10.1088/1361-6668/aadbfd	Q2
97	Electric and magnetic properties of ferromagnetic/piezoelectric bilayered composite	JOURNAL OF MATERIALS SCIENCE,53, pp.14160-14171	Cernea, M; Vasile, BS; Surdu, VA; Trusca, R; Bartha, C; Craciun, F; Galassi, C	2.993	0.554	10.1007/s10853-018-2673-x	Q2
98	Effects of a surfactant on the morphology and photocatalytic properties of polycrystalline Fe-doped ZnO powders	JOURNAL OF PHYSICS AND CHEMISTRY OF SOLIDS,121, pp.319-328	Diamandescu, L; Cernea, M; Trusca, R; Enculescu, M; Tanase, L; Baibarac, M; Feder, M; Nicoara, AI; Popescu, T	2.207	0.371	10.1016/j.jpccs.2018.05.041	Q2
99	Edge-state mechanism for the anomalous quantum Hall effect in a diatomic square lattice	PHYSICAL REVIEW B,98,125403	Ostahie, B; Nita, M; Aldea, A	3.813	1.142	10.1103/PhysRevB.98.125403	Q2
100	Synthesis and Characterization of Chitosan-Coated Cobalt Ferrite Nanoparticles and Their Antimicrobial Activity	JOURNAL OF INORGANIC AND ORGANOMETALLIC POLYMERS AND MATERIALS,28, pp.1932-1941	Gingasu, D; Mindru, I; Patron, L; Ianculescu, A; Vasile, E; Marinescu, G; Preda, S; Diamandescu, L; Oprea, O; Popa, M; Saviuc, C; Chifiriuc, MC	1.754	0.196	10.1007/s10904-018-0870-3	Q2
101	Effect of mixing complexing agents on the properties of electrodeposited CZTS thin films	OPTICAL MATERIALS,83, pp.252-256	Zaki, MY; Nouneh, K; Touhami, ME; Belakhmima, RA; Galca, AC; Pintilie, L; Enculescu, M; Baibarac, M; Taibi, M	2.32	0.403	10.1016/j.optmat.2018.06.030	Q2

No	Title	Journal	Authors	FI	AIS	DOI	Q
102	Production and annealing of the paramagnetic defects in as-grown and oxygen doped floating zone silicon irradiated with high fluence 3.5 MeV and 27 MeV electrons	MATERIALS SCIENCE IN SEMI-CONDUCTOR PROCESSING,83, pp.1-11	Joita, AC; Nistor, SV	2.593	0.379	10.1016/j.mssp.2018.04.003	Q2
103	Removal of Zinc Ions Using Hydroxyapatite and Study of Ultrasound Behavior of Aqueous Media	MATERIALS,11,1350	Iconaru, SL; Motelica-Heino, M; Guegan, R; Predoi, MV; Prodan, AM; Predoi, D	2.467	0.625	10.3390/ma11081350	Q2
104	Bioceramic Layers with Antifungal Properties	COATINGS,8,276	Predoi, D; Iconaru, SL; Predoi, MV	2.35	0.51	10.3390/coatings8080276	Q2
105	Investigation of sol-gel derived BaCl <sub>2</sub> :Eu <sup>2+</sup> luminescent nanophosphor and the corresponding PVP@BaCl <sub>2</sub> :Eu <sup>2+</sup> polymer nanocomposite	JOURNAL OF PHYSICS D-APPLIED PHYSICS,51,305302	Secu, CE; Negrila, C; Secu, M	2.373	0.696	10.1088/1361-6463/aace7c	Q2
106	Organic heterostructures obtained on ZnO/Ag/ZnO electrode	VACUUM,154, pp.366-370	Socol, M; Preda, N; Breazu, C; Florica, C; Costas, A; Istrate, CM; Stanculescu, A; Girtan, M; Gherendi, F	2.067	0.36	10.1016/j.vacuum.2018.05.039	Q2
107	Study of point-and cluster-defects in radiation-damaged silicon	NUCLEAR INSTRUMENTS & METHODS IN PHYSICS RESEARCH SECTION A-ACCELERATORS SPECTROMETERS DETECTORS AND ASSOCIATED EQUIPMENT,898, pp.15-23	Donegani, EM; Fretwurst, E; Garutti, E; Klanner, R; Lindstroem, G; Pintilie, I; Radu, R; Schwandt, J	1.336	0.394	10.1016/j.nima.2018.04.051	Q2
108	An X-ray photoelectron spectroscopy depth profile study on the InGeNi/(110) cleaved GaAs structure	MATERIALS SCIENCE IN SEMI-CONDUCTOR PROCESSING,82, pp.62-66	Negrila, CC; Lazarescu, MF; Logofatu, C; Ghita, RV; Cotirlan, C	2.593	0.379	10.1016/j.mssp.2018.02.022	Q2
109	Photoanode for solar water oxidation based on titania and hematite films	THIN SOLID FILMS,658, pp.7-11	Sima, M; Vasile, E; Sima, A	1.939	0.356	10.1016/j.tsf.2018.05.019	Q2
110	Characterization of Surface and Interface of Fe-C Steel Under Electrolytic Galvanization	Proceedings of the Romanian Academy Series A-Mathematics Physics Technical Sciences Information Science,19, Pp.423-430	Bibicu, I; Bulea, C; Diamandescu, L; Rus, V; Popescu, T; Mercioniu, I	1.752	0.251		Q2
111	Osteoblast Cell Response to Naturally Derived Calcium Phosphate-Based Materials	MATERIALS,11,1097	Mitran, V; Ion, R; Miculescu, F; Necula, MG; Mocanu, AC; Stan, GE; Antoniac, IV; Cimpean, A	2.467	0.625	10.3390/ma11071097	Q2
112	Theoretical investigation of the structural, optical and magnetic properties of Mn doped and (Mn, Cr) co-doped CdS in its cubic structure	MATERIALS CHEMISTRY AND PHYSICS,213, pp.249-258	Aimouch, DE; Meskine, S; Birsan, A; Kuncser, V; Zaoui, A; Boukourt, A	2.21	0.421	10.1016/j.matchemphys.2018.03.089	Q2
113	On the hydrophilicity of Ni-doped TiO <sub>2</sub> thin films. A study by X-ray absorption spectroscopy	THIN SOLID FILMS,657, pp.42-49	Macovei, D; Tiron, V; Adomnitei, C; Luca, D; Dobromir, M; Antohe, S; Mardare, D	1.939	0.356	10.1016/j.tsf.2018.04.045	Q2

No	Title	Journal	Authors	FI	AIS	DOI	Q
114	Synthesis and characterization of novel ferrite-piezoelectric multi-ferroic core-shell-type structure	JOURNAL OF MATERIALS SCIENCE,53, pp.9650-9661	Cernea, M; Vasile, BS; Ciuchi, IV; Surdu, VA; Bartha, C; Iuga, A; Galizia, P; Galassi, C	2.993	0.554	10.1007/s10853-018-2264-x	Q2
115	Annealing-Induced High Ordering and Coercivity in Novel L1(0) CoPt-Based Nanocomposite Magnets	METALS,8,466	Crisan, AD; Vasiliu, F; Merconiu, I; Bartha, C; Enculescu, M; Crisan, O	1.704	0.35	10.3390/met8060466	Q2
116	Structure and magnetic behavior of unpredictable EE-azide bridged tetranuclear Mn(II) complex with ONO-donor hydrazone ligand and its transformation to dinuclear Mn(III) complex	POLYHEDRON,147, pp.142-151	Bikas, R; Kuncser, V; Sanchiz, J; Schinteie, G; Siczek, M; Hosseini-Monfared, H; Lis, T	2.067	0.276	10.1016/j.poly.2018.03.019	Q2
117	Strain induced magnetism and superexchange interaction in Cr substituted nanocrystalline cobalt ferrite	MATERIALS CHEMISTRY AND PHYSICS,211, pp.54-64	Kumar, L; Kumar, P; Kuncser, V; Greculeasa, S; Sahoo, B; Kar, M	2.21	0.421	10.1016/j.matchemphys.2018.02.008	Q2
118	Incipient low-temperature formation of MAX phase in Cr-Al-C films	JOURNAL OF ADVANCED CERAMICS,7, pp.143-151	Crisan, O; Crisan, AD	1.605	0.346	10.1007/s40145-018-0265-5	Q2
119	Phase change cellular automata modeling of GeTe, GaSb and SnSe stacked chalcogenide films	MODELLING AND SIMULATION IN MATERIALS SCIENCE AND ENGINEERING,26,45006	Mihai, C; Velea, A	1.793	0.785	10.1088/1361-651X/aab62f	Q2
120	Many-body effects in transport through a quantum-dot cavity system	PHYSICAL REVIEW B,97,195442	Dinu, IV; Moldoveanu, V; Gartner, P	3.813	1.142	10.1103/PhysRevB.97.195442	Q2
121	Properties of Basil and Lavender Essential Oils Adsorbed on the Surface of Hydroxyapatite	MATERIALS,11,652	Predoi, D; Groza, A; Iconaru, SL; Predoi, G; Barbuceanu, F; Guegan, R; Motelica-Heino, MS; Cimpeanu, C	2.467	0.625	10.3390/ma11050652	Q2
122	Production and aging of paramagnetic point defects in P-doped floating zone silicon irradiated with high fluence 27MeV electrons	JOURNAL OF APPLIED PHYSICS,123,161531	Joita, AC; Nistor, SV	2.176	0.561	10.1063/1.4998518	Q2
123	Effect of electron injection on defect reactions in irradiated silicon containing boron, carbon, and oxygen	JOURNAL OF APPLIED PHYSICS,123,161576	Makarenko, LF; Lastovskii, SB; Yakushevich, HS; Moll, M; Pintilie, I	2.176	0.561	10.1063/1.5010965	Q2
124	Kinetics of cluster-related defects in silicon sensors irradiated with monoenergetic electrons	JOURNAL OF APPLIED PHYSICS,123,161402	Radu, R; Pintilie, I; Makarenko, LF; Fretwurst, E; Lindstroem, G	2.176	0.561	10.1063/1.5011372	Q2
125	Filling in the voids of electrospun hydroxypropyl cellulose network: Dielectric investigations	EUROPEAN PHYSICAL JOURNAL PLUS,133,159	Maximean, DM; Danila, O; Ganea, CP; Almeida, PL	2.24	0.406	10.1140/epjp/i2018-11997-8	Q2
126	One-Pot Enzymatic Production of Lignin-Composites	FRONTIERS IN CHEMISTRY,6,124	Ion, S; Opris, C; Cojocaru, B; Tudorache, M; Zgura, I; Galca, AC; Bodescu, AM; Enache, M; Maria, GM; Parvulescu, VI	4.155	1.237	10.3389/fchem.2018.00124	Q2
127	Defect states and room temperature ferromagnetism in cerium oxide nanopowders prepared by decomposition of Ce-propionate	MATERIALS CHEMISTRY AND PHYSICS,209, pp.121-133	Mihalache, V; Secu, M; Grivel, JC	2.21	0.421	10.1016/j.matchemphys.2018.01.053	Q2

No	Title	Journal	Authors	FI	AIS	DOI	Q
128	Improved Optical and Morphological Properties of Vinyl-Substituted Hybrid Silica Materials Incorporating a Zn-Metalloporphyrin	MATERIALS,11,565	Dudas, Z; Fagadar-Cosma, E; Len, A; Romaszki, L; Almasy, L; Vlad-Oros, B; Dascalu, D; Krajnc, A; Kriechbaum, M; Kuncser, A	2.467	0.625	10.3390/ma11040565	Q2
129	Gold nanoparticles stabilized on SBA-15 functionalized NNN-pincer ligand; highly effective catalyst for reduction of nitroarenes in aqueous medium	CATALYSIS COMMUNICATIONS,108, pp.93-97	Hosseini, SH; Zohreh, N; Alipour, S; Busuioc, C; Negrea, R	3.463	0.596	10.1016/j.catcom.2018.01.002	Q2
130	The Effect of Film Thickness on the Gas Sensing Properties of Ultra-Thin TiO <sub>2</sub> Films Deposited by Atomic Layer Deposition	SENSORS,18,735	Wilson, RL; Simion, CE; Blackman, CS; Carmalt, CJ; Stanoiu, A; Di Maggio, F; Covington, JA	2.475	0.554	10.3390/s18030735	Q2
131	Synthesis and characterization of dextran-coated iron oxide nanoparticles	ROYAL SOCIETY OPEN SCIENCE,5,111525	Predescu, AM; Matei, E; Berbecaru, AC; Pantilimon, C; Dragan, C; Vidu, R; Predescu, C; Kuncser, V	2.504	0.947	10.1098/rsos.171525	Q2
132	1532 nm sensitized luminescence and up-conversion in Yb,Er:YAG transparent ceramics	OPTICAL MATERIALS,77, pp.221-225	Vorona, I; Yavetskiy, RP; Dobrotvorskaya, MV; Doroshenko, AG; Parkhomenko, SV; Tolmachev, AV; Kosyanov, DY; Gheorghe, L; Gheorghe, C; Hau, S; Enculescu, M	2.32	0.403	10.1016/j.optmat.2018.01.038	Q2
133	Wet chemical synthesis of ZnO-CdS composites and their photocatalytic activity	MATERIALS RESEARCH BULLETIN,99, pp.174-181	Zgura, I; Preda, N; Socol, G; Ghica, C; Ghica, D; Enculescu, M; Negut, I; Nedelcu, L; Frunza, L; Ganea, CP; Frunza, S	2.873	0.407	10.1016/j.materresbull.2017.11.013	Q2
134	A Study of Extended Defects in Surface Damaged Crystals	CRYSTALS,8,67	Ferrari, C; Ghica, C; Rotunno, E	2.144	0.416	10.3390/cryst8020067	Q2
135	A Mathematical Account of the NEGF Formalism	ANNALES HENRI POINCARÉ,19, pp.411-442	Cornean, HD; Moldoveanu, V; Pillet, CA	1.74	1.326	10.1007/s00023-017-0638-2	Q2
136	Charge carrier traps in tris-(8-hydroxyquinoline) aluminum	JOURNAL OF LUMINESCENCE,194, pp.91-95	Secu, M; Polosan, S	2.732	0.423	10.1016/j.jlum.2017.10.003	Q2
137	Irradiation of nuclear materials with laser-plasma filaments produced in air and deuterium by terrawatt (TW) laser pulses	JOURNAL OF PHYSICS D-APPLIED PHYSICS,51,25302	Avotina, L; Lungu, M; Dinca, P; Butoi, B; Cojocaru, G; Ungureanu, R; Marcu, A; Luculescu, C; Hapenciuc, C; Ganea, PC; Petjukevics, A; Lungu, CP; Kizane, G; Ticos, CM; Antohe, S	2.373	0.696	10.1088/1361-6463/aa9b0f	Q2
138	Local configurations and atomic intermixing in as-quenched and annealed Fe <sub>1-x</sub> Cr <sub>x</sub> and Fe <sub>1-x</sub> Mox ribbons	PHILOSOPHICAL MAGAZINE,98, pp.1053-1067	Stanciu, AE; Greculeasa, SG; Bartha, C; Schinteie, G; Palade, P; Kuncser, A; Leca, A; Filoti, G; Birsan, A; Crisan, O; Kuncser, V	1.632	0.535	10.1080/14786435.2018.1425556	Q2
139	AC magnetic response of superconducting single crystals exhibiting a second peak on the DC magnetization curves	PHYSICA C-SUPERCONDUCTIVITY AND ITS APPLICATIONS,555, pp.1-6	Miu, L; Ionescu, AM; Miu, D; Petrisor, T; Park, A; Tamegai, T; Crisan, A	1.453	0.331	10.1016/j.physc.2018.10.002	Q3
140	Ultra-High Vacuum Deposition of Pyrene Molecules on Metal Surfaces	PHYSICA STATUS SOLIDI B-BASIC SOLID STATE PHYSICS,255,1800235	Schleicher, S; Borca, B; Rawson, J; Matthes, F; Burgler, DE; Kogerler, P; Schneider, CM	1.729	0.412	10.1002/pssb.201800235	Q3

No	Title	Journal	Authors	FI	AIS	DOI	Q
141	Investigation of the interactions of PVDF shell films with Ni core submicron wires and AAO matrix	PHYSICA B-CONDENSED MATTER,545, pp.503-509	Sima, M; Baibarac, M; Vasile, E; Sima, M; Schinteie, GA; Kuncser, V	1.453	0.28	10.1016/j.physb.2018.07.015	Q3
142	Synthesis and Mechanical Properties of Polyurea-Based Hybrid Composites for Ballistic Individual Protection	MATERIALE PLASTICE,55, pp.315-319	Petre, R; Zecheru, T; Petrea, N; Ginghina, R; Sandu, S; Muresan, M; Matache, LC; Sava, AC; Neatu, F	1.248	0.066		Q3
143	Flexible organic heterostructures obtained by MAPLE	APPLIED PHYSICS A-MATERIALS SCIENCE & PROCESSING,124,602	Socol, M; Preda, N; Breazu, C; Stanculescu, A; Costas, A; Stanculescu, F; Girtan, M; Gherendi, F; Popescu-Pelin, G; Socol, G	1.604	0.327	10.1007/s00339-018-1960-3	Q3
144	A straightforward route to obtain organic/inorganic hybrid network from bio-waste: Electroless deposition of ZnO nanostructures on eggshell membranes	CHEMICAL PHYSICS LETTERS,706, pp.24-30	Preda, N; Costas, A; Bergegoi, M; Enculescu, I	1.686	0.429	10.1016/j.cplett.2018.05.073	Q3
145	Thermal Stress Effect on the Structure and Properties of Single and Double Stacked Films of GeTe and SnSe	PHYSICA STATUS SOLIDI B-BASIC SOLID STATE PHYSICS,255,1700552	Sava, F; Borca, CN; Galca, AC; Socol, G; Grolimund, D; Mihai, C; Velea, A	1.729	0.412	10.1002/pssb.201700552	Q3
146	A Comparative Study of Ge-Based Organometallic Additions to MgB2	IEEE TRANSACTIONS ON APPLIED SUPERCONDUCTIVITY,28,7000205	Batalu, D; Nakamura, T; Enculescu, M; Popa, S; Pasuk, I; Aldica, G; Ionescu, AM; Badica, P	1.288	0.248	10.1109/TASC.2018.2808366	Q3
147	Alternative valorization of red mud waste as functional materials with catalytic activity for sulfide oxidation in wastewater	INTERNATIONAL JOURNAL OF ENVIRONMENTAL SCIENCE AND TECHNOLOGY,15, pp.895-908	Cruceanu, A; Zavoianu, R; Pavel, OD; Florea, M; Mara, L	2.037	0.374	10.1007/s13762-017-1449-1	Q3
148	The Cu- and Zn-complex-catalyzed methanolysis of the chemical warfare nerve agents soman, sarin, and VX	COMPTES RENDUS CHIMIE,21, pp.339-345	Petrea, N; Petre, R; Pretorian, A; Toader, C; Somoghi, V; Neatu, F; Florea, M; Neatu, S	1.877	0.29	10.1016/j.crci.2017.08.006	Q3
149	Selective catalytic oxidation reaction of p-xylene on manganese-iron mixed oxide materials	COMPTES RENDUS CHIMIE,21, pp.354-361	Nicolae, S; Neatu, F; Florea, M	1.877	0.29	10.1016/j.crci.2017.06.005	Q3
150	Electroluminescence Properties of IrQ(pppy)(2) Dual-Emitter Organometallic Compound in Organic Light-Emitting Devices	JOURNAL OF ELECTRONIC MATERIALS,47, pp.1490-1496	Ciobotaru, CC; Polosan, S; Ciobotaru, IC	1.566	0.302	10.1007/s11664-017-5945-3	Q3
151	Optical Coatings For Eli Experiments Prepared By Laser Ablation	ROMANIAN JOURNAL OF PHYSICS,63,606	Bercea, A; Filipescu, M; Moldovan, A; Brajnicov, S; Colceag, D; Ion, V; Nistor, LC; Zorila, A; Dinescu, M	1.433	0.259		Q3
152	Tuning Wall Thicknesses in Mesoporous Silica Films for Optimization of Optical Anti-Reflective Properties	JOURNAL OF NANOSCIENCE AND NANOTECHNOLOGY,18, pp.100-103	Abdullah, N; Hossain, MSA; Konstantinov, K; Tanabe, H; Matsuura, M; Maekawa, K; Fatehmulla, A; Farooq, WA; Islam, MT; Bando, Y; Kaneti, YV; Yamauchi, Y	1.354	0.156	10.1166/jnn.2018.14558	Q3
153	CoFe <sub>2-x</sub> CrxO <sub>4</sub> ferrites: synthesis, characterization and their catalytic activity	CHEMICAL PAPERS,72, pp.3203-3213	Mindru, I; Gingasu, D; Diamandescu, L; Patron, L; Marinescu, G; Culita, DC; Calderon-Moreno, JM; Preda, S; Oprea, O; Parvulescu, V	0.963	0.204	10.1007/s11696-018-0553-0	Q4

No	Title	Journal	Authors	FI	AIS	DOI	Q
154	Conductivity losses in ferroelectric phase of TGS	JOURNAL OF OPTOELECTRONICS AND ADVANCED MATERIALS,20, pp.676-681	Marinel, D; Alexandru, HV; Ganea, CP	0.39	0.055		Q4
155	Martensitic transformation and related properties of Fe <sub>69.4</sub> Pd <sub>30.6</sub> ferromagnetic shape memory ribbons	JOURNAL OF OPTOELECTRONICS AND ADVANCED MATERIALS,20, pp.701-706	Tolea, F; Sofronie, M	0.39	0.055		Q4
156	Electrochemical Synthesis of the Composites Based on Multi-Wall Carbon Nanotubes and Polypyrrole Doped with Phosphomolybdic Acid Heteropolyanions and Their Vibrational Properties	INTERNATIONAL JOURNAL OF ELECTROCHEMICAL SCIENCE,13, pp.10514-10526	Baibarac, M; Serbschi, C; Stroe, M	1.369	0.231	10.20964/2018.11.07	Q4
157	Ex Situ Spark Plasma Sintering of Short Powder-in-Tube MgB <sub>2</sub> Tapes with Open and Closed Ends	JOURNAL OF SUPERCONDUCTIVITY AND NOVEL MAGNETISM,31, pp.3423-3432	Aldica, G; Burdusel, M; Popa, S; Pasuk, I; Ionescu, AM; Kuncser, A; Badica, P	1.142	0.176	10.1007/s10948-018-4616-9	Q4
158	ORGANIC HETEROSTRUCTURES DEPOSITED BY MAPLE ON PATTERNED AZO ELECTRODES	DIGEST JOURNAL OF NANOMATERIALS AND BIOSTRUCTURES,13, pp.1045-1053	Socol, M; Preda, N; Breazu, C; Rasoga, O; Stanculescu, A; Popescu-Pelin, G; Gherendi, F; Socol, G; Vacareanu, L	0.673	0.143		Q4
159	Performant silver-based biohybrids generated from orange and grapefruit wastes	JOURNAL OF OPTOELECTRONICS AND ADVANCED MATERIALS,20, pp.551-557	Barbinta-Patrascu, ME; Ungureanu, C; Suica-Bunghes, IR; Iordache, AM; Petrovic, SM; Ispas, A; Zgura, I	0.39	0.055		Q4
160	Structural, dielectric and piezoelectric properties of the ferroelectric PZT-BT ceramic compounds	JOURNAL OF OPTOELECTRONICS AND ADVANCED MATERIALS,20, pp.558-565	Miclea, C; Miclea, CF; Amarande, L; Miclea, CT; Cioanher, M	0.39	0.055		Q4
161	Pinning-Induced Vortex-System Disorder at the Origin of the Second Magnetization Peak in Superconducting Single Crystals	JOURNAL OF SUPERCONDUCTIVITY AND NOVEL MAGNETISM,31, pp.2329-2337	Ionescu, AM; Miu, D; Crisan, A; Miu, L	1.142	0.176	10.1007/s10948-017-4487-5	Q4
162	Irreversibility in Rolled Tantalum	JOURNAL OF SUPERCONDUCTIVITY AND NOVEL MAGNETISM,31, pp.2047-2054	Sandu, V; Cimpoiasu, E	1.142	0.176	10.1007/s10948-017-4433-6	Q4
163	Low energy electron irradiation of carbon thin films	MATERIALS RESEARCH EXPRESS,5,55607	Pacala, O; Ciuca, I; Logofatu, C; Polosan, S	1.151	0.239	10.1088/2053-1591/aac472	Q4
164	Hydrogenolysis of lignin over Ru-based catalysts: The role of the ruthenium in a lignin fragmentation process	MOLECULAR CATALYSIS,450, pp.65-76	Verziu, M; Tirsoaga, A; Cojocaru, B; Bucur, C; Tudora, B; Richel, A; Aguedo, M; Samikannu, A; Mikkola, JP	Not Available	Not Available	10.1016/j.mcat.2018.03.004	Q4
165	High temperature thermo-physical properties of SPS-edW-Cu functional gradient materials	MATERIALS RESEARCH EXPRESS,5,26502	Galatanu, M; Enculescu, M; Galatanu, A	1.151	0.239	10.1088/2053-1591/aaa860	Q4
166	Dwell Time Influence on Spark Plasma-Sintered MgB <sub>2</sub>	JOURNAL OF SUPERCONDUCTIVITY AND NOVEL MAGNETISM,31, pp.317-325	Aldica, G; Popa, S; Enculescu, M; Pasuk, I; Ionescu, AM; Badica, P	1.142	0.176	10.1007/s10948-017-4236-9	Q4

No	Title	Journal	Authors	FI	AIS	DOI	Q
167	Ceramic thin films deposited by spin coating as coating for metallic implants	REVISTA ROMANA DE MATERIALE-ROMANIAN JOURNAL OF MATERIALS,48, pp.401-406	Busuioc, C; Constantinoiu, I; Enculescu, M; Beregoi, M; Jinga, SI	0.661	0.07		Q4
168	Modeling issues regarding thermal conductivity of graphene-based nanocomposites	ROMANIAN JOURNAL OF INFORMATION SCIENCE AND TECHNOLOGY,21, pp.82-92	Sandu, T; Gologanu, M; Voicu, R; Boldeiu, G; Moagar-Poladian, V	0.288	0.082		Q4
169	Low temperature formation of 312 phase in Ti-Si-C ternary compound	DIGEST JOURNAL OF NANOMATERIALS AND BIOSTRUCTURES,13, pp.155-162	Crisan, AD; Crisan, O	0.673	0.143		Q4
170	Exploiting surface plasmon resonance in Au/ZnO photocatalysts for the selective oxidation of phenols	ABSTRACTS OF PAPERS OF THE AMERICAN CHEMICAL SOCIETY,255, pp.-	Lin, F; Cojocaru, B; Colaciello, LW; Cadigan, C; Tian, CX; Grecu, M; Xin, HL; Vyas, S; Parvulescu, V; Richards, R	not available	not available		not available
171	New Lasing Regimes of High-beta Nanolasers	2018 IEEE PHOTONICS SOCIETY SUMMER TOPICAL MEETING SERIES (SUM), pp.23-24	Lohof, F; Barzel, R; Gartner, P; Gies, C	not available	not available		not available
172	Intrinsic losses in dielectrics investigated by terahertz spectroscopy	2018 43RD INTERNATIONAL CONFERENCE ON INFRARED, MILLIMETER, AND TERAHERTZ WAVES (IRMMW-THZ), pp.-	Nedelcu, L; Geambasu, CD; Banciu, MG; Mogildea, G; Mogildea, M	not available	not available		not available
173	Structural, Magnetic and Hyperfine Properties of Molybdenum Dioxide-Hematite Mixed Oxide Nanostructures	MRS ADVANCES,3, pp.2887-2892	Trotta, R; Tolea, F; Valeanu, M; Diamandescu, L; Grabias, A; Sorescu, M	not available	not available	10.1557/adv.2018.420	not available
174	Analysis of Pdge-based contact on N-Gasb	7TH INTERNATIONAL CONFERENCE ON STRUCTURAL ANALYSIS OF ADVANCED MATERIALS (ICSAAM 2017),1932,UNSP 030017	Ghita, RV; Negrila, CC; Predoi, D; Trusca, R	not available	not available	10.1063/1.5024167	not available
175	Fabrication and Characterization of Iron Oxide Dextran Composite Layers	7TH INTERNATIONAL CONFERENCE ON STRUCTURAL ANALYSIS OF ADVANCED MATERIALS (ICSAAM 2017),1932,UNSP 030019	Iconaru, SL; Predoi, SA; Beuran, M; Ciobanu, CS; Trusca, R; Ghita, R; Negoii, I; Teleanu, G; Turculeu, SC; Matei, M; Badea, M; Prodan, AM	not available	not available	10.1063/1.5024169	not available

No	Title	Journal	Authors	FI	AIS	DOI	Q
176	Application of Biocompatible Magnetite Nanoparticles for the Removal of Arsenic and Copper from Water	7TH INTERNATIONAL CONFERENCE ON STRUCTURAL ANALYSIS OF ADVANCED MATERIALS (ICSAAM 2017),1932,UNSP 030018	Iconaru, SL; Beuran, M; Turculet, CS; Negoii, I; Tel-eanu, G; Prodan, AM; Motelica-Heino, M; Guegan, R; Ciobanu, CS; Jiga, G; Predoi, D	not available	not available	10.1063/1.5024168	not available
177	Physico-Chemical Characteristics and Antimicrobial Studies of Silver Doped Hydroxyapatite	7TH INTERNATIONAL CONFERENCE ON STRUCTURAL ANALYSIS OF ADVANCED MATERIALS (ICSAAM 2017),1932,UNSP 030034	Predoi, D; Predoi, MV; El Kettani, MEC; Leduc, D; Iconaru, SL; Ciobanu, CS; Buton, N; Petre, CC; Prodan, AM	not available	not available	10.1063/1.5024184	not available
178	The Influence of the Relaxation Time on the Dynamic Hysteresis in Perovskite Solar Cells	MATHEMATICAL MODELING AND COMPUTATIONAL PHYSICS 2017 (MMCP 2017),173,UNSP 03017	Palici, A; Nemnes, GA; Besleaga, C; Pintilie, L; Anghel, DV; Pintilie, I; Manolescu, A	not available	not available	10.1051/epj-conf/201817303017	not available
179	Synthesis and Characterization of Jellified Composites from Bovine Bone-Derived Hydroxyapatite and Starch as Precursors for Robocasting	ACS OMEGA,3, pp.1338-1349	Miculescu, F; Maidaniuc, A; Miculescu, M; Batalu, ND; Ciocoiu, RC; Voicu, SI; Stan, GE; Thakur, VK	not available	not available	10.1021/acsomega.7b01855	not available
180	Exploiting surface plasmon resonance in Au/ZnO photocatalysts for the selective oxidation of phenols	ABSTRACTS OF PAPERS OF THE AMERICAN CHEMICAL SOCIETY,255, pp.-	Lin, F; Cojocar, B; Colaciello, LW; Cadigan, C; Tian, CX; Grecu, M; Xin, HL; Vyas, S; Parvulescu, V; Richards, R	not available	not available		not available
181	New Lasing Regimes of High-beta Nanolasers	2018 IEEE PHOTONICS SOCIETY SUMMER TOPICAL MEETING SERIES (SUM),, pp.23-24	Lohof, F; Barzel, R; Gartner, P; Gies, C	not available	not available		not available

**CONFERENCES**

No.	Name of scientific event	Author
1	Efficiency enhancement of iridium-based organometallic light emitting diodes 18th International Balkan Workshop on Applied Physics and Materials Science-IBWAP 2018", July 10 <sup>th</sup> - 13 <sup>th</sup> 2018, Constanta, Romania (invited lecture)	S. Polosan, I.C. Ciobotaru, C.C. Ciobotaru
2	Sensors and actuators: from functional nanostructures to novel architecture 18th International Balkan Workshop on Applied Physics and Materials Science-IBWAP 2018", July 10 <sup>th</sup> - 13 <sup>th</sup> 2018, Constanta, Romania (invited lecture)	M. Barsan, M. Beregoi, I.C. Ciobotaru, C.C. Ciobotaru, A. Costas, V. Diculescu, A. Enache, I. Enculescu, M. Enculescu, A. Evanghelidis, C. Florica, E. Matei, S. Polosan, N. Preda, M. Apostol, M. Bunea, A. Aldea, D. Crisan, M. Constantinescu, M. Onea
3	High Surface Area Flexible Electrodes for Wearable Devices and Actuators The Fifth Edition of International Conference on Analytical and Nanoanalytical Methods for Biomedical and Environmental Sciences. IC-ANMBES 2018, May 23 <sup>th</sup> -25 <sup>th</sup> 2018, Brasov, Romania. (invited lecture)	Victor C. Diculescu, A. Aldea, M. Beregoi, A. Evanghelidis, I. Enculescu
4	Half-split Dielectric Resonator Antennas Using High-Dielectric Permittivity Barium Neodymium Titanate International Symposium on Fundamentals of Electrical Engineering, ISFEE-2018, 2018, November 1 <sup>th</sup> - 3 <sup>th</sup> , Bucharest, Romania (invited lecture)	Banciu M. G., Militaru N., Nedelcu L., Geambasu D. C., Trupina L., Avadanei O. G
5	Comparative in vitro behavior of bioglass coatings in simulated body media with improved biomimicry The 5 <sup>th</sup> International Conference on Analytical and Nanoanalytical Methods for Biomedical and Environmental Sciences (IC-ANMBES 2018), May 23 <sup>th</sup> -25 <sup>th</sup> 2018, Brasov, Romania (invited lecture)	Stan GE, Popa AC, Husanu MA, Mercioniu I, Ferreira JMF, Fernandes HR, Santos LF
6	Recent developments in the field of epitaxial ferroelectrics 18 <sup>th</sup> International Balkan Workshop on Applied Physics and Materials Science-IBWAP 2018", July 10 <sup>th</sup> - 13 <sup>th</sup> 2018, Constanta, Romania (invited lecture)	L. Pintilie
7	Spectroscopic signature of depletion state in buried hole-doped manganite The 6 <sup>th</sup> International Colloquium „Physics of Materials”, November 15 <sup>th</sup> -16 <sup>th</sup> 2018, Bucharest, Romania (invited lecture)	D.G. Popescu, M.A. Husanu

No.	Name of scientific event	Author
8	Density of adsorbed surface species for cyanophenyls confined to support nano/micropores  The 6 <sup>th</sup> International Colloquium "Physics of Materials (PM 6)", November 15 <sup>th</sup> -16 <sup>th</sup> 2018 Bucharest, Romania. (invited lecture)	L. Frunza, C. P. Ganea, I. Zgura, and A. Schönhals
9	Dielectric spectroscopy in ferroelectric transition of TGS crystals  The 6 <sup>th</sup> International Colloquium "Physics of Materials (Pm 6)", November 15 <sup>th</sup> -16 <sup>th</sup> 2018, Bucharest, Romania. (invited lecture)	H. V. Alexandru, M. Pavelescu, C. P. Ganea, M. Dan
10	Main concerns related to the magnetic activation of nanoparticulates systems  RADIOMAG Annual Action Progress Conference & MC meeting, March 22 <sup>th</sup> -23 <sup>th</sup> , Timisoara, Romania (invited lecture)	V.Kuncser
11	Microstructure and metallurgical phase composition in Fe containing intermetallics by Mössbauer Spectroscopy  8 <sup>th</sup> International Conference on Material Science & Engineering; October 11 <sup>th</sup> -13 <sup>th</sup> 2018, Dunarea de Jos University, Galati, Romania (invited lecture)	V. Kuncser, G. Filoti, P. Palade, G. Schinteie, S. Gre-culeasa, A. Stanciu, C. Locoe, A .Leca, F. Tolea, M. Sofronie, M. Valeanu
12	Biossensor eletroquímico para a avaliação da atividade, inibição com compostos farmacêuticos e detecção do biomarcador proteasoma 20S  SIBAE 2018 - XXIII Congreso de la Sociedad Ibero-Americana de Electroquímica, May 28 <sup>th</sup> -June 11 <sup>th</sup> 2018, Cusco, Peru. (invited lecture)	V.C. Diculescu, M. Barsan, C.S.H. Jesus, A.M. Chiorcea Paquim
13	DNA-based Electrochemical Biosensors on Conductive Electrospun Polymeric Fibers  ISE 2018 - 69th Annual Meeting of the International Society of Electrochemistry, September 1 <sup>st</sup> -8 <sup>th</sup> 2018, Bologna, Italy. (invited lecture)	V. C. Diculescu, M. M. Barsan, T. A. Enache
14	Layer-by-layer label-free biosensor for improved glucose sensing using poly(3,4-ethylenedioxythiophene) conducting polymer  9th Meeting of Division of Analytical Chemistry, March 26 <sup>th</sup> -27 <sup>th</sup> 2018, Porto, Portugal. (invited lecture)	M. David, M.M. Barsan, M. Florescu, C.M.A. Brett
15	Epitaxial growth of ferroelectric thin films and their potential applications  EMS Meeting on Epitaxy, June 18 <sup>th</sup> -23 <sup>rd</sup> 2018, Vienna, Austria (invited paper)	C. Chirila, A. Boni, M. Botea, L. Hrib, L. Trupina, I. Pasuk, R. Negrea, I. Pintilie, L. Pintilie, G.Le Rhun

No.	Name of scientific event	Author
16	Nanowire based field effect transistors: Influence of geometrical properties 7th International Conference NA-NO-structures and nanomaterials SElf-Assembly - NANOSEA 2018", July 2 <sup>th</sup> -6 <sup>th</sup> , Carquerainne, France (invited lecture)	E. Matei, N. Preda, C. Florica, A. Costas, A. Evangelidis, M. Beregoi, M. Enculescu, V. Diculescu, I. Enculescu
17	Biocompatible submicron fibers obtained by electrospinning 7th International Conference NA-NO-structures and nanomaterials SElf-Assembly - NANOSEA 2018", uly 2 <sup>th</sup> -6 <sup>th</sup> , Carquerainne, France (invited lecture)	E. Matei, A. Evangelidis, M. Beregoi, M. Enculescu, V. Diculescu, I. Enculescu
18	Semiconductor nanowire channel field effect transistors Applied Nanotechnology and Nanoscience International Conference, October 22 <sup>th</sup> -24 <sup>th</sup> 2018, Berlin, Germany (invited lecture)	C. Florica, A. Costas, N. Preda, E. Matei, M. Onea, I. Enculescu
19	Electrodeposited ZnO hierarchical nanostructures for photocatalytic applications Applied Nanotechnology and Nanoscience International Conference, 22 <sup>th</sup> -24 <sup>th</sup> 2018, Berlin, Germany (invited lecture)	E. Matei, A. Evangelidis, M. Beregoi, M. Enculescu, I. Enculescu
20	New Flexible Materials for Wearable Biosensors ESEAC 2018-17th International Conference of Electroanalysis, June 3 <sup>rd</sup> -7 <sup>th</sup> 2018 Rodos, Greece (invited lecture)	A. Aldea, M. Beregoi, A. Evangelidis, I. Rau, V.C.Diculescu
21	High Surface Flexible Electrodes for Biomedical Applications ISE 2018-69 <sup>th</sup> Annual Meeting of the International Society of Electrochemistry, September 2 <sup>th</sup> -7 <sup>th</sup> 2018, Bologna, Italy (invited lecture)	A. Aldea, V.C. Diculescu, I. Enculescu, M. Beregoi, A. Evangelidis, I. Rau
22	Recent developments in the field of ferroelectrics for electronic applications E-MRS International Conference Fall 2018, September 17 <sup>th</sup> - 19 <sup>th</sup> 2018, Warsaw, Poland (invited lecture)	Andra Georgia Boni, Cristina Chirila, Luminita Hrib, Lucian Dragos Filip, Lucian Trupina, Iuliana Pasuk, Raluca Negrea, Lucian Pintilie
23	Recent results in the field of epitaxial ferroelectrics 4 <sup>th</sup> International Ceramic, Glass, Porcelain, Enamel, Glaze and Pigment Congress-SERES 2018, Eskisehir, October 10 <sup>th</sup> -12 <sup>th</sup> 2018, Turkey (invited lecture)	L. Pintilie
24	Titanium, GaSb and GaAs substrates in biomaterial coating application EMN Greece Meeting, May 14 <sup>th</sup> -18 <sup>th</sup> 2018, Heraklion, Crete (invited lecture)	R.V. Ghita, D. Predoi, S.L. Iconaru

No.	Name of scientific event	Author
25	Cellular automata model of phase change in stacked chalcogenide films 12th International Conference on Physics of Advanced Materials (ICPAM-12), September 22 <sup>nd</sup> -28 <sup>th</sup> 2018 Heraklion, Greece (invited lecture)	C. Mihaj, A. Velea
26	Evidences for pinning-induced vortex system disordering at the origin of the second magnetization peak ICSM 2018, April 29 <sup>th</sup> - May 5 <sup>th</sup> 2018, Antalya, Turkey (invited lecture)	L. Miu, A. M. Ionescu, A. Crisan, D. Miu, T. Adachi, K. Omori, T. Noji, Y. Koike, A. Park, and T. Tamegai
27	Disappearance of the second magnetization peak in underdoped cuprate and pnictide superconducting single crystals 14th International Workshop on Magnetism & Superconductivity at Nanoscale, June 30 <sup>th</sup> - July 7 <sup>th</sup> 2018, Coma-Ruga, Spain (invited lecture)	L. Miu
28	The study of the Second Magnetization Peak in Superconducting Single Crystals The 7 <sup>th</sup> Conference on Nanomaterials (CN 2018), January 13 <sup>th</sup> -15 <sup>th</sup> 2018, Sanya, China (invited lecture)	V. Sandu
29	Pinning potential in YBa <sub>2</sub> Cu <sub>3</sub> O <sub>7</sub> superconducting films with nanoengineered pinning centres 6 <sup>th</sup> International Conference on Superconductivity and Magnetism (ICSM2018), Beldibi, April 24 <sup>th</sup> - May 5 <sup>th</sup> 2018, Antalya, Turkey (invited lecture)	A. Crisan and L. Miu
30	Nanodots, nanorods and nanolayers: synergetic pinning centres in YBCO superconducting films 14 <sup>th</sup> International Workshop on Magnetism & Superconductivity at the Nanoscale, June 30 <sup>th</sup> - July 7 <sup>th</sup> 2018, Coma-Ruga, Spain (invited lecture)	A. Crisan, A.M. Ionescu, L. Miu
31	Magnetism and magneto-optical effects in rare-earth based amorphous-like Compounds 2 <sup>nd</sup> International Workshop on Magnetic Materials and Nanomaterials, October 1 <sup>st</sup> - 4 <sup>th</sup> 2018, Boumerdes, Algeria (invited lecture)	V. Kuncser, G. Schinteie, N. Iacob, A. Stanciu

No.	Name of scientific event	Author
32	Low-Temperature Formation of MAX Phases of 211 and 312 Symmetry in Cr-Al-C and Ti-Si-C Carbide Ternary Compounds European Advanced Materials Congress EAMC 2018, August 20 <sup>th</sup> - 23 <sup>rd</sup> Stockholm, Sweden (invited lecture)	O. Crisan
33	Static and dynamic properties of magnetite nanoparticles grown in glass matrices The 7 <sup>th</sup> Conference on Nanomaterials (CN 2018), January 13 <sup>rd</sup> -15 <sup>th</sup> 2018, Sanya, China (invited lecture)	V. Sandu,
34	Dynamic Properties of Nanomagnetite Crystallized in Borosilicate Glass, Advanced Materials World Congress (AMWC-2018), February 4 <sup>th</sup> -8 <sup>th</sup> 2018, Singapore, Malaysia (invited lecture)	V. Sandu, V. Kuncser , M. S. Nicolescu , S. Greculeasa , A. Kuncser
35	Preparation and characterization of 1D Ce <sup>3+</sup> -doped BaTiO <sub>3</sub> nanostructures, Electroceramics XVI, July 9 <sup>th</sup> - 12 <sup>th</sup> 2018, Hasselt, Belgium (invited lecture)	A. C. Ianculescu, C. A. Stanciu, R. Trusca, B. S. Vasile, A. I. Nicoara, L. Trupina, M. Cernea
36	Incipient phase separation in lead titanate-based multiferroics revealed by various spectroscopic techniques: impact on ferroelectric and ferromagnetic properties European Conference on Applications of Polar Dielectrics (ECAPD-2018), June 25 <sup>th</sup> - 28 <sup>th</sup> , 2018, Moscow, Russia (invited lecture)	F. Craciun, F. Cordero, B. S. Vasile, V. Fruth, M. Zaharescu, I. Atkinson, N. Stanica, R. Trusca, L. Diamandescu, L. C. Tanase, A. Iuga, P. Galizia, M. Cernea, and C. Galassi
37	Synthesis and characterization of novel lead free multiferroic structures Materials.it 2018, Bologna- Area della Ricerca CNR-Centro Congressi, October 22 <sup>nd</sup> -26 <sup>th</sup> 2018, Bologna, Italy (invited lecture)	M. Cernea, B. S. Vasile, V. A. Surdu, C. Bartha, A. Iuga, P. Galizia, and C. Galassi
38	EPR characterization of doped wide-bandgap semiconductors International Workshop „Nanotechnology: From Materials to Science”, February 15 <sup>th</sup> -16 <sup>th</sup> 2018 Prague, Czech Republic (invited lecture)	M. Stefan
39	Analytical HRTEM characterisation of thin films and nanostructural materials International Workshop „Nanotechnology: From Materials to Science”, February 15 <sup>th</sup> -16 <sup>th</sup> 2018 Prague, Czech Republic (invited lecture)	C. Ghica

No.	Name of scientific event	Author
1	Dye-doped polymer nanofibers fabricated by electrospinning technique  18 <sup>th</sup> International Balkan Workshop on Applied Physics and Materials Science-IBWAP 2018", July 10 <sup>th</sup> – 13 <sup>th</sup> 2018 Constanta, Romania. (oral presentation)	M. Enculescu, A. Evangelidis, I. Enculescu
2	Protein carbonyl electrochemical detection  The Fifth Edition of International Conference on Analytical and Nanoanalytical Methods for Biomedical and Environmental Sciences" IC-ANMBES 2018" May 23 <sup>rd</sup> -25 <sup>th</sup> 2018, Brasov, Romania, (oral presentation)	T.A. Enache, V. Diculescu
3	Physical properties of optimized amorphous Ge-Te alloy thin films for memory applications  18 <sup>th</sup> International Balkan Workshop on Applied Physics and Materials Science, July 10 <sup>th</sup> – 13 <sup>th</sup> 2018, Constanta, Romania (oral presentation)	Galca AC, Besleaga C, Dumitru V, Bucur C, Sava F, Velea A
4	Influence of the concentration of boric acid on the properties of electrodeposited CZTS thin films  18 <sup>th</sup> International Balkan Workshop on Applied Physics and Materials Science, July 10 <sup>th</sup> – 13 <sup>th</sup> 2018, Constanta, Romania. (oral presentation)	Zaki MY, Nouneh K, Ebn Touhami M, Galca AC, Enculescu M, Baibarac M, Pintilie L
5	Characterization and evaluation of biosensor architectures incorporating nanomaterials as sensitive tools for analytical detection of glucose  5 <sup>th</sup> International Conference on Analytical and Nanoanalytical Methods for Biomedical and Environmental Sciences, (IC-ANMBES 2018), May 23 <sup>rd</sup> -25 <sup>th</sup> May, Brasov, Romania. (oral presentation)	M. David, M.M. Barsan, M. Florescu, C.M.A. Brett
6	Printed Monopole Arrowhead Antenna Compared to Microstrip Rectangular Antenna on High Dielectric Constant Substrate  International Symposium on Fundamentals of Electrical Engineering, ISFEE-2018, 2018, November 1 <sup>st</sup> - 3 <sup>rd</sup> Bucharest, Romania. (oral presentation)	Banciu M.G., Ion V., Nedelcu L., Geambasu D.C., Trupina L., Besleaga-Stan C., Scarisoreanu N.D.
7	Photosensing of Ge-TiO <sub>2</sub> nanocrystalline films assisted by gating and surface photovoltage  Expert evaluation and Control of Compounds of Semiconductor Materials and Technologies, May 16 <sup>th</sup> -18 <sup>th</sup> 2018, Bucharest, Romania. (oral presentation)	C. Palade, A.-M. Lepadatu, A. Slav, I. Dascalescu, M. Enculescu, S. Iftimie, S. Lazanu, V. S. Teodorescu, T. Stoica, and M. L. Ciurea

No.	Name of scientific event	Author
8	GeSn nanocrystals in GeSn-SiO <sub>2</sub> composite films obtained by magnetron sputtering deposition  Expert evaluation and Control of Compounds of Semiconductor Materials and Technologies, May 16 <sup>th</sup> -18 <sup>th</sup> 2018 Bucharest, Romania. (oral presentation)	A. Slav, M. Braic, V.S. Teodorescu, C. Palade, A. Lepadatu, I. Stavarache, M.P. Prepelita, C Logofatu, S. Lazanu, M.L. Ciurea, and T. Stoica
9	Ge NCs in HfO <sub>2</sub> for floating gate dosimeter capacitor  Expert evaluation and Control of Compounds of Semiconductor Materials and Technologies, May 16 <sup>th</sup> -18 <sup>th</sup> 2018 Bucharest, Romania. (oral presentation)	C. Palade, A. Slav, I. Dascalescu, A.-M. Lepadatu, I. Stavarache, T. Stoica, M.L. Ciurea, S. Lazanu
10	Physical parameters of trilayer structures in FG memory based on Ge NCs  18 <sup>th</sup> International Balkan Workshop on Applied Physics and Materials Science, July 10 <sup>th</sup> -13 <sup>th</sup> 2018, Constanta, Romania. (oral presentation)	C. Palade, A. Slav, A.-M. Lepădatu, I. Stăvărache, I. Dăscălescu, O. Cojocar, S. Lazanu, T. Stoica, V. S. Teodorescu, M. L. Ciurea
11	Enhanced broad band photoconductivity in GeSi nanocrystals embedded in oxide films  The sixth edition of the International Colloquium 'Physics of Materials' - PM-6, November 15 <sup>th</sup> -16 <sup>th</sup> 2018, Polytechnic University, Bucharest, Romania. (oral presentation)	M L Ciurea, T Stoica, I Stavarache, C Palade, A Slav, VS Teodorescu, C Logofatu, AM Lepadatu, S Lazanu, IM Dascalescu, O Cojocar
12	Growth and thermal stability of MoS <sub>2</sub> flakes  3 <sup>rd</sup> International workshop on Materials Physics, May 29 <sup>th</sup> -30 <sup>th</sup> 2018, Magurele, Romania. (oral presentation)	T. Stoica, I. Stavarache, G. Aldica, M. Stoica, M. Duchamp, D. Buca, and B. Kardinal
13	World War I - The Beginning of the Chemical Warfare Agents Era and their Impact on Mankind along the last 100 Years  Humboldt Kolleg, September 17 <sup>th</sup> -19 <sup>th</sup> 2018, Bucharest, Romania (oral presentation)	S. Neatu
14	Optical properties of TiO <sub>2</sub> in doped state : the influence of the SiO <sub>2</sub> and silver nanoparticles  18 <sup>th</sup> International Balkan Workshop on Applied Physics and Materials Science July 10 <sup>th</sup> -13 <sup>th</sup> 2018, Bucharest, Romania (oral presentation)	A. Nila, M. Baibarac, A.O. Mateescu, G. Mateescu
15	Activity of inorganic nanoparticiles against fungal isolates colonising buildings includd in the Romanian National Heritage  First Balkan Conference of Medical Mycology and Mycotoxicology (Balkan Fungus 2018) September 13 <sup>th</sup> -15 <sup>th</sup> 2018, Timisoara, Romania (oral presentation)	Alina Sirghi, Irina Gheorghe, Luminita marutescu, Dan Batalu, Petre Badica, Badea Mihaela, Rodica Olar, Omar Sadik, Guath Aldin Aziz, Ionela Avram, ZhiyongZong, Mariana Carmen Chifiriuc

No.	Name of scientific event	Author
16	Kaolin ware discovered at Romula 31 <sup>st</sup> Congress of the Rei Cretariae Romanae Fautores International Association, September 23 <sup>rd</sup> -30 <sup>th</sup> 2018, Cluj-Napoca, Romania (oral presentation)	Mircea Negru, Dan Batalu, Petre Badica
17	Synergetic pinning centers developed at the SrTiO <sub>3</sub> /YBa <sub>2</sub> Cu <sub>3</sub> O <sub>7-x</sub> interface in nanostructured superconducting films 3 <sup>rd</sup> International Workshop on Materials Physics, May 29 <sup>th</sup> -30 <sup>th</sup> 2018, Magurele, Romania (oral presentation)	A. Crisan, A. M. Ionescu, Ion Ivan, L. Miu
18	Specific magnetism and magneto-functionalities in amorphous RE-TM thin films International Workshop on Advances in Nanomaterials, September 17 <sup>th</sup> -19 <sup>th</sup> 2018, NIMP Magurele, Romania, (oral presentation)	V. Kuncser, N.Iacob, G.Schinteie, P.Palade, A.Catrina, A.Stanciu
19	Mesoporous Cobalt Ferrite Nanoparticle Systems: Synthesis, Magnetic and Catalytic Properties IBWAP July 10 <sup>th</sup> -13 <sup>th</sup> 2018, Constanta, Romania, (oral presentation)	C. Comanescu, P. Palade, V. Kuncser
20	Concentration dependent magnetic properties of amorphous Fe-Gd thin films Annual Scientific Session of the Faculty of Physics, University of Bucharest, June 21 <sup>st</sup> -22 <sup>nd</sup> 2018, Bucharest(oral presentation)	A. Stanciu, A. Kuncser, A. Leca, N. Iacob, G. Schinteie, A. Catrina, V. Kuncser
21	Magneto-strictive effects via local atomic configurations in Fe-Dy and Fe-Dy-B amorphous intermetallics Annual Scientific Session of the Faculty of Physics, University of Bucharest June 21 <sup>st</sup> -22 <sup>nd</sup> 2018, Bucharest (oral presentation)	C. Locovei, A. E. Stanciu, A. Leca, N. Iacob, G. Schinteie, V. Kuncser
22	Multifunctional and tunable iron oxide nanoparticles prepared by laser pyrolysis International Workshop on Advances in Nanomaterials, September 17 <sup>th</sup> -19 <sup>th</sup> , 2018, NIMP, Măgurele, România, (oral presentation)	S.G. Greculeasa, P. Palade, G. Schinteie, A. Leca, F. Dumitrache, I. Morjan, A. Badoi, I. Lungu, V. Kuncser
23	Transient transport properties of nano-electrochemical system International Workshop on Advances in Nanomaterials, September 17 <sup>th</sup> -19 <sup>th</sup> , 2018, NIMP, Măgurele, România, (oral presentation)	R. Dragomir
24	Enzyme one-pot system for the construction of artificial lignin-based composites 8 <sup>th</sup> Tokyo Conference on Advanced Catalytic Science and Technology (TOCAT8), August 5 <sup>th</sup> -10 <sup>th</sup> 2018, Yokohama, Japan. (oral presentation)	Tudorache M, Ion S, Opris C, Cojocaru B, Zgura I, Galca AC, Bodescu A, Copolovici L, Enache M, Maria GM, Parvulescu VI

No.	Name of scientific event	Author
25	Functional Polymer Nanofibers Obtained by Electrospinning  Sixth European Conference on Crystal Growth, September 16 <sup>th</sup> -20 <sup>th</sup> , 2018, Varna, Bulgaria (oral presentation)	Enculescu, M, Evanghelidis, A, Enculescu, I
26	Nanocomposite hybrid materials based on carbon nanotubes and poly(methylene blue) films synthesized in deep eutectic solvents for biosensor development  69 <sup>th</sup> Annual Meeting of the International Symposium of Electrochemistry (ISE 2018), September 2 <sup>nd</sup> -7 <sup>th</sup> 2018, Bologna, Italy (oral presentation)	O. Hosu, M.M. Barsan, C. Cristea, R. Sandulescu, C.M.A. Brett
27	Structural, optical, morphological and electrical properties of core-shell nanowires based on ZnO and CuO for energy applications  3 <sup>rd</sup> International Nanotechnology Conference & Expo, May 7 <sup>th</sup> -9 <sup>th</sup> 2018, Rome, Italy (oral presentation)	C. Florica, A. Costas, M. Beregoi, A. Kuncser, N. Apostol, C. Popa, G. Socol, V. Diculescu, N. Preda, I. Enculescu
28	Electrical Properties of Single Core-Shell Radial Heterojunction Nanowires Based on ZnO and CuO  3 <sup>rd</sup> International Nanotechnology Conference & Expo, May 7 <sup>th</sup> -9 <sup>th</sup> 2018, Rome, Italy (oral presentation)	A. Costas, C. Florica, A. Kuncser, N. Apostol, N. Preda, I. Enculescu
29	Ferroelectric thin films epitaxially grown and their potential applications  6 <sup>th</sup> Venice International School on Lasers in Materials Science – SLIMS, July 8 <sup>th</sup> -15 <sup>th</sup> 2018, Venice, Italy (oral presentation)	C. Chirila, A. Boni, M. Botea, L. Hrib, L. Trupina, I. Pasuk, R. Negrea, I. Pintilie, L. Pintilie
30	Ge <sub>1-x</sub> Sn <sub>x</sub> nanocrystal formation in (Ge <sub>1-x</sub> Sn <sub>x</sub> ) <sub>1-y</sub> (SiO <sub>2</sub> ) <sub>y</sub> layers obtained by sputtering deposition  1 <sup>st</sup> Joint ISTDM / ICSI 2018 Conference, May 27 <sup>th</sup> - 31 <sup>st</sup> 2018, Potsdam, Germany (oral presentation)	T. Stoica, M. Braic, V.S. Teodorescu, A. Slav, C. Palade, I. Stavarache, M.P. Prepelita, A. Lepadatu, S. Lazanu, M.L. Ciurea, I. Povstugar, D. Stange, D. Grützmacher, D. Buca
31	Doped ceria materials prepared by modified precipitation route for fuel cells fed with biogas  7 <sup>th</sup> EuCheMS Chemistry Conference, August 26 <sup>th</sup> -30 <sup>th</sup> 2018, Liverpool, UK (oral presentation)	M. Florea, F. Neatu, S. Neatu, A. Urda, F. Matei-Rutkowska, G. Postole, L. Massin, P. Gelin
32	Study of phase change in stacked chalcogenide films  12 <sup>th</sup> International Conference on Physics of Advanced Materials (ICPAM-12), September 22 <sup>nd</sup> -28 <sup>th</sup> 2018, Heraklion, Greece (oral presentation)	A. Velea, F. Sava, C. Borca, G. Socol, A. C. Galca, C. Mihai, D. Grolimund

No.	Name of scientific event	Author
33	Nature of the second magnetization peak in superconducting single crystals 8 <sup>th</sup> Forum on New Materials, June 10 <sup>th</sup> -16 <sup>th</sup> 2018, Perugia, Italy (oral presentation)	L. Miu
34	High vortex activation energies in the AC magnetic response of superconducting films and coatings Materials Science and Engineering, MSE 2018, September 25 <sup>th</sup> -29 <sup>th</sup> 2018, Darmstadt, Germany (oral presentation)	L. Miu
35	Passive magnetic shielding by machinable MgB2 bulks 4 <sup>th</sup> edition of SuperFox Conference on Superconductivity and Functional Oxides, September 13 <sup>th</sup> -15 <sup>th</sup> 2018, Salerno, Italy (oral presentation)	L. Gozzelino, R. Gerbaldo, G. Ghigo, F. Laviano, D. Torsello, V. Bonino, M. Truccato, D. Batalu, M. Grigoroșcuta, M. Burdusel, G. Aldica, P. Badica.
36	Passive magnetic shielding by machinable MgB2 bulks: measurements and numerical simulations 6 <sup>th</sup> International Workshop on numerical modelling of high-temperature superconductors, June 26 <sup>th</sup> -29 <sup>th</sup> 2018, Caparica, Portugal (oral presentation)	L. Gozzelino, R. Gerbaldo, G. Ghigo, F. Laviano, D. Torsello, V. Bonino, M. Truccato, D. Batalu, M. Grigoroșcuta, M. Burdusel, G. Aldica, P. Badica.
37	Orientation control of Bi2Sr2CaCu2O8 thin films by MOCVD HTSHFF 2018, June 5 <sup>th</sup> -8 <sup>th</sup> , 2018, Yamagata, Japan (oral presentation)	K. Endo, S. Arisawa, P. Badica
38	Up conversion of Yb/Er-co-doped CeO2 films on silicon solar cell for enhanced power efficiency Science and Applications of Thin Films, Conference and Exhibition (SATF 2018), Cesme, September 17 <sup>th</sup> -21 <sup>st</sup> 2018, Izmir, Turkey (oral presentation)	M.A. Grigoroșcuta, M. Secu, L. Trupina, M. Enculescu, C. Besleaga, I. Pintilie, P. Badica
39	High quality epitaxial non-c axis thin films of Bi2Sr2CaCu2O8+δ, Science and Applications of Thin Films Science and Applications of Thin Films, Conference and Exhibition (SATF 2018), Cesme, September 17 <sup>th</sup> -21 <sup>st</sup> 2018, Izmir, Turkey (oral presentation)	K. Endo, S. Arisawa, P. Badica
40	Recycling of Roman bricks from Romula HERITAGE 2018 6 <sup>th</sup> International Conference on Heritage and Sustainable Development, June 12 <sup>th</sup> -15 <sup>th</sup> 2018, Granada, Spain (oral presentation)	Mircea Negru, Dan Batalu, Petre Badica, Florica Mișuț, Ingrid Poll

No.	Name of scientific event	Author
41	Spark Plasma Sintered MgB <sub>2</sub> co-added with c-BN and Ge <sub>2</sub> C <sub>6</sub> H <sub>10</sub> O <sub>7</sub> Workshop Coherent Superconducting Hybrids and Related Materials, March 26 <sup>th</sup> -29 <sup>th</sup> 2018 France (Les Arcs 1800) (oral presentation)	A. M. Ionescu, P. Badica, G. Aldica, A. Crisan, L. Miu
42	Transitions of Nanosized Magnetite in Glass-Ceramics International Congress on Technology-Engineering & Science-ICONTEs 2018, February 1 <sup>st</sup> -3 <sup>rd</sup> 2018, Kuala Lumpur, Malaysia (oral presentation)	V. Sandu, V. Kuncser, M. S. Nicolescu, S. Greculeasa, A. Kuncser
43	YBa <sub>2</sub> Cu <sub>3</sub> O <sub>7-x</sub> Superconducting Thin Films with Nanostructured Synergetic Pinning Centers grown by PLD International Conference "Science and Applications of Thin Films", September 16 <sup>th</sup> -22 <sup>th</sup> 2018, Cesme, Izmir, Turkey (oral presentation)	A. Crisan, A.M. Ionescu, L. Miu
44	Anomalous Vortex Dynamics in Isovalent Optimally Doped Pnictide Superconductor BaFe <sub>2</sub> (As <sub>0.68</sub> P <sub>0.32</sub> ) <sub>2</sub> revealed by AC and DC magnetic measurements „School on Quantum Materials for Nanoscale Coherent Quantum Devices and Workshop on Vortex Behavior in Unconventional Superconductors”, COST Action CA16218 „Nanoscale Coherent Hybrid Devices for Superconducting Technologies”, October 7 <sup>th</sup> -13 <sup>th</sup> 2018, Braga, Portugal (oral presentation)	A. Crisan, A.M. Ionescu, L. Miu
45	Vortex Dynamics in Isovalent Optimally Doped Pnictide Superconductor BaFe <sub>2</sub> (As <sub>0.68</sub> P <sub>0.32</sub> ) <sub>2</sub> investigated by AC and DC magnetic measurements 31 <sup>st</sup> International Superconductivity Symposium ISS 2018, December 12 <sup>th</sup> -14 <sup>th</sup> 2018, Tsukuba, Japan (oral presentation)	A. Crisan, A.M. Ionescu, L. Miu
46	Mn influence on phase evolution in FePt-based compounds XIV International Conference on Nanostructured Materials, NANO 2018, June 24 <sup>th</sup> -29 <sup>th</sup> 2018, Hong Kong, China (oral presentation)	O. Crisan, F. Vasiliu, I. Mercioniu, C. Bartha, A.D. Crisan
47	Novel L <sub>10</sub> -based Nanocomposite Magnetic Materials 4 <sup>th</sup> International Conference on Smart Materials Research ICSMR 2018, November 16 <sup>th</sup> -18 <sup>th</sup> 2018, Sydney, Australia (oral presentation)	O. Crisan, P. Palade, F. Vasiliu, I. Mercioniu, A.D. Crisan
48	Transport properties of quantum-dot cavity systems Workshop on "Analytical and Numerical Methods in Quantum Transport", May 27 <sup>th</sup> -31 <sup>th</sup> 2018, Aalborg, Denmark (oral presentation)	V. Moldoveanu

No.	Name of scientific event	Author
1	Organic cation engineering for improved perovskite based solar cells 18 <sup>th</sup> International Balkan Workshop on Applied Physics and Materials Science- IB-WAP 2018 <sup>o</sup> , July 10 <sup>th</sup> – 13 <sup>th</sup> 2018, Constanta, Romania (poster presentation)	L.N. Leonat, A. Tomulescu, V. Stancu, M. Florea, F. Neatu, M. Enculescu, I. Mercioniu, L. Pintilie, I. Pintilie
2	Studies on the enhancement of electrical conductivity in PEDOT:PSS films 18 <sup>th</sup> International Balkan Workshop on Applied Physics and Materials Science- IB-WAP 2018 <sup>o</sup> July 10 <sup>th</sup> – 13 <sup>th</sup> 2018, Constanta, Romania (poster presentation)	L.N. Leonat, F. Neatu, M. Florea, V. Stancu, A. Tomulescu, I. Mercioniu, I. Pintilie
3	Structural, electrical and optical properties of amorphous tin oxide thin films prepared by rf magnetron sputtering 18 <sup>th</sup> International Balkan Workshop on Applied Physics and Materials Science- IB-WAP 2018 <sup>o</sup> July 10 <sup>th</sup> – 13 <sup>th</sup> 2018, Constanta, Romania (poster presentation)	Ziani N, Galca AC, Belkaid MS, Stavarache I, Radu R, Besleaga C, Pintilie I
4	Graphene Based Electrochemical Biosensors for Bio-Medical Applications 3 <sup>rd</sup> International Workshop on Materials Physics, May 29 <sup>th</sup> -30 <sup>th</sup> 2018, Magurele, Romania (poster presentation)	M.M. Barsan
5	Investigation on the attenuation process by plasma on the THz beam International Balkan Workshop of Applied Physics and Materials Science, IBWAP 2018, July 10 <sup>th</sup> -13 <sup>th</sup> 2018, Constanta, Romania (poster presentation)	Mogildea M, Mogildea G, Craciun V, Craciun D, Nedelcu L, Banciu MG, Popa C, Lungu P, Porosnicu C
6	Millimeter wave Terahertz investigations on some dielectric materials International Semiconductor Conference, CAS 2018, October 10 <sup>th</sup> -12 <sup>th</sup> 2018, Sinaia, Romania (poster presentation)	Banciu M.G., Furuya T., Geambasu C. D., Nedelcu L., Pantelica P, Dracea M. D., Ionescu P., Iuga A., Chirila C., Hrib L., Trupina L., Tani M
7	Epitaxial growth of iridium thin film as bottom electrode for high frequency tunable capacitors International Balkan Workshop of Applied Physics and Materials Science, IBWAP 2018, July 10 <sup>th</sup> -13 <sup>th</sup> 2018, Constanta, Romania (poster presentation)	Trupina L., Nedelcu L., Banciu M. G., Boulle A., Huitema L., Madrangeas V., Crunteanu A., Ghalem A., Passerieux D
8	Nanostructured bioactive glass coatings synthesized by pulsed laser deposition onto biodegradable metallic implants The 12 <sup>th</sup> European Symposium on Thermal Analysis and Calorimetry (ESTAC12), August 27 <sup>th</sup> -30 <sup>th</sup> 2018, Brasov, Romania (poster presentation)	Mihailescu N, Sopronyi M, Ficai I, Floroian L, Negut I, Ristoscu C, Stan GE, Ferreira JMF, Mihailescu IN

No.	Name of scientific event	Author
9	Study on conversion methodology for dolomitic marble derived-calcium phosphates and complementary image processing  7 <sup>th</sup> International Conference on Materials Science and Technologies – RoMat 2018, November 15 <sup>th</sup> -18 <sup>th</sup> 2018, Bucharest, Romania (poster presentation)	Mocanu, AC, Miculescu M, Maidaniuc A, Dascalu CA, Antoniac IV, Stan GE, Miculescu F
10	Influence of calcination temperature on the sinterability of fish derived-calcium phosphates  7 <sup>th</sup> International Conference on Materials Science and Technologies – RoMat 2018, November 15 <sup>th</sup> -18 <sup>th</sup> 2018, Bucharest, Romania (poster presentation)	Miculescu M, Boldu LM, Butte TM, Maidanuc A, Mocanu AC, Ciocoiu RC, Stan GE, Miculescu F
11	The effect of different sintering strategies on the characteristics of hydroxyapatite-silver microcomposites  7 <sup>th</sup> International Conference on Materials Science and Technologies – RoMat 2018, November 15 <sup>th</sup> -18 <sup>th</sup> 2018, Bucharest, Romania (poster presentation)	Butte TM, Nitu S, Maidaniuc A, Ciocoiu RC, Miculescu M, Stan GE, Miculescu F
12	Enhanced photocurrent in GeSi NCs / TiO <sub>2</sub> multilayers  International Semiconductor Conference, CAS 2018, October 10 <sup>th</sup> -12 <sup>th</sup> 2018, Sinaia, Romania (poster presentation)	C. Palade, A. Slav, O. Cojocaru, V.S. Teodorescu, S. Lazanu, T. Stoica, M.T. Sultan, H.G. Svavarsson, M.L. Ciurea
13	GeSi nanocrystals in SiO <sub>2</sub> matrix with extended photoresponse in near infrared  International Semiconductor Conference, CAS 2018, October 10 <sup>th</sup> -12 <sup>th</sup> 2018, Sinaia, Romania (poster presentation)	I. Stavarache, L. Nedelcu, V.S. Teodorescu, V.A. Maraloiu, I. Dascalescu, M. L. Ciurea
14	The effect of H <sub>2</sub> /Ar plasma treatment on photoconductivity of Si <sub>1-x</sub> Ge <sub>x</sub> nanocrystals embedded in silicon oxide matrix  International Semiconductor Conference, CAS 2018, October 10 <sup>th</sup> -12 <sup>th</sup> 2018, Sinaia, Romania (poster presentation)	M.T. Sultan, J.T. Gudmundsson, A. Manolescu, M.L. Ciurea, H.G. Svavarsson
15	Enhanced photoconductivity of SiGe-trilayer stack by retrenching annealing conditions  International Semiconductor Conference, CAS 2018, October 10 <sup>th</sup> -12 <sup>th</sup> 2018, Sinaia, Romania (poster presentation)	M.T. Sultan, J.T. Gudmundsson, A. Manolescu, M.L. Ciurea, C. Palade, A.V. Maraloiu, H.G. Svavarsson
16	Band bending at Au/BaTiO <sub>3</sub> and Cu/BaTiO <sub>3</sub> interfaces investigated by XPS  The 6 <sup>th</sup> International Colloquium „Physics of Materials”, November 15 <sup>th</sup> -16 <sup>th</sup> 2018, Bucharest, Romania (poster presentation)	M.A. Husanu, D.G. Popescu

No.	Name of scientific event	Author
17	Functional metasurfaces for localized surface plasmon resonance enhanced angle-resolved evanescent-wave cavity ring-down spectroscopy  18 <sup>th</sup> International Balkan Workshop on Applied Physics and Materials Science, July 11 <sup>th</sup> -14 <sup>th</sup> 2018, Constanta, Romania (poster presentation)	C. Cotirlan-Simioniuc, C.C. Negrila, C. Logofatu
18	Composite materials based on oxide semiconductors and metallic nanoparticles with applications in health  The 6 <sup>th</sup> International Colloquium "Physics of Materials (PM 6)", November 15 <sup>th</sup> -16 <sup>th</sup> 2018, Bucharest, Romania (poster presentation)	I. Zgura, M. E. Barbinta-Patrascu, M. Bacalum, M. Enculescu, N. Preda, C. Istrate, R. Negrea and C.P. Ganea
19	Trends in PDLC devices: carbon nanotubes doping  The 6 <sup>th</sup> International Colloquium "Physics of Materials (PM 6)", November 15 <sup>th</sup> -16 <sup>th</sup> 2018, Bucharest, Romania (poster presentation)	D. Mănăilă-Maximean, V. A. Loiko, V. Cîrcu, P. C. Ganea, A.V. Konkolovich, O. Dănilă, Ana Bărar
20	Thermal analysis on raw materials and Roman bricks from Romula  ESTAC12, the 12 <sup>th</sup> European Symposium on Thermal Analysis and Calorimetry", August 27 <sup>th</sup> -30 <sup>th</sup> 2018, Brasov, Romania (poster presentation)	Gheorghe V. Aldica, Dan Batalu, Mircea Negru, Petre Badica
21	New Polymeric Composite for 3D printing  14 <sup>th</sup> International Symposium PRIOCHEM, October 10 <sup>th</sup> -12 <sup>th</sup> , 2018, Bucharest, Romania (poster presentation)	N. Pons, A. Bunescu, P. Badica, D. Batalu
22	Thermal analysis on raw materials and Roman bricks from Romula  ESTAC12, the 12 <sup>th</sup> European Symposium on Thermal Analysis and Calorimetry", August 27 <sup>th</sup> -30 <sup>th</sup> 2018, Brasov, Romania (poster presentation)	G. Aldica, D. Batalu, M. Negru, P. Badica
23	Magnetoelastic properties in polycrystalline Fe-Pd based ferromagnetic shape memory alloys  8 <sup>th</sup> International Conference on Material Science & Engineering, October 11 <sup>th</sup> -13 <sup>th</sup> 2018, Dunarea de Jos University, Galati, Romania (poster presentation)	F. Tolea, M. Sofronie, B. Popescu, A.D. Crisan, M. Valeanu
24	Effect of Cr, C, B and Mo substitutions on the structure and magnetic properties of Zr-Co Rare-Earth-free magnetic alloy  8 <sup>th</sup> International Conference on Material Science & Engineering, October 11 <sup>th</sup> -13 <sup>th</sup> 2018, Dunarea de Jos University, Galati, Romania. (poster presentation)	F. Tolea, P. Palade, M. Sofronie, B. Popescu, M. Valeanu, V. Kuncser

No.	Name of scientific event	Author
25	Magnetic Properties of CoFeZrSi Compound: First Principle Investigations IBWAP July 10 <sup>th</sup> -13 <sup>th</sup> 2018, Constanta, Romania (poster presentation)	A. Birsan
26	The Effect of Interfacial Distortions on the Half-Metallic Properties in Quaternary Heusler Compounds IBWAP July 10 <sup>th</sup> -13 <sup>th</sup> 2018, Constanta, Romania (poster presentation)	A. Birsan
27	Magnetic Fluid Hyperthermia Related Issues by Numerical Simulations Using Dedicated Softwares IBWAP July 10 <sup>th</sup> -13 <sup>th</sup> 2018, Constanta, Romania (poster presentation)	N. Iacob, A. Kuncser, V. Kuncser
28	Microwave dielectric properties of Ba <sub>2/3</sub> Sr <sub>1/3</sub> TiO <sub>3</sub> ferroelectric thick films IBWAP July 10 <sup>th</sup> -13 <sup>th</sup> 2018, Constanta, Romania (poster presentation)	Nedelcu L., Trupina L., Geambasu C.D., Banciu M.G., Constantinescu C., Passerieux D., Huitema L., Crunteanu A., Dumas-Bouchiat F., Champeaux C
29	Synthesis and properties of C <sub>3</sub> N <sub>2</sub> H <sub>5</sub> PbI <sub>3</sub> powders as precursors for hybride perovskite based solar cells The 7 <sup>th</sup> EuCheMS Chemistry Congress, Molecular frontiers & global challenges, August 26 <sup>th</sup> -30 <sup>th</sup> 2018, ACC Liverpool, UK (poster presentation)	M. Florea, F. Neațu, S. Neațu, C. Mozăceanu, S. Derbali, C. Bartha, L. N. Leonat, A. G. Tomulescu, V. Stancu, V. Toma, I. Pintilie
30	Prion protein: Voltammetric and Scanning Electron Microscopy Characterization 17 <sup>th</sup> International Conference on Electroanalysis, June 3 <sup>rd</sup> -7 <sup>th</sup> 2018, Rhodes, Greece (poster presentation)	TA Enache, M Enculescu, VC Diculescu
31	Electrochemical Sensor for Carbonylated Protein Detection 69 <sup>th</sup> Annual Meeting of the International Society of Electrochemistry, September 2 <sup>nd</sup> -7 <sup>th</sup> 2018 Bologna, Italy (poster presentation)	TA Enache, VC Diculescu
32	Faraday rotators based on dysprosium ions-doped aluminophosphate glass 15 <sup>th</sup> International Conference on Physics of Non-Crystalline Solids and 14 <sup>th</sup> European Society of Glass Conference, July 9 <sup>th</sup> -13 <sup>th</sup> 2018, Saint Malo, France (poster presentation)	Elisa M, Stefan R, Sava B, Boroica L, Valeanu M, Kuncser V, Galca AC, Beldiceanu A

No.	Name of scientific event	Author
33	Effect of the combination of trisodium citrate and multiple complexing agents on the properties of electrodeposited CZTS thin films  3 <sup>rd</sup> International Symposium on Dielectric Materials and Applications (ISyDMA'2018), April 17 <sup>th</sup> -20 <sup>th</sup> 2018. Beni Mellal, Morocco (poster presentation)	Zaki MY, Nouneh K, Ebn Touhami M, Galca AC, Enculescu M, Baibarac M, Pintilie L
34	Pd Doped Magnetic Ni Electrodes as Substrates for Interference-free Enzyme Biosensors  69 <sup>th</sup> Annual Meeting of the International Symposium of Electrochemistry (ISE 2018), September 2 <sup>nd</sup> -7 <sup>th</sup> 2018, Bologna, Italy (poster presentation)	M.M. Barsan, T.A. Enache, V.C. Diculescu
35	A new amperometric 20s proteasome biosensor based on specific antibody-20s interaction  17 <sup>th</sup> International Conference on Electroanalysis" (ESEAC 2018), June 3 <sup>rd</sup> -7 <sup>th</sup> 2018, Rhodes, Greece (poster presentation)	M.M. Barsan, V.C. Diculescu
36	Plasma optical on-off switch for THz radiation  EMRS Spring Meeting, June 18 <sup>th</sup> -22 <sup>nd</sup> 2018, Strasbourg, France (poster presentation)	Mogîldea M, Nedelcu L, Mogîldea G, Craciun D, Banciu MG, Popa C, Mingireanu, F, Craciun V
37	Intrinsic losses in dielectrics investigated by terahertz spectroscopy  43 <sup>th</sup> International Conference on Infrared, Millimeter, and Terahertz Waves, IRM-MW-THz 2018, September 9 <sup>th</sup> -14 <sup>th</sup> 2018, Nagoya, Japan (poster presentation)	Nedelcu L, Geambasu CD, Banciu MG, Mogîldea G, Mogîldea M
38	Lithium-doped biological hydroxyapatite coatings for biomedical applications  EMRS Spring Meeting, June 18 <sup>th</sup> -22 <sup>nd</sup> 2018, Strasbourg, France (poster presentation)	Duta L, Popescu AC, Stan GE, Popescu-Pelin G, Florian PE, Roseanu A, Zgura I, Oktar FN
39	Physico-chemical and biological evaluation of synthetic and lithium-doped biological hydroxyapatite coatings obtained by PLD  EMRS Spring Meeting, June 18 <sup>th</sup> -22 <sup>nd</sup> 2018, Strasbourg, France (poster presentation)	Popescu-Pelin G, Stan G, Ciuca S, Oktar FN, Achim A, Berbecaru A, Duta L
40	Lead-free halide perovskite for field effect thin film transistors  E-MRS Fall Meeting and Exhibit September 17 <sup>th</sup> -20 <sup>th</sup> 2018, Warsaw, Poland (technical sessions).	C. Besleaga, R. Radu, L. Bălescu, V. Stancu, L. Pintilie

No.	Name of scientific event	Author
41	Commercial hydroxyapatite powders for lead removal from aqueous solution  9 <sup>th</sup> International Conference on Times of Polymers and Composites-From Aerospace to Nanotechnology, June 17 <sup>th</sup> -21 <sup>st</sup> , 2018, Ischia, Naples, Italy (poster presentation)	C. C. Negrila, S. L. Iconaru, M. Motelica-Heino, Regis Guegan, G. Predoi, F. Barbuceanu, R. V. Ghita, C. C. Petre, G. Jiga, M. L. Badea, A. M. Prodan, D. Predoi
42	Structural and biological characterization of antimicrobial layers obtained by magnetron sputtering technique  EMN Greece Meeting, May 14 <sup>th</sup> -18 <sup>th</sup> 2018, Heraklion, Crete (poster presentation)	C.C. Negrila, S.L. Iconaru, A. Groza, R.V. Ghita, C.M. Chifiriuc, P. Chapon, S. Gaiaschi, D. Predoi
43	Reduced graphene oxide/transition metal oxide/ urea composite materials for photocatalytic degradation of organic pollutants in aqueous medium  7 <sup>th</sup> International Symposium on Transparent Conductive Materials - TCM 2018, October 14 <sup>th</sup> -19 <sup>th</sup> 2018, Platanias - Chania, Crete, Greece (poster presentation)	R. Ivan, C. Popescu, A. Perez del Pino, C. Logofatu, E. György
44	Steam reforming of methane in the presence of H <sub>2</sub> S on doped ceria materials  4 <sup>th</sup> International Conference on Advanced Complex Inorganic NanoMaterials (ACIN2018), July 14 <sup>th</sup> -21 <sup>st</sup> 2018, Namur, Belgium (poster presentation)	M. Florea, G. Postole, F. Matei-Rutkovska, A. Urda, F. Neațu, L. Massin, P. Gelin
45	Synthesis and properties of C <sub>3</sub> N <sub>2</sub> H <sub>5</sub> PbI <sub>3</sub> powders as precursors for hybride perovskite based solar cells  7 <sup>th</sup> EuCheMS Chemistry Conference, August 26 <sup>th</sup> -30 <sup>th</sup> 2018, Liverpool, UK (poster presentation)	F. Neatu, M. Trandafir, S. Neațu, M. Florea
46	Selective oxidation of aromatic hydrocarbons in the presence of heterogeneous Mn and Co-based catalysts  7 <sup>th</sup> EuCheMS Chemistry Conference, August 26 <sup>th</sup> -30 <sup>th</sup> 2018, Liverpool, UK (poster presentation)	S. Neatu, F. Neatu, M. Florea, M. M. Barsan, N. G. Apostol, T. A. Enache, V. C. Diculescu
47	Effect of dopants on the properties of aromatic derivatives crystals  ECCGS (Sixth European Conference on Crystal Growth), September 16 <sup>th</sup> -20 <sup>th</sup> 2018, Varna, Bulgaria (poster presentation)	A. Stanculescu, M. Socol, O. Rasoga, N. Preda, F. Stanculescu, I. Ionita, C. Breazu, G. Petre
48	Assessment of some new polymeric composites used for 3D printing  18 <sup>th</sup> European Conference on Composite Materials (ECCM 18), June 24 <sup>th</sup> -28 <sup>th</sup> 2018, Athens, Greece (poster presentation)	D. Batalu, A. Bunescu, P. Badica

No.	Name of scientific event	Author
49	Assessment of Antibacterial Behavior of some Polymer Composites used for 3D printing  4 <sup>th</sup> International Conference on Biomedical Polymers & Polymeric Biomaterials (ISBPPB 2018), July 15 <sup>th</sup> - 18 <sup>th</sup> 2018, Krakow, Poland (poster presentation)	D. Batalu, A. Bunescu, M. Popa (Bucur), L. Marutescu, M.C. Chifiriuc, P. Badica
50	In vitro activity of novel inorganic nanoparticles based on halogenated magnesium salts on MRSA cells in planktonic and adherent growth state  28 <sup>th</sup> European Congress of Clinical Microbiology and Infectious Diseases (28 <sup>th</sup> ECCMID), April 21 <sup>st</sup> -24 <sup>th</sup> 2018, Madrid, Spain (poster presentation)	Othman Almahdawy, Petre Badica, Dan Batalu, Irina Gheorghe, Marcela Popa, Omar Sadik, Otilia Banu, Luminita Marutescu, Grigore Mihaescu, Mariana Carmen Chifiriuc
51	Advanced characterization of the Roman brick from Romula  The International Symposium on Inorganic and Environmental Materials 2018 (ISIEM 2018), Ghent University, , June 17 <sup>th</sup> -21 <sup>st</sup> 2018, Ghent, Belgium (poster presentation)	P. Badica et al.
52	Magnetization Relaxation across the Second Magnetization Peak in Iron Based Superconductors  International Conference on Superconductivity and Magnetism, April 29 <sup>th</sup> - May 5 <sup>th</sup> 2018, Turkey , Antalya (poster presentation)	A. M. Ionescu, A. Crisan, and L. Miu
53	The study of the Second Magnetization Peak in Superconducting Single Crystals  School on Quantum Materials for Nanoscale Coherent Quantum Devices October 7 <sup>th</sup> -13 <sup>th</sup> 2018, Bom Jesus- Braga, Portugal (poster presentation)	A. M. Ionescu, A. Crisan, L. Miu
54	Magneto-Optical properties of amorphous Fe-Gd thin films crossing the magnetization compensation point  European School on Magnetism, September 17 <sup>th</sup> -28 <sup>th</sup> 2018 Krakow, Poland (poster presentation)	A.E. Stanciu, A. Kuncser, A. Catrina, A. Leca, N. Iacob, G. Schinteie, V. Kuncser
55	Mapping Twins in B4C using ASTAR Electron Precession System in Transmission Electron Microscope, Electron Microscopy of Nanostructures  ELMINA 2018 Conference, August 27 <sup>th</sup> -29 <sup>th</sup> 2018, Belgrade, Serbia (poster presentation)	A. Kuncser, C. Ghica, O. Vasylykiv, P. Badica, I. Mercioniu



**INTERNATIONAL COLLABORATIONS**

## Large projects

---

*Pintilie I*

**CERN RD50 “Radiation hard semiconductor devices for very high luminosity colliders”** (<http://rd50.web.cern.ch/rd50/>): 48 research institutions from 27 countries around the world

Scientific coordinator of the workpackage “Defect/Material Characterization”

---

### **H2020 și EURATOM**

*Galatanu A*

**EUROfusion Consortium, Grant agreement No. 633053**

2014-2018

---

*Galatanu A*

**EURATOM Enabling Research** “Low-activation cemented carbides for high heat flux applications”, coord Jožef Stefan Institute (JSI), Slovenia, partners INCDFM (Romania), CIEMAT (Spain) și FZJ (Germany).

2017-2018

---

*Galatanu A*

**EUROfusion WPMAT, GA633053** “Romanian participation in the EUROfusion WPMAT and complementary research”

2014-2018

---

*Galatanu A*

**H2020** “Accelerator Research and Innovation for European Science and Society (ARIES)”, GA730871

2017-2021

---

*Pintilie L*

**H2020** “Energy efficient Embedded Non-volatile Memory Logic based on Ferroelectric Hf(Zr)O<sub>2</sub>” GA780302

2018-2021

---

### **Romania-Bulgaria Cross-border projects**

*Galatanu A*

**D-EMERSYS-** “Rapid intervention force to chemical, biological, radiological and nuclear emergencies on the Danube River.” Interreg ro-bg Cod e-MS ROBG - 123 coord INCDFM

2016-2018

---

*Galatanu A*

**JEROME**- “Capabilities and interoperability for joint RO-BG cross-border first responder intervention to chemical-biological-radiological-nuclear-high yield explosive emergencies.” Interreg ro-bg Cod e-MS ROBG - 121 coord INCDFM

2016-2018

---

### **Proiecte COST**

*Pintilie L*

**COST action MP1308 “Towards Oxide-Based Electronics (TO-BE)”** ([http://www.cost.eu/COST\\_Actions/mpns/Actions/MP1308](http://www.cost.eu/COST_Actions/mpns/Actions/MP1308)) Coordinator: Dr Fabio Miletto Granozio (IT)

2014-2018

---

*Ciurea ML*

**COST action HERALD (MP1402) “Hooking together European research in Atomic Layer Deposition (HERALD)”**

([http://www.cost.eu/COST\\_Actions/mpns/MP1402](http://www.cost.eu/COST_Actions/mpns/MP1402))

Coordonator: Dr. Simon Elliott, Ireland

2014-2018

---

*Crisan A*

**COST CA16218 Nanoscale Coherent Hybrid Devices for Superconducting Technologies (NANOCOHYBRI).**

Main representative of Romania in the Management Committee.

2017-2021

---

### **Proiecte ERA-NET**

*Trupina L*

**Integration of new and improved materials for smart millimeter-wave sensors**

**Project M-ERA.NET**

French partner: Universitatea din Limoges, AirMems (SME)

2016 – 2019

---

*Ciurea ML*

**Project M-ERA NET Call 2014**

**PhotoNanoP (High photoconductive oxide films functionalized with GeSi nanoparticles for environmental applications)**

Partners from Romania (IMT, OPTOELECTRONICA- 2001 S.A) and Iceland (Reykjavik University (School of Science and Engineering) - RU-SSE, Pi Technology)

2016-2018

---

*Stoica TS*

**Project M-ERA NET Call 2015**

**GESNAPHOTO (Nano-structured GeSn coatings for photonics)**

Partners from Romania (INOE-2000, OPTOELECTRONICA- 2001 S.A) and Germany (Forschungszentrum Jülich, Peter Grünberg Institute PGI-9, nanoplus Nanosystems and Technologies GmbH)

2016-2019

---

*Vlaicu ID*

**Project M-ERA NET**

Innovative nano-materials and architectures for integrated piezoelectric energy harvesting applications (HarvEnPiez)

Coordinator: Iosef Stefan Institute din Ljubljana, Slovenia

Partners: Institute of Solid State Physics, University of Latvia (ISSP UL), Latvia; National Institute of Materials Physics (NIMP), Romania; Faculty of Electrical Engineering, Power Engineering and Information Technology, (Intelectro Iasi SRL), Romania; Technical University Iasi (TU Iasi), Romania

2016-2019

---

*Badica P*

**COFUND M-ERA.NET II / Contract 74/2017**

Advanced biodegradable materials based on MgB<sub>2</sub> resistant to microbial colonization,

Coordinator: INCDFM

Partners: UPB, UB, U. Torino

2017-2020

---

**C-ERIC**

*Ghica C*

**Graphene for Water in Life Science,**

**CERIC Grant**

Coordinator: Elettra Sincrotrone Trieste

Partners: Technical University Graz (Austria), Charles University Prague (Czech Republic), INCDFM (Romania)

## Other international projects

*Predoi D*

### **Nanoparticles for remedy of contaminated soils**

Project PICS

French partner: Institut des Sciences de la Terre d'Orléans.

---

*Chirila C*

### **Optimised pyroelectric elements on Si wafers for sensing and energy harvesting**

Project IFA-CEA

French partner: CEA Grenoble Laboratory for Micro-Actuators components

2016-2019

---

*Crisan O*

### **Programme Hubert Curien PHC Brancusi**

#### **Surface-functionalized nanostructures for applications in photonics and spin manipulation technologies**

Partner: Laboratoire Léon Brillouin UMR12 CEA-CNRS, Commissariat à l'Énergie Atomique et aux Énergies Alternatives CEA Saclay, France: Prof. A. Filoramo

2016-2018

---

## **Bilateral Agreements**

*Crisan O*

### **Bilateral cooperation agreement Romania-France PN-III-P3-3.1-PM-RO-FR-2016-0043**

Project Director

---

*Kuncser V*

**Task Partner of the National Research Council (CNR) Italy**, within the FREECATS project financed by the European Institute of Technology, RawMaterials.

2017-2018

---

*Badica P*

**Romania (INCDFM+UPB) - Ukraine (National Technical University of Ukraine**. Kiev Polytechnical Institute”), Bilateral Cooperation PN3-P3-127.3BM/2016, “New composite materials New hard ceramic composite materials for cutting tools”

2016-2017.

*Grigoroscuta M*

**INCDFM – NIMS**, cooperation by the NIMS “MSc, PhD scholarships for internships” programme, Textured Ceramics (c-axis oriented MgB<sub>2</sub> bulks by high magnetic field), Tsukuba, Japonia,

11 Sept-1 Dec. 2017

---

*Stan GE*

**University of Aveiro, Portugal**

Development of a new generation of highly biocompatible dental titanium implants functionalized by sputtering techniques with novel bioactive glass materials

2016 – 2020

---

*Stanculescu A*

**University of Angers- Photonics Laboratory, France**

Accord de coopération scientifique dans le domaine des films minces notamment sur les thématiques suivantes: structures multicouches organiques à basse dimension et composites organiques et hybrides.

---

*Stanculescu A*

**University of Western Cape, Departament of Chemistry, SensoLab, South Africa**

Polymeric single/multilayer heterostructures for photovoltaic and electronic applications; polymeric field effect transistors for sensing applications; organic and hybrid devices (realisation, characterization)

---

*Badica P*

**Tohoku University, Japan**

Joints of superconducting tapes: fabrication and characterization

Project: ICC-IMR Visiting Prof. collaboration and exchange of researchers/students INCD-FM- HFSLM-Tohoku University

---

*Baibarac M.*

**Institut des Materiaux Jean Rouxel, Nantes, France**

Surface plasmons enhancement of optical properties of SWNTs, highly separated in metallic and semiconducting components, electrochemically functionalized with conjugated polymers.

---

## International cooperation projects

*Ciurea ML*

**Department of Physics and Astronomy, University of Catania, CNR-IMM, Catania, Italy**

Ge-based nanostructures for applications as photodetectors or transparent electrodes for photovoltaic cells

---

*Ciurea ML, Lepadatu AM*

**Istituto Nazionale di Fisica Nucleare-Laboratori Nazionali di Frascati, Frascati, Italy**

Nanostructures based on Ge nanoparticles immersed in oxidic matrices for optical sensors applications

---

*Ciurea ML*

**Reykjavik University, School of Science and Engineering, Iceland**

GeSi nanocrystals in oxides with targeted photoconductive properties in VIS-NIR

---

*Kuncser V*

**Applied Materials Laboratory, Universitatea Portsmouth, UK, Asoc. Prof. Melvin M. Vopson**

---

*Crisan O*

**Swiss Federal Laboratory for Materials Research & Technology, EMPA, Thun, Switzerland**

Prof. Patrik Hoffman

---

*Crisan O*

**John Dalton Institute, Manchester Metropolitan University, Manchester, UK**

Prof. John Colligon

---

*Crisan O*

**Institut des Materiaux et Molecules du Mans I3M, Fac. Des Sciences, Universite du Maine, Le Mans, France**

Prof. N. Randrianantoandro

---

*Crisan O*

**Department of Renewable Energy, University of Sharjah, United Arab Emirates**

Prof. Hamid al-Naimyi

---

*Miclea CF*

**Los Alamos National Laboratory, Los Alamos, NM. USA**

Measurements, co-publication, specimen exchange

---

*Miclea CF*

**Max Planck Institute for Chemical Physics of Solids, Dresden, Germany**

Measurements, co-publication, specimen exchange

---

*Nedelcu L*

**Research Center for Development of Far-Infrared Region, University of Fukui, Japan**

Measurements, specimen exchange

---

*Nistor SV*

**Institute of Physics, Czech Academy, Prague**

Investigation by magnetic electronic resonance techniques and optical spectroscopy of the semiconducting II-VI materials optically activated with transitional ions

---

*Nistor SV*

**Physics Department, Antwerp University, Belgium**

Development of new advanced multifunctional materials containing defects

---

*Pintilie L*

**UMP CNRS-Thales, Palaiseau, France and Université Paris-Sud**

Measurements, specimen exchange

---

*Pintilie L, Pintilie I*

**University of Oulu, Finland**

Ferroelectric measurements

---

*Pintilie L*

**Technical University Darmstadt, Germany**

Specimen exchange, co-publication

---

*Pintilie I*

**Oslo University, Norway**

Specimen exchange, working stages

---

*Pintilie L*

**UMP CNRS-Thales, 1 Av. Fresnel, Palaiseau, 91767, France and Université Paris-Sud**

Specimen exchange, common measurements

---

*Preda N*

**Yildiz Technical University, Turkey**

Learning Agreement for Traineeships within the ERASMUS Program

---

*Predoi D*

**Institut de Chimie de la Matière Condensée de Bordeaux CNRS-UPR 9048 France**

Elemental analysis, hydrogen storage

---

*Predoi D*

**Universite Bordeaux, EA 4592 Géoresources&Environnement, ENSEGID, France**

Collaboration project IFA CEA C2-06, TEM, environment tests

---

*Predoi D*

**Marcoule Institute for Separative Chemistry, France**

---

*Predoi D*

**Technical University Ostrava, Czech Republic**

---

*Predoi D*

**Institute of Life Sciences Research and Technologies: Laboratory of Chemistry and Biology of Metals (LCBM) Grenoble, France**

Collaboration project IFA CEA C4-05- biological tests

---

*Predoi D*

**Institut des Sciences de la Terre d'Orléans, France**

Raman, ICP, magnetic measurements

*Predoi D*

**Université du Havre, France**

Ultrasound studies

---

*Predoi D*

**Horiba Jobin Yvon S.A., France**

Zeta potential, DLS, photoluminescence

---

*Predoi D*

**University of Dayton, Research Institute, USA**

Carbon nanotubes

---

*Stoica T*

**Peter Grünberg Institute, Forschungszentrum Jülich, Germany**

2D materials based on chalcogenides of transition metals, 2D-TMD

---

*Teodorescu CM*

**Elettra Trieste (Italy)**

CoSMoS -Combined Spectroscopy and Microscopy operating at SuperESCA

---

*Teodorescu CM*

**IRAMIS CEA Saclay (France)**

Chemical switching of ferroelectric surface topology (RO-FR PN-II-ID-JRP-2011-2 project)

# VISITORS

---

## Invited within the C-ERIC consortium

---

### Hassan WAHAB

Pakistan Institute of Nuclear Science & Technology (PINSTECH), Electronic and Magnetic Materials Group, NPD PAKISTAN

Temperature dependent structural phase transition of novel Zn and in co-doped Fe<sub>3</sub>O<sub>4</sub> nanoparticles

Consortium C-ERIC, Lab. 50 electron microscopy group

(invitation Dr. C. Ghica)

**16-17.04.2018**

---

### Anna DMITRUK

Wrocław University of Science and Technology, Faculty of Mechanical Engineering POLAND

Investigation of the interface between Al matrix and MAX phase reinforcement in composite materials fabricated by squeeze casting infiltration of porous Ti-Al-C or Ti-Si-C MAX phase performs

Consortium C-ERIC, Lab. 50 electron microscopy group

(invitation Dr. C. Ghica)

**02-07.05.2018**

---

### Barbara CAVALAZZI

Università di Bologna ITALY

Nanocrystals as biosignatures in 3.5 billion years old microbial remains

Consortium C-ERIC, Lab. 50 electron microscopy group

(invitation Dr. C. Ghica)

**14-17.05.2018**

---

### Amjad NISAR

Pakistan Institute of Nuclear Science & Technology (PINSTECH) Materials Division, NPD PAKISTAN

Morphological and structural investigation of polyoxometalate nanobuilding block, (DODA)<sub>3</sub>P-W<sub>12</sub>O<sub>40</sub>, self-assembly behavior exposed to high temperature and pressure conditions

Consortium C-ERIC, Lab. 50 electron microscopy group

(invitation Dr. C. Ghica)

**21-25.05.2018**

---

### Johannes MUNKE

FRM II - Forschungs-Neutronenquelle Heinz Maier-Leibnitz GERMANY

HRTEM study of the high temperature phase present at the new VDM-780 Premium Ni-base superalloy

Consortium C-ERIC, Lab. 50 electron microscopy group

(invitation Dr. C. Ghica)

**28-31.08.2018**

---

**Navpreet KAUR**

Università di Brescia ITALY

Surface doping of nanostructured MOX chemical sensors by ion beam irradiation

Consortium C-ERIC, Lab. 50 electron microscopy group

(invitation Dr. C. Ghica)

**05-09.11.2018**

---

**Jose da SILVA**

Departamento de Fisica Universidade do Minho PORTUGAL

Ferroelectric/TMDs hybrid structures for memory applications

Consortium C-ERIC, Lab. 50 electron microscopy group

(invitation Dr. C. Ghica)

**19-23.11.2018**

---

**Working stages (foreign students or researchers who came to work in INCDFM)**

---

**Mr. Ricardo Leote (PhD)**

Project contract: Nr. 27/01.09.2016

**Date of hiring: 24.10.2018**

---

**Mr. Francisco Martinez (PhD, scholarship granted by the university of origin)**

Pontifical Catholic University of Chile, Santiago, Chile

Work stage within Laboratory 10 -Functional Nanostructures Group **(15.02 - 15.05.2018)**Research theme: Development of an electrochemical immunosensor for the detection of cancer-specific biomarkers

---

**Ms. Nora Ziani (PhD student, Eugen Ionescu scholarship- AUF/MAE)**

Mouloud Mammeri University of Tizi-Ouzou, Tizi-Ouzou, Algeria

Work stage within Laboratory 10 - Heterostructures Group **(23.04 - 20.07.2018)**Research theme: Obtaining and characterization of new thin film materials for photo-voltaic applications

---

**Ms. Sara Laafar** (PhD student, Eugen Ionescu scholarship- AUF/MAE)

Cady Ayyad University, Marrakesh, Morocco

Work stage within Laboratory 10 – Heterostructures Group (**23.04 – 21.07.2018**)

Research theme: Modeling the electrical characteristics of field effect transistors

---

**Ms. Sarah Derbali** (PhD student, co-financing granted by the University of Origin and the Physics and Cultural Foundation at Magurele)

Ibn Tofail University, Kenitra, Morocco

Work stage within Laboratory 10 – Heterostructures Group (**01.04 – 28.06.2018**)

Research theme: Obtaining and characterization of new halogenated organic perovskites

---

**Mr. Mohamed Yassine Zaki** (PhD, co-financing granted by university of origin)

Ibn Tofail University, Kenitra, Morocco

Work stage within Laboratory 10 -(**29.04 – 26.07.2018**)

Research theme: Obtaining and characterization of Cu<sub>2</sub>ZnSnS<sub>4</sub> films

---

**Ms. Yethreb Essouda** (PhD student, Eugen Ionescu scholarship- AUF/MAE)

Monastir University, Monastir, Tunisia

Work stage within Laboratory 10 – Heterostructures Group (**21.05 – 31.07.2018**)

Research theme: Development of new ferromagnetic materials

---

**Ms. Lamyaa Kreit** (PhD student, OEA mobility scholarship granted by ICTP/UNESCO)

Ibn Tofail University, Kenitra, Morocco

Work stage within Laboratory 10 – Heterostructures Group (**10.08 – 31.12.2018**)

Research theme: Analysis of structural, thermal and dielectric properties of biocomposites

---

**Mr. Abdelbassat KENANE** (PhD, PNE scholarship granted by the Algerian government)

Mustapha Stambouli University of Mascara, Mascara, Algeria

Work stage within Laboratories 10 and 40 (**22.10.2018 – 30.05.2020**)

Research theme: Synthesis and characterization of new hybrid polymer materials / clays

---

**Mr. Marwene Oumezzine** (PhD, mobility scholarship granted by the university of origin)

Monastir University, Monastir, Tunisia

Work stage within Laboratory 10 – Heterostructures Group (**4.09 – 18.09.2018**)

Research theme: New ferro-magnetic materials

---

**Ms. Raya Engazou** (master's degree, mobility scholarship granted by the university of origin)

Tunis - El Manar University, Tunis, Tunisia

Work stage within Laboratory 20 - Superconductors Group (29.09. - 27.10.2018)

Research theme: Characterization of calcganogenic films obtained by chemical methods

---

**Ms. Raouia Ben Sadok** (PhD, mobility scholarship granted by the university of origin)

University of Science and Technology - Houari Boumediene, Bab-Ezzouar (Algiers), Algeria

Work stage within Laboratory 20 - Magnetism Group (20.09 - 05.12.2018)

Research theme: Electronic, dielectric and dynamic properties in ABX<sub>3</sub> halogenated perovskites

---

**Ms. Maria Khacheba** (PhD, mobility scholarship granted by the university of origin)

Mohamed Khider University of Biskra, Biskra, Algeria

Work stage within Laboratory 10 - Heterostructures Group (02.11. - 30.11.2018)

Research theme: Structural and electrical design (dielectric, piezoelectric, ferroelectric) of PZT and BT doped ceramics

---

**Ms. Emine Demiryürek** (student, ERASMUS scholarship)

Abant Izzet Baysal University, Bolu, Turkey

Work stage within Laboratory 20 - Superconductors Group (28.09. - 04.12.2018)

Research theme: Manufacturing and characterization of superconducting materials

---

**Mr. Etienne Lallemand** (master's degree, ERASMUS scholarship)

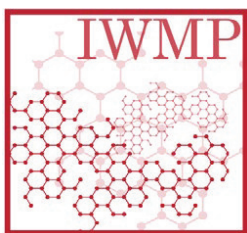
University of Clermont Auvergne, Clermont-Ferrand, France

Work stage within Laboratory 20 - Superconductors Group (01.05. - 01.07.2018)

Research theme: Hard composites based on B<sub>4</sub>C, TiB<sub>2</sub> and Co

---

EVENTS



## 3rd edition of the INTERNATIONAL WORKSHOP OF MATERIALS PHYSICS

**29-30 May 2018**

The National Institute of Materials Physics (NIMP) announces the organization of the 3rd edition of the International Workshop of Materials Physics (IWMP). The topic for 2018 edition is dedicated to 2 dimensional (2D) systems and materials (2D electron gas, graphene, phosphorene, other 2D materials, 2D systems like interfaces, domain walls, etc.). Aspects related to modeling, fabrication, characterization and potential applications of 2D materials and systems will be presented and discussed.

Similar to the first two editions, held in 2016 and 2017, the 3rd edition of IWMP is organized on invitation only. The aim is to attract well known researchers in the field, the final purpose being to establish new collaborations concretized in common publications, projects and exchange of personnel.

Young researchers willing to present their latest results on topics related to the main topic of the workshop are invited to submit a 2 page abstract (A4, Times New Roman 11, single spacing, 2 cm margins, including figures and references) to the organizers ([pintilie@infim.ro](mailto:pintilie@infim.ro)). The best abstracts will be selected for oral presentations during the workshop.

The workshop will take place at NIMP premises located in Magurele, Romania.

The topics for the next two editions:

2019-New materials for renewable energy sources and energy storage

2020-Materials and structures for bio-applications

## IWMP 2018 – Programme

### 29-May-2018

8:45 – 8:55 Opening Ceremony, Ionuț Enculescu, NIMP Măgurele

#### Session I

8:55 – 9:35 Daniela Dragoman (University of Bucharest, Romania)

**Configurations for quantum computing on graphene**

9:35 – 10:15 H. J. W. Zandvliet (University of Twente, the Netherlands)

**The silicon and germanium analogues of graphene**

10:15-10:30 Ionel Stavarache

**Growth and thermal stability of MoS<sub>2</sub> flakes**

10:30 – 10:45 coffee break

#### Session II

10:45 – 11:25 Lucian Baia („Babes-Bolyai” University, Cluj, Romania)

**Understanding the particularities of 2D carbon materials in 3D laminar and porous materials**

11:25 – 12:05 Mauricio Terrones (Pennsylvania State University, USA)

**A review of Defects in Metal Dichalcogenides: Doping, Alloys, Interfaces, Vacancies and Their Effects in Catalysis & Optical Emission**

12:05 – 13:20 lunch

#### Session III

13:20 – 14:00 Vladimir Stokov (Paul Scherrer Institute, Switzerland)

**Electronic structure of buried heterostructure and impurity systems explored by soft-X-ray ARPES**

14:00 – 14:40 Cristoph Stampfer (RWTH Aachen, Germany)

**Van-der-Waals heterostructures based on dry transferred high-mobility CVD graphene**

14:40-14:55 Nicoleta Apostol (NIMP)

**Graphene-like carbon layers grown on ferroelectric Pb(Zr,Ti)O<sub>3</sub>(001)**

14:55 – 15:10 coffee break

#### Session IV

15:10 – 15:50 Andreea Ferrari (University of Cambridge, UK)

15:50 – 16:30 Zahid Hasan (Princeton University, USA)

**Theoretical and Experimental Discovery of Weyl, Nodal-line and Chiral Anomaly Materials**

16:30 – 16:45 Madalina Barsan

**Graphene Based Electrochemical Biosensors for Bio-Medical Applications**

16:45 – 18:00 short visit to NIMP facilities; discussions with NIMP researchers

18:00 – departure for dinner

**30-May-2018****Session V**

9:00 – 9:40 Michel Barsoum (Drexel University, USA)

**From MAX to MXene - From 3D to 2D**

9:40 – 10:20 Simion Simon („Babes-Bolyai” University, Cluj, Romania)

**Self-assembled layers on the surface of oxide biomaterials**

10:20 – 10:35 Adrian Crisan (NIMP)

**Synergetic pinning centers developed at the SrTiO<sub>3</sub>/YBa<sub>2</sub>Cu<sub>3</sub>O<sub>7-x</sub> interface in nanostructured superconducting films**

10:35 – 10:50 coffee break

**Session VI**

10:50 – 11:30 Andrei Bernevig (Princeton University, USA)

**Topological Quantum Chemistry**

11:30 – 12:10 Dimitrie Culcer (University New South Wales, Australia)

**Quantum kinetic theory of magneto-transport in topological materials**

12:10 – 12:25 Marius Husanu

**Modulation of the electron-phonon coupling and effective mass at LSMO/PZT interface**

12:25 – 13:45 lunch

**Session VII**

13:45 – 14:25 Cristian Enachescu („Alexandru Ioan Cuza” University, Iasi, Romania)

**Spin crossover molecular magnets. Theoretical and experimental investigations.**

14:25 – 15:05 Simion Astilean („Babes-Bolyai” University, Cluj, Romania)

**Plasmonic Nanomaterials: From Fabrication to Functional Applications in Nanomedicine**

15:05 – 15:20 Mirela Ilie

**Optical properties of the PPV/RGO composites: insight of the chemical and electrochemical synthesis**

15:20– 15:40 coffee break

**Session VIII**

15:40 – 16:20 Pavlo Zubko (London Center for Nanotechnology, UK)

**Nanoscale domains in artificially layered ferroelectrics**

16:20 – 17:00 invited from ICTP Trieste (TBC)

17:00 – 17:15 Lucian Filip (NIMP)

**Size-driven effects in ferroelectric interfaces with ultrathin layers**

17:15 – 17:30 Raluca Negrea (NIMP)

**Atomic scale characterization of interfaces and extended defects in ferroelectric heterostructures**

17:30 – 17:55 Concluding remarks and workshop closure

18:00 – departure for dinner

# International workshop on Advances in Nanomaterials

[www.infm.ro/iwan\\_2018](http://www.infm.ro/iwan_2018)

## September 17-19, 2018

**Venue: Conference Hall of the National Institute for Materials Physics, 405A Atomistilor Street, Magurele, Romania**

The workshop, devoted to several domains of nanophysics, will be mainly focused to (i) Low dimensional systems and heterojunctions, (ii) Size effects, quantum dots and nanomagnetism, (iii) Spintronics and multifunctionality, and (iv) Photovoltaics, photocatalysis and photonics

The workshop will put together researchers with different profiles - experimental, theoretical and computational physicists, chemists and engineers - providing an excellent opportunity for disseminating of the newest research results and for establishing new research directions of common interest as well as for the preparation of new scientific projects.

The lectures will be presented by active researchers in these fields, mainly from Central European countries.

The workshop is organized by:

- ♦ National Institute of Materials Physics (NIMP, Magurele - Bucharest, Romania) with its International Center for Training and Advanced Research (Centre International de Formation et Recherche Avancee - CIFRA)
- ♦ University of Bucharest, Physics Department
- ♦ National Institute for Physics and Nuclear Engineering
- ♦ UNESCO Chair of the Horia Hulubei Foundation

**Scientific directors:** Stefan Antohe (University of Bucharest), Ionut Enculescu (NIMP), Nicola Seriani (ICTP)

**Scientific Secretaries:** Victor Kuncser (NIMP), Victor Baraan (HHF), Gabriel Schintele (NIMP)

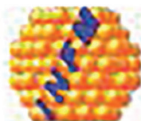
**Local Organizer:** Cristina Militaru, Narcis Barascu

**Sponsors:**

ICTP Trieste  
National Institute of Materials Physics



The Abdus Salam  
International Centre  
for Theoretical Physics



CIFRA  
International Centre for  
Training and Advanced Research



**17<sup>th</sup> September 2018**

**9.15 - 9.30 Official opening Nicola Seriani, Stefan Antohe, Sabin Stoica, Lucian Pintilie**

**2.1**

**9.30 - 11.00 Size effects, quantum dots and nanomagnetism**

**Chairperson Nicola Seriani**

**9.30 - 10.00 Mira Ristić, Rudjer Boskovic Institute, Zagreb, Croatia: Microstructural and optical properties of electrospun metal oxide nanofibers**

**10.00 - 10.30 Stjepko Krehula, Rudjer Boskovic Institute, Zagreb, Croatia: Influence of Metal Doping on the Properties of 1D Iron Oxide Nanoparticles**

**10.30 - 11 Marko Boskovic, Vinca Institute of Nuclear Sciences, Belgrade, Serbia: AC magnetometry for hyperthermia applications**

**11-11.30 Coffee Break**

**2.2**

**11.30 - 13.00 Size effects, quantum dots and nanomagnetism**

**Chairperson Mira Ristić**

**11.30 - 12.00 Madalina Cursaru, National Institute of Non-ferrous and Rare Metals, Bucharest: The influence of synthesis parameters on iron oxide nanoparticles**

**12.00 - 12.30 S. Greculeasa, National Institute for Materials Physics, Magurele - Bucharest: Multifunctional and tunable iron oxide nanoparticles prepared by laser Pyrolysis**

**12.30 - 13.00 V. Barsan, National Institute for Physics and Nuclear Engineering and the Horia Hulubei Foundation, Magurele - Bucharest: Applications of generalized Lambert functions in nanomagnetism**

**13.00-14.15 Lunch**

**3.1**

**14.15 - 16.15 Photovoltaics, Photocatalysis and Photonics**

**Chairperson Stefan Antohe**

**Suzana Topuzoski, Sts. Kiril and Metodius University, Skopje: Shaping Laguerre-Gaussian laser modes (with or without phase singularities) by using fork-shaped gratings (14.15 - 14.45)**

**14.45 - 15.15 Sorina Iftimie, Physics Department, Bucharest University: Organic and biologic thin films based photovoltaic devices: preparation, characterization and optimization**

**15.15 - 15.45 Lucia Leonat, National Institute for Materials Physics, Magurele - Bucharest: Degradation and Defects in perovskite solar cells**

**15.45 - 16.15 Silviu Polosan: Organic Light Emitting Diodes (OLED). Past and Future**

**16.15-18.00 Coffee Break + Visits + Discussions**

**Dinner**

18<sup>th</sup> September 2018

## 3.2

9.30 - 11.00 Photovoltaics, Photocatalysis and Photonics

Chairperson Suzana Topuzoski

9.30 - 10.00 Nicola Seriani, ICTP - Trieste: Photoelectrochemistry of water splitting from first principles

10.00 - 10.30 Ana-Maria Panaitescu, Physics Department, Bucharest University : Fabrication and characterization of Cu nanowire arrays for photovoltaic applications

10.30 - 11.00 Camelia Florica, National Institute for Materials Physics, Magurele - Bucharest: Semiconducting metal oxide nanowires for energy applications.

11-11.30 Coffee Break

## 3.3.

11.30 - 13.00 Photovoltaics, Photocatalysis and Photonics

Chairperson Nenad Novkoski

11.30 - 12.00 Radu Dragomir, National Institute for Materials Physics, Magurele - Bucharest: Transient transport properties of nanoelectrochemical system

12.00 - 12.30 Mihai Grigoroscuta, National Institute for Materials Physics, Magurele - Bucharest: Spectral up-conversion of Yb/Er doped CeO<sub>2</sub> thin films on Si solar cells

12.30 - 13.00 Andreea Nila, National Institute for Materials Physics, Magurele - Bucharest: The optical properties of TiO<sub>2</sub> in the doped state. The influence of SiO<sub>2</sub> and Silver nanoparticles.

13-14.15 Lunch

14-15-15.30: Discussions with the Humboldt Foundation Representatives

## 4.1

15.30 - 17.00 Low dimensional systems and heterojunctions

Chairperson Felicia Tolea

15.30 - 16.00 Nenad Novkovski, Sts. Kiril and Metodius University, Skopje: Interface state densities in different heterojunctions

16.30 - 17.00 Andra Georgia Boni, National Institute for Materials Physics, Magurele - Bucharest: Ferroelectric/Multiferroic heterostructures: potential applications in electronics

17.00 - 17.30 Victor Kuncser, National Institute for Materials Physics- Bucharest: Specific magnetism and magneto-functionalities in amorphous RE-TM thin films

Discussions

Dinner

---

**19<sup>th</sup> September 2018**

---

**4.1**

---

**9.30 - 10.30 Low dimensional systems and heterojunctions****Chairperson Svetozar Music**

---

**(9.30 - 10.00) Erick Vesselli, University of Trieste: Vibronic and chemical properties of supported single metal atom catalysts**

---

**Cristian M. Teodorescu, National Institute for Materials Physics, Magurele - Bucharest: Heterostructures realized on surfaces of ferroelectric thin films (10.00-10.30)**

---

**10.30-10.45 Coffee Break**

---

**4.2**

---

**10.45 - 11.15 Low dimensional systems and heterojunctions****Chairperson Erik Vesseli**

---

**10.45 - 11.15 Felicia Tolea, National Institute for Materials Physics, Magurele - Bucharest: Multifunctional magnetic materials: Superposed shape memory and magneto-caloric effects**

---

**11.15 - 11.30 Nicola Seriani, ICTP, Final Remarks**

---

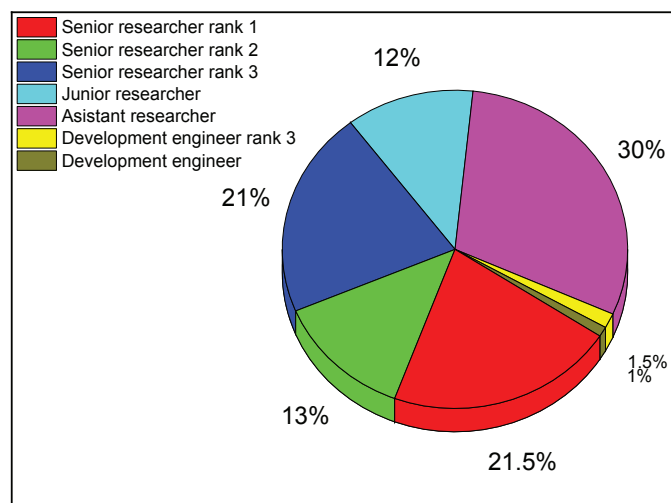
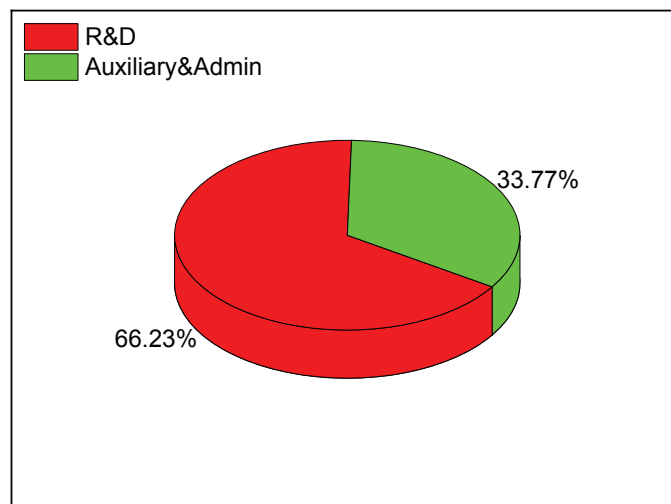
**11.45-12.45 Lunch**

---

# PERSONNEL SUMMARY

# PERSONNEL SUMMARY

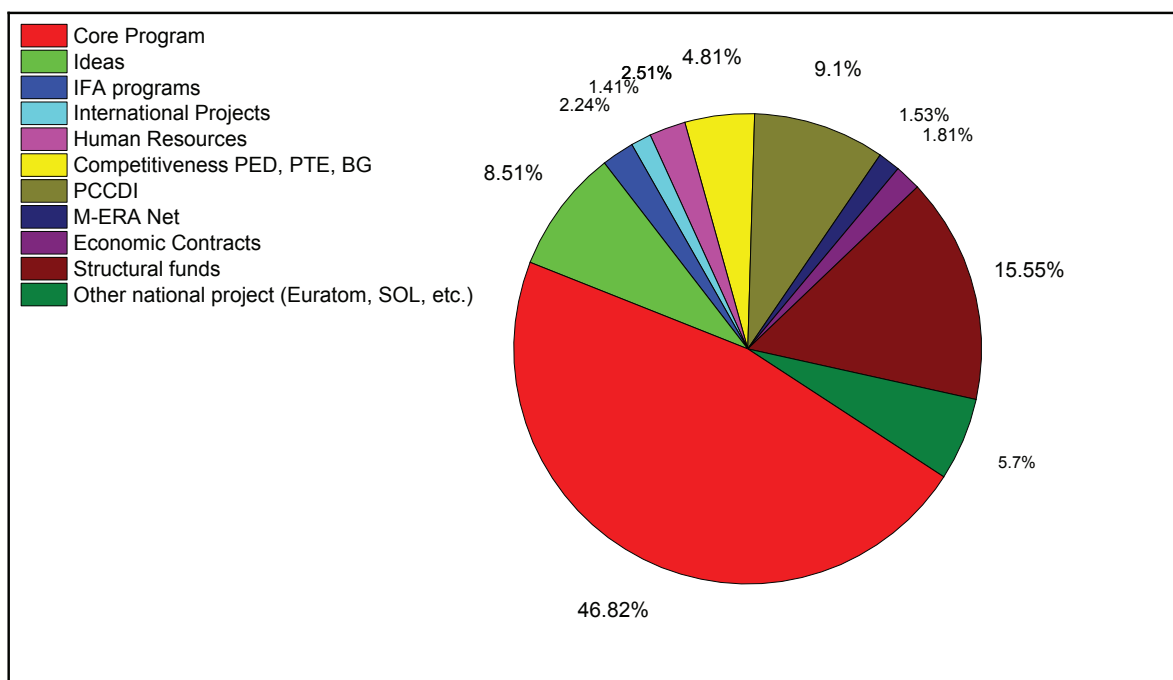
R&D	200	Senior researcher rank 1	43
Auxiliary&Admin	102	Senior researcher rank 2	26
		Senior researcher rank 3	42
		Junior researcher	24
		Assistant researcher	60
		Development engineer rank 3	3
		Development engineer	2



# FUNDING SUMMARY

## Funding Summary (in lei)

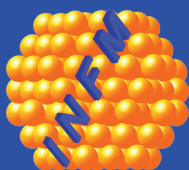
Core Program	19,797,823
Structural funds	6,573,728
Ideas	3,598,588
PCCDI	3,848,835
Competitiveness PED, PTE, BG	2,033,508
Human Resources	1,061,725
IFA programs	948,000
International Projects	598,240
M-ERA Net	645,256
Other national project (Euratom, SOL, etc.)	2,410,976
Economic Contracts	765,014







Scan the QR code, for  
electronic version



## National Institute of Materials Physics

405A Atomistilor Street, 077125, P. O. Box: MG 7 Magurele, Ilfov, Romania

Phone: +4021 369 01 85, Fax: +4021 369 01 77, e-mail: [director@infim.ro](mailto:director@infim.ro), [www.infim.ro](http://www.infim.ro)